Imaging Three-Dimensional Cell-Culture Models for Pre-Clinical Biopharmaceutical Testing

Lucy Ellen Flint

A thesis submitted in partial fulfilment of the requirements of Sheffield Hallam University for the degree of Doctor of Philosophy

In collaboration with AstraZeneca

May 2021

CANDIDATE DECLARATION

I hereby declare that:

- I have not been enrolled for another award of the University, or other academic or professional organisation, whilst undertaking my research degree.

- None of the material contained in the thesis has been used in any other submission for an academic award.

- I am aware of and understand the University's policy on plagiarism and certify that this thesis is my own work. The use of all published or other sources of material consulted have been properly and fully acknowledged.

- The work undertaken towards the thesis has been conducted in accordance with the SHU Principles of Integrity in Research and the SHU Research Ethics Policy. The DESI-MSI data presented in Chapter 4 and 5 in this thesis was obtained through acquisition carried out by Dr Gregory Hamm at AstraZeneca, Cambridge. I played a major role in the preparation and execution of the experiment and preparing the samples, in addition the data analysis and interpretation are entirely my own work.

- The word count of the thesis is 45035.

Name	Lucy Ellen Flint
Award	PhD
Date of Submission	17th May 2021
Faculty	Health and Wellbeing
Director(s) of Studies	Professor Malcolm Clench

ACKNOWLEDGEMENTS

Firstly, I would just like to thank everyone old and new in my life over the past few years. I have thoroughly enjoyed every bit of my PhD, the highs and even the lows. I have met so many amazing, intelligent people from all over the world who have guided and supported me. Even the smallest bit of advice or comfort has helped me along the way, and I have learned so much, for that I am truly grateful.

I would like to give a special thank you to my Director of Studies, Professor Malcolm Clench, for giving me this incredible opportunity. All your support and guidance has given me the confidence to become an independent researcher. I am so grateful for all the knowledge you have passed on and the experiences you have given me, and especially your trust.

With that, I would also like to thank the rest of my supervisory team, Dr Neil Cross, Dr Laura Cole and Dr David Smith. I could not have asked for a better team. I am so appreciative of all the time you put aside to help and support me. In particular, thank you David for encouraging me to apply for the PhD in the first place. A big thank you to Dr Catherine Duckett, you were so friendly and caring, as well as being so enthusiastic about my work.

I would like to thank the MSI team at AstraZeneca for the amazing opportunity to work within their laboratory, teaching me the industry way of research and allowing me to play with their really cool expensive instruments. Thanks to Dr Richard Goodwin for taking me on board and establishing an official collaboration during my project. In addition, a special thanks to Dr Gregory Hamm who has become my mentor and friend. I am forever grateful for everything you have taught me and all your support. You helped me become a true mass spectrometrist.

A huge thank you to everyone in the BMRC, you have been my big crazy science family. Everyone has been so supportive and caring through my absolute highest and lowest. I have made so many amazing memories with you all. To the “BMRC Team” who started this journey with me, I could not have asked for a better group of people to get me through the toughest times. You have given me so much laughter with the most bizarre conversations and drunken antics. Also, a personal thank you to Joe Ready for letting me bug you with millions of questions about the LA-ICP and letting me facetime you constantly when I was trying to work the bloody thing. You always had so much faith that my experiments were going to work even though I had little, thank you for spending so much time helping me.

The biggest thanks of all is to the girls, Cristina, Paula, Oana, Sonia and Katie. You have no idea how much you mean to me. I am so grateful for all the weird and wonderful moments with lots of stupidity and laughter getting me through the stress and tears. You have been so supportive and loving; I know our friendship is going to last a lifetime.

I would also like to thank my amazing friendship group at home, the “Seven Wonders of the World”, you are my rock. Thank you for understanding all the times I had to hide away and focus on my work but being there at the end of it all, you have been my cheerleaders keeping me going. To “The Power Studs” I am so lucky to have you all as friends.

Finally, I would like to thank my family from the bottom of my heart. To the Laing’s and the Flint’s, I am so grateful to have such a big and wonderful family that is so loving and supportive. You have been there through all of the stressful times and given me so much love (and wine) through the tears. Thank you for listening to me ramble on about my work and trying your best to understand what it is I actually do. Thank you for encouraging me to try my hardest and being so proud of me, without you I would not have been able to get through it. I love you all so much. A special thank you also to my grandpa, Professor Adrian Allen for all your tutoring in science when I was younger. My teenage self would not believe where I am today. You truly deserve one of the biggest thanks, as without your help I would not have found my passion.

Lastly, I would like to dedicate my thesis to my late Granny Flint who always believed in me and thought one day I was going to cure cancer. I know you will be so proud of me for finishing my PhD, and as Frank said, “I did it my way”.

ABSTRACT

Mass spectrometry imaging (MSI) is a multiplex methodology that has the capability to map molecular distributions within biological tissues via an unlabelled approach. The ability of MSI to detect a drug, its active metabolites and the molecular changes to treatment has demonstrated value for pre-clinical efficacy and toxicity studies in the pharmaceutical industry. Parallel to the developments in MSI, three-dimensional (3D) cell cultures have emerged as biologically relevant models for pre-clinical therapeutic research in part as an attempt to address the economic and societal issues of the use of animals in science. The combination of MSI with 3D cell culture models has previously been shown to provide an elegant method for small molecule drug analysis; however, with recent progress in the development of biopharmaceuticals there are increasing demands for advancements in this field.

Within this thesis, a multimodal MSI approach to analyse a novel aggregated 3D cell culture model for the use in pre-clinical biopharmaceutical testing was developed. Firstly, three “aggregoid” models of cancer were established: two osteosarcoma (MG63 and SAOS-2) and a HCC827 lung adenocarcinoma. Multimodal MSI techniques: DESI, LA-ICP and IMC were employed for a detailed characterisation of the endogenous metabolite, protein and metal content within the tumour models. These methods determined molecular heterogeneity and identified the biological functions that contributed to the phenotypical proliferative and hypoxic microenvironments. Metabolic similarities between the osteosarcoma aggregoid models and clinical tissue was also observed.

The use of multivariate statistics in combination with DESI-MSI analysis of the aggregoid models enabled mapping of metabolic responses to three biologic treatments and revealed potential mechanistic drug resistance. In addition, use of the multimodal MSI strategy was successful in the detection of a biopharmaceutical (cetuximab) within the HCC827 aggregoid. A bottom-up MALDI-MSI proteomics approach enabled the preliminary detection of cetuximab via its unique proteotypic peptides. A complementary targeted approach of metal-labelled cetuximab detection by LA-ICP-MSI was also successfully employed.

CONTENTS

LIST OF TABLES

LIST OF FIGURES

ABBREVIATIONS

α-CHCA: alpha-cyano-4-hydroxycinnamic acid

αMEM: alpha modified Eagles medium

µg: microgram

µL: microliter

µm: micrometre

2D: two dimensional

3D: three dimensional

9AA: 9-aminoacridine

ACN: acetonitrile

AcOH: acetone

AP: atmospheric pressure

AUC: area under the curve

$CaCl_2$: calcium chloride

CMC: sodium carboxymethylcellulose

CTOS: cancer-tissue originating spheroids

Da: Dalton

DAN: 1,5-diamionapthalene

DESI: desorption electrospray ionisation

DHB: 2,5-dihydroxybenzoic acid

DMEM: Dulbecco's modified Eagles medium

ECM: extracellular matrix

EDTA: ethylenediaminetetraacetic acid

EGF: epidermal growth factor

EGFR: epidermal growth factor receptor

ESI: electrospray ionisation

EtOH: ethanol

FBS: foetal bovine serum

FFPE: formalin-fixed paraffin-embedded

FT-ICR: Fourier transform-ion cyclotron resonance

FWHM: full width at half maximum

g: gram

GB: gigabyte

H&E: haematoxylin and eosin

HPMC: Hydroxypropyl-methylcellulose

IMC: imaging mass cytometry

IMS: ion mobility spectrometer

imzML: imaging mass spectrometry mark-up language

IPA: isopropanol

ITO: indium tin oxide

kDa: kilodalton

LA-ICP-MS: laser ablation inductively coupled plasma mass spectrometry

LC-MS: liquid chromatography mass spectrometry

LC-MS/MS: liquid chromatography tandem mass spectrometry

LESA: liquid extraction surface analysis

LSE: living skin equivalent

M: molar

MALDI: matrix assisted laser desorption ionisation

MCTS: multicellular tumour spheroids

MeOH: methanol

mg: milligram30

mL: millilitre

mm: millimetre

mM: millimolar

MRI: magnetic resonance imaging

MS: mass spectrometry

MS/MS: tandem mass spectrometry

MSI: mass spectrometry imaging

MVA: multivariate analysis

m/z: mass to charge ratio

NaCl: sodium chloride

Nd:YAG: neodymium-doped yttrium aluminium garnet

ng: nanogram

nL: nanolitre

NSCLC: Non-small-cell lung cancer

OCT: optimal cutting temperature

OS: osteosarcoma

PBS: phosphate buffered saline

PC: phosphatidylcholine

PCA: Principal component analysis

PE: phosphatidylethanolamine

PEG: polyethylene glycol

PET: positron emission tomography

pHPMA: poly[N-(2-hydroxypropyl) methacrylamide]

PI: phosphatidylinositol

PI: propidium iodide

PLS: partial-least squares

PLS-DA: partial-least squares discriminant analysis

ppm: parts per million

PS: phosphatidylserine

PVP: polyvinylpyrrolidone

QTOF: quadrupole time of flight

qWBA: quantitative whole-body autoradiography

ROC: receiver operating characteristic

ROI: region of interest

RMS: root mean square

RT: room temperature

SA: sinapinic acid

SIMS: secondary ion mass spectrometry

S/N: signal to noise

TFA: trifluoroacetic acid

TIC: total ion current

TOF: time of flight

ULA: ultra-low attachment plates

v/v: volume to volume

w/v: weight to volume

w/w: weight to weight

CHAPTER 1. INTRODUCTION

1.1 Introduction

The aim of pre-clinical studies is to determine the safety and efficacy of a drug before it is tested in humans at the clinical stage. The essential information obtained from drug development research includes the delivery and biological effect of a therapeutic, the cellular response to treatment, and its toxicity. Untargeted analytical techniques are highly desired for the bioanalysis of drugs. The current principal technique used in drug development is liquid chromatography (LC) coupled with tandem mass spectrometry (MS/MS) as it can offer a combination of high sensitivity and specificity for a dynamic range of analytes, in addition to the quantitative capabilities that are of considerable interest in the pharmaceutical industry (Rönquist-Nii & Edlund, 2005; Xu *et al.*, 2007; Punt *et al.*, 2019). Whilst LC-MS/MS is of significant relevance in pre-clinical studies, the measurement of a drug is typically achieved through the analysis of blood plasma or tissue homogenates. The limitation of analysing such biological samples is the loss of valuable spatial information. The ability to visualise endogenous and exogenous molecules within tissues can provide vital information of how a therapeutic penetrates, distributes, and metabolises, in addition to observing the biological responses to the treatment. The analysis of blood plasma or tissue homogenates is therefore an inaccurate representation of drug concentrations within organs or specific regions of tissues.

Traditional methodologies employed in pharmaceutical research to spatially localise drugs and endogenous molecules within tissue samples or *in vivo* include immunofluorescence microscopy (Hess, Girirajan, & Mason, 2006), positron emission tomography (PET) (Piel, Vernaleken, & Rösch, 2014), magnetic resonance imaging (MRI) (Chen *et al.*, 2015) or quantitative whole-body autoradiography (qWBA) (Solon & Kraus, 2001). A drawback of these techniques, however, is the targeted nature of the methods that requires prior knowledge about the analyte of interest for which fluorescent tags or radiolabels are needed, and thus the number of molecules that can be visualised simultaneously is restricted. In addition, the conjugation of probes onto drugs can affect their ability to reach its target or alter its biological effect, and therefore could misrepresent its true therapeutic nature (Liu *et al.*, 2018). The analysis of drugs using probes has also limited use within human subjects and can add

complications when comparing between pre-clinical and clinical results (Krohn *et al*., 2007).

On the other hand, mass spectrometry imaging (MSI) is an established analytical technique that has the capability to localise thousands of analytes simultaneously in an untargeted manner. MSI allows the visualisation of molecules *in situ* in two- and more recently three- dimensions without the use of labels or probes (Goodwin, Takats & Bunch, 2020). The benefits of MSI in drug development studies are the capabilities to detect the drug, its active metabolites and molecular changes in response to the treatment without prior knowledge (Swales *et al*., 2019). It is also significant in terms of understanding the complex cellular environments within a biological sample through the detection of heterogeneous distributions of molecular species which can facilitate the identification of disease biomarkers (Buchberger *et al*., 2018). A diverse range of MSI techniques have demonstrated the ability to spatially resolve endogenous molecules including small molecules such as metabolites (Ly *et al.*, 2015; Tucker *et al.*, 2019), and lipids (Angel *et al.*, 2012; Henderson *et al.*, 2020), as well as larger molecules such as peptides (Guenther *et al.*, 2011; Ly *et al.*, 2019) and proteins (Stoeckli *et al.*, 2001; Quanico *et al.*, 2013), in addition to exogenous compounds and drugs in biological tissue (Trim *et al.*, 2008; Nilssoni *et al.*, 2015; Dexter *et al.*, 2019). Recent developments have also expanded the capabilities of quantifying analytes of interest *in situ* (Vismeh *et al.,* 2012; Pirman *et al.,* 2013; Swales *et al.*, 2018; Sammour *et al.,* 2019; Handler *et al.*, 2021). The continuous advancements of MSI, including the high sensitivity and specificity of analyte detection as well as the increasing spatial resolution, have rapidly progressed the technique in drug development and has gained a credible reputation within the pharmaceutical industry.

1.2 Mass spectrometry imaging

Imaging mass spectrometers are composed of three main components: an ionisation source which generates charged ions from the tissue sample; a mass analyser that separates the ions based on their mass to charge (*m/z*); and an ion detector that measures the relative abundance of the selected ions. The basic principle of MSI is the movement of the ionisation beam rastering across a tissue sample in the x, y direction. At each point across the tissue, chemical species are

ionised and desorbed, which are subsequently extracted into the mass spectrometer. The ions are then sorted by a mass analyser prior to a detector measuring the relevant abundance of the ions of interest. Software is used to reconstruct an image in which each pixel contains a mass spectrum that represents the ions detected from that specific point in the tissue. An image can be generated for any specific *m/z* value detected showing the distribution of that species and its relative abundance within the region of interest (ROI), similar to that of a heat map (Figure 1.1).

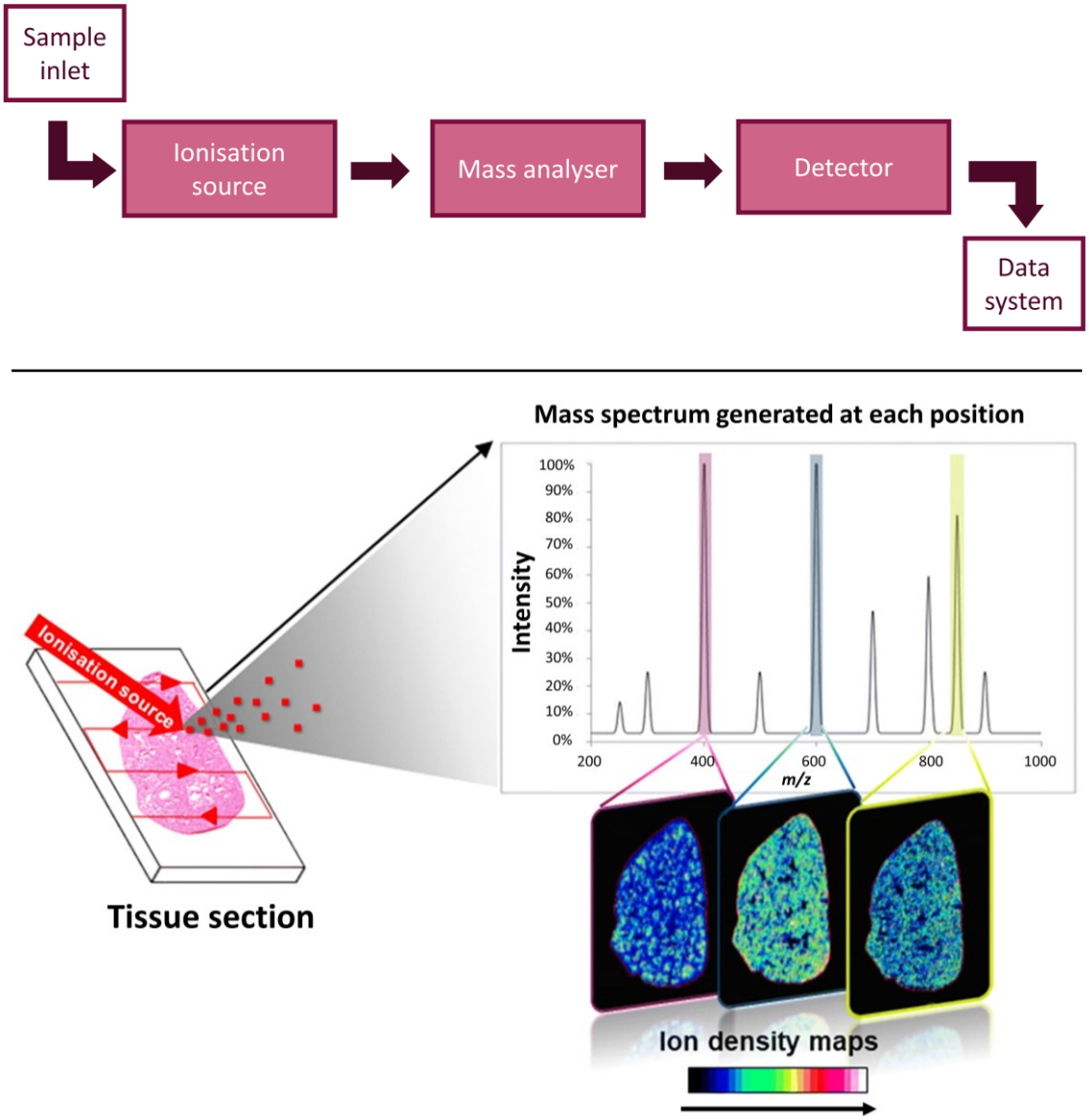

Figure 1.1 Basic principles of MSI. (Above image) The main components of an imaging mass spectrometer from the sample inlet to the ionisation source where ions are formed. The mass analyser separates the ions based on *m/z* values where they are measured by the detector and the data system generates the image from the measurable signal. (Below image) The fundamentals of MSI: an ionisation source rastering across a tissue section, producing ions which are detected by the mass spectrometer, generating a mass spectrum at each position of the tissue. Below figure from Porta Siegel *et al*., (2018).

The MSI workflow in pre-clinical research is generalised into sample preparation, data acquisition and data analysis. An overview of an undefined MSI workflow is shown in Figure 1.2, however following a specific workflow is determined by differing parameters. A major variant that effects the MSI workflow is the ionisation technique. Many different ionisation techniques have been developed and utilised in drug development and this has been previously reviewed (Swales *et al.*, 2019; Xiao *et al.*, 2020). Table 1.1 highlights some of the main ionisation modalities used in MSI and the attributes of the techniques that influence their use in different imaging applications. The aim of this introduction is to focus on the MSI workflows in relation to the four modalities used in this thesis, these include: matrix-assisted laser desorption ionisation (MALDI), desorption electrospray ionisation (DESI), laser ablation inductively coupled plasma (LA-ICP) and imaging mass cytometry (IMC). The specific considerations of sample preparation for each technique used in this thesis are discussed in section 1.2.2.1.

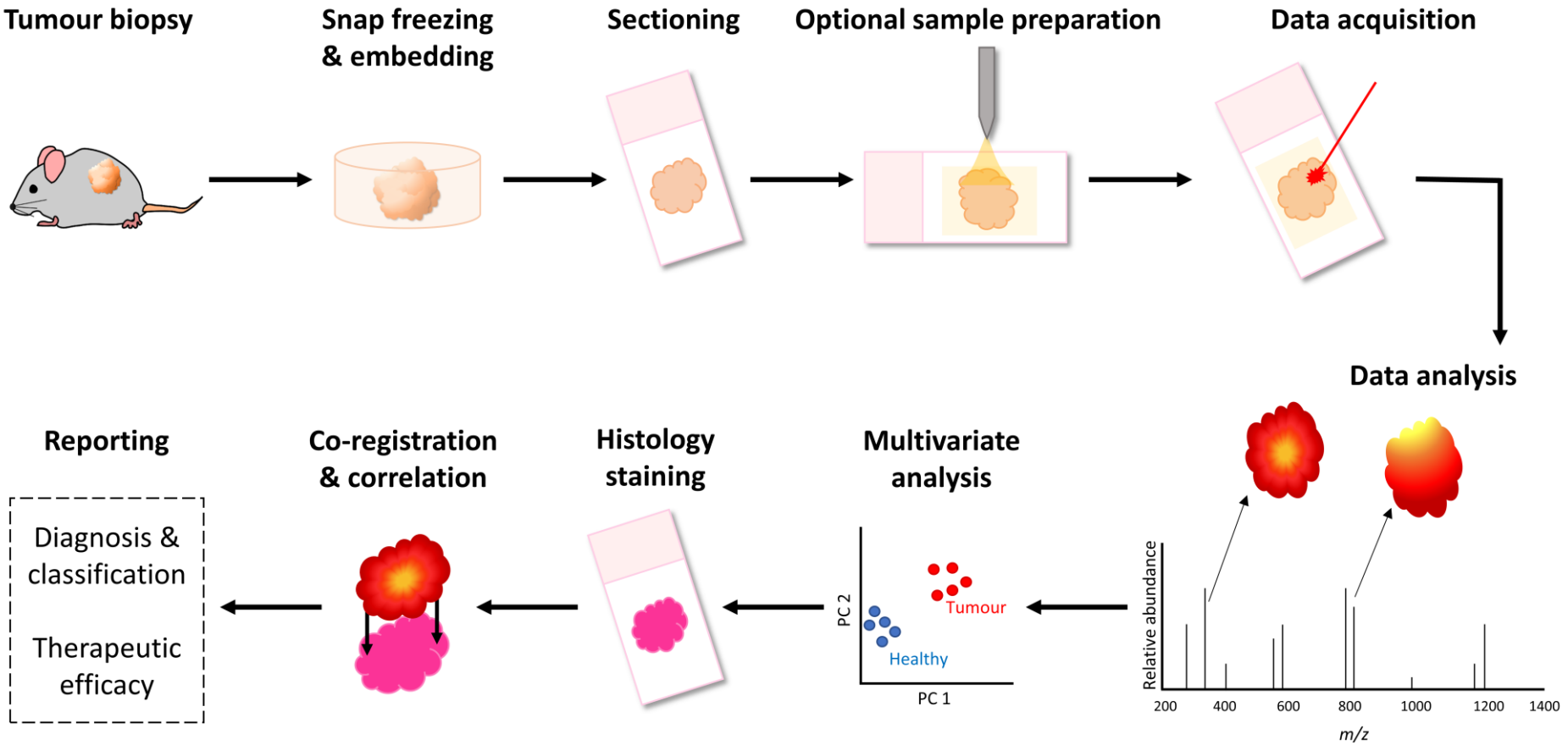

Figure 1.2 An overview of a generic MSI workflow showing the key steps involved from extracting the tumour biopsy to producing the final report.

Ionisation modality	Conditions	Ionisation source	Formation of ions	Matrix	Mass range	Spatial resolution	Application area	Reviewed
Matrix-assisted laser desorption ionisation (MALDI)	Vacuum	UV or IR laser beam (e.g., Nd:YAG at 355 nm)	Primary	α-CHCA, DHB, DAN, 9AA, SA	< 100 kDa	~ 30 – 100 µm < 10 µm reported (Smith *et al.*, 2019)	Metabolites Lipids Peptides Proteins Drug distribution and quantitation	Prideaux, Staab, & Stoeckli, (2010); Schulz *et al.*, (2019)
Atmospheric pressure (AP)-MALDI	Atmospheric	UV laser	Primary	α-CHCA, DHB, DAN, 9AA, SA	< 100 kDa	5 - 20 µm	Metabolites Lipids Peptides Proteins	Guenther *et al.*, (2011); Hiraide *et al.*, (2016)
MALDI-2	Vacuum	UV laser	Secondary (post-ionisation)	α-CHCA, DHB, norhar-mane (NOR)	< 100 kDa	~ 15 – 100 µm	Lipids Small molecule drugs Peptides	Soltwisch *et al.*, (2015); Ellis *et al.*, (2017); Barré *et al.*, (2019)
Secondary ion mass spectrometry (SIMS)	Vacuum	Primary ion beam (e.g., Au^+ or Bi^+)	Secondary	N/A	< 10 kDa	< 10 µm	DNA Metabolites Lipids Peptides Proteins Nanoparticles	Van der Heide, (2014); Massonnet & Heeren, (2019)

Desorption electrospray ionisation (DESI)	Ambient	Charged nebulising solvent (i.e., 95% methanol v/v)	Primary	N/A	< 2 kDa	~ 30 – 100 µm	Metabolites Lipids Drug distribution and quantitation Neurotransmitters	Takáts, Wiseman, & Cooks, (2005); Wu *et al.*, (2013); Xiao *et al.*, (2020)
Nano-DESI	Ambient	Charged nebulising solvent	Primary	N/A	< 2 kDa	~ < 12 µm	Metabolites Lipids Drug distribution and quantitation	Roach, Laskin, & Laskin, (2010); Yin *et al.*, (2019)
Liquid extraction surface analysis (LESA) or liquid micro-junction surface sampling probe (LMJ-SSP)	Ambient	Charged nebulising solvent via nano-electrospray source	Primary	N/A	~ 800 kDa	500 µm – 1000 µm	Metabolites Proteins Drug distribution and quantitation	Van Berkel *et al.*, (2008); Kertesz & Van Berkel, (2010); Swales *et al.*, (2016)

Laser ablation inductively coupled plasma (LA-ICP)	Atmospheric	Plasma	Primary	N/A	6-250 Da Metal isotopes	5 - 200 μm	Endogenous metals Metallodrugs Nanoparticles	Becker, (2013)
Imaging mass cytometry (IMC)	Atmospheric	Plasma	Primary	N/A	75-209 Da Lanthanide metals	< 1 μm	Proteins and protein modifications	Chang *et al.*, (2017)

Table 1.1 A comparison of the main MSI ionisation techniques.

→

1.2.1 Sample preparation

Sample preparation is an important factor of the workflow as the collection and handling of a sample can have a significant influence on the quality of the data acquired. Robust sample preparation protocols have been established for application across MSI methods and have been previously reviewed (Goodwin, 2012). The basic sample preparation workflow starts from the collection of a sample, such as a tumour biopsy from a patient or animal. The sample is then stabilised typically through snap freezing (i.e., in liquid nitrogen), which is then stored at - 80°C until use. In addition, the use of a fixative (e.g., formalin) in imaging studies has also been reported (Ly *et al.*, 2019), although can limit the nature of the study to peptide detection. The purpose of stabilising tissue is to maintain the sample integrity and minimise degradation of molecules. Samples can be embedded using materials such as gelatin to assist handling of smaller fragile tissues or to decrease sample preparation time by embedding several samples in one mould. In the case of frozen samples, tissues are then cryosectioned at subfreezing temperatures (- 15 to - 25°C) typically at a thickness between 10-20 µm, with 12 µm a typical thickness used for MSI (Stoeckli *et al.*, 2001). Sections are thaw mounted onto compatible slides such as glass microscope slides or indium tin oxide (ITO) slides depending on the instrument used for analysis. Frozen tissue sections are then typically stored at - 80°C until use. Prior to analysis, slides are generally desiccated using freeze-dry techniques to remove moisture in order to minimise molecular degradation and delocalisation.

1.2.2 Data acquisition

1.2.2.1 Imaging modalities

The ionisation method chosen for analysis can affect the imaging workflow by the requirement for additional sample processing steps. In this thesis, four ionisation techniques have been employed: MALDI, DESI, LA-ICP and its variant, IMC. The specific steps for the analysis of analytes by these methods are discussed. Figure 1.3 describes the interfaces of each technique.

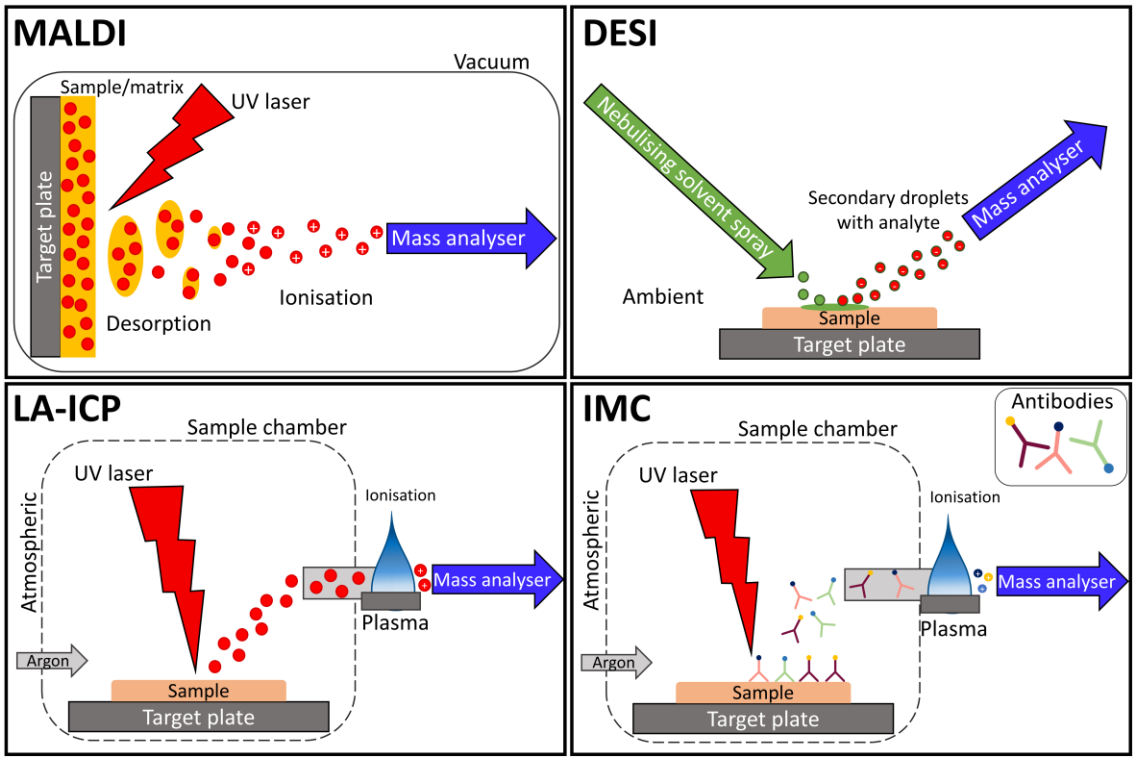

Figure 1.3 A schematic of the MALDI, DESI, LA-ICP and IMC interfaces. These ionisation modalities are the MSI platforms discussed in this thesis.

1.2.2.1.1 MALDI-MSI

In this thesis, MALDI-MSI has been employed for the detection of abundant endogenous lipid species to assess the success of the experiment and exogenous biotherapeutics with the development of a bottom-up proteomics workflow. For the detection of lipids by MALDI, samples are prepared with matrix prior to acquisition, which is discussed later within this section. To detect protein-originated peptides following a bottom-up proteomics approach however, additional sample preparation steps are necessary. Firstly, to enhance the detection of peptides samples can be washed with organic solvents such as ethanol and chloroform to remove salts and lipid species that cause ion suppression of peptide signal due to their high abundance in tissues. A variety of sample washing protocols have been assessed to increase the sensitivity of peptide imaging studies (Schwartz, Reyzer, & Caprioli, 2003; Lemaire *et al.*, 2006; Seeley *et al.*, 2008). In a bottom-up proteomics workflow, proteins undergo enzymolysis to generate peptides by on-tissue digestion in a humid environment. Typically, an enzyme such as trypsin is used to cleave proteins into their constituent peptides at the lysine or arginine amino acid sites. The approach

enables the identification of intact proteins (> 40 kDa) through the detection of proteotypic peptides of a lower mass range (< 4 kDa) which are more ionisable and therefore easier to measure. A comprehensive study comparing multiple on-tissue digestion protocols with MALDI-MSI has been previously reported (Diehl *et al.*, 2015).

The detection of analytes including both lipids and peptides is highly dependent on the selected matrix that is applied to the sample. The MALDI matrix must be capable of absorbing the photon energy emitted by the UV light of the laser at an appropriate wavelength (i.e., 355 nm for a Nd:YAG laser) to promote the desorption and ionisation of analytes. The basic requirements for a matrix are to be stable under a vacuum, accept or donate a proton to the analytes during ionisation, have a similar solubility in solvents as the analytes and the ability to crystalise. Typical matrices used in MALDI-MSI experiments for the detection of lipids and peptides are α-cyano-4-hydroxycinnamic acid (α-CHCA) or 2,5-dihydroxybenzoic acid (DHB) in positive mode. However, other matrices including 9-aminoacridine (9AA) and 1,5-diaminoapthalene (DAN) have been used for the extraction of lipids in negative mode, in addition to sinapinic acid (SA) for the detection of proteins in positive mode. The solvent to dissolve the matrix can also have impact on analyte extraction. Typically, solvents such as acetonitrile, methanol or ethanol are mixed with small concentrations of an organic acid (commonly trifluoroacetic acid (TFA), 0.1-1% v/v) in water to dissolve both hydrophobic and water-soluble molecules in solution. The concentration of organic solvent and acid, in addition to the matrix concentration are generally optimised for different analytes of interest.

The application of matrix is also an important parameter in MALDI-MSI analysis. It is fundamental that the matrix is applied homogenously to minimise variation in analyte signal across the sample. In addition, the crystal size of the matrix can have great influence on the spatial resolution of the image. The most conventional method of matrix deposition is by spray-coat, typically using commercial systems including HTX TM Sprayer™ or SunChrom's SunCollect™ MALDI Sprayer. These automated systems have enabled a rapid and reproducible method of applying matrix (Djidja *et al*., 2010; Barré *et al.,* 2019; Hermann *et al.,* 2020). Alternatively, micro-spotting techniques, such as the Portrait™ 360 acoustic spotter, dispense picolitre volumes of matrix across the tissue in a predefined

array creating matrix spots 100-200 µm apart (Aerni, Cornett & Caproli, 2006). However, the micro-spotting method can hinder the spatial resolution capabilities of MSI analysis. Aside from these 'wet' matrix applications, 'dry' methods are also heavily employed in MALDI-MSI studies (Hankin, Barkely & Murphy, 2007; Angel *et al.,* 2012; Handler *et al*., 2021). Sublimination offers a way of generating sub-micron sized crystals applied homogenously across the tissue which gives the opportunity to generate images of high spatial resolution. The advantage of using a dry technique also minimises the possibility of analyte delocalisation which commonly occurs in the presence of a solvent in the matrix. The signal intensity of analytes by sublimination can be relatively low due to the lack of solvent which normally facilitates the extraction of analytes.

After analysis, post-preparation of MALDI samples is possible due to the 'soft' ionisation nature of the technique. Most commonly, samples are prepared for histology staining after MSI analysis. An additional step of removing matrix using a solvent such as 100% ethanol prior to the staining process is required. The benefits of post-preparation such as histology staining the same section allows co-registration with the MALDI image to correlate molecular distributions with morphological ROIs.

1.2.2.1.2 DESI-MSI

The use of DESI in the MSI workflow generally requires relatively limited to no sample preparation, according to the application or the nature of the biological sample. Due to the ambient conditions of the technique, whole living tissue samples can be imaged directly, however DESI is generally restricted to flat and regular surfaces therefore in the case of animal organs or tissues, cryosections are still most commonly analysed. The use of DESI-MSI in this thesis was for the detection of metabolites in tissue cryosections which were analysed directly without sample preparation. Due to the use of a specific nebulising solvent (i.e., 95% methanol/water, v/v) for the ionisation of analytes there is minimal destructive sampling. This is beneficial, since it permits further analysis by mass spectrometric methods such as MALDI-MSI and IMC, or other visualisation methods (i.e., histology) in order to obtain a greater amount of data that is complementary.

1.2.2.1.3 LA-ICP-MSI

Similar to DESI, no additional sample preparation is required for LA-ICP-MSI analysis. Tissue sections can be analysed directly in the laser ablation chamber under atmospheric pressure. Using LA-ICP-MSI, the sample is near to fully ablated using a high energy 213 nm Nd:YAG laser and therefore post-preparation analysis of tissue sections is normally not possible. Typically, optical images of the sections are taken prior to analysis or serial sections are used for histological staining.

1.2.2.1.4 IMC

Analysing samples by IMC is a novel approach that requires tissue sections to undergo immunostaining with rare lanthanide metal-labelled antibodies prior to laser ablation. The detection of proteins and protein-modifications are achieved through measuring the relative abundance of the metal isotopes. Unlike the conventional MSI techniques that are commonly performed in an untargeted manner, IMC requires some prior knowledge of the protein content within the biological sample. Compared to traditional immunostaining methods, however, IMC has the capability to analyse up to 50 specific markers simultaneously within a single tissue section (Chang *et al.*, 2017). A limitation of IMC is the added time needed to prepare the sample for analysis. Established protocols generally require two days due to the overnight incubation of the antibody cocktail on the tissues to ensure significant antibody binding to the protein targets. Though, due to the nature of the staining protocol, samples can be prepared in advance and left at room temperature for months before analysis. Therefore, bulk staining samples in earlier preparations can reduce the workflow time in future IMC analysis. IMC also fully ablates the tissue and therefore optical images prior to acquisition or staining of serial sections is used to correspond to IMC data.

1.2.3 Data processing

After imaging acquisition, data processing and analysis is the next fundamental part of the MSI workflow in order to generate the images and interrogate the data. The data generated from MSI experiments results in large data files that are typically > 10 GB in size for one image, with some nearing 100 GB. Analysing such complex files thus requires a multitude of image processing steps including data normalisation, baseline correction and spectral alignment before producing

a representative image of the peak of interest. Software packages typically generate an image based on the relative abundance of the analyte of interest by combining the spatial coordinates with the spectral data acquired. Data processing platforms have been developed by various instrument vendors. Previously the aim of using their specific software was to process the unique file type created by the vendor, however this created limitations on multimodal imaging workflows and hindered collaborative studies by being unable to share data across research groups. The MSI community have since introduced imzML as a common file format that can be used universally across most software packages, at least in the case for MALDI and DESI data (Römpp *et al.*, 2010; Schramm *et al.*, 2012). A review summarising the software tools that support the imzML file format currently used in MSI has been previously discussed (Russo *et al.*, 2020).

Developments in software packages have made them more versatile and they now contain additional data processing options to enable improved data mining. For example, the non-commercial software package SpectralAnalysis provides statistical capabilities such as multivariate analysis (MVA) (e.g., Principal component analysis (PCA) and partial-least squares (PLS)) which have allowed interpretation of complex datasets with the prospective of biomarker discovery and treatment assessment (Dexter *et al.*, 2016; Race *et al.*, 2016). In addition, specific quantitation software packages (e.g., msIQuant) have progressed the application of MSI in drug quantitation studies by providing a tool to calculate unknown amounts of an analyte through generating mean relative abundances of calibrants to produce calibration curves (Källback *et al.*, 2016). A powerful MSI software tool, SCiLS™ Lab offers additional data processing capabilities that support untargeted data analysis including spectral spatial segmentation, discriminative receiving operating characteristics (ROC) analysis, 3D image construction and tissue classification of data sets based on training data allowing for further data mining than most software packages (Krasny *et al.*, 2015; Mallah *et al.*, 2018; Ly *et al.*, 2019). The software also facilitates the option to import complementary optical images such as histological or immunofluorescent staining of the same or serial tissue section after analysis. This enables the MSI data to be co-registered with the data obtained from traditional visualisation

methods in order to differentiate and correlate analytes to heterogeneous regions within complex tissues.

In the case of processing data obtained from LA-ICP-MSI and IMC instrumentation, common data analysis platforms used for MALDI or DESI cannot typically support their specific file types. Alternatively, the development of LA-ICP-MSI specific software, such as Igor Pro Iolite Software, has been required, which specialises in time-resolved data reduction with the capabilities of baseline subtraction and normalisation to reference materials in addition to the ability to perform quantitative analysis (Paton *et al.*, 2011). Nevertheless, advancements in software packages such as ProteoWizard (Chambers *et al.*, 2012) have demonstrated an indispensable tool for converting LA-ICP-MSI Excel generated file types (xlsx) to the mzML format for the versatile use in most MSI processing programs. A review evaluating the software platforms used to analyse LA-ICP-MSI data has been recently published (Weiskirchen *et al.*, 2019).

For vendor specific IMC data files (generated in the proprietary mcd format), producing the images is performed by the MCD Viewer software developed by Fluidigm®. This open-source platform allows for the visualisation of the protein markers to produce quality images for publication; however, it is limited to a viewing tool only. Alternatively, in-depth processing of IMC data requires specialist software that is typically commercialised and expensive. For example, advanced imaging software that was initially developed for histological analysis can also support the IMC raw data files. HALO® from Indica Laboratories enables single-cell segmentation allowing for tissue classification and quantification of positive staining within tissues, which can be performed on large data groups through training data sets.

1.3 Pre-clinical disease models studied by MSI

The use of animals in research has become prominent for drug development due to their complex biological environment within a whole organism that provides an advanced *in vivo* representation, modelling specific aspects of human diseases. Animals have been considered the ‘gold standard’ model system in some research for the evaluation of new therapeutic approaches in cancer and disease biology (Hooijmans, Leenaars & Ritskes-Hoitinga, 2010). The combination of MSI with animal models has been demonstrated in numerous drug studies (Chen *et*

al., 2008; Trim *et al.*, 2008; Vismeh *et al.*, 2012; Takai, Tanaka, & Saji, 2014; Swales *et al.*, 2014), with the first MS images of pharmaceutical detection achieved in mouse tumour and rat brain tissues in 2003 by MALDI-MSI (Reyzer *et al.*, 2003). For MALDI-MSI, robust methods of handling and preparing animal specimens have been established, from freezing and sectioning tissues to matrix application (Swales *et al.*, 2018; Huizing *et al.*, 2019; Dannhorn *et al.*, 2020). Therefore, MALDI-MSI is highly validated for pharmaceutical analysis. Continuous developments in other MSI modalities, such as the detection of a wide molecular coverage from DESI-MSI, are also expanding the capabilities of pharmaceutical analysis (Dexter *et al.*, 2019). The value of animal studies as an appropriate model to predict human responses has been challenged (Mignini & Khan, 2006). It is strongly argued that the failure of animal models to replicate human conditions contributes to the failure of the majority of therapeutics at clinical trials (Seok *et al.*, 2013; Ugarte *et al.*, 2018). Further challenges are also raised regarding the regulatory, economic, and societal issues with the use of animal models involved (Russo *et al.*, 2018).

Alternatively, a conventional technique routinely used for *in vitro* research is two-dimensional (2D) cell cultures. The simplicity and low-cost maintenance of monolayer culture is an appealing strategy in biological studies to achieve reproducible high throughput analysis. The applications of SIMS-MSI with 2D cell cultures has been a leading approach to study pharmaceutical development (Passarelli *et al.*, 2015; Vanbellingen *et al.*, 2016). The submicron resolution and nanometre depth of the technique can enable a three-dimensional imaging capability to localise and quantify molecules at single-cell level (Gilmore, 2013). However, the sensitivity and matrix effects of SIMS have impacted its progression in drug efficacy and toxicity studies (Passarelli & Ewing, 2013). Advancements in the spatial resolution capabilities of MALDI, which can provide higher mass resolution across a larger mass range, has demonstrated the ability to profile individual cells of cancer cell lines (Schober *et al*., 2012; Zavalin *et al.*, 2012). Though due to the low volume of material and small quantity of analytes in 2D cultures, the application in pharmaceutical analysis is limited (Comi *et al.*, 2017). Alternatively, the recent developments in IMC has also improved the level of detail of detecting protein expressions at single-cell resolution in drug treated cell cultures (Bouzekri, Esch, & Ornatsky, 2019).

A major criticism of 2D cell cultures in pharmaceutical research, however, is the inability of monolayer cells to reproduce the complexity and heterogeneity of human tissues (Duval *et al.*, 2017). Two-dimensional cell cultures form a monolayer growth, which can influence the interactions between cells and impact components such as the extracellular matrix (ECM) formation, cell signalling, and gene and protein expression that are all vital in drug analysis. The monolayer growth thus alters the function within cell cultures and can result in drug behaviours and responses that do not truly represent the outcome of the *in vivo* environment. Consequently, 2D cell culture experiments often cannot accurately predict drug reactions in a tissue environment, and therefore exhibit substantial limitations for such research (Kapałczyńska *et al*., 2018).

There is high demand for alternative biological models that accurately replicate the *in vivo* environment and responds to the societal requirements to impact on the 3Rs – reduction, replacement and refinement – for the use of animal in research (Russo *et al.*, 2018). Three-dimensional (3D) cell cultures are an advanced system that bridges the gap between 2D cultures and animal models, by having the cheap and high-throughput qualities from 2D cell cultures whilst providing the cellular and molecular complexity of animal models. Growing cells in 3D enhances the organisation and intricacy of cellular cultures so that they more closely mimic the *in vivo* microenvironment of primary tissues. These 3D models promote levels of cell differentiation and tissue organisation, which replicate typical tumour characteristics of gene and protein expression, nutrient diffusion, and cell-cell and cell-matrix interactions (Edmondson *et al.*, 2014). A variety of 3D culture models have been developed to meet the biological requirements for specific research including drug analysis (Reynolds *et al.*, 2017), patient-derived treatment (Huang *et al.*, 2015), and biological crosstalk (Maschmeyer *et al.*, 2015). These models include tumour spheroids, organoids, and microfluidic systems or 'organ-on-a-chip'. Each model varies in their levels of complexity and yet requires relatively low maintenance to achieve representative *in vivo* qualities. With the additional advantages of low cost and high throughput, the use of 3D models is appealing for early stage drug research and development prior to *in vivo* studies.

Studies which combine MSI with 3D cell culture models are currently of considerable interest. Over the last decade, a significant amount of literature has

reported extensive applications in MSI analysis of 3D cultures for pre-clinical drug efficacy and toxicity research. The detection of endogenous molecules including metabolites, lipids and proteins have characterised the tumoral phenotypes of the 3D models. Drug distribution studies have localised therapeutics and their active metabolites, in addition to the cellular response to treatment within specific substructural regions. In addition, developments in MSI have also demonstrated quantitative analysis of drugs in 3D cultures. The current literature in these areas is discussed in detail within this thesis and are summarised in Table 1.3.

1.4 Application of MSI with 3D cell culture models

1.4.1 Tumour spheroids

Tumour spheroids have become invaluable tools for *in vitro* research due to their ability to replicate the important aspects of the *in vivo* microenvironment. First developed in 1971 by Robert Sutherland, these tumour models were initially formed to resemble cancer nodules seen in animal and human carcinomas (Sutherland, McCredie & Rodger, 1971). Spheroids blend the flexibility of cell culture systems with the ability to assume complex cellular architecture. They display a gradient of oxygen and nutrients that can be divided into three regions: a necrotic core, which experiences a high rate of apoptosis due to the extremely poor delivery of oxygen and nutrients; a non-proliferative region, where the cells display a state of dormancy as a result of hypoxia; and a proliferative edge with an abundant supply of nutrients, which accelerates tumour growth (Figure 1.4). These phenotypical microenvironments have a subsequent effect on the endogenous molecules within the spheroid and thus the distribution of such species can determine molecular processes significantly affected by hypoxic conditions, as depicted in Figure 1.5

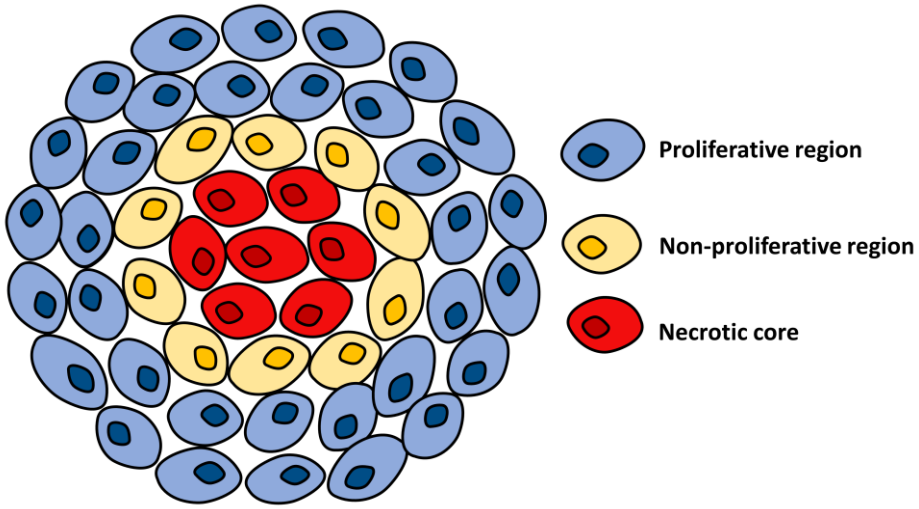

Figure 1.4 A basic diagram showing the phenotypical regions of a necrotic core, non-proliferative and a proliferative region within the tumour spheroid model.

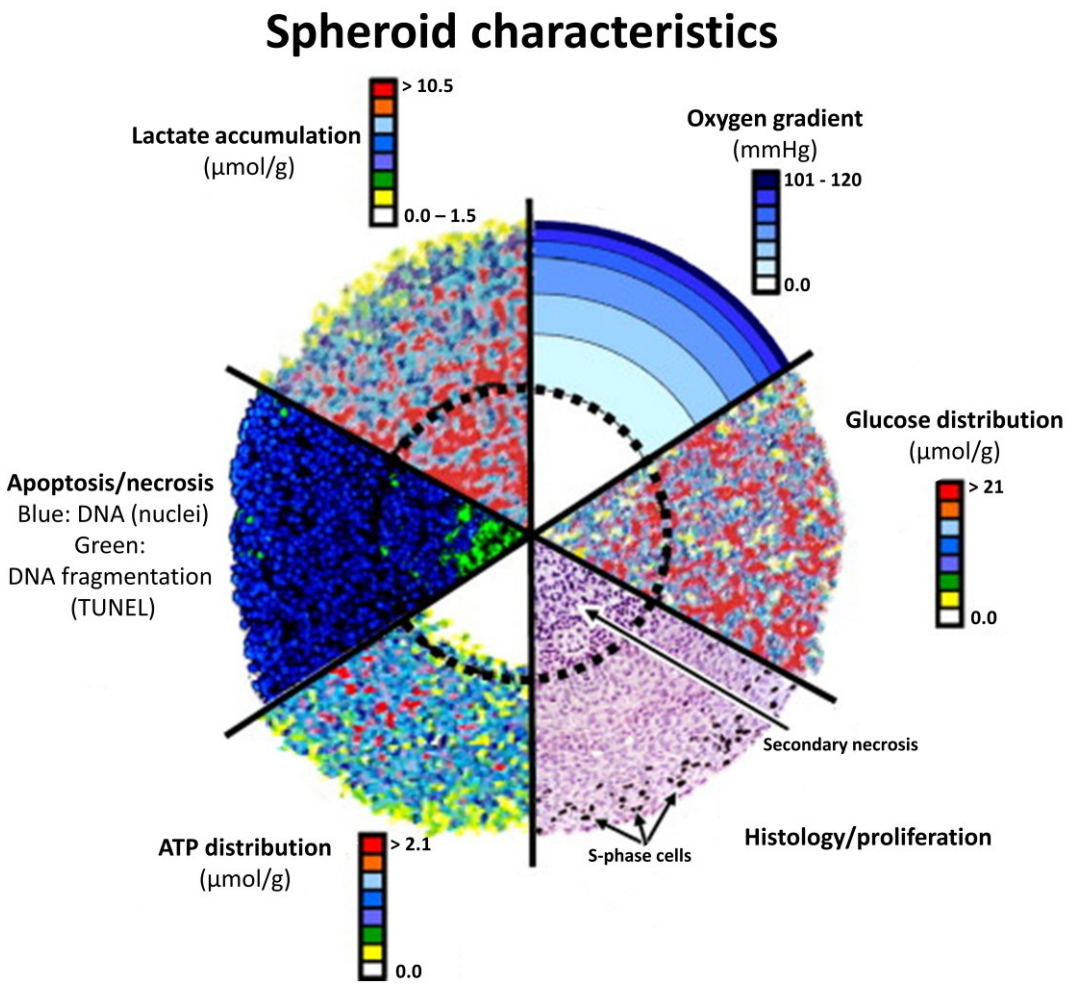

Figure 1.5 Spheroid characteristics from the effects of oxygen and nutrient gradients. Combination of analytical images of spheroid sections obtained by different technologies including autoradiography, the TUNEL assay, bioluminescence imaging and probing with oxygen microelectrodes. These techniques enable the concentric arrangement of cell proliferation, viability, the microenvironment in tumour spheroids to be understood. Figure from Hirschhaeuser *et al*., 2010.

The creation of spheroids can be achieved by a variety of means, either as an independent culture or co-culture with different cell lines. Most conventionally, tumour spheroids are developed through the aggregation of cells from an independent culture via attachment prevention techniques. This is a simple method to produce highly reproducible spheroids relatively fast and at low costs which benefit high throughput drug analysis. Such methods include the use of attachment prevention surfaces such as commercial ultra-low attachment (ULA) plates or matrix coatings like agarose, or the suspension of cells within a droplet of liquid termed 'hanging-drop' (Timmins & Nielsen, 2007; Bartosh *et al.*, 2010). In each technique, cells accumulate together and are forced to interact forming a single spheroid, otherwise known as a multicellular tumour spheroid (MCTS). Some cell lines, however, are unable to form robust spheroid cultures using these methods and different techniques can influence experimental outcome from the same cell line (Nagelkerke *et al.*, 2013; Bresciani *et al.*, 2019).

Alternatively, the use of natural or synthetic scaffolds or culturing with embedding gels may be incorporated into the model. Such scaffolds can bring external ECM properties to facilitate the structure of a cellular environment and develop cell-matrix interactions found *in vivo*. Typical materials used include basement membranes (i.e., Matrigel), collagen, alginate or cellulose, which are derived from natural ECM components (Ma *et al.*, 2003; Fischbach *et al.*, 2007). Synthetic materials such as biopolymer hydrogels can also be tailored to mimic a specific environment for different applications (Li, Yunfeng & Kumacheva, 2018). Using scaffolds allows a single-cell suspension to proliferate into isogenic spheroid populations to enable a more natural development of cultures that resemble *in vivo* properties. The development of spheroids in this manner, however, can be time consuming and the diameter of the cultures are generally smaller than MCTS, which with the spatial resolution capabilities of MSI could present challenges to generate an image with sufficient data points in order to observe the invaluable detail of the tissue.

Type of culture	Cost	Variability	Complexity	Throughput	Ease of culture	Extended incubation
2D cell culture	Low	Low	Low	High	Easy	X
Attachment prevention e.g., ULA or hanging drop	Low-Medium	Low	Medium	High	Easy – Moderate	~ 7 days
Scaffold e.g., alginate or hydrogel	Medium – High	Medium – High	High	Low – Medium	Easy – Moderate	~ 14 days

Table 1.2 Comparison of tumour spheroid types. (Adapted from Palubeckaite, 2018).

1.4.1.1 Characterisation of tumour spheroids by MSI

The Hummon group were the first to publish work describing the combination of MSI with spheroids and have continued leading research utilising spheroid cultures with MSI for drug analysis. Their initial study used colon carcinoma MCTS from the HCT 116 cell line and adapted previous MALDI-MSI protocols for imaging tissue sections, to examine the protein distribution within spheroids (Li & Hummon, 2011). To assist the handling of tumour spheroids, the group embedded the samples within gelatin prior to flash freezing and cryosectioned tissues at a thickness of 10 µm. A protocol describing the workflow of tumour spheroids with MALDI-MSI was published by the group and included the development of the MCTS, sample handling, matrix application and data acquisition (Ahlf Wheatcraft, Liu, & Hummon, 2014). From the study, protein images of the sectioned spheroids were obtained in positive mode at a spatial resolution of 75 µm (~13 pixels across a typical MCTS). MALDI-MSI was able to detect species within specific regions of a spheroid; with the majority of peaks distributed across the section, and a specific unidentified peak at *m/z* 12,828 localised predominantly within the central necrotic region. The individual peaks detected were not identified directly from the MSI data. For protein identification, the group employed an in-gel tryptic digest of the spheroids and identified

species, including Histone H4 and cytochrome c, by MALDI profiling and nanoLC-MS/MS, correlating the *m/z* values to the MSI ion maps. The detection of protein species localised within specific regions of the spheroid identified phenotypic differences that corresponded to the tumour microenvironment, highlighting the hypoxic gradient. The initial MALDI-MSI study of MCTS therefore enabled an understanding of the heterogeneity of protein distributions within the model.

The characterisation of tumour spheroid models has since been explored with MALDI techniques that provide higher mass accuracy and resolving power capabilities for more definitive identifications of molecular species. Hiraide *et al.*, (2016) utilised AP-MALDI-MSI to characterise lipids throughout HCT 116 and DLD-1 MCTS. The group used an MS/MS imaging approach to identify *m/z* 885.5 as an arachidonic acid containing phospholipid PI 38:4 specifically accumulated in the outer edge of the colorectal cancer models. It was suggested this phospholipid was associated with the migration of cancer cells, which thus identified the species as a potential biomarker for metastatic colorectal cancer. In addition, Tucker *et al.*, (2019) employed Fourier-transform ion cyclotron resonance (FT-ICR)-MALDI-MSI for an untargeted approach to identify metabolites in MCF-7 breast cancer spheroids at 50 μm spatial resolution. The localisation of metabolites involved in the adenosine triphosphate (ATP) metabolism, which is fundamental for energy production, determined the oxygen gradient across the spheroid; correlating higher ATP levels with higher proliferative activity in the outer region compared to the central region. The group mapped the ion images of key metabolites to distinct biochemical processes including glycolysis and the hexosamine biosynthetic pathways to improve the understanding of the molecular microenvironment.

In addition, similarities in metabolic signatures including the glutamine, fatty acid and phospholipid metabolism pathways were recently identified between KYSE-30 oesophageal cancer spheroids and clinical patient tissue samples determined by MALDI-MSI at a greater spatial resolution (12 μm) (Zang *et al.*, 2021). The corresponding detection of metabolites to *in vivo* demonstrated the spheroid model as an accurate representative of cancer metabolism. As demonstrated by these studies, characterising the spatial localisation of key endogenous molecules within spheroid models by MSI gives valuable opportunities to unravel

the cellular functions in tumours and can benefit the discovery of biomarkers for drug targeting to improve biological outcome.

1.4.1.2 Analysis of therapeutics in tumour spheroids

The combination of spheroids with MSI has further progressed for drug developmental research. Liu, Weaver, & Hummon (2013) investigated the efficacy of drug penetration by analysing the spatial distribution of irinotecan, an anticancer drug and topoisomerase I inhibitor, over a time-dependent course within HCT 116 colon carcinoma MCTS. Using MALDI-MSI irinotecan (*m/z* 587.3) was observed within the necrotic core only after 12 h of incubation. At 24 h, appreciably higher levels of the parent drug were observed within the central hypoxic region and necrotic core, and higher levels of irinotecan metabolites including the cytotoxic SN-38 (*m/z* 393.1) and SN-38 glucuronide (*m/z* 569.2) were located within the outer region. This study reported that a higher enzymatic activity localised in the proliferative outer layer of the MCTS. The data was validated by nanoLC-MS/MS; however quantitative analysis was not conducted. Rather, an additional study of a simpler and more accurate experimental method to analyse individual cells from spheroid cultures with spatial specificity by serial trypsinisation was published (Liu & Hummon, 2015). The group followed a novel method initially demonstrated by McMahon *et al*., (2012) of short trypsin treatments to sequentially remove cells from the outside of the spheroid in concentric radial layers and compared the process to like ‘peeling an onion’. The concentrations of irinotecan and SN-38 were detected by nanoLC-MS/MS in a time-dependent manner showing the movement of the parent drug from the outer region to the core over 72 h, as the cytotoxic metabolite was quantifiable after 12 h and was more abundant in the outer and middle regions than the core at 72 h. Using a combination of advanced analytical techniques, the Hummon group therefore successfully demonstrated the quantification and localisation a parent drug and its metabolites, determining regions of metabolic activity within a spheroid model.

A similar approach employing the ambient technique, single-probe MSI determined the influence of a series of time- and concentration-dependent irinotecan treatments on metabolite distributions in HCT 116 MCTS (Tian *et al.*, 2019). The group used advanced MVA methods to identify significant changes in metabolite abundances such as a significantly higher relative intensity of PC 32:1

(*m/z* 732.5) of the treated 3D cultures compared to the control, in addition to five times lower abundance of PC 34:2 (*m/z* 758.6) specifically in the inner region of the treated spheroids. These studies therefore demonstrated the analysis of therapeutically treated spheroids by different ionisable imaging modalities to study drug metabolism and cellular response.

The Hummon group has further exploited the MSI-spheroid technique to study the penetration of a range of drugs including platinum-based (Liu & Hummon, 2016), epigenetic-targeting (Lukowski, Weaver, & Hummon, 2017) and liposomal delivery (Feist *et al.*, 2017). LaBonia *et al.*, (2018) recently investigated the penetration of a combinational drug, FOLFIRI (folinic acid, 5-fluorouracil and irinotecan), within HCT 116 MCTS by an innovative 3D printed dosing platform to mimic the dynamic flow of chemotherapeutics used *in vivo*. Similar to the previous study, high levels of cytotoxic metabolites within the outer proliferative region were observed, as parent drugs, irinotecan and folinic acid, were localised within the necrotic core. Further analysis determined the proteomic changes to treatment with FOLFIRI by iTRAQ proteomic analysis acquired on a nano-ultra-performance (UP)LC-MS/MS system. Tryptic peptides labelled with iTRAQ tags allowed for identification of proteins in addition to quantitative fold changes between treated and untreated samples; however, the spatial resolution within the MCTS by this method was lost. Nonetheless, the study provided evidence that MALDI-MSI can detect clinically approved combination therapeutics treated through a representative drug administration route and the active metabolites within the different regions of the spheroid, alongside detecting the proteomic response to treatment using complementary quantitative analysis. Not only does this further support the proposition that spheroids display differing metabolically active regions within the tumour microenvironments, but it also gives valuable insights into the cellular behaviour in response to drug treatment, which could help predict clinical outcome.

Another demonstration of the diverse applications for drug distribution analysis within spheroid cultures is the evaluation of metal-based drugs by LA-ICP-MSI. Although the literature is limited, there has been some interest regarding the localisation of platinum-based drugs and hypoxia-responsive cobalt complexes (Theiner *et al.*, 2017; O'Neill *et al.*, 2017). For example, LA-ICP-MSI analysis of different platinum compounds, including satraplatin, detected heterogenous

distributions between HCT 116 colon carcinoma and CH1-PA-1 ovarian teratocarcinoma spheroid models (Theiner *et al.*, 2016). The study demonstrated high sensitivity with achievable spatial resolution (10 μm laser spot size) for detecting platinum within the periphery and necrotic regions of the spheroid models.

From small molecule chemotherapy to immunotherapy, the Hummon group studied HT 29 and DLD-1 colon cancer spheroid cultures to observe the distribution of the monoclonal antibody, cetuximab by MALDI-MSI. In order to achieve this a direct on-tissue reduction with dithiothreitol (DTT) followed by alkylation was developed by Liu *et al.*, (2018). In this method, a protein is reduced to break the disulphide bonds and alkylated to prevent re-formation by modifying the cysteine residues. Cetuximab was detected using a signal arising from the light chain variable domain at *m/z* 23,412.5. The group observed a difference in the distribution of the light chain domain between the two spheroid models; at 72 h cetuximab was primarily localised within the core of the HT 29 spheroids, whereas in the DLD-1 spheroids it was detected in the outer region. It was confirmed by immunofluorescent staining that this was due to the different expression levels of the antibody target, epidermal growth factor receptor (EGFR) in both cell lines. The light chain domain of cetuximab was also detected within colorectal-tumour organoids at 72 h; however, information about the distribution of the antibody within the organoid section was not given. In addition, the study examined the treatment response by detecting higher intensity signals of ATP (*m/z* 506.0) in the core of the HT 29 spheroids, indicating an increase in apoptosis in the presence of cetuximab. Overall, the study provided proof-of-concept that MALDI-MSI has the capabilities to detect the presence of a complex biopharmaceutical (~150 kDa) within an emerging 3D *in vitro* model, the tumour spheroid, and analyse the cellular response to treatment.

1.4.1.3 Considerations of tumour spheroid analysis by MSI

It is clear from the literature discussed in section 1.4.1 that the combination of spheroids with MSI is a powerful tool to investigate the biological behaviour of replicate *in vitro* tissues and study the efficacy of therapeutic drugs. Although there are a range of applications demonstrated, there are still gaps within the literature. MALDI-MSI has demonstrated great potential with tumour spheroids and is clearly the dominant technique (Table 1.3). However, employing other

imaging modalities could further expand the opportunities in drug analysis with tumour spheroids, such as by detecting a larger amount of metabolite information for biomarker identification or the detection of metal-based drugs as demonstrated by DESI and LA-ICP methods, respectively (Theiner *et al.*, 2016; Robison *et al.*, 2020).

The main spheroid culture investigated by MSI has been MCTS of colon cancer cell lines. Although recent reports of MSI with other models of cancer (i.e., breast and ovarian cancer) have been published, there is still a need to expand the research for range of *in vitro* cancer models. This is primarily to demonstrate heterogeneity of spatially resolved molecules between cancer types and determine their independent response to treatment. Within this thesis, two cancer types have been studied: lung adenocarcinoma and osteosarcoma. Lung adenocarcinoma is one of the most common cancers effecting 1 in 15 people in the UK. The low patient outcome (< 15% at 5 years) has been linked to the aggressiveness of the cancer leading to inconsistent patient results and high resistance to therapeutics (Molinier *et al.*, 2020). On the other hand, osteosarcoma is a rare bone disease more prevalent within adolescents, however the survival rate is relatively low at < 50% at 5 years (Stiller *et al.,*2018). This low rate is again due to a poor understanding of the cancer and thus there is a lack of an effective treatment. Both cancer types have an unmet clinical need, with many of the therapeutics that have initially passed the pre-clinical studies failing at the clinical stage. The development of representative 3D cultures of both cancer types therefore has the potential to progress research towards finding effective therapies.

As previously mentioned, there are various types of spheroids models, such as those made within a biomimetic hydrogel scaffold, which act to recapitulate the behaviour of a native ECM giving an extra dimension to the spheroid model. A MSI experiment with these spheroid types could potentially provide additional information of drug behaviour and biological crosstalk within the ECM, which is essential for certain tissue types that grow within a filamentous structure *in vivo*. Furthermore, spheroids of co-cultured cell lines would provide an extra level of complexity and induce cell-cell interactions between different cellular phenotypes (i.e., epithelial and fibroblastic) and thus possibly give data of greater clinical relevance.

It is argued that spheroid cultures are unable to fully recapitulate the morphological, phenotypic and genetic heterogeneity of *in vivo* tumours (Liu *et al.*, 2018). This is in-part due to the spherical shape they adopt, which does not necessarily capture the complex phenotypical structures observed in patient tumours, thus impacting how the drug behaves and penetrates the system. In addition to this, spheroids of certain cancer cell lines can be difficult to grow large in size (< 100 μm) and prove challenging for MSI to generate an image with sufficient raster spots to observe the sub structure, as well as the low quantity of material available to analyse (David *et al.*, 2018). Although, continuous developments in MSI spatial and mass resolution are demonstrating achievable efforts to overcome this challenge. Nevertheless, it is an understandable requirement to use more advanced models that can be grown large enough to study the spatial distribution of molecules. Moreover, MSI analysis of tumour spheroids alongside clinical tissue has shown great impact for the application of 3D cultures in pre-clinical research (Zang *et al.*, 2021). The similarities in metabolic signatures between spheroids and *in vivo* tissue supports the development of a representative *in vitro* model of cancer. With the considerations of enhancing the tumour spheroid model, this thesis aimed to address an alternative method of culturing 3D spheroids by the use of a natural scaffold followed by aggregation in attempt to increase the complexity of the spheroid model for a closer representation of *in vivo.* A detailed explanation of the model is described in Chapter 2.

1.4.2 Organoids

Derived from patient stem cells or biopsies, organoids are small-scale constructs that adopt the morphological structures of *in vivo* tumours and organs. Like spheroids, these self-organised systems allow for the study of biological processes including cell behaviour, tissue repair and drug response. As organoids are derived from patients, these systems hold the potential to assist in the prediction of drug response in a personalised manner. The first reported organoid structure dates back to 1975 by Rheinwald & Green, who cultivated a living skin replacement from epidermal keratinocytes which was later used to treat burn patients (Rheinwald & Green, 1975). Although organoids first received interest back in the 1970s, within the last decade the 3D models have witnessed a revival. Since its first development, the human skin organoid has been

successfully commercialised by several businesses for experimental use. These include: a human reconstructed epidermis (HRE) and a 3D differentiated epidermis cultures derived from human keratinocytes known as EpiSkin (Episkin, Lyon, France) and EpiDerm (Mattek, Ashland, USA), as well as full thickness living skin equivalents (LSE) that is T-skin (Episkin, Lyon, France) and Labskin (Labskin U.K. Ltd, York, U.K.).

The development of alternative organoid cultures have been used in a range of studies to investigate healthy and diseased organs or the behaviours of primary tumours to drug treatment. For example, Dye *et al.*, (2015) generated lung organoids from human pluripotent stem cells and observed their remarkable similarities to human foetal lungs, thus stating it an excellent model for human lung development, maturation and disease studies. In addition, a study conducted by Crespo *et al.*, (2017) developed colonic organoids to observe the blocking effects of a chemotherapeutic, geneticin in hyperproliferation, which has been associated with colon cancer *in vivo*.

1.4.2.1 MSI analysis of LSE models

The combination of human skin models and MALDI-MSI has been extensively utilised to study the drug absorption into the different layers of the skin. The benefits of using the skin models with MALDI-MSI analysis, is that the skin can be treated similarly to animal tissues in terms of sample preparation and imaging acquisition. The earliest work of the MALDI-MSI approach was conducted by Avery *et al.*, (2011), who examined the absorption of an antidepressant drug, imipramine into a model of the human epidermis, ‘Straticell’. A considerable difference in the intensities of imipramine at 2 h and 8 h was observed, with higher signals of the drug in the epidermis at 8 h. No quantifiable data analysis was conducted to achieve a significant concentration; however, this is partly due to the lack of quantitative methodologies for MALDI-MSI data at the time the study was conducted. The study stated some data remained inconclusive and additional experimentation is required to determine biotransformation of the drug. Avery *et al.*, (2011) however, clearly understood the potential capabilities of MALDI-MSI to determine drug penetration..

Since this work, a comprehensive study has characterised the endogenous lipid content within the LSE model, Labskin, by MALDI-MSI detecting abundant

species including phosphatidylcholine (PC), sphingolipids (SM) and lysphosphatidylcholine (LPC) (Mitchell *et al*., 2015). Using MVA (PCA), changes in the lipid localisations of PC 32:1 (*m/z* 732.6) and PC 38:0 (*m/z* 759.6) over a time-dependent course were observed; from initial detection of the PC species solely within the epidermis to a homogenous distribution throughout the skin sections after 24 h. The changes in distribution were associated with cell differentiation in the dermis and epidermis of the skin model. The data obtained from this study was further used to determine the effects of a topical treatment in order to differentiate between the pharmacodynamic effects arising from the compounds and the normal processes of cellular differentiation in the LSE model. Mitchell *et al*., (2016) determined the lipid changes in response to emollient creams. Both emollient treatments were detectable by ions characteristic to each cream, in addition to the detection of endogenous lipid species previously observed within the Labskin model. After 24 h of treatment, differences in PC 32:1 (*m/z* 732.6) and PC 36:1 (*m/z* 758.6) distributions were observed; both species were abundant solely within the epidermis of the untreated skin, compared to their distribution within the dermis and throughout the treated skin. This was an interesting study to show the effects of treatment on the spatial localisation of lipid species and can be used to determine the metabolic changes in response to topical therapeutics, as well as the simultaneous detection of the emollients.

A following study by Harvey *et al.*, (2016) examined the absorption of the drug, acitretin in a psoriasis induced Labskin model. It was demonstrated by MALDI-MSI acitretin penetrated the epidermis at 24 h then further infiltrated the dermal layer of the skin after 48 h. To confirm the location of the drug in the LSE model a sodiated sphingomyelin at *m/z* 725.4, which correlated to the epidermis, was detected. This time-dependent approach allowed for the evaluation of the drug's penetration and stability properties within a living tissue. In this study, MALDI-MSI successfully demonstrated the capabilities of analysing drug delivery, whilst also identifying specific regions of a complex organoid skin equivalent model.

The use of MSI to study skin has been further developed to achieve absolute quantification. A study conducted by Russo *et al.*, (2018) developed a quantitative MSI (QMSI) approach to determine the amount of an antifungal agent, terbinafine hydrochloride within the epidermis of the Labskin model. The study optimised a

micro-spotting methodology to achieve precise and uniform analytical and internal standards at nanolitre volumes solely within the epidermal layer, in order to mimic the cell-type ionisation response in treated tissues. Increasing concentrations of the internal standard were successfully detected at *m/z* 148 by MALDI-MSI to generate a calibration curve. Signals from the ROIs observed from endogenous species that defined the epidermis (PC at *m/z* 184) and stratum corneum (*m/z* 264) were employed to ensure that the drug calibration signals extracted were true to the specified region. In addition, the study evaluated the performance of the penetration enhancer Dimethyl Isosorbide (DMI) added to the delivery formulation. QMSI detected an increase in concentration of terbinafine with an increase in percentage of DMI within the epidermis of the LSE. Validation analysis observed no statistical significance between the values from QMSI and the values from the 'gold standard' LC-MS/MS, thus proving MALDI-MSI as a powerful quantitative method. This study demonstrated the potential impact QMSI with tissue engineered models will have on drug development, as by determining the amount of drug present within a tissue, information of its pharmacological activity can be obtained.

1.4.2.2 MS imaging of tumour organoids

The combination of MSI with tumour organoids is a relatively new approach. The development of tumour organoids, also known as cancer tissue originating spheroids (CTOS), is a similar process to generating tumour spheroids. Generally, patient derived cells are cultured in hydrogels such as basement membrane extract (BME), which are made with native ECM components and growth factors. CTOS are similar in size to tumour spheroids, and therefore require embedding medium, such as gelatin, to assist sample handling prior to preparation for MSI analysis following conventional protocols. More conventional imaging techniques such as fluorescence microscopy have mainly been used to observe these tumour models (Shah, Heaster, & Skala, 2017). However, efforts using MSI strategies to analyse CTOS have been reported, either in combination with fluorescent microscopy to detect the penetration of small molecule drugs that are inherently non-fluorescent (Bergmann *et al.*, 2018), or the development of sample preparation methods to improve high-throughput analysis (Johnson *et al.*, 2020).

Liu *et al.*, (2018) reported the use of MALDI-MSI with patient derived colorectal tumour organoids to observe the drug distribution of irinotecan in a time-dependant dosage. MALDI-MSI detected high intensities of irinotecan at *m/z* 587.3 and its metabolites SN-38 (*m/z* 393.1) and SN-38 glucuronide (*m/z* 569.2) distributed heterogeneously within the CTOS at 24 h of dosage. It was stated that this was possibly due to the various cell types including ISCs, differentiated enterocytes, goblet cells, entero-endocrine cells and Paneth cells that form the organoid model, which could have metabolised irinotecan differently. Thus, it demonstrated the benefits of utilising organoids over single-cell type spheroids to understand the metabolism of therapeutics within a structure comprised of many cell-types. The study also employed a QMSI approach to determine the amount of irinotecan present in the CTOS compared to its metabolites at a higher dosage at 72 h, observing lower signal of SN-38 and indicating less conversion of the active metabolite from irinotecan. This approach proved a valuable insight in the capabilities of QMSI to determine drug efficacy and potential chemo-resistance in patient derived CTOS, which in turn could predict clinical outcome that is specific to the patient.

1.4.2.3 Considerations of MSI organoid analysis

Alternative organoid cultures that mimic *in vivo* tissues other than skin or colorectal tumours have yet to be studied by MSI. Various challenges of cell culturing or MSI ionisation may be within optimisation; however, there is progress towards the development of the MSI-organoid approach. For example, a study conducted by David *et al.*, (2018) developed a method to study tumour explants of breast cancer xenografts. This was to overcome the issues of being unable to grow large enough breast cancer spheroids for spatial distributional analysis. The group developed xenografts in mice, to which the tumours were harvested and divided into explants of desired size and then treated *in vitro*. Following this, the tumours were embedded in gelatin and prepared following conventional protocols for MSI analysis. MALDI-MSI spatially localised the distribution of macrocyclic peptides and small molecule treatments including cyclosporin A and tamoxifen in the *ex vivo* mice organoids. Although the group utilised mouse tissue, the idea was to demonstrate the ability to extract biopsies and detect the uptake of therapeutics for a promising analytical method to examine patient specific treatment for prevalent diseases such as breast cancer.

The reported use of MSI techniques other than MALDI-MSI is limited for organoid cultures. This is most likely due to the analysis of organoids with MSI being a relatively new concept, especially in terms of CTOS. However, as the literature has demonstrated with the analysis of tumour spheroids, the ability to analyse organoids by other MS imaging techniques has potential. The growth of CTOS are typically reduced due to being primary cultures compared to the fast growth of MCTS from immortalised cell lines. The size of certain CTOS and the spatial capabilities of MSI may therefore limit spatial distribution studies. Though, in terms of larger cultures such as the LSE model similar approaches for the MSI analysis of animal tissues can be applied. Overall based on the current success, imaging complex organoid cultures has demonstrated the ability to spatially locate and quantify drugs. This emerging technique could be extremely valuable, and it will be interesting to see where organoid imaging can take drug developmental research further.

Recent developments of cutting-edge technology have enabled further advancements with organoid cultures. Three-dimensional bioprinting enables automated fabrication of highly complex multicellular tissues by combining cells, growth factors, and biomimetic materials. This technology has revolutionised tissue engineering due to its versatile processing capabilities to recapitulate important structural features of functional organs, which in the long-term could be considered for transplantable tissue in regenerative medicine (Akizuki *et al.*, 2018). Bioprinting also has the potential to be used for personalised medicine for cancer treatment. For example, Zhao *et al.*, (2012) constructed an *in vitro* cervical cancer model by the fabrication of HeLa cells with hydrogel-based materials, observing a significant difference in chemo-resistance to the anti-cancer drug, paclitaxel, compared to 2D cell culture. Evaluation of anti-cancer treatment using 3D bioprinting is still a relatively new concept, in addition analysis by MSI has not been exploited so far. However, the potential to analyse more complex models of *in vivo* tissue is an exciting avenue for research and could in future be used as a valuable *in vitro* tool for pre-clinical drug development.

1.4.3 Microfluidic systems

Technically microfluidic systems mostly contain 2D cell cultures, the complex structure is designed to recreate the multiscale architecture and tissue-tissue interfaces that are crucial for organs and tissues to function. Otherwise known as

‘organ-on-a-chip’ the purpose of this system is not to build a whole living organ within a representative native environment, but rather to synthesise minimal functional units that recapitulate tissue and organ level processes. The benefits of using the microfluidic system facilitates the generation of microscale dimensions and volumes that are similar to those typically found in biological systems (Chiu *et al.*, 2017). The microfluidic device can be designed in multiple ways depending on the complexity of the tissue that is modelled. The basic concept of the system is that the cells are plated within patterns on a chip that is coated with biocompatible materials such as polymer substrates. These materials allow for the passage of nutrients from the microchannels that provide a continuous flow of fluid. Unlike 2D cell cultures and 3D models, including spheroids and organoids, which are typically grown and treated sitting within a well of media. The continuous flow allows for the manipulation of the chemical gradients for cell survival and function over a long time period in addition to enabling treatment of drugs in a more representative manner such as recapitulating the oral or IV injection administration route. In more complex designs, numerous microchannels are connected by different porous membranes for different cell types. This constructs the interfaces between different tissue types to recreate a model of the human body. The many attributes of microfluidic systems identify this method of culture as one of the most advanced 3D tissue engineered models.

1.4.3.1 MSI potential with microfluidic systems

An extensive range of research has already utilised these microfluidic systems with mass spectrometry techniques in pharmacological studies. Santbergen *et al.*, (2020) designed an on-line UPLC-MS technique coupled to a ‘gut-on-a-chip’ model fabricated with a co-culture of colonic adenocarcinoma cell lines, Caco-2 and HT29-MTX. The dynamic system had switching valves to switch between the apical and basolateral sides of the *in vitro* model, allowing for permeability analysis of the oral drugs, verapamil and granisetron. Qualitative and quantitative analysis of the anti-cancer drug, genistein was demonstrated by Chen *et al.*, (2012) developing a stable isotope labelling assisted microfluidic chip (SIL-chip)-ESI-MS platform. The device cultivated MCF-7 breast cancer cells with the tumour growth inhibitor to study drug-induced apoptosis and cell metabolism, and

subsequently calculated the concentration of the eluting drug to determine genistein absorption.

Typically, imaging organ-on-chip cultures is performed by either fluorescence or optical microscopy. Microfluidic devices may be amenable to MSI, however there is no literature to date that has utilised this approach. This simply could be due to the fact the microfluidic system is much more complex and lacks accessibility to image these cells. In addition, the sample size of the cultures in a microfluidic system is very small. This is a limitation for multiple reasons, including the inability to reproduce the spatial heterogeneity found in larger 3D models, such as tumour spheroids and organoids. In addition to the spatial resolution challenges of MSI; although, the developments in spatial resolution technology hold potential. Ambient MSI methods such as DESI or LESA may be better suited with microfluidic devices, as for MALDI required sample preparations and the laser desorption technique could impact the biological composition.

An unconventional approach, however, has interfaced a microfluidic device with MALDI-MSI. Jo *et al.*, (2007) stimulated neurons cultured onto a microfluidic system and collected the neuronal release on a functionalised surface that is compatible for direct MALDI-MSI analysis. An estimated amount of neuropeptides released including acidic peptide and α-BCP, was calculated by imaging the distance the peptides flowed through the measured channels of the functionalised surface. The group further adapted the MALDI-MSI method to achieve improved accuracy and precision (Zhong *et al.*, 2012). This method utilised the abilities of MALDI-MSI to image the spatial distribution of the peptides as a measurement tool. Although the study did not directly analyse the spatial integrity of the neurons in culture, the group demonstrated the MSI method as a novel approach to examined biological behaviour.

As demonstrated by the extensive range of studies, conducted to date, MSI has proven strength in the investigation of pharmacological activity in 3D cell culture models. With the expanding surge of microfluidic systems for the study of therapeutics and the biological response, it can be contemplated that there is a high possibility the MSI-microfluidics approach will be exploited within the foreseeable future. This is especially true when the recent advances in microfluidics to further enhance the complexity of the 3D culture systems are considered. For example, macrofluidic systems or ‘organoid-on-a-chip’ platforms

have been engineered to combine the complexity of microfluidic devices with *ex vivo* tissues, spheroids and organoids, rather than 2D cell cultures, to replicate the *in vivo* microenvironments for patient-derived cultures (Yu & Choudhury, 2019). A similar concept of a macrofluidics system with spheroids was previously discussed, used as a 3D printed dosing platform device to treat HCT 116 MCTS with FOLFIRI (LaBonia *et al.*, 2018). Alternatively, Spencer *et al.*, (2020) reported the preliminary work of a developed macrofluidics device cultivating an *ex vivo* small intestine tissue on a Quasi Vivo 600 Liquid-Liquid Interphase *in vitro* system to model the GI tract and the oral-drug administration route. After treatment, the *ex vivo* tissue was removed from the fluidics system, snap frozen and cryo-sectioned prior to preparing the sample with matrix by sublimation. MALDI-MSI analysis was able to detect regions of lymphatic tissue, known as Peyer's patches (*m/z* 389), identifying substructures within the small intestine. The sodium adduct of the oral drug, atorvastatin (*m/z* 581) within the apical side of tissue after a 6 h incubation was localised outside of the Peyer's patches and indicated an absorption by passive diffusion. Not only did this demonstrate advanced manipulation of *ex vivo* tissue, but it also allowed for even more accurate drug analysis than previously mentioned 3D models, such as spheroids or organoid cultures by MALDI-MSI. These advancements in 3D culture models can offer an ideal testing platform in drug developmental studies, which also hold potential to be exploited for analysis by MSI.

Paper	Disease	3D Model	3D Method	Ionisation	Spatial Resolution	Summary
Li & Hummon, (2011)	HCT 116 colon carcinoma	Spheroid	Aggregation	MALDI	75 µm	Detected specific regional distributions of proteins across spheroids and highlighted a central necrotic region. Proteins Histone H4 and cytochrome c identified, validated by LC MS/MS.
Liu *et al.*, (2013)	HCT 116 colon carcinoma	Spheroid	Aggregation	MALDI	75 µm	Drug penetration of irinotecan mapped over a 72 h time-dependent course, moving from outer region of spheroid into the core. Detection of drug metabolites within spheroid validated by nanoLC-MS/MS.
Ahlf *et al.*, (2014)	HCT 116 colon carcinoma	Spheroid	Aggregation	MALDI	Not reported	Combination of confocal Raman microscopy and MALDI-MSI to determine structure of spheroids by protein secretion and small molecules distribution.
Ahlf Wheatcraft *et al.*, (2014)	HCT 116 colon carcinoma	Spheroid	Aggregation	MALDI	Not reported	Spheroid-MSI workflow protocol. Includes the culture, preparation and analysis of spheroid samples by MALDI-MSI.
Hiraide *et al.*, (2016)	HCT 116 & DLD-1 colon carcinoma	Spheroid	Aggregation followed by Cellmatrix type I-A scaffold gel	AP-MALDI	5 µm (laser spot size)	Tandem MS identified specific lipid species arachidonic acid containing PI 38:4 within the outer region in spheroid culture. Phospholipid associated with metastatic behaviour.
Liu & Hummon, (2016)	HCT 116 colon carcinoma	Spheroid	Aggregation	MALDI	75 µm	Localisation of platinum-based drugs and their metabolites displayed heterogeneous distributions within

						spheroids. On-tissue chemical derivatization. UPLC-MS/MS quantification.
Theiner *et al.*, (2016)	HCT 116 colon carcinoma & CH1-PA-1 ovarian terato-carcinoma	Spheroid	Aggregation	LA-ICP-MSI	10 µm (laser spot size)	Analysis of platinum-based compounds including satraplatin, showed heterogeneous distributions between the two spheroid models. Platinum was detected in the periphery and necrotic regions of spheroids.
Lukowski *et al.*, (2017)	HCT 116 colon carcinoma	Spheroid	Aggregation	MALDI	75 µm	Demonstrated doxorubicin-encased liposome delivery into spheroids. Detection of doxorubicin and active metabolites throughout spheroid at 72 h.
Feist *et al.*, (2017)	HCT 116 colon carcinoma	Spheroid	Aggregation	MALDI	75 µm	Proteomic imaging of histone peptides and their post-translational modifications determined the response to epigenetic drug within serial sections of spheroids, generating samples from core, the mid and external areas.
O'Neill *et al.*, (2017)	DLD-1 colon carcinoma	Spheroid	Aggregation	LA-ICP-MSI	25 µm (laser spot size)	Multimodal analysis employing LA-ICP-MSI and MRI to study hypoxia responsive cobalt complexes, detecting Co(II)TPAx in the core of the spheroid sections.
Theiner *et al.*, (2017)	HCT 116 Colon carcinoma	Spheroid	Aggregation	LA-ICP-MSI	5 µm (laser spot size)	Analysis of metal-based cancer drugs in spheroids determined hypoxic, non-proliferative and proliferative regions

						within the spheroid based on platinum and phosphorous ratios.
LaBonia *et al.*, (2018)	HCT 116 colon carcinoma	Spheroid	Aggregation	MALDI	75 µm	Proteomic changes from a dynamic flow dosing with FOLFIRI treatment investigated and quantified by iTRAQ analysis. Heterogeneous distribution of drugs and active metabolites throughout spheroid.
Liu *et al.*, (2018)	HT-29 & DLD1 colon carcinoma	Spheroid	Aggregation	MALDI	70 µm	On-tissue reduction and alkylation method to detect time-dependent penetration and distribution of monoclonal antibody, Cetuximab. Different localisations of immuno-drug determined between two cell lines. Detection in organoid cultures also demonstrated.
	Patient derived colorectal cancer	Tumour organoids	Aggregation with BME type 2			
Tucker *et al.*, (2019)	MCF-7 breast cancer	Spheroid	Aggregation	FT-ICR MALDI	50 µm	Untargeted metabolite mapping in spheroids identified proliferative and hypoxic regions via ATP metabolism pathway. Ion images mapped onto biological pathways including glycolysis.
Mittal *et al.*, (2019)	Patient derived ovarian cancer	Spheroid	Aggregation	MALDI	50 µm	On-tissue digestion workflow embedded spheroids in Matrigel prior to FFPE. Co-localised proteotypic peptides within the outer layer and necrotic region of spheroids.
Machálková *et al.*, (2019)	HT-29 colon carcinoma	Spheroid	Aggregation	MALDI	50 µm	Multimodal co-registration of MALDI and IHC images of perifosine treated spheroids at 24 h. Lipid distributions in

						MALDI analysis and protein expressions in IHC identified proliferative and hypoxic regions. Quantification of perifosine by LC-MS.
Michálek *et al.*, (2019)	HT-29 colon carcinoma	Spheroid	Aggregation	MALDI	50 µm	Multimodal approach of spheroid analysis: Perifosine drug detection by MALDI; Identification of proliferative and apoptotic cells by laser scanning confocal fluorescence microscopy (LSCM).
Tian *et al.*, (2019)	HCT-116 colon carcinoma	Spheroid	Aggregation	Single-probe	Not reported	Spatially resolved metabolic profiles in spheroids treated with irinotecan. MVA determined the drug effected abundances in metabolites in different regions of spheroids.
Palubeckaitė *et al.*, (2019)	SAOS-2 osteo-sarcoma	"Spheroid aggregate"	Alginate scaffold followed by aggregation	MALDI FTICR MALDI	60 µm 75 µm	Local apoptotic and necrotic regions identified by metabolite distributions. Changes in metabolic activity in doxorubicin treated cultures and localisation of drug detected by FTICR.
Xie *et al.*, (2020)	MDA-MB-231 breast cancer	Spheroid	Aggregation	MALDI	50 µm	Metabolic changes in response to environmental contaminant BPS identified in phenotypic regions of spheroids associated with cancer proliferation.
Robison *et al.*, (2020)	MDA-MB-231 breast cancer	Spheroid	Aggregation	DESI	50 µm	Spatial mapping of lipids identified metastatic potential metabolites in the necrotic core of spheroids.

Flint *et al.*, (2020)	HCC827 lung adeno-carcinoma	"Aggregoid"	Alginate scaffold followed by aggregation	DESI IMC LA-ICP-MSI	30 µm 1 µm 6 µm (laser spot size)	Characterization of a novel aggregated spheroid model by multimodal MSI techniques detecting metabolites, proteins and metals determined phenotypic regions of the tumour microenvironment. Identified proliferative outer region and hypoxic core of aggregoid and presented a 3D reconstruction.
Zang *et al.*, (2021)	KYSE-30 oesophageal cancer	Spheroid	Aggregation	MALDI	12 µm	Spatial resolved metabolomics defined phenotypic regions within spheroids, ion images mapped onto biological pathways. Similarities of metabolic signatures identified between clinical tissue and spheroids.
Avery *et al.*, (2011)	Healthy human epidermal skin	Skin organoid	Straticell-RHE-EPI-001 Reconstruct-ed Human Epidermis	MALDI	150 µm	Demonstrated a MALDI-MSI method of an artificial skin model analysis by detection of imipramine absorption.
Francese *et al.*, (2013)	Healthy LSE	Skin organoid	Evocutis "LabSkin"	MALDI	50 µm	The evaluation of curcumin as a matrix for MALDI across different applications, lung tissue, artificial skin and fingermark. Lipid imaging identified epidermis and dermis regions within the LSE. Detection of acitretin distribution within LSE.

Mitchell *et al.*, (2015)	Healthy LSE	Skin organoid	Evocutis "LabSkin"	Evocutis "LabSkin"	50 µm	Characterisation of lipid changes in a time-dependent course by MALDI-MSI were associated with processes of cellular differentiation across the epidermis and dermis of the skin.
Mitchell *et al.*, (2016)	Healthy LSE	Skin organoid	Evocutis "LabSkin"	Evocutis "LabSkin"	50 µm	MALDI-MSI detected emollient creams within the skin model and determined changes in lipid distributions in response to treatment. The lipids that defined the epidermis in the untreated were localised throughout the treated skin sections.
Harvey *et al.*, (2016)	Healthy and psoriatic LSE	Skin organoid	Innovenn "Labskin"	MALDI	100 µm	Absorption of acitretin within psoriatic LSE by MALDI-MSI determined a larger depth of penetration in psoriatic model compared to healthy LSE.
Russo *et al.*, (2018)	Healthy LSE	Skin organoid	Innovenn "Labskin"	MALDI	60 µm	Quantitation of terbinafine hydrochloride absorption into epidermal region of LSE by MALDI-MSI. Regions of LSE identified by detection of abundant lipid species. Penetration enhancer DMI increased the concentration of drug. Validated by LC-MS/MS.
Bergmann *et al.*, (2018)	Blood-brain-barrier (BBB) of endothelial cells,	Tumour organoid	Co-culture by low-adhesion conditions	MALDI	Not reported	Development of a BBB organoid platform for drug analysis by fluorescent microscopy and MALDI-MSI. Analysis of BKM120 and

	pericytes and astrocytes					dabrafenib permeability with BBB organoids.
Liu *et al.*, (2018)	Colorectal cancer	Tumour organoid	Aggregation with Cultrex BME	MALDI	35 µm	Heterogeneous distribution of irinotecan and its active metabolites within organoid cultures demonstrated metabolic variability in complex tissue samples.
David *et al.*, (2018)	MCF-7 breast cancer	Tumour organoid	Mice xenograft	MALDI	Not reported	*Ex vivo* method of visualising peptides and small molecules in breast cancer tumour explants as an alternative to spheroid cultures. Detection of small molecule drug (4-hydroxytamoxifen) and peptide drug (cyclosporin A) as proof-of-concept.
Lewis *et al.*, (2018)	Healthy LSE	Skin organoid	Innovenn "Labskin"	MALDI	75 µm	Examined the skin barrier repair/wound healing process through identification of lipid biomarkers.
Johnson *et al.*, (2020)	Pancreatic cancer	Tumour organoid	Patient biopsies	MALDI	75 µm	Method development of organoid cultures into gelatin microarrays for high-throughput MSI analysis. Organized array of organoids in the same z-axis for multi-sample imaging.
Jo *et al.*, (2007)	Aplysia californica bag cell neurons	Microfluidics system	Cells coated onto a poly-L-lysine coated area on surface of PDMS	MALDI	100 µm to 200 µm	Characterised released neuropeptides from stimulated neurons by potassium chloride solution.

			microfluidic device.			
Zhong *et al.*, (2012)	Aplysia californica bag cell neurons	Microfluidics system	Cells coated onto a poly-L-lysine coated area on surface of PDMS microfluidic device.	MALDI	100 µm to 200 µm	Quantification of released neuropeptides from stimulated neurons by potassium chloride solution. Measured the length of peptides released from the images.
Spencer *et al.*, (2020)	Healthy small intestine tissue	Macrofluidics system	Quasi Vivo 600 Liquid-Liquid Interphase *in vitro* system	MALDI	Not reported	Detection of metabolites identified substructures within small intestine tissue including the lymphatic tissue. Detection of atorvastatin sodium adduct within apical side of tissue demonstrating passive diffusion of drug.

Table 1.3 A summary of the literature reporting the analysis of 3D cell culture models by MSI.

1.5 Future perspectives

MSI has demonstrated significant value for the use in pre-clinical drug efficacy and toxicity studies. Parallel to the developments in MSI, 3D cell culture models have established robust *in vitro* tools that accurately represent the microenvironments of biological tissues and disease in humans. The multiplex nature of MSI has enabled the analysis of a variety of 3D models including spheroid and organoid cultures across applications of tumour characterisation by the detection of metabolites, peptides and proteins. In addition, a plethora of studies have evaluated the distribution of drugs and their metabolites simultaneously *in situ*, with some including quantitative capacity (Table 1.3).

Although an extensive amount of research on the combination of MSI with 3D models has been reported, there are still areas of development to be made. The research of 3D models by MSI techniques have been limited to specific cancer and disease types, for instance the spheroid model of colon carcinoma. Henceforth, to establish the combination of 3D models with MSI as a valuable pre-clinical tool it is necessary to broaden the topic areas to alternative cancer and disease types that are just as prevalent (e.g., lung adenocarcinoma and osteosarcoma). The conflicting views on 3D cultures accurately representing true *in vivo* structure and functionality clearly show the need for establishing more complex models that include molecular heterogeneity and essential structural components. This is to ensure an accurate prediction of drug outcome *in vivo*. Developments in the sample preparation workflow need to keep pace to allow accessibility of the 3D models for MSI analysis. Furthermore, the combination of 3D cell culture models with MALDI has been the primary imaging platform. The use of alternative ionisation modalities can allow for the study of a wider range of molecular content, expanding the opportunities in pre-clinical drug analysis for a variety of drugs and endogenous molecules, including the spatial resolution capabilities that have potential for single-cell analysis.

In addition, MSI analysis of therapeutics within not only 3D cultures but all tissues have predominately focussed on the evaluation of small molecule drugs. This is mainly due to the effectiveness of the compounds as a treatment. However, over recent years progress towards the developments of complex biopharmaceuticals that offer high efficacy treatments with few side effects have become one of the fastest growing sectors in the pharmaceutical industry. There is very limited

literature reporting the detection of biologics *in situ* by MSI techniques, with only two studies published to date (Ait-Belkacem *et al.*, 2014; Liu *et al.*, 2018). This is mainly due to the size and complexity of the therapeutic proteins which create issues of low ionisation and poor sensitivity that have hindered the development of an established MSI workflow. It is therefore a requirement for MSI methods to keep with the momentum of pharmaceutical development in order to maintain its reputation as a valuable tool in pre-clinical drug analysis.

1.6 Aims and objectives of this project

The aim of this project was to develop a multimodal MSI approach to analyse a 3D cell culture model for pre-clinical biopharmaceutical testing. In order to achieve this the following objectives were investigated:

- Develop a novel 3D cell culture model of two cancer types (lung adenocarcinoma and osteosarcoma) and optimise the sample preparation workflow for universal application across MSI modalities.
- Apply a multimodal MSI approach to characterise the lung adenocarcinoma model for an in-depth understanding of the tumour microenvironment.
- To use the multimodal MSI approach to characterise and compare the 3D osteosarcoma models and investigate their molecular relevance to clinical osteosarcoma patient samples.
- Employ an untargeted DESI-MSI approach to determine the metabolic response to biopharmaceutical treatment in the 3D cell culture models.
- Optimise a multimodal MSI strategy to detect a biopharmaceutical in the 3D lung adenocarcinoma model.

CHAPTER 2. OPTIMISATION OF A 3D CELL CULTURE MODEL FOR MASS SPECTROMETRY ANALYSIS

2.1 Introduction

As discussed in Chapter 1.4, the combination of MSI with 3D cell culture models is a promising tool in early stage drug development. The ability to study the distribution of a parent drug and its metabolites, whilst simultaneously measuring the cellular metabolism within an artificially created environment expands the possibilities for pre-clinical research (Russo *et al*., 2018).

Spheroids are the most common 3D model of cancer studied by MSI, specifically MCTS in combination with MALDI imaging (Chapter 1.4.1). The spheroid model can mimic key tumour characteristics with regards to cellular morphology and metabolic activity that make it a valuable tool for evaluating drug toxicity. Hypoxia is of particular significance due to its effects on cellular function and drug activity, which can give rise to drug resistance (Donovan *et al.*, 2010; Jing *et al.,* 2019). In addition, the biological and physical barriers of the periphery, such as the active metabolism and lessened permeability, can also prevent the delivery of a drug (Soo-Hyun, Hyo-Jeong, & Crispin, 2011). The spheroid model also provides a cost-effective and versatile method of analysing the biological processes within the tumour environments, with added benefits of high throughput results. These qualities in combination with the spatial resolution capabilities and high-speed of acquisition of MALDI-MSI makes this method highly desirable for drug development studies.

Recent publications have criticised MCTS because of their lack of heterogeneity (Liu *et al.,* 2018; Palubeckiatė *et al*., 2019). This is due to the way in which the spheroids are formed through aggregation techniques. Aside from the phenotypic differences of hypoxia and proliferation that spheroids exhibit, the 3D constructs are seen as predominately homogenous cultures. In comparison, *in vivo* tumours are highly complex tissues that are comprised of a variety of differentiated cells (e.g., stromal and immune cells) within a dynamic ECM and vascularised environment, rather than a singular mass of cancer cells (Fong *et al.*, 2016). As tumour heterogeneity is a factor contributing to drug resistance, the homogeneity of MCTS can negatively impact true biological behaviour and lead to therapeutic failure further down the line. The paradigm of modelling cancer *in vitro* is therefore seeing a shift away from spheroid cultures towards more accurate pre-clinical models sourced from primary cells (i.e., tumour organoids) that consist of multiple cell types. MSI in particular, has demonstrated pharmacological benefits of

studying these cultures (Liu *et al.*, 2018). The implementation of patient derived tumour organoids in experiments, however, is far more complex than the spheroid model with regards to the ethical implications, the lengthy culturing periods and added expenses.

Alternatively, enhancing the complexity of the spheroid model is a more preferred method in drug development when aiming for high-throughput results. Such advancements involve the way in which the spheroid is cultured. For example, scaffold-based techniques provide an ECM structure to the cellular environment which more closely resembles the native cell-matrix interactions found *in vivo.* Scaffolds can also be adapted and tailored to mimic a specific environment for individual cell lines. In contrast to the aggregation method which cannot form robust spheroid cultures in a range of cell lines (Nagelkerke *et al.*, 2013). Additionally, culturing within scaffold-based materials enforces the single cell suspension to proliferate in 3D, generating clonal populations through a more natural process. A recent study reported, 3D cell cultures promoted survival mechanisms in spheroid formation similar to *in vivo.* A marked increased levels of an oxidant defence transcription factor, NRF2 had significant effects on cellular proliferation and protection of cells within a hypoxic microenvironment (Takahashi *et al.*, 2020). Thus, the results demonstrated the importance of cells proliferating in 3D rather than the aggregation method in order to create their own ECM components and promote gene expressions required for tumour survival.

In terms of analysing such enhanced spheroid models by MSI, the literature has been limited to none. Potentially this is due to the ease of generating MCTS by the aggregation method. In addition, the size of the spheroid cultures within scaffolds can be limited (< 500 μm) and creates issues in terms of retrieving molecular information in spatial distribution studies (David *et al*., 2018). Some materials used to aid scaffold-based spheroids (e.g., PEG containing hydrogels) can also cause spectral interferences during analysis and therefore the choice of material needs careful consideration (Palubeckaite *et al*., 2018).

With this in mind, a novel 3D culture model has been developed that addresses the limitations regarding the heterogeneity of spheroid models and their compatibility for quality MSI analysis. Palubeckaitė *et al.*, (2019) generated a “spheroid aggregate” model through the aggregation of tumour spheres. The method combines the basis of using an alginate scaffold to generate isogenic

spheroids through proliferation, which are then isolated and aggregated together using an ultra-low attachment technique. The scaffold-based method of spheroid formation is clonal and creates multiple spheroids of different sizes and of genetic variability within a single alginate bead. The individual spheres are then aggregated to form a larger construct of cells of a diameter of ~ 1 mm. This is achieved by following a similar technique to the aggregation method utilising agarose coatings to prevent cells adhering to surface of well plates, enforcing the cells to aggregate together (Costa *et al.*, 2014; Gong *et al.*, 2015; Das *et al.*, 2017). Theoretically, the aggregation of the individual colonies creates areas within the spheroid aggregate that exhibit different genetic phenotypes. Thus, the 3D model provides a more heterogeneous tissue than the typical spheroid model (Figure 2.1). The spheroid aggregate still displays the typical tumour microenvironment characteristics with proliferative and hypoxic regions demonstrating a viable 3D culture for pharmacological studies.

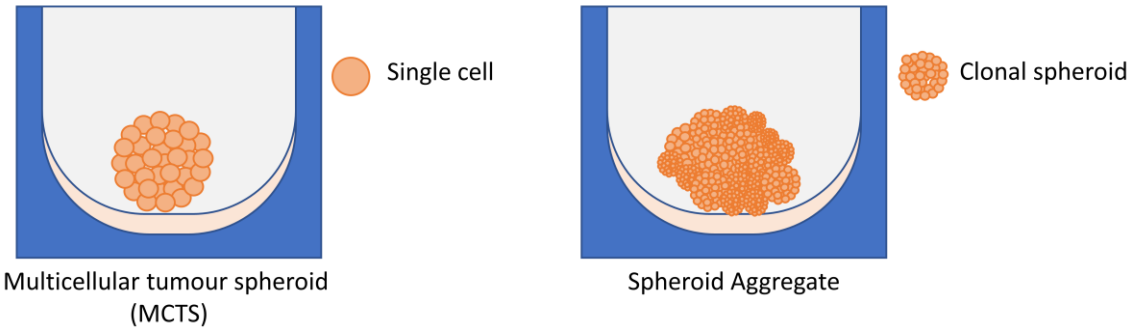

Figure 2.1 Diagram depicting a comparison between the conventional MCTS model vs the spheroid aggregate model. MCTS formed through aggregation of a single cell suspension as the spheroid aggregate is generated through the aggregation of isolated, clonal spheroids.

MALDI-MSI analysis of the osteosarcoma (SAOS-2) spheroid aggregate showed that it was possible to detect endogenous metabolites within specific regional localisations (Palubeckaitė *et al.*, 2019). The proof-of-principle study showed heterogenous distributions that co-localised unidentified metabolites exhibiting signals at *m/z* 281.3 within the periphery and *m/z* 403.1 in the necrotic core of the aggregate model. In addition, distributional changes of metabolites were observed in response to the chemotherapeutic, doxorubicin, as well as the detection of the drug as a protonated cation at *m/z* 544.2 within the SAOS-2 aggregate. The study showed the combination of the spheroid aggregate model with MSI to be a promising method in studies of drug efficacy and toxicity. Although the model has shown to be suitable for metabolomics studies and chemotherapeutic applications, there is not enough evidence to demonstrate the full capabilities of this novel model across different MSI techniques and no data has yet been produced in the emerging field of biopharmaceutical applications. Therefore, further studies of the spheroid aggregate with MSI are of interest.

2.2 Aims of chapter

In the following chapter the aim was to culture additional novel 3D culture models using the methodology developed previously from Palubeckaitė *et al.*, (2019). The objectives were to recreate the tumour microenvironment within three cancer cell line models, two osteosarcoma (MG63, SAOS-2) and one lung adenocarcinoma (HCC827) for the purpose of developing an *in vitro* tool in MSI applications for pre-clinical research in biopharmaceutical development. In order to conduct these experiments, optimisation of the sample preparation workflow for MS analysis of the 3D culture models was required. An investigation of sample handling and storage was performed in order to retain sample integrity and reduce analyte delocalisation of the 3D models. MALDI-MS profiling and imaging of the 3D models were employed to evaluate the technical parameters.

2.3 Materials and methods

2.3.1 Materials

α-CHCA, DHB, alginic acid, aniline, calcium chloride ($CaCl_2$), sodium carboxymethylcellulose (CMC), ethylenediaminetetraacetic acid (EDTA), eosin, gelatin, haematoxylin, phosphorus red, paraformaldehyde (PFA),

polyvinylpyrrolidone (PVP), propidium iodide (PI), sodium chloride (NaCl), sodium citrate, TFA and xylene substitute were purchased from Sigma-Aldrich (Gillingham, UK). Acetonitrile (ACN), ethanol (EtOH), Hoechst 33342 and methanol (MeOH) were purchased from Fisher Scientific (Loughborough, UK). Pertex mounting medium was obtained from Leica Microsystems (Milton Keynes, UK). Hydroxypropyl-methylcellulose (HPMC) was purchased from Alfa Aesar (Thermo Fisher Scientific, Heysham, UK).

2.3.2 2D cell culture

Epithelial HCC827 (lung adenocarcinoma) cell line was obtained from ATCC and cultured in Dulbecco's modified Eagle's medium (DMEM) (Lonza Ltd, U.K.) supplemented with 10% foetal bovine serum (FBS) and 1% penicillin-streptomycin (Lonza Ltd, U.K.). Osteosarcoma cell lines, MG63 and SAOS-2 cell lines were obtained from ATCC and were cultured in alpha modified Eagle's medium (αMEM) supplemented with 10% FBS and 1% penicillin-streptomycin. All cell lines were maintained in a humid atmosphere at 37°C, 5% CO_2 and grown to 80% confluence prior to use for 2D experiments and 3D culture. Confluent cell lines were passaged by trypsinisation, followed by centrifugation, and resuspension in fresh media. Cell lines were routinely tested for mycoplasma every few months.

2.3.3 3D cell culture

The aggregated 3D cell culture models were generated based on the method of Palubeckaitė *et al.*, (2019) and is described below.

2.3.3.1 Alginate culture

Monolayer cells were suspended in 1.2% (w/v) alginic acid in 0.15 M NaCl at an approximate cell density of 1 x10^6 cells/mL. The cell density was determined by Trypan blue staining (Lonza Ltd, UK) and calculated on the Countess® Automated Cell Counter (Thermo Fisher Scientific, U.K.). The alginic acid solution containing cells was extruded out of a 20-gauge needle into 10 mL 0.2 M $CaCl_2$ to polymerise the alginate into beads. Beads were incubated at room temperature (RT) for approximately 2-3 min before they washed with 0.15 M NaCl twice before culturing in the appropriate media. All cell lines were initially cultured up to 21 days to determine the optimum spheroid growth. From this a culture period of 11-

14 days for each cell line was decided to yield spheroids of approximately 100 µm. Beads were subjected to a media change every 72 h.

2.3.3.2 Releasing spheroids from alginate beads

Alginate beads were dissolved in an alginate buffer (55 mM sodium citrate, 30 mM EDTA, 0.15M NaCl) for 10 min at 37°C after breaking up the beads in solution with a pipette. Approximately 30 beads were dissolved in 10 mL of buffer. The spheroid solution was gently centrifuged for 3 min at RT to form a pellet. The supernatant was removed, and the pellet was washed in the appropriate culture media twice, followed by centrifugation between each wash.

2.3.3.3 Aggregoid formation

To form tumour spheroid aggregates, the required amount of culture media was added to resuspend the spheroids so that there was approximately half of one alginate bead per well of a 1% agarose-coated 96-well plate. Spheroid aggregates were cultured for 7 days in the appropriate media to form aggregoids of an approximate diameter of 1 mm.

2.3.3.4 Analysis of spheroid and aggregoid development

Spheroid and aggregoid development were analysed by fluorescent staining with Hoechst 33342 and PI staining (10 µg/mL each) and incubated at 37°C for 30 min. After incubation, the stain solution was replaced with fresh culture media for imaging analysis. Fluorescent images were obtained using either the Olympus IX81 Microscope (Southend-on-Sea, U.K.) where images were captured using Cell^F Multi-fluorescence and Imaging Software (Europa Science Ltd, Cambridge, U.K.), or the Cytation™ 5 Cell Imaging Multi-Mode Reader (BioTek, UK).

2.3.4 Tissue processing

2.3.4.1 Sample embedding

To handle the aggregoid cultures a series of embedding media were tested, these included: (1) 10% gelatin; (2) 5% CMC; or (3) 7.5% HPMC and 2.5% PVP as described by Dannhorn *et al.*, (2020). For the embedding procedure, media (1) and (2) were incubated at 50°C to form a liquid solution. Media (3) was pre-conditioned on ice for 30 min before use. Prior to embedding, aggregoids were washed in PBS twice, carefully removing the media each time. Aggregoids were

carefully transferred from the well into embedding media coated moulds using a 100 µL pipette tip, which the end was cut so that the tip had a larger diameter to ensure the aggregoid integrity was retained. Once the aggregoid was transferred to the media coated moulds, excess PBS was removed to the extent possible. Additional embedding media was coated over the aggregoid samples before flash freezing in liquid nitrogen for approximately 1-2 min. Fresh frozen samples were stored in - 80°C prior to sectioning.

2.3.4.2 Sectioning

Embedded tissues were cryosectioned on a CM1950 cryostat (Leica Biosystems, U.K.) set to a temperature of - 24°C for the cryochamber and - 20°C for the sample holder. Samples were mounted onto circular cork rings with a diameter ~ 3 cm using H_2O and left for 30 min to thermally equilibrate before sectioning. Sections were cut at 10 µm thickness, thaw mounted onto either positively charged X-tra® adhesive slides (Leica Biosystems, U.K.) or onto Indium-Tin oxide (ITO)-coated slides (Visiontek Systems Ltd, UK) dependant on the instrumentation used for analysis.

2.3.4.3 Sample storage

To ensure aggregoid samples are stabilised and to prevent degradation of endogenous molecules an experimental protocol established by Swales *et al.*, (2018) for optimum sample storage and preparation was followed. Briefly, samples were desiccated with N_2 immediately after the section was adhered onto the glass slide. Following this, samples were vacuum packed in plastic pouches and stored (- 80°C), and after left to air-dry before taking out of vacuum conditions. A comparison of this method with the conventional storage of slides not desiccated or vacuum packed and stored (- 80°C) is included in section 2.4.2.3.

2.3.5 Optimisation of mass spectrometry imaging

2.3.5.1 Mass spectrometric profiling of aggregoid cultures

Profiling of the aggregoid samples and embedding media was performed by spotting 0.5 µL of α-CHCA (5 mg/mL) in 70% ACN:0.1% TFA with equimolar amounts of aniline (2.4 uL aniline to 5 mg/mL α-CHCA) onto the tissues.

Mass spectra were manually acquired on a Waters MALDI HDMS Synapt G2 mass spectrometer (Waters Corporation, U.K.) equipped with a Nd:YAG laser operated at 1 kHz. Instrument calibration was performed using phosphorus red before analysis. Spectra were acquired in positive mode, full scan sensitivity mode within a *m/z* range 100-2000 (resolution 10 000 FWHM) and a laser energy at 320 arbitrary units. Ion mobility function was not enabled. Data were acquired and converted to .txt file format using MassLynx™ software (Waters Corporation, UK) and analysed using mMass 3 open-source software (Strohalm *et al.*, 2010). Peak picking settings were set at a signal to noise (S/N) threshold of 5, and the picking height was 100%. Both the absolute intensity threshold and the relative intensity threshold was set to 0 with baseline correction and smoothing applied. Identification of values were based on putative assignments using METLIN (http://metlin.scripps.edu), LIPID MAPS® (https://www.lipidmaps.org/tools/ms/LMSD_search_mass_options.php) and published literature.

2.3.5.2 MALDI-MSI

2.3.5.2.1 Matrix deposition

All sample sections were removed from - 80°C and left to air-dry before removing from vacuum packaging to avoid delocalisation of the analyte and to preserve the integrity of the tissue. For the spray-coat method, matrix (5 mg/mL α-CHCA in 70% ACN:0.1% TFA with equimolar amounts of aniline) was deposited onto the tissues using a SunCollect™ MALDI Sprayer (KR Analytical, Sandbach, UK). Ten layers of matrix were sprayed with a flow rate of 3 µL/min for the first layer then 4 µL/min for the remaining layers with the sprayer nozzle positioned at a height of 38 mm.

Matrix deposited by sublimation was achieved by evenly spreading 300 mg of α-CHCA at the bottom of the Ace vacuum-sublimation apparatus (Sigma-Aldrich). Polylysine slides with aggregoid sections were attached to the flat top of the chamber using autoclave tap at either end of the slide. The flat top of the chamber was placed within the sublimation apparatus and sealed by vacuum at 2.5 $x10^{-2}$ Torr. The top was filled with ice-water. The apparatus was set to a temperature of 180°C prior to starting the sublimation process. The application of matrix was performed for approximately 20 mins, or until an amount of 0.2 mg/cm^2 of α-

CHCA was achieved. This was calculated by weighing the slide before and after sublimation, calculating the difference (mg) and dividing by the area of the sublimed slide (cm^2).

2.3.5.2.2 Imaging acquisition

Small molecule MALDI images were acquired using the Waters MALDI HDMS Synapt G2 mass spectrometer. Instrument calibration was performed using phosphorus red. Spectra were acquired in positive ion full scan sensitivity mode within a *m/z* range 100-1000 at a spatial resolution 40 µm and a laser energy set to 350 arbitrary units. Ion mobility function was not enabled.

2.3.5.2.3 Data processing

MALDI-MSI data were processed using the HDI 1.4 software tool (Waters Corporation, UK) to initially determine the quality of the data after acquisition. For more in-depth data processing, files were converted into imzML and ibd before being uploaded on to the SCiLS™ Lab MVS Version 2020a Core (Bruker Daltonics, Germany). Total ion count (TIC) normalisation was applied, the peak list was generated from the maximum 100 peaks per spectrum. The peak list was used for further data analysis including spatial segmentation and co-localisation of *m/z* images. The spatial segmentation method was performed by bisecting k-means, with weak denoising and a correlation distance metric, working on all individual spectra.

2.3.5.3 DESI-MSI

Small molecule imaging was performed using a Q-Exactive mass spectrometer (Thermo Fisher Scientific Inc, Germany) operated in negative ion mode. No prior sample preparation was required to analyse the aggregoid cultures. The mass spectrometer was equipped with a custom-built automated DESI ion source. The mass resolution was set to 70,000 and mass spectra were collected in the mass range *m/z* 80-900 at a spatial resolution of 30 µm. The electrospray solvent was MeOH/water (95:5 v/v) set at a flow rate of 1 µL/min with nebulizing nitrogen used as gas at pressure of 2 bar. Imaging analysis was performed by combining individual horizontal line scans and converting into imzML format using the imzML converter V.1.1.4.5 (www.maldi-msi.org). The images were analysed by SCiLS Lab MVS Premium 3D Version 2020a (Bruker Daltonics, Germany) employing root mean square (RMS) normalization.

2.3.6 Histological analysis

Aggregoid sections were stained with Mayer's haematoxylin and eosin (H&E) solutions. After MALDI-MSI analysis, slides were washed with 100% EtOH to remove the presence of matrix. Sections were then rehydrated in 100% EtOH (3 min) and 18 MΩ water (2 min) prior to staining with filtered haematoxylin (1 min). Tissues were then blued in running tap water (5 min) before submerging in 100% EtOH twice (3 min). Tissues were subsequently stained with eosin (1 min) prior to washing with 100% EtOH twice (3 min). Finally, tissues were submerged in 2 changes of xylene substitute (5 min) and mounted using Pertex® mountant. For slides that were not used for MALDI-MSI analysis, sections were immediately stained with haematoxylin. An initial 4% PFA fixation step was included prior to the haematoxylin step for optimisation of one set of samples. Optical images were obtained using the Olympus BX60 microscope (Olympus, U.K.) and images captured using QImaging Micropublisher 5.0 RTV camera and Capture-Pro 8.0 software (QImaging, Canada).

2.4 Results and discussion

2.4.1 Optimisation of an aggregated tumour spheroid model

In this study, a novel aggregated tumour spheroid model was developed for multiple reasons: a) to form a larger tissue for mass spectrometry spatial distribution studies, and b) to create a more heterogeneous model than the conventional tumour spheroid suitable for early stage drug development studies. Three cell lines were cultured following a similar method to that described by Palubeckaitė *et al.*, (2019). The cell lines included were two osteosarcoma (OS) cell lines, MG63 and SAOS-2, which have been previously shown to be robust spheroid aggregate models for the analysis by MALDI-MSI (Palubeckaite, 2018). Additionally, a HCC827 lung adenocarcinoma cell line was cultured following this protocol to further demonstrate the diversity of the 3D culture model across different cancer types. Initially, a single-cell suspension was cultured within an alginate bead over a period to examine the growth of spheroids scaffold, as previously demonstrated by Akeda *et al.*, (2009) and Stock *et al.*, (2016). Typically, the formation of clonal spheres takes a longer period compared to the aggregation method due to the development of the spheroid through single cell proliferation (Gencoglu *et al.*, 2018). The formation of tumour spheres within the

alginate bead culture was therefore assessed over a 14-day period by Hoechst 33342/PI fluorescent staining to determine the size of the colony and the development of a hypoxic core.

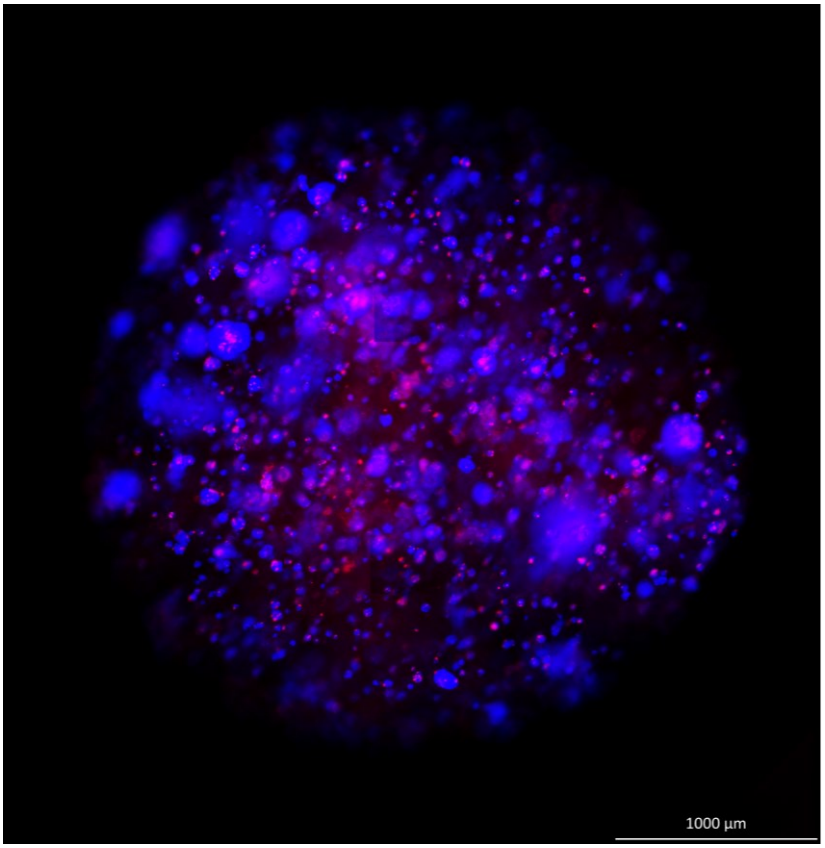

Figure 2.2 A whole alginate bead culture of SAOS-2 spheroids (day 11). Fluorescent image obtained by Hoechst 33342/PI staining to identify viable (blue) and necrotic (red) regions. Scale bar 1000 µm.

From day 2, images showed initial proliferation of single cells for each cell line. Noticeable formation of spheres, approximately 4-5 cells, were found within the MG63 cultures, indicating a faster rate of proliferation (Figure 2.3). By day 14, all three cell lines had grown a substantial amount of spheroids (~ 70%) per alginate bead. Both OS cell lines cultured spheroids, the majority of which had diameters of approximately 200 µm with the beginnings of a hypoxic/necrotic core (Figure 2.3 and Figure 2.4).

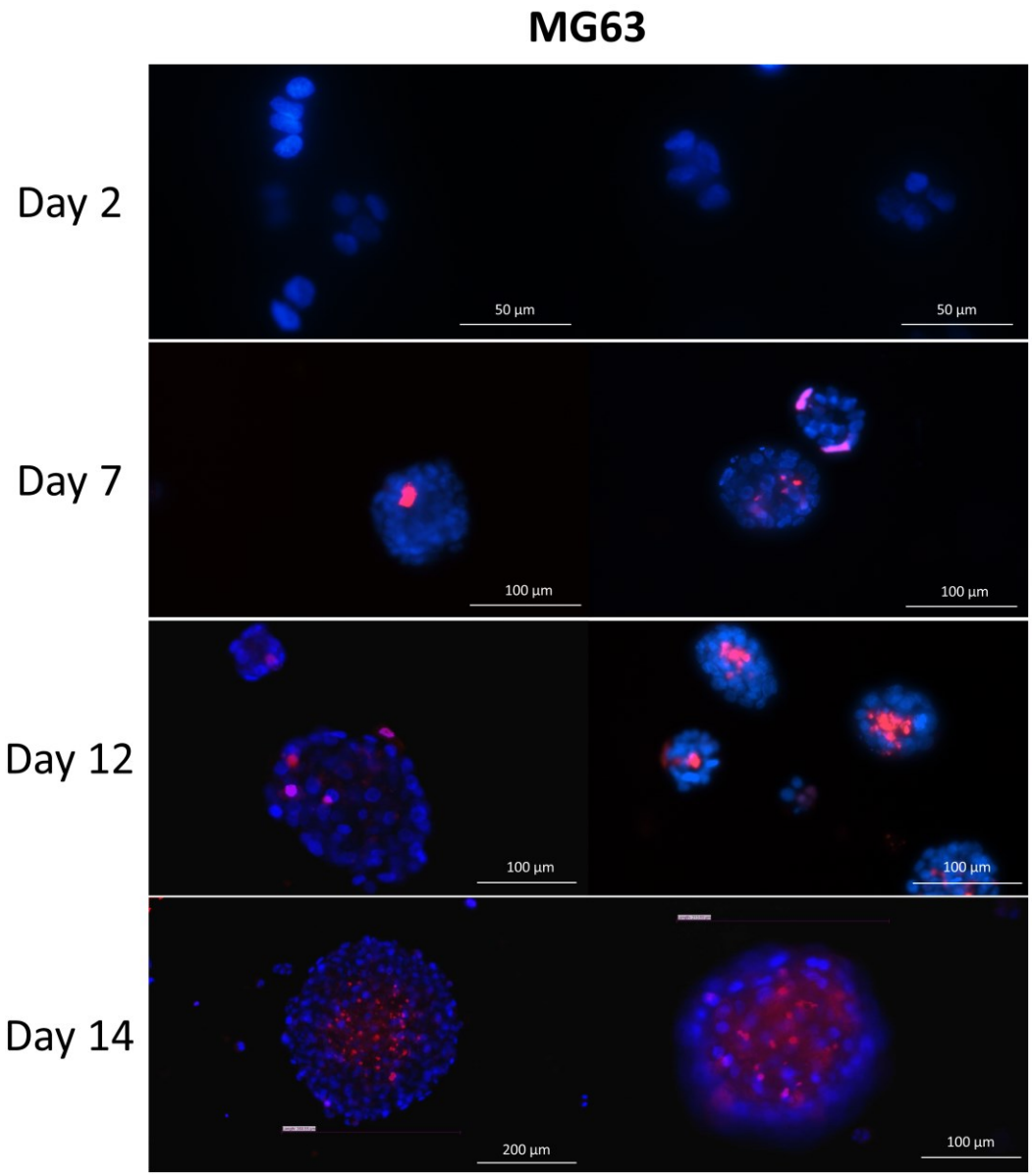

Figure 2.3 Spheroid development of MG63 OS cell line. Fluorescent images obtained by Hoechst 33342/PI staining to identify viable (blue) and necrotic (red) regions. Spheroid formation was observed within an alginate bead culture over 14 day period. Scale bar 50 µm (day 2), 100 µm (day 7, 12 and 14).

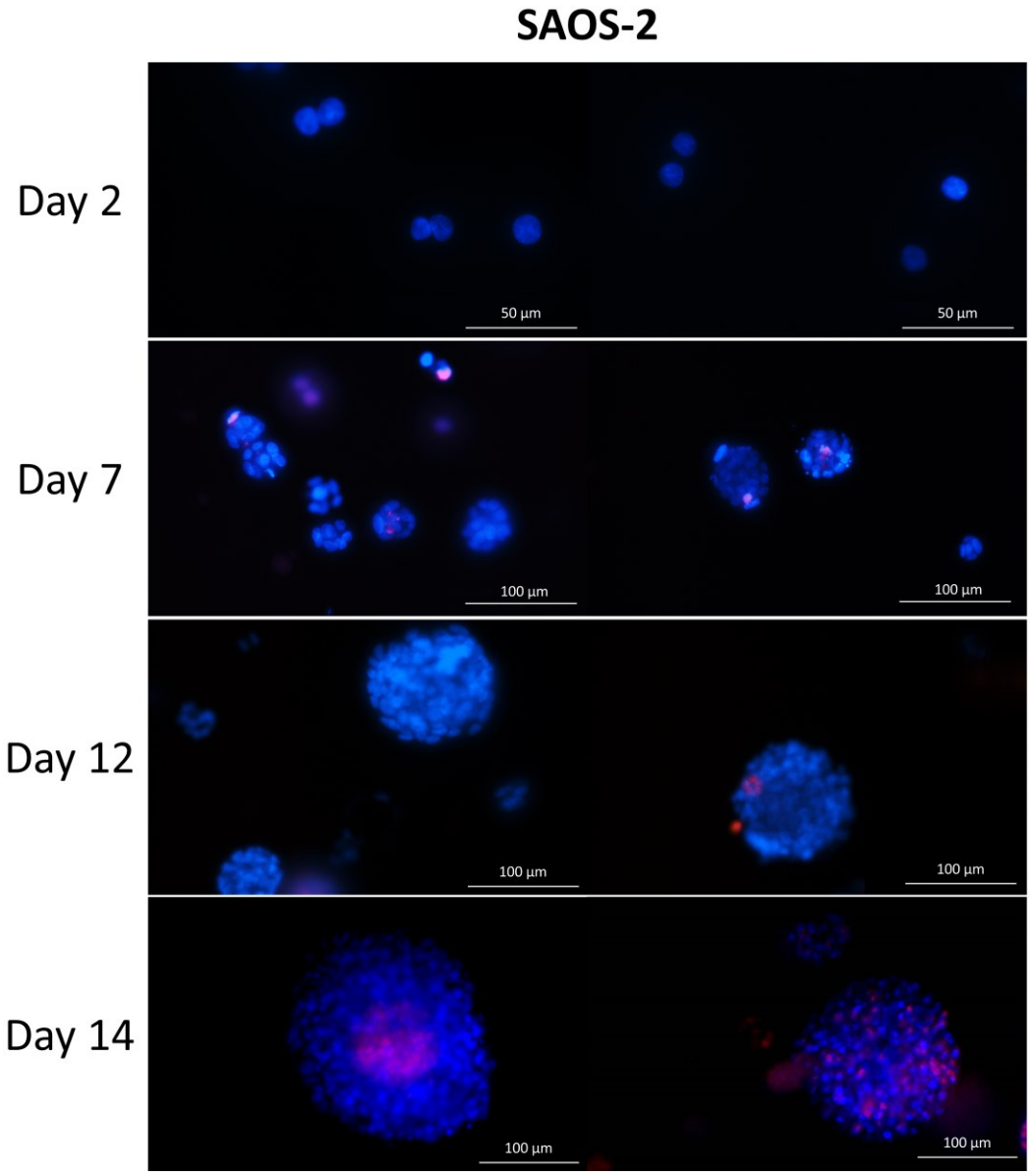

Figure 2.4 Spheroid development of SAOS-2 OS cell line. Fluorescent images obtained by Hoechst 33342/PI staining to identify viable (blue) and necrotic (red) regions. Spheroid formation was observed within an alginate bead culture over 14 day period. Scale bar 50 µm (day 2), 100 µm (day 7, 12 and 14).

The HCC827 spheroids at day 14 were smaller in diameter of around 100 μm, with a small indication of hypoxia (Figure 2.5). The larger and faster growth of the OS cell lines in comparison to the lung cell line is potentially due to the microenvironment from which the cells originated. OS cells were derived from low oxygenated regions within the human body, thus are accustomed to surviving in hypoxic conditions. The lung cells, however, were derived from high oxygenated areas therefore growing the cells in alginate, where there is a decreasing gradient of oxygen and nutrients towards the core of the bead, will impact the growth of the cells. Adapting the conditions of the alginate scaffold, in which the HCC827 cell line were cultured, could help improve the growth rate of the cells. Nevertheless, HCC827 cells were successfully grown to spheroids with the majority at the optimum diameter (> 70 μm) for the generation of large enough spheroid aggregates (700 – 1000 μm diameter). It was therefore decided that the alginate method used for the two OS cell lines was applicable to the lung cell line also.

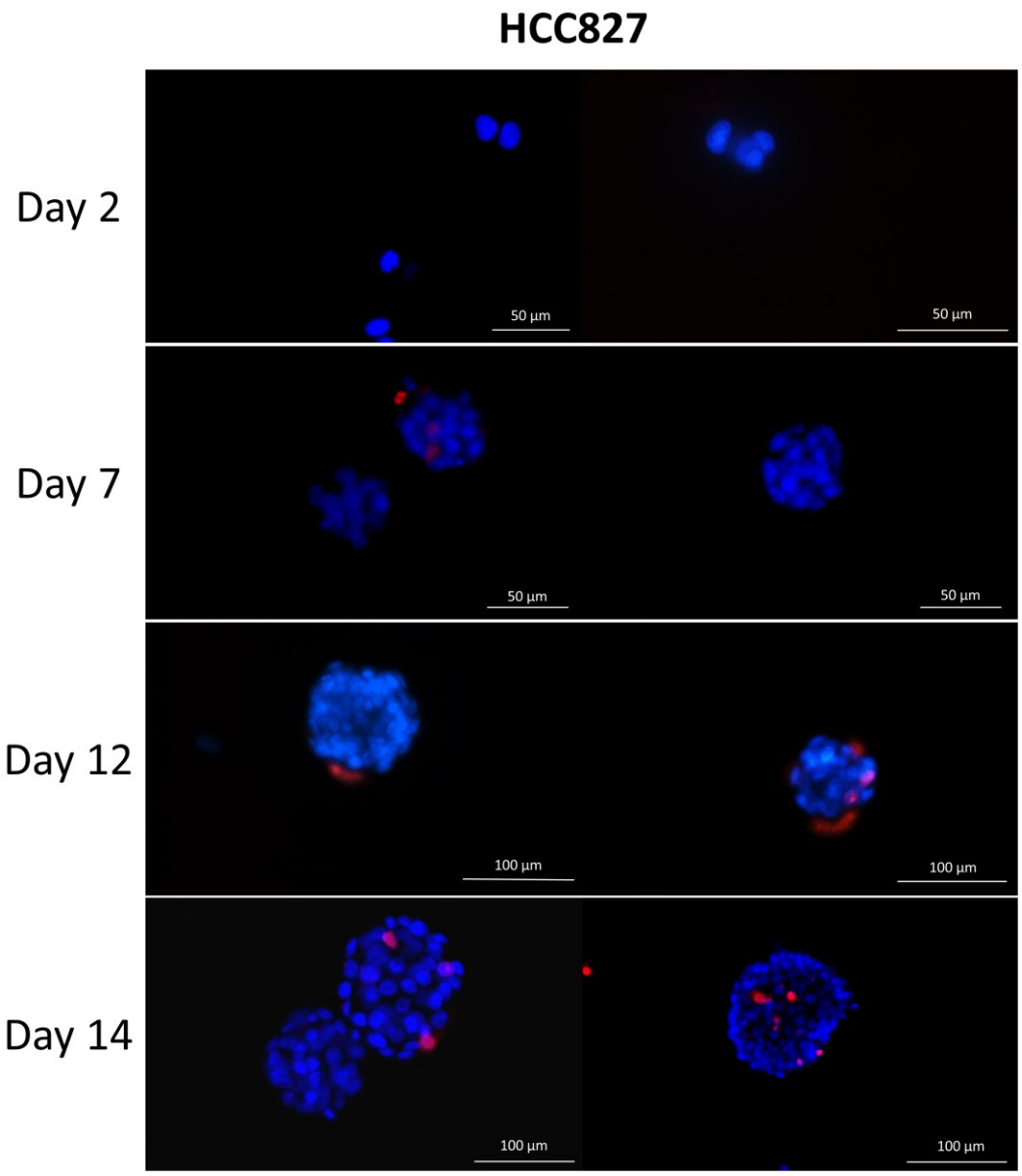

Figure 2.5 Spheroid development of HCC827 lung adenocarcinoma cell line. Fluorescent images obtained by Hoechst 33342/PI staining to identify viable (blue) and necrotic (red) regions. Spheroid formation was observed within an alginate bead culture over 14 day period. Scale bar 50 µm (day 2 and 7), 100 µm (day 12 and 14).

Following the method described by Palubeckaitė *et al.*, (2019), the spheroids were aggregated using agarose coated wells. The ultra-low attachment technique provided a non-adherent surface, forcing the spheroids to form into a single cluster and initiate spheroid-spheroid interaction. By documenting the growth of the SAOS-2 aggregates over a 7-day period, the formation of a compact aggregate model could be observed (Figure 2.6). From day 2, the cultures were large in diameter (> 1 mm) with obvious gaps, this showing the initial formation of the tissue whereby the clonal spheroids are still individual masses beginning to interact with each other. Throughout the culturing period, more spheroid-spheroid interactions were being formed, the aggregates were smaller in diameter than day 2 but have developed into robust aggregate masses.

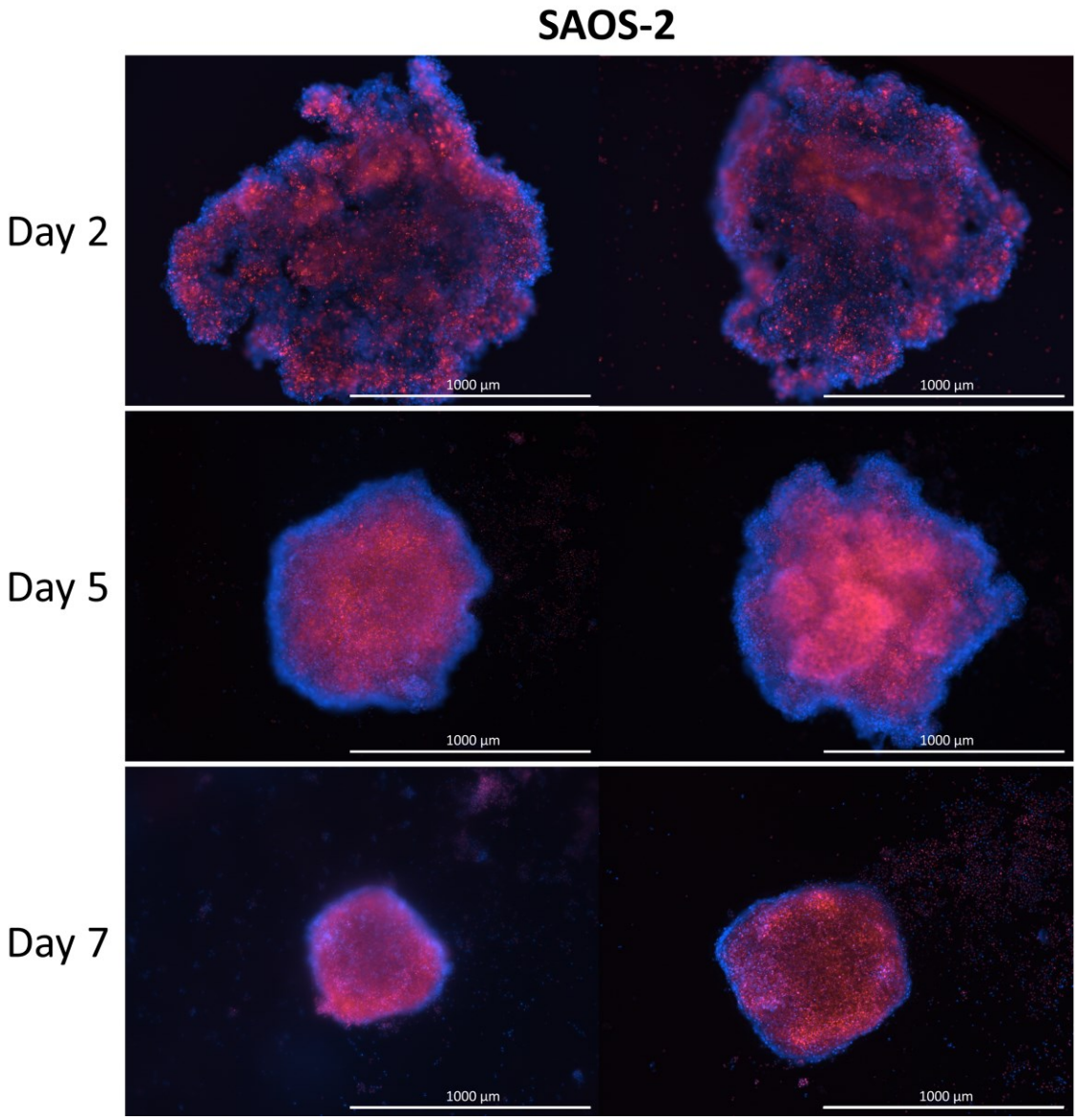

Figure 2.6 The formation of a SAOS-2 spheroid aggregate over a 7-day period. Fluorescent images obtained by Hoechst 33342/PI staining to identify viable (blue) and necrotic (red) regions. Scale bar 1000 µm.

Each cell line produced spheroid aggregates with large diameters of approximately > 700 µm displaying an outer area of viable cells and an inner necrotic region, likely due in part to hypoxia (Figure 2.7). A previous spheroid study reported that cultures over 500 µm begin to form a necrotic region (Däster *et al.*, 2017). This is highly beneficial as the model provides areas of heterogeneity. As previously mentioned, there is correlation of hypoxia with chemoresistance due to depleted oxygen levels, and apoptotic and necrotic activity that impact the drug's delivery and cellular uptake (Muz *et al.*, 2015). In addition, the majority of chemotherapeutics are most active when cells are within their cell cycle, the lack of oxygen and thus the presence of non-proliferative cells can impact the cytotoxic activity of a drug. Therefore, the large area of hypoxia with necrotic activity within the spheroid aggregates is an ideal model for studying a drug's behaviour and efficacy, screening drugs at the early stage of development.

The morphology of the aggregates showed some irregularity across replicate cultures of the same cell line, possibly due to the different sizes of spheroids within the culture leading to randomised direction of growth. Although variance across cultures could be seen as a disadvantage in terms of the size of the phenotypic areas having an impact on drug efficacy results. Variance in morphology can also be seen as beneficial to study true tumour behaviour as cancer growth is exponential and irregular and does not lead to the formation of uniformed spheres (unlike the spheroid model). This variance leads to the need for biological repeats throughout analysis when studying drug behaviour and the cellular processes within the aggregate model.

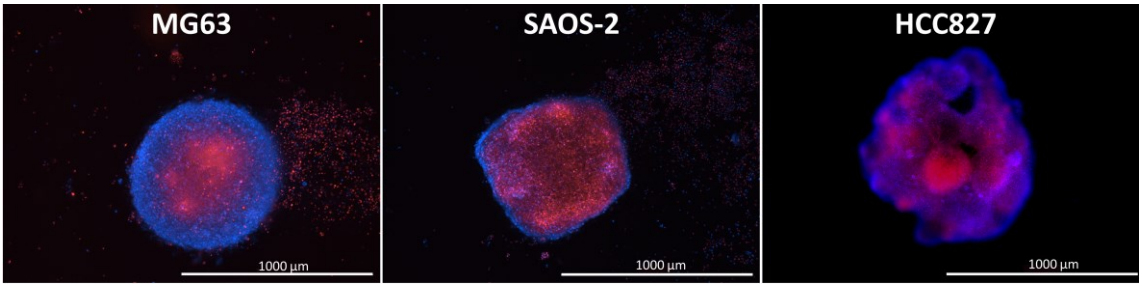

Figure 2.7 Spheroid aggregates of MG63, SAOS-2 and HCC827 at day 7. Fluorescent images obtained by Hoechst 33342/PI staining to identify viable (blue) and necrotic (red) regions. Scale bar 1000 µm.

During this study, the spheroid aggregate was re-termed an “aggregoid” from the basis of describing the model as the aggregation of spheroids, and therefore the 3D model will be described as an aggregoid throughout the remainder of the thesis.

2.4.2 Sample handling for MS analysis

Maintaining the integrity of tissues is imperative for spatial distribution studies to preserve the localisation and abundance of molecules in biological samples. The aim is to retain the tissue as close to its native state in order to obtain a true representation of the chemical processes within the sample. The processes of the collection and handling of samples are the most important steps of the imaging workflow to achieve quality results during MSI analysis. Many protocols have been developed with the aim of being universally applicable across ionisation methods to allow for an in-depth evaluation of species within tissues (Goodwin, 2012). Components of sample collection and handling include the stabilisation, processing and storage of tissues.

2.4.2.1 Sample stabilisation

Commonly, tissues are immediately snap-frozen directly in liquid nitrogen or isopentane at point of collection as a method of stabilising the sample. Fresh frozen tissues can then be stored at - 80°C until use, for a typical period of up to a year before molecular degradation would impact the abundance of protein distribution (Schwartz *et al.*, 2003; Lemaire *et al.*, 2006). Alternatively, following suit from histological preparation, MSI analysis can also be performed on formalin-fixed paraffin-embedded (FFPE) samples (Djidja *et al.*, 2017; Ly *et al.*, 2019). The fixation of tissues enables preservation of biological samples suitable for indefinite storage and aids the sectioning process by increasing the rigidity of tissues (Howat & Wilson, 2014). However, the analysis of FFPE tissues by MSI is limited to proteotypic peptides, with very little literature published on the detection of other species (Ly *et al.*, 2016; Denti *et al.*, 2020). This is due to additional sample preparation methods required including, deparaffinisation with numerous washing steps, which consequently impacts the presence of metabolites and lipids (Vos *et al.*, 2019).

For smaller, fragile tissues, such as tumour aggregoids, supportive materials have been employed for better sample handling prior to snap freezing, especially

when considering sectioning of tissues. MSI compatible materials that do not interfere with the analysis of compounds nor impact the morphological features of the tissue are essential. Optimal cutting temperature compound (OCT), traditionally used in histology, is universally known to cause severe polymeric interference which subsequently suppresses analyte detection and therefore it is avoided (Schwartz *et al.*, 2003). Materials more suitable for MSI studies include gelatin (Gill *et al.*, 2017), carboxymethylcellulose (CMC) (Potchoiba *et al.*, 1995; Stoeckli *et al.*, 2007) and poly[N-(2-hydroxypropyl) methacrylamide] (pHPMA) (Strohalm *et al.*, 2011). With many imaging studies reporting gelatin as an acceptable embedding medium for 3D cell culture models (Ahlf Wheatcraft *et al.*, 2014; Liu & Hummon, 2015; Liu *et al.*, 2018; Palubeckaitė *et al.*, 2019). Additionally, a hydrogel composed of hydroxypropyl methylcellulose (HPMC) and polyvinylpyrrolidone (PVP) was recently developed. Dannhorn *et al.*, (2020) demonstrated the compatibility of this new hydrogel matrix across MALDI, DESI and SIMS techniques.

To determine the optimum conditions for embedding the aggregoid model, three embedding media: gelatin; CMC; and HPMC & PVP, were evaluated. During the embedding process, both gelatin and CMC required heating at 50°C for the media to be liquid prior to coating the moulds, whereas HPMC & PVP was pre-conditioned on ice. The high temperature of the gelatin and CMC was of initial concern in terms of the effect on the cellular viability of the aggregoid, potentially increasing the risk of sample degradation and altering the morphology of the tissue. Although as previously mentioned, gelatin has been demonstrated a suitable embedding media in spheroid studies and may not have such an impact. All samples were frozen in liquid nitrogen immediately after the aggregoids were covered with the embedding media and stored at - 80°C to reduce the possible risk of sample degradation from the heated media temperatures.

2.4.2.2 Sample processing

In terms of sectioning the samples, gelatin provided some rigidity to the aggregoid, where sections appeared whole with little to no splintering or fracturing to the tissue. However, the ability to see the aggregoid within the gelatin was difficult due to their similarity in colour, which led to over sectioning some of the samples. The aggregoids embedded in CMC on the other hand were more easily identified. The media itself had a consistency of frozen water which impacted how

the sample was sectioned, causing fracturing to the aggregoid sections and therefore were more fragile when handling. The HPMC & PVP media however, provided some qualities of both gelatin and CMC. The aggregoid samples were easily located within the embedded mould and the sections maintained the sample integrity with minimal fracturing to the tissues.

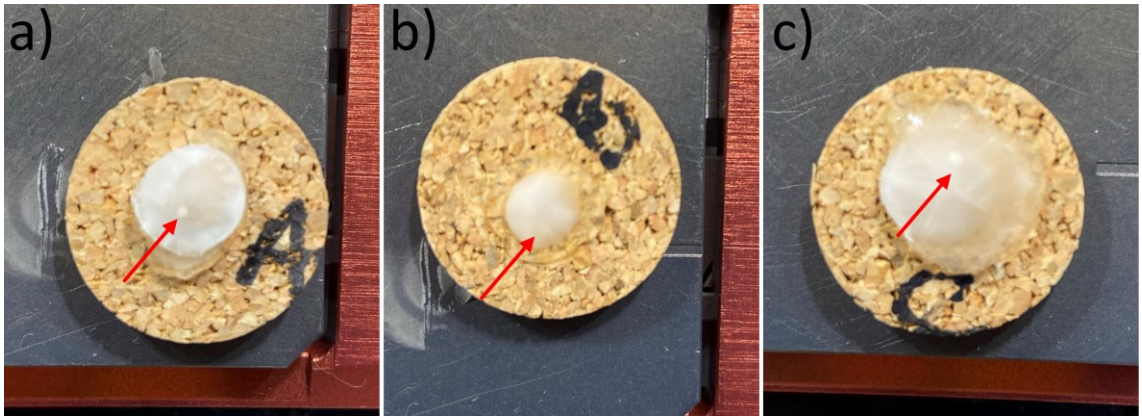

Figure 2.8 SAOS-2 aggregoids embedded within a) HPMC & PVP; b) Gelatin; c) CMC after trimming the embedding mould to reach the tissue. Red arrows identify the aggregoid within each embedding media.

The morphology of the aggregoid sections within the different media was observed by histological staining (Figure 2.9). Slight fissures to the sections were observed, which most likely occurred during sectioning. From the gelatin and HPMC & PVP embedded aggregoids, the tissues appeared to be more cohesive in structure with less dense areas typically within the core. This was as expected as this is a region of necrosis, where some cell interactions are lost due to cell death. In comparison, the HPMC & PVP embedded samples showed the best preservation of the aggregoid tissue. The CMC embedded samples showed a lot of fracturing to the sections, which could be the result of the consistency of the media and the impact it had on sectioning. An additional step of fixing the tissues with PFA at the beginning of the histology stain was included to ensure the loss of tissue was not due to the staining process. The fixation step, however, showed very little impact on improving the preservation of the CMC embedded aggregoids (Figure 2.9b). Interestingly, the morphology around the outer region of the aggregoids in some samples embedded in gelatin and CMC showed obvious disturbance to cells, as the HPMC & PVP embedded aggregoids showed intact tissue. The impact on the tissue is potentially from the temperature of the media

during the embedding process. The subsequent effects of this could therefore affect the cellular viability around the edge of the model and could lead to inconsistency across samples. This was taken into consideration for MSI analysis of the aggregoids, when identifying phenotypic areas such as the outer proliferative region and how it could distort the results.

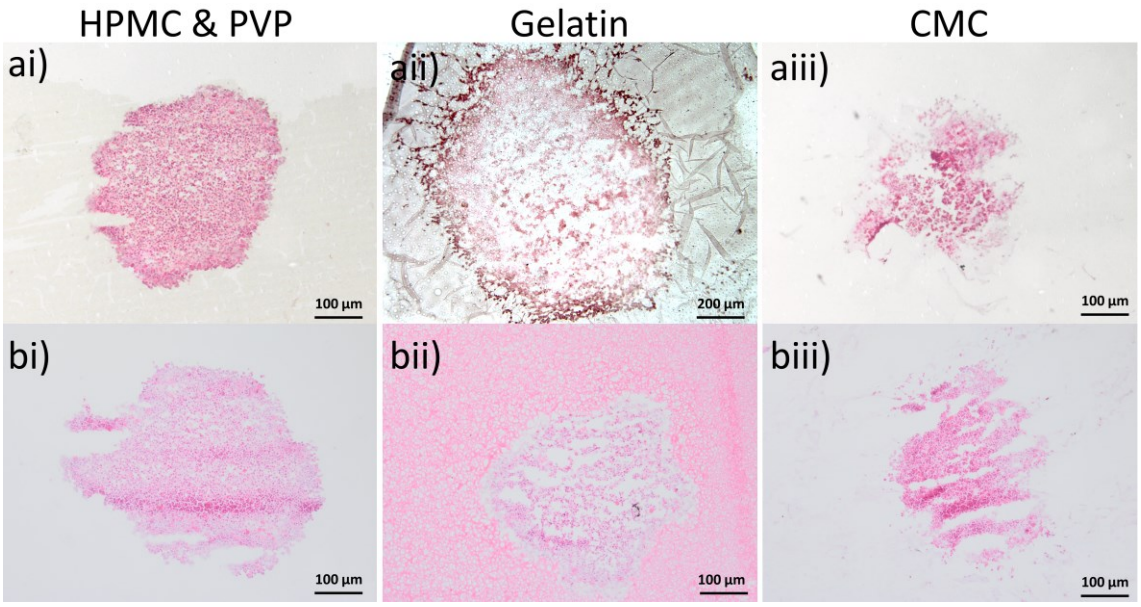

Figure 2.9 Histology staining of SAOS-2 aggregoid sections within embedding media. i) HPMC & PVP; ii) Gelatin; iii) CMC. a) Histology staining with Mayer's haematoxylin (purple) to identify nuclear components and eosin (pink) to identify the cytoplasm. b) The same histology protocol with an initial fixation step by 4% PFA. Slight fissures identified in the sections due to the sectioning process. Gelatin surrounding aggregoids showed staining from eosin due to the collagen components present (ai, bi). Scale bar 100 µm, (ai) 200 µm.

MALDI-MS profiling of each embedding media was performed to determine the molecular profile and identify any significant signals that may cause interferences with the sample. PEG containing media, such as OCT, typically show a series of signals within the range of 1100-2000 Da that can cause major ion suppression effects in proteomic analysis (Weston & Hummon, 2013). No polymeric-like signals were identified across the tested media within the targeted mass range for peptide species, or within the lower mass range for metabolites and lipids (*m/z* 100-2000) (Figure 2.10). HPMC & PVP and CMC had similar molecular profiles, with no obvious peak differences. Gelatin, on the other hand, displayed a background of signals from approximately *m/z* 700 onwards. This potentially could have effects on detecting abundant species within the lipid and peptide mass range, however the relative intensity of the peaks is somewhat low. Overall, none of the embedding media showed significant peaks that could have impact on the detection of molecules with the aggregoid model.

From the analysis of the embedding media, HPMC & PVP was found to be the most appropriate for use with the aggregoids. This was in terms of retaining the morphology of the tissue, but also the ease of handling samples. Additionally, with the reported compatibility of this media across different imaging technologies (Dannhorn *et al.*, 2020), it was of added interest for the multimodal MSI objectives within this thesis.

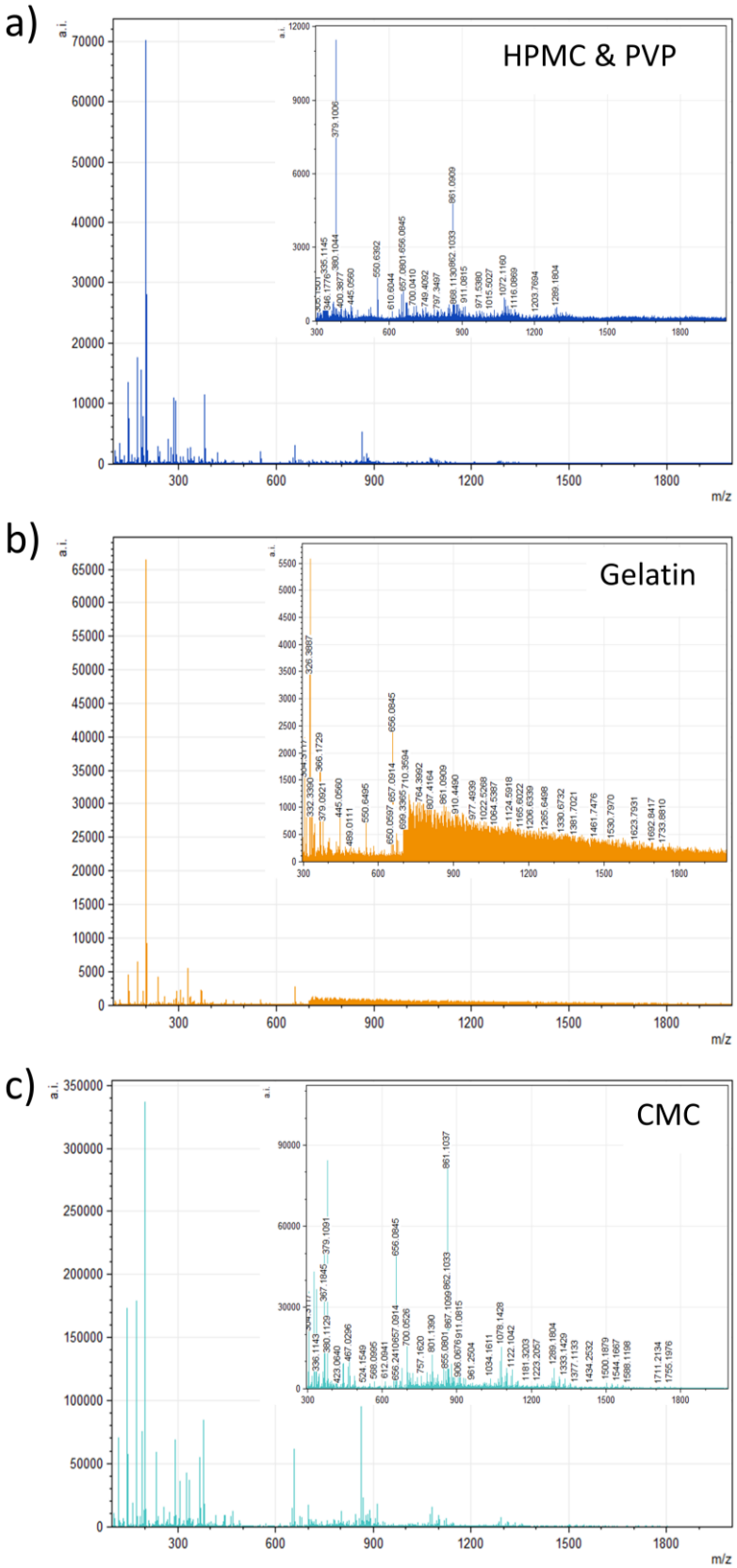

Figure 2.10 MALDI-MS profile of embedding media: a) HPMC & PVP, b) Gelatin, c) CMC. Embedding media profiled with 5 mg/mL α-CHCA (70% ACN 0.1% TFA, 2.4 µL aniline). Mass spectra acquired in positive mode, *m/z* 100-2000. Spectra was processed by mMass and normalised to the highest peak (α-CHCA, *m/z* 198.09) to obtain the relative intensity.

2.4.2.3 Storage of sections

A brief investigation on the effect of storage conditions on sectioned aggregoid samples was also performed. It is common knowledge that storage of tissue sections on slides over a long period of time can have an effect on analyte stability and can lead to less-than-optimal results (Goodwin, 2012). Slides are typically stored at - 80°C to retain the life-like state of the tissue sections and have shown to have no significant degradation on lipids over a 7-month period (Dill *et al.*, 2011). However, storage of slides at this low temperature can present challenges for MSI as the tissue sections are vulnerable to excessive ice formation and condensation, leading to potential analyte delocalisation (Russo *et al.*, 2020). Efforts to reduce this effect have resulted in methods of desiccation and freeze-drying techniques to remove excessive moisture before sample preparation for MSI analysis (Sjövall, Johansson, & Lausmaa, 2006; Porta Siegel *et al.*, 2018). The addition of these steps, however, can add time to the sample preparation workflow and is not completely effective. A study conducted by Swales *et al.*, (2018) assessed the effects of molecular stability within tissue sections under different storage conditions. The study established a novel protocol of desiccating sections immediately after thaw mounting onto slides with a nitrogen airflow, then subsequently vacuum packing the slides prior to storage at - 80°C.

A comparison of aggregoid slides stored using the conventional methodology, whereby slides are sealed in a slide box container at - 80°C, versus the methodology validated by Swales *et al.*, (2018), was carried out. From the image analysis, significant delocalisation of the abundant metabolite lactate (*m/z* 89.023) was observed in the conventional storage method (Figure 2.11a). High intensity levels of lactate were observed in the region immediately surrounding the aggregoid sections and with noticeable levels detected across the embedding media. The sections that were dried with a nitrogen airflow and vacuum packed before storage showed levels of lactate solely within the aggregoid sections, with some small artifact areas within the embedding media (Figure 2.11b). With the size of the aggregoid sections being considerably smaller than most tissue sections, such as animal organs or human biopsies, the delocalisation effects are amplified. Thus, after observing a significant difference in the spatial localisation of a key metabolite between the two storage methods, it was decided that the

method developed by Swales *et al.*, (2018) was the optimum protocol to achieve quality aggregoid imaging analysis.

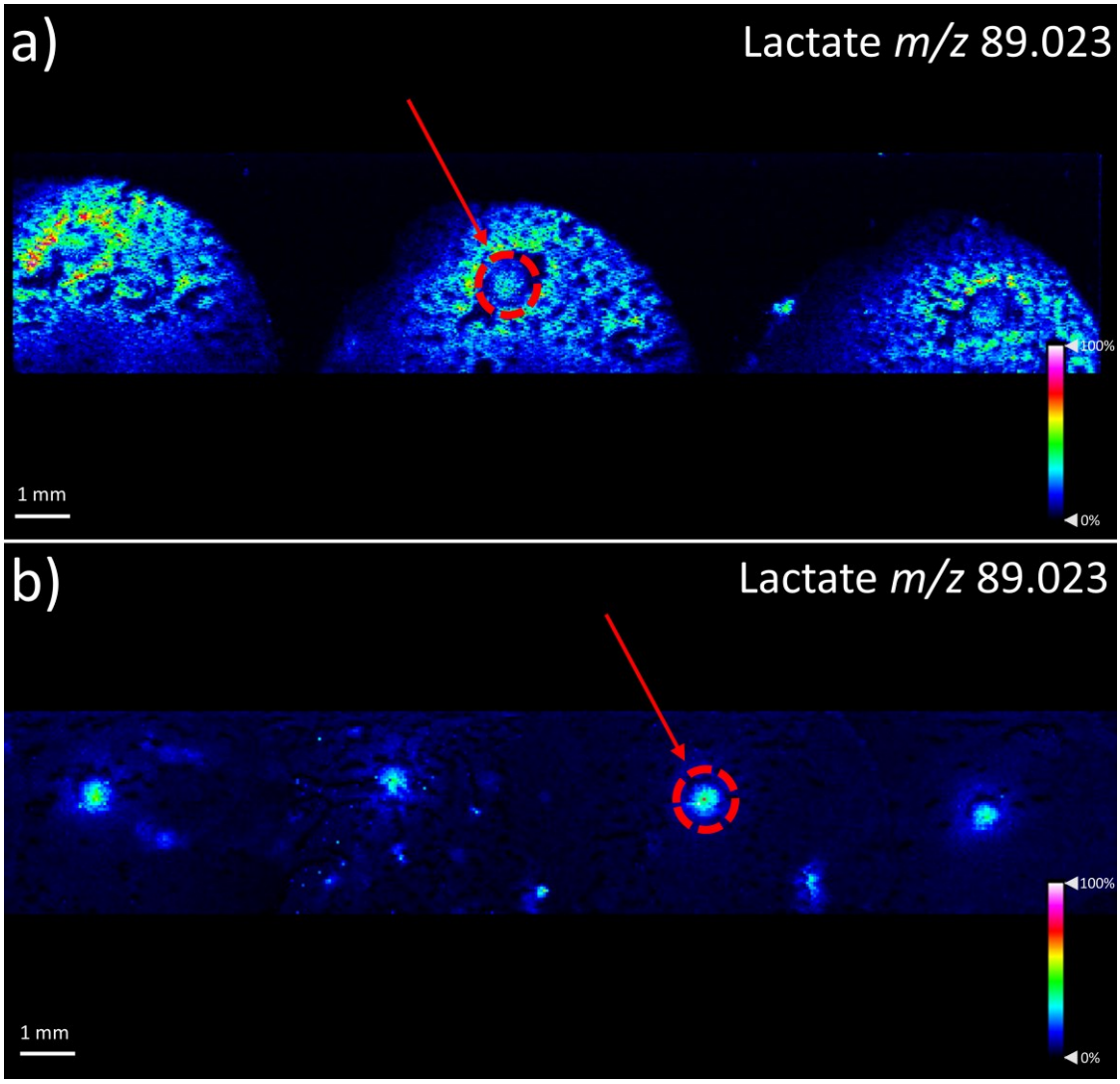

Figure 2.11 DESI-MSI analysis of MG63 aggregoid sections on slides prepared and stored in different conditions. Lactate (*m/z* 89.023) distribution displays the delocalisation effects of each storage condition: a) Slides sealed in a slide box mailer at - 80°C. b) Slides desiccated with a nitrogen airflow immediately after thaw mounting sections, vacuum packed and stored at - 80°C. Red arrows and dotted circles outline the aggregoid section. Scale bar 1 mm.

2.4.3 MS analysis

2.4.3.1 Direct lipid profiling and imaging of aggregoid sections using MALDI-MS

Using the optimised sample handling protocol discussed in section 2.4.2, MS analysis of small molecule species was performed. The purpose of this was to demonstrate the compatibility of the aggregoid model with MS imaging by employing MALDI-MSI for the detection of abundant molecules. An assessment of ion suppression effects arising from the HPMC & PVP embedding media was performed. In addition, two matrix application methods for imaging were investigated for optimum analyte detection.

Initially, each aggregoid model was profiled by MALDI-MS in positive ion mode. Sections from three biological replicates from each aggregoid model were analysed and spectra were acquired within the mass range *m/z* 100-2000. No signal interferences were identified from HPMC & PVP confirming the observation previously made when profiling the embedding media alone. Numerous peaks, specifically within the lipid range *m/z* 700-850, were identified within the aggregoid tissues (Figure 2.12). The most abundant lipid signals detected within each aggregoid model included phospholipid species, specifically of the phosphatidylcholine (PC) group, PC 32:1 at *m/z* 732.5, PC 34:1 at *m/z* 760.6, and PC 36:4 at *m/z* 782.5, identified through putative assignments. PC species are highly abundant in cancerous tissue due to their role in energy production and signalling for tumour progression (Cheng, Bhujwalla, & Glunde, 2016). It is therefore expected that the three aggregoid models of cancer have similar lipid profiles.

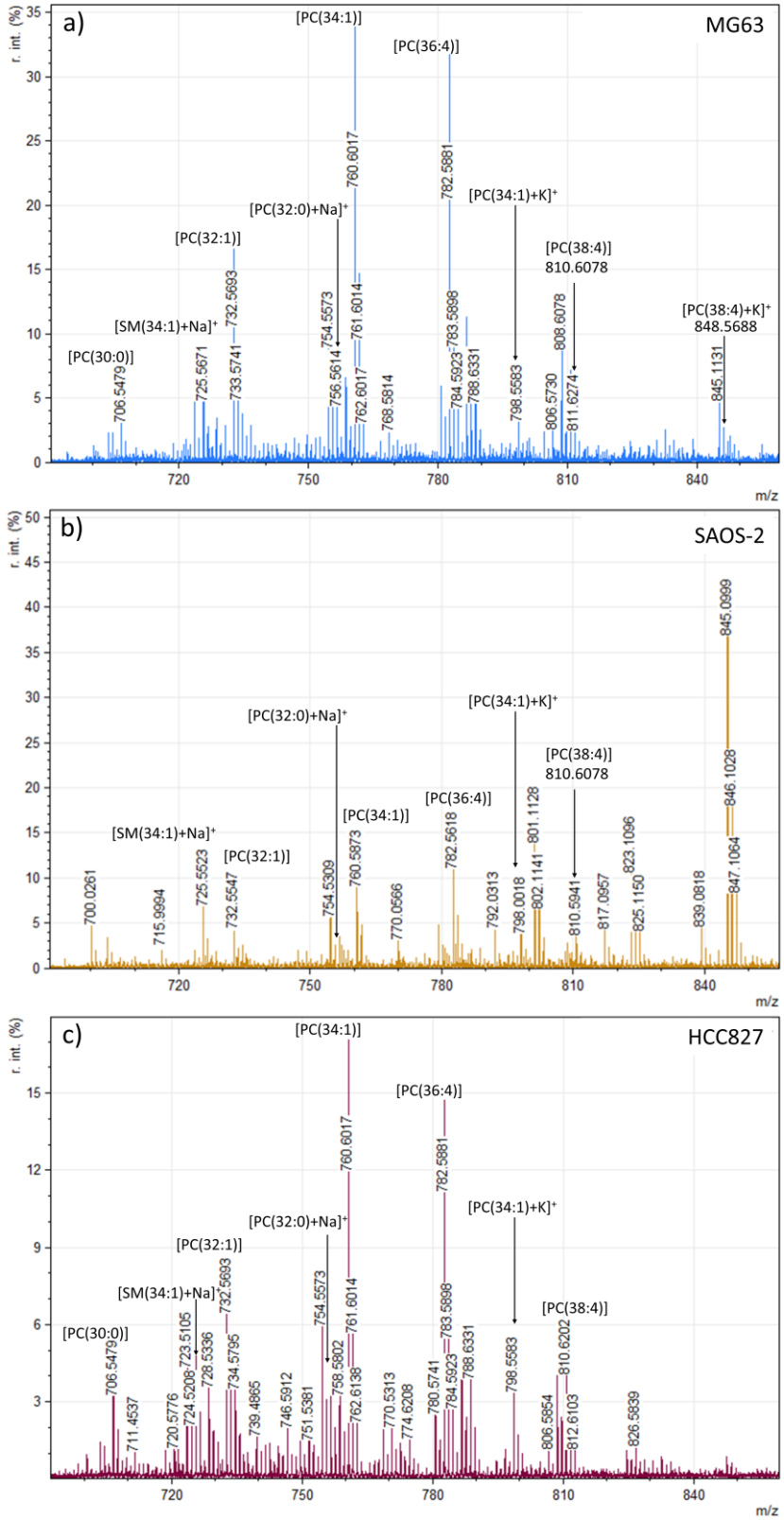

Figure 2.12 MALDI-MS lipid profile a) MG63 b) SAOS-2 and c) HCC827. Mass spectra acquired in positive mode; spectra display peaks within the mass range *m/z* 700-850. a) MG63 spectrum annotated with lipid species. Spectra was processed by mMass and normalised to the highest peak (α-CHCA, *m/z* 198.09) to obtain the relative intensity. b) SAOS-2 shows high α-CHCA peak at *m/z* 845.1 increasing the intensity scale bar to r. int. 50%.

The intensity of the lipid signals varied across the aggregoid models. SAOS-2 aggregoids showed a slightly lower intensity of PC 32:1, PC 34:1, and PC 36:4. However, there was no significant difference between the aggregoid models for each abundant peak (Figure 2.13).

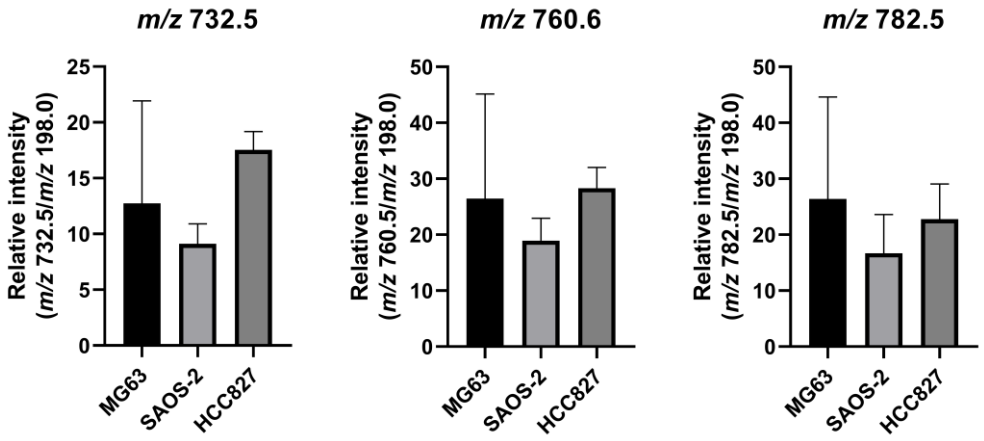

Figure 2.13 Relative intensities of lipid species PC 32:1 at *m/z* 732.5, PC 34:1 at *m/z* 760.6 and PC 36:4 at *m/z* 782.5. Biological replicates of each aggregoid were profiled (n=3). Each relative intensity was calculated from the most abundant α-CHCA peak at *m/z* 198.09. A one-way ANOVA determined there were no significant differences between the aggregoid models for each *m/z* value ($p > 0.05$).

To determine the distribution of lipid species in the aggregoid models, MALDI-MS images were acquired. In order to obtain the images, α-CHCA was deposited onto the aggregoid sections using the spray-coat method by the SunCollect™ automated sprayer. This is a conventional method of matrix application for MSI studies that has been used and investigated for many tissue types (Djidja *et al.*, 2010; Patel *et al.*, 2015; Huizing *et al.*, 2019). Figure 2.14 shows MALDI-MS images of the distribution of lipid species within a HCC827 aggregoid section. Abundant lipid species previously identified by profiling were also detected within the aggregoid samples, MG63 and SAOS-2 (data not shown). The images were acquired at a spatial resolution of 40 µm to enable in-depth data processing of the aggregoid to determine phenotypic regions that potentially corresponded to the tumour microenvironment. By employing segmentation analysis using SCiLS™ Lab software (Bruker Daltonics), whereby similar spectral characteristics are grouped together into a segment and are classified into phenotypical regions within the tissue. From the segmentation analysis, two

regions were identified: an outer region and an inner core. From the data of the fluorescent images of the aggregoid model in section 2.4.1, it can be assumed that these specific areas highlight the proliferative and hypoxic regions.

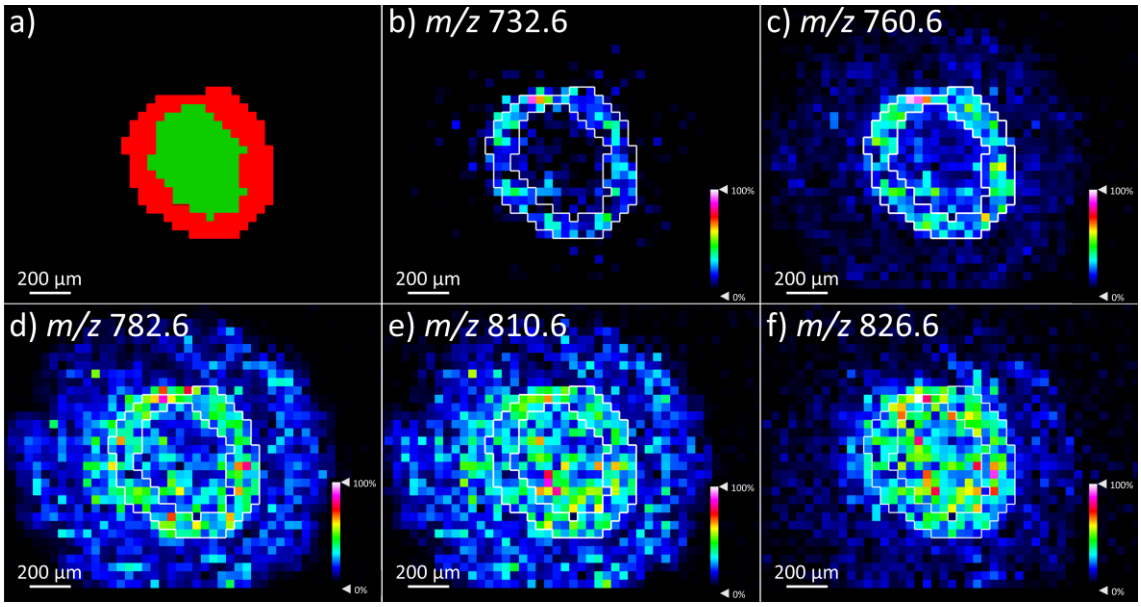

Figure 2.14 MALDI-MS image of a HCC827 aggregoid section. a) spectral segmentation identifying two phenotypical regions: an outer and core. The areas were outlined on the *m/z* images to determine distribution of abundant lipid species b) *m/z* 732.6, c) *m/z* 760.6, d) *m/z* 782.6, e) *m/z* 810.6, f) *m/z* 826.6. Images were normalised using TIC. α-CHCA applied by spray-coat method. Scale bar 200 µm.

By identifying the two regions within the aggregoid model, the distribution of lipid species could be associated to the outer proliferative region or inner hypoxic core (Figure 2.14a). Signals at *m/z* 732.6 (PC 32:1) and *m/z* 760.6 (PC 34:1) were distributed within the outer region of the aggregoid and therefore are assumed to be associated with cellular proliferation. A study analysing human breast cancer tissues by MALDI-MSI reported a positive correlation of the PC 32:1 signal with the proliferation cellular marker Ki-67 (Hosokawa *et al.*, 2017). This is therefore in agreement with the distribution of PC 32:1 in the aggregoid section. In contrast, a peak at *m/z* 826.6 (PC 36:1) was distributed throughout the aggregoid. PC 36:1 has been recognised as a hypoxia-regulated lipid in another MALDI-MSI breast cancer study (Jiang *et al.*, 2015), which would explain its presence within the aggregoid core but not in the periphery. This initial imaging analysis demonstrates

that there are differences in lipid distributions across the tissue and allows two distinct regions of the tumour microenvironment to be identified.

Interestingly, the detection of peaks *m/z* 782.6 (PC 36:4) and *m/z* 810.6 (PC 38:4) displayed analyte delocalisation into the area surrounding the aggregoid (Figure 2.14d, e). It is possible that this occurred during the application of matrix via the spray-coat method. As the matrix requires a solvent for wetting the tissue during spraying, it can influence the migration and diffusion of analytes (Schwartz *et al.*, 2003). Optimisation of the SunCollect™ spraying parameters such as the flow rate, pressure, nozzle movement and height, may help minimise the delocalisation effects. As the diffusion was observed in selected species, it suggests it is due to the solubility of the analyte with the solvent opposed to the spraying parameters.

Sublimation, an alternative method of matrix application, was evaluated in attempt to improve the spatial resolution and minimise delocalisation effects. This is a solvent-free matrix application therefore the migration of highly soluble molecules should be reduced and has been demonstrated as an efficient method for lipid analysis (Hankin, Barkley, & Murphy, 2007; Angel *et al.*, 2012; Ly *et al.*, 2015). It was recognised in the literature that DHB was reported as the conventional matrix used in sublimation for the detection of lipid species. Profiling and imaging using DHB on the Synapt G2 mass spectrometer resulted in no signal of matrix or analytes (data not shown). Therefore α-CHCA was used to achieve analyte signal and for a comparison with the spray-coat method.

The aggregoid images were acquired with the same parameters of the images of sections exposed to the spray-coat method. Figure 2.15 shows the MALDI-MS images of a HCC827 aggregoid section for the two analytes that displayed large delocalisation effects from the spray-coat matrix application. From the analysis of the images there was a significant reduction in analyte diffusion by the sublimation technique. However, the overall sensitivity of the lipid species was diminished, this was observed across all *m/z* values and in both MG63 and SAOS-2 aggregoid samples (data not shown). The lack of sensitivity also impacted determining the true localisation of analytes as background signal had similar intensities for the *m/z* values and could be identified as false signal within the aggregoid. This therefore is not ideal for distribution studies. By comparing the mean intensity of *m/z* values (n=1), sublimation detected lipid species at a

lower signal than the spraying method. This is most likely due to the solvent in the matrix required for the spray-coat method which assists the extraction of the analyte. It is important to note that the samples from the spray-coat method and sublimation cannot be directly compared as the analysis was performed on different sections on different days.

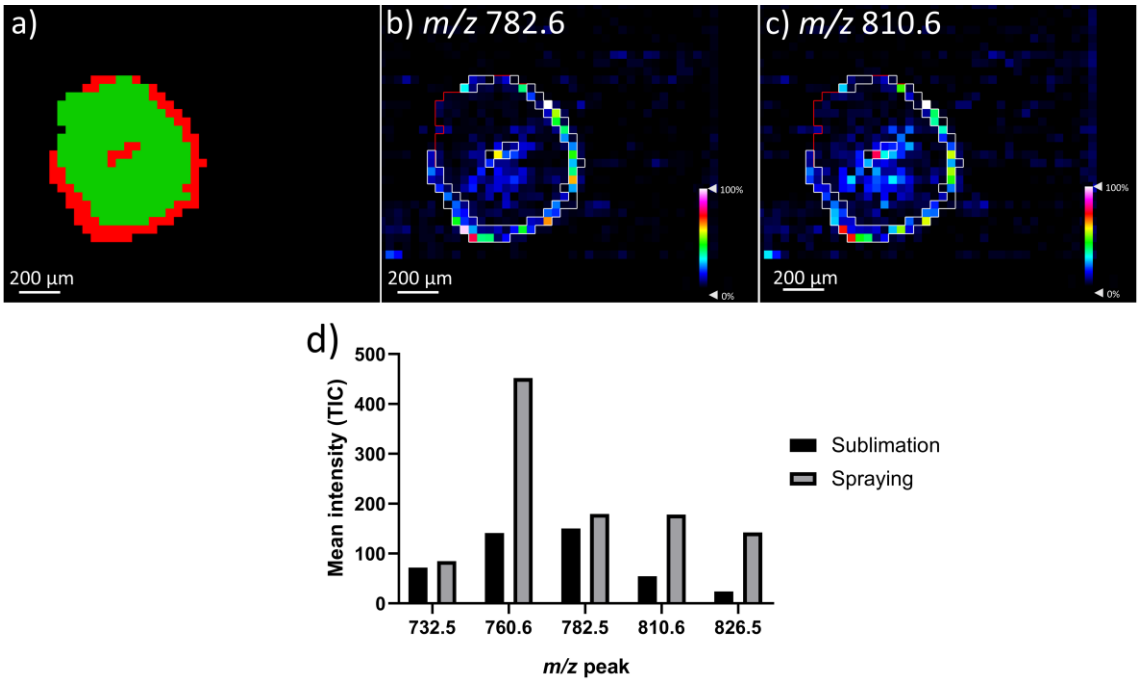

Figure 2.15 MALDI-MS image of a HCC827 aggregoid section achieved through matrix sublimation. a) spectral segmentation identifying two regions. The areas were outlined on the *m/z* mages to determine distribution of abundant lipid species b) *m/z* 782.6, c) *m/z* 810.6. Images normalised using TIC. Scale bar 200 µm. d) Mean intensity of *m/z* images obtained through matrix spraying or sublimation.

An additional step of matrix recrystallisation after sublimation could be performed to increase the sensitivity of lipids. The recrystallisation step creates a solvent vapour that rehydrates the sublimed samples. Re-introducing a solvent, however, could increase analyte diffusion and the recrystallisation step may not have a significant effect on the analyte signal, as has been reported (O'Rourke *et al.*, 2015). Optimisation of this step would require an investigation of solvents and incubation times to achieve quality images.

It was decided that despite the small amount of analyte delocalisation observed, the spray-coat method was still the most appropriate technique to detect

abundant lipid species within the 3D cultures. In addition, the ability to discriminate peaks within regions of the tumour microenvironment, demonstrated the capabilities of MALDI imaging with the aggregoid model.

2.5 Concluding remarks

In this chapter, establishment of a novel 3D cell culture in three models of cancer: MG63, SAOS-2 and HCC827 was described. The aggregoid model demonstrated phenotypic regions similar to the *in vivo* tumour microenvironment through live cell imaging and initial MALDI-MSI analysis. To achieve MS analysis and obtain quality images, sample handling techniques were evaluated. The use of HPMC & PVP embedding media showed the best preservation of the aggregoid tissues, created ease of handling for the imaging workflow and showed no spectral interferences. In addition, a new method of storing sectioned samples through desiccation and vacuum packaging of slides proved beneficial for reducing delocalisation of analytes within the aggregoids. Data obtained from two methods of matrix application demonstrated that the spray-coat method gave better sensitivity and enabled the detection of abundant lipid species within the aggregoid when compared to sublimation. Delocalisation effects were observed in some lipid images however, with the spatial resolution capabilities of MALDI-MSI, it was still possible to discriminate species within the outer region and inner core of the aggregoid models.

CHAPTER 3. THE CHARACTERISATION OF AN AGGREGATED 3D CELL CULTURE MODEL BY MULTIMODAL MSI

3.1 Introduction

The spatial localisation of a molecule can determine the interplay of biological functions and interactions within a tissue. This also enables a greater biological understanding of cellular phenotypes, their structural organisation, and relationship to the surrounding microenvironment. MSI has therefore had an influential impact on cancer research and drug development by providing information on the spatial localisation of biomarkers, therapeutics, their active metabolites, and cellular responses which have resulted in new patient treatments (Swales *et al.*, 2019).

Depending on the biological sample and the molecules of interest, different MSI techniques can be employed for optimum analysis. MALDI is the most widely used MSI technique across many applications due to its high spatial resolution and speed of acquisition. MALDI-MSI can detect a wide range of analytes in an untargeted manner including metabolites, lipids, peptides and proteins (Stoeckli *et al.*, 2001; Weaver & Hummon, 2013; Buchberger *et al.*, 2018). DESI-MSI has gained considerable attention in drug development studies particularly when used in combination with Orbitrap and QTOF type mass analysers for the generation of images with high mass specificity for metabolites and small molecule therapeutics in tissue samples (Chen *et al.*, 2005; Guenther *et al.*, 2015). In addition, the minimal sample preparation requirement of this ambient ionisation methodology limits experimental variability and reduces the timescale of the project (Takats *et al.*, 2004). The requirement for the analysis of trace elements or metal isotope distribution in tissues has also seen the development of LA-ICP-MSI (Pozebon *et al.*, 2014; Hare *et al.*, 2015), a technique that has been applied to the analysis of metal-containing therapeutics such as cisplatin (Theiner *et al.*, 2016; Theiner *et al.*, 2017). A major advancement in LA-ICP-MSI is the evolution of IMC, a novel multiplex method capable of tissue phenotyping, and imaging biological processes through the detection of proteins and protein modifications at a high spatial resolution (< 1 μm). IMC has demonstrated high-dimensional single-cell analysis capabilities on numerous tissue types (Giesen *et al.*, 2014; Chang *et al.*, 2017), and directly visualised platinum-based therapeutics and the biological responses to treatment (Chang *et al.*, 2016). Furthermore, studies have demonstrated the benefits of employing multimodal MSI for the extraction of complementary molecular information (Chughtai *et al.*, 2012;

Veličković *et al.*, 2018). By using different MSI techniques, a wider detection of a diverse range of analytes can be obtained within corresponding samples and therefore yield a better understanding of the biological processes that drive cellular metabolism.

As discussed in detail in Chapter 1.4.1, advancements in MSI technology, especially the achievable spatial resolution, have enabled analysis of the pathophysiology in tumour spheroids. Applications of MALDI-MSI have characterised colon carcinoma and breast cancer spheroid models based on their endogenous metabolite and protein distributions (Li & Hummon, 2011; Hiraide *et al.*, 2016; Tucker *et al.*, 2019). More recently, MALDI-MSI detected similar tendencies in metabolic activity between KYSE-30 oesophageal cancer MCTS and clinical tissue samples (Zang *et al.*, 2021). In addition, progress in the development of the ambient technique, single-probe MSI, was able to spatially resolve endogenous metabolites within colon carcinoma MCTS (Tian *et al.*, 2019). However, limited literature has been reported on the use of multimodal MSI techniques with spheroid models. With the aim of characterising the tumour aggregoids for the purpose of pre-clinical biopharmaceutical testing, the idea of employing multiple MSI modalities was an appealing approach and a novel method to obtain a greater amount of detail for an in-depth understanding of the tumour metabolism.

In this study, the application of multimodal MSI was used to characterise the HCC827 lung adenocarcinoma aggregoid model. Lung adenocarcinoma is the most common subtype of non-small-cell lung cancer (NSCLC) and accounts for 40% of all lung cancers (Coroller *et al.*, 2015). NSCLC is an epithelial lung cancer that effects approximately 1 in 15 people in the UK. Although there have been considerable efforts in the development of effective therapeutic treatments, the patient outcome for lung adenocarcinoma is still significantly poor with < 15% survival rate at 5 years (Molinier *et al.*, 2020). The reasons for this low survival rate are due to the aggressiveness of the primary cancer, its heterogeneity between patients and the high resistance to drugs, which have hindered the development of effective therapies. Therefore, it is necessary to develop accurate *in vitro* models that can closely represent the metabolic behaviour of lung adenocarcinoma. Some tumour spheroid models derived from lung cancer cell lines and primary patient cells have been utilised in previous therapeutics studies

through the analysis of PCR and immunostaining techniques (Endo *et al.*, 2013; Ekert *et al.*, 2014; Zhang *et al.*, 2018). Specifically, spheroids of the EGFR mutant HCC827 cell line showed a promising tool for studying pharmaceutical response to small molecule therapeutics including gefitinib and erlotinib (Jacobi *et al.*, 2017). Nevertheless, there is a significant gap in the literature relating to the molecular profile of lung cancer spheroids by high performance MS techniques, let alone with MS imaging methods. Therefore, there is an opportunity to demonstrate the capabilities of MSI to analyse the HCC827 aggregoid model in an attempt to improve the understanding of lung adenocarcinoma based on the spatial information of a broad range of molecules.

3.2 Aims of the chapter

The following chapter reports the characterisation of a HCC827 lung adenocarcinoma aggregoid model using multiple MSI modalities: DESI, IMC and LA-ICP. The aim of this work was to demonstrate how the aggregoid model displays similar phenotypical characteristics to typical tumour spheroid cultures, and its potential as an *in vitro* research tool. The objective was to detect and identify specific molecular markers through the analysis of metabolites, proteins and protein modifications, and elemental compounds by the respective imaging platforms to define regions of proliferation and hypoxia, in addition to key biological processes that drive cancer metabolism in lung adenocarcinoma. Through obtaining a large amount of molecular information with a complementary nature, it was possible to determine an in-depth understanding of the biological processes within the novel tumour model.

3.3 Materials and methods

3.3.1 Materials

Alginic acid, $CaCl_2$, casein solution, DPX mountant, eosin, EDTA, EtOH, haematoxylin, PFA, PVP, sodium citrate, Triton™ X-100 and xylene substitute were purchased from Sigma-Aldrich (Gillingham, UK). HPMC was purchased from Alfa Aesar (Thermo Fisher Scientific, Heysham, UK).

3.3.2 3D culture growth

Culturing of HCC827 lung adenocarcinoma aggregoids is described in Chapter 2.3.3.

3.3.3 Tissue preparation

Aggregoids were prepared for imaging analysis based on the tissue embedding and processing protocol described in Chapter 2.3.4. Frozen aggregoids were sectioned at 10 µm thickness and thaw-mounted onto polylysine glass slides followed by immediate desiccation with N_2 and subsequent vacuum packing for storage at - 80°C.

3.3.4 Small molecule imaging

3.3.4.1 DESI-MSI

Small molecule imaging by DESI-MSI was performed on a Q-Exactive mass spectrometer (Thermo Fisher Inc, Germany) as described in Chapter 2.3.5.3. The images were collected in the mass range *m/z* 80-900 at a spatial resolution of 30 µm and analysed by SCiLS Lab MVS Premium 3D Version 2020a (Bruker Daltonics, Germany) employing RMS normalization.

3.3.4.2 Discriminatory analysis

The aggregoid DESI-MSI data file was segregated into regional clusters by spatial segmentation processing by which the “core”, “intermediate” and “outer” regions were identified (SCiLS, Bruker Daltonics). Discrimination between the two regions was achieved by automatically finding *m/z* values by employing the ROC tool to calculate the area under the curve (AUC) value. The raw data file from the DESI-MSI was uploaded to METASPACE (https://metaspace2020.eu) for metabolite identification of the discriminated *m/z* values by employing the Human Metabolome Database (HMDB) (tolerance < 1 ppm). Metabolic pathways were assigned based on the KEGG database by importing identified *m/z* values into Pathos software (http://motif.gla.ac.uk/Pathos/). The ion abundances for the *m/z* values were generated into histograms for comparison between regions using GraphPad™ Prism® software (La Jolla, USA).

3.3.5 Single-cell imaging

3.3.5.1 IMC staining

Tissues were fixed with 4% PFA for 10 min at RT. Prior to staining, tissues were permeabilised with 1x casein solution (v/v) containing 0.1% Triton™ X-100 (5 min) at RT. Tissues were then incubated with blocking buffer (1x casein solution) for 30 min at RT. An antibody cocktail was made containing the appropriate dilutions for the antibodies. Tissues were incubated with the antibody cocktail overnight at 4˚C. DNA Ir-Intercalator (Fluidigm®) was diluted 1:400 and applied to tissues for 30 min at RT. Washes with PBS were performed three times between each step, with the last step washed in deionized water for 30 s. Slides were left to air dry until analysis.

3.3.5.2 IMC analysis

Images were acquired using the Hyperion Imaging System (Fluidigm®), rasterizing at 200 Hz and with the laser tuned to fully ablate the tissue without etching the glass. TIFF files of each acquisition were then exported for analysis in the HALO® image analysis platform (Indica Labs). Using a random forest machine learning Tissue Classifier module which was the sole segmentation process provided by HALO®, each image was segmented into the background and inner, core and outer area of each aggregoid. Using the Hiplex module, the DNA intercalator was used to first segment the nucleus of each cell, and a proxy for the cytoplasm of each cell defined in a 1 µm radius from the nucleus, before thresholds set to define positive cell staining for each marker. Percentage positivity of each cell was then defined within the inner and outer region of the aggregoid.

3.3.6 LA-ICP-MS analysis

Experiments were conducted using a NexION 350X ICPMS (Perkin Elmer, USA) coupled to an UP-213 LA system (New Wave Research, USA) with a frequency quintupled 213 nm Nd: YAG laser. Laser parameters were optimised to 6 µm spot size with, 25 µm/s scan speed, 0.07 Jcm^{-2} laser fluence, and 20 Hz repetition rate. The sample was ablated line by line with 6 µm raster spacing at 1.31 min acquisition time. For the ICP-MS instrument there was a direct flow with a rate of 1.4 L/min. The following settings were used in standard mode with an 18 L/min plasma gas flow, 1.2 L/min auxiliary gas flow at 1600 W RF power. Isotopes

monitored included ^{24}Mg, ^{66}Zn and ^{63}Cu and the instrument was controlled using Syngistix software. Data analysis was achieved using Iolite Software on Igor Pro (WaveMetrics, USA).

3.3.7 Histological staining

After DESI-MSI, aggregoid sections were stained using Mayer's haematoxylin and eosin solutions following a different protocol reported in Chapter 2.3.6. Sections were fixed in 4% PFA (10 min) before staining with haematoxylin (1 min). Tissues were rinsed in tap water before and after submerging in acid alcohol. Tissues were subsequently stained with eosin for 30 s prior to washing tap water, then subsequently washed in 3 x absolute EtOH (1 min). Finally, tissues were submerged in xylene substitute (1 min) twice and mounted using DPX mountant. Stained tissues were imaged with Aperio CS2 digital pathology scanner (Aperio Tech., Oxford, UK) at 40 x magnification and visualized with ImageScope software (Aperio Tech.).

3.4 Results and discussion

3.4.1 Metabolite imaging

One major hallmark of cancer is an altered cellular metabolism to generate a sufficient energy source contributing to the initiation, growth, and maintenance of tumours (Hanahan & Weinberg, 2011). In the present study, the metabolic profile within the lung adenocarcinoma aggregoid model was investigated by employing a DESI Thermo Q-Exactive MSI to classify regions of a necrotic/hypoxic core and a viable outer area. Initial processing of the aggregoid images was conducted to spatially segment the data. These segments are then classified into regions which represent phenotypical features of a tissue. The aggregoid data was segmented into three main regions that depicted a gradient-like phenotype: a core (corresponding to the blue cluster), an annular zone (corresponding to the yellow cluster), and an outer region (corresponding to the red cluster) (Figure 3.1b, c). From the 2- and 3-dimensional images the clear discrimination of the regional clusters corresponded to the histology stain of the same section after MSI analysis (Figure 3.1a). From this, the spectra from each region were extracted to distinguish the distributions of key metabolites within the aggregoid. For the purpose of separating metabolites to distinct regions, the core and the outer

zones were the focus when observing the distribution of species, as the intermediate region was anticipated to be non-discriminatory.

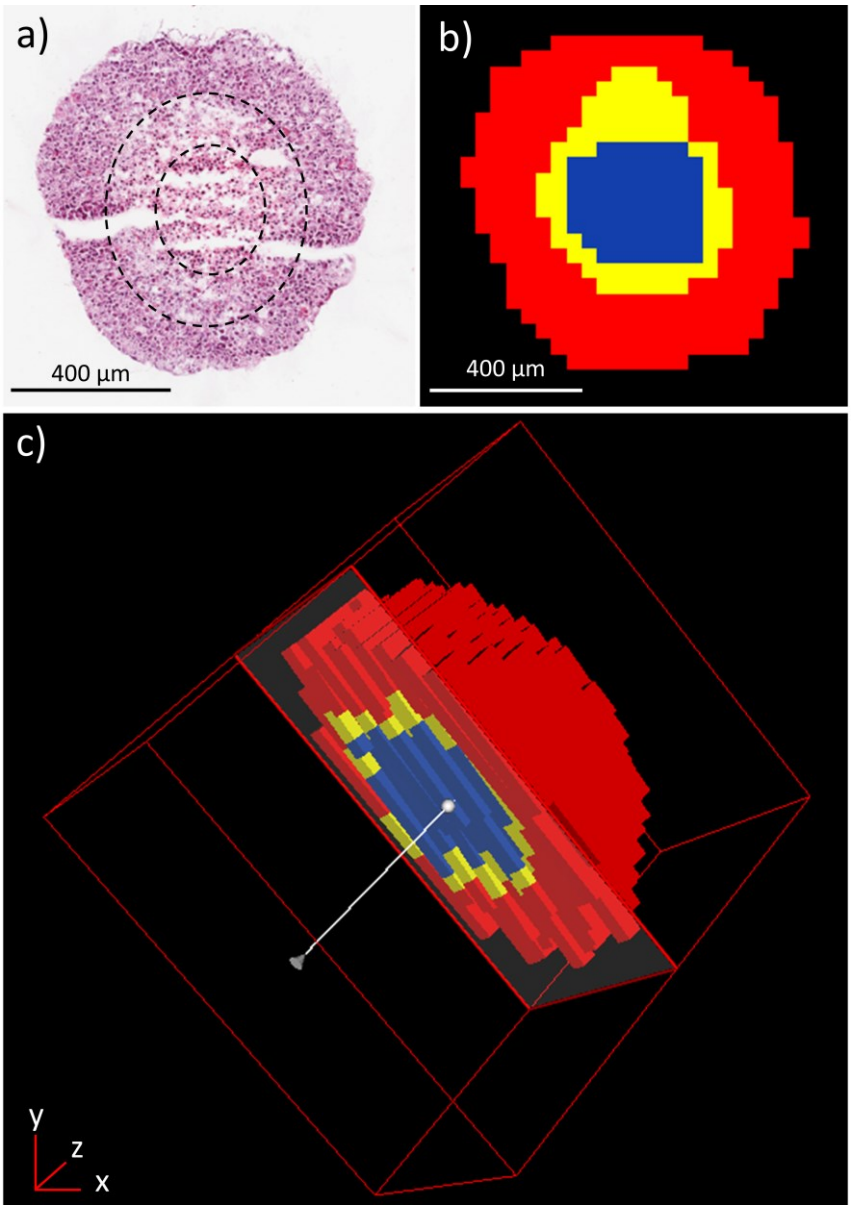

Figure 3.1 Spatial segmentation of HCC827 aggregoid model from metabolite data. a) H&E stain of central aggregoid section. Black dotted lines were manually included to show estimate regions of different cellular morphology that corresponds similar to segmentation image. Scale bar 400 µm. b) Spatial segmentation of central aggregoid section identified three clustering regions that correspond to the hypoxia gradient: Core (blue cluster), intermediate/annual region (yellow cluster), and the outer region (red cluster)c) Realigned 3D construct of aggregoid displaying segmentation pattern throughout the model.

Within the aggregoid model, key metabolites involved in cancer metabolism were identified with a mass error of < 0.5 ppm (Table 3.1). A major metabolic substrate that is regulated by the tumour microenvironment is lactate. Within the aggregoid, a high intensity of lactate (*m/z* 89.02440) was distributed throughout indicating the presence of glycolysis rather than oxidative phosphorylation (Figure 3.3b). An elevated expression of lactate in the core of the aggregoid implies the presence of hypoxia. In anaerobic conditions, the rate of glycolysis increases due to insufficient oxygen levels to promote tumour survival. In cancer cells, lactate is generated irrespective of the hypoxic or aerobic conditions to act as a primary metabolic fuel. An increase in the expression of lactate converted from glucose via the glycolysis reaction is thought to be the predominant pathway to promote tumour survival and growth rather than following oxidative metabolism, this is otherwise known as the Warburg effect (Warburg, 1956). It has also been recently hypothesised that the induced glycolysis reaction by cancer cells can also metabolically support adjacent cancer cells to further promote ATP production, increase proliferation and reduced cell death, also known as the reverse Warburg effect (Wilde *et al.,* 2017). Hence, the high intensity levels observed in the aggregoid model could be explained.

A similar distribution of a glycolysis intermediate, pyruvate (*m/z* 87.00880) was also observed (Figure 3.3a). The localisation of pyruvate across the aggregoid, with elevated levels in the core validates the assumption of an increased rate of glycolysis in response to hypoxia. A key protein associated with increased lactate production in low oxygen levels is hypoxia-inducible factor alpha (HIF-1α), which is stabilised in a hypoxic environment due to the lack of oxygen and therefore a direct marker of hypoxia. HIF-1α is responsible for regulating the expression of numerous genes under hypoxic conditions. Specifically, HIF-1α promotes the transportation of glucose into the cell by increasing the expression of the glucose transporter 1 (Glut1) (Hayashi *et al.*, 2004). Additionally, HIF-1α promotes a high glycolysis rate by inducing both pyruvate dehydrogenase kinase (PDK) and lactate dehydrogenase A (LDH-A), to prevent the metabolism of pyruvate into acetyl-CoA to feed the tricarboxylic acid (TCA) cycle, and rather by favouring the conversion of lactate (Kim *et al.*, 2006; Cui *et al.*, 2017).

Compound Name	*m/z* (measured)	Mass error (ppm)	AUC
Pyruvate	87.00880	0.4	0.240
Lactate	89.02440	0.2	0.138
Succinate	117.01940	0.9	0.640
Malate	133.01430	0.4	0.700
Glutamine	145.06190	0.2	0.114
Glutamate	146.04590	0.1	0.396
Citrate	191.01980	0.4	0.903
FA 18:2	279.23280	0.7	0.639
FA 20:4	303.23300	0.2	0.564
Glutathione (GSH)	306.07650	0.1	0.991

Table 3.1 Assignments and errors for $[M-H]^-$ adducts, and discriminatory analysis of metabolites between the core and outer from SCiLS Lab software. Mass accuracy of metabolites with the measured *m/z* values and calculated *m/z* values (< 2.5 ppm). AUC determined by ROC analysis, represents the discrimination power of *m/z* signal. A perfect discrimination would yield an AUC equal to 0 or 1. An AUC closer to 0.5 defines the *m/z* value less suitable as a univariate criterion. In this case an AUC equal to 0 discriminates the *m/z* value to the core, 1 to the outer.

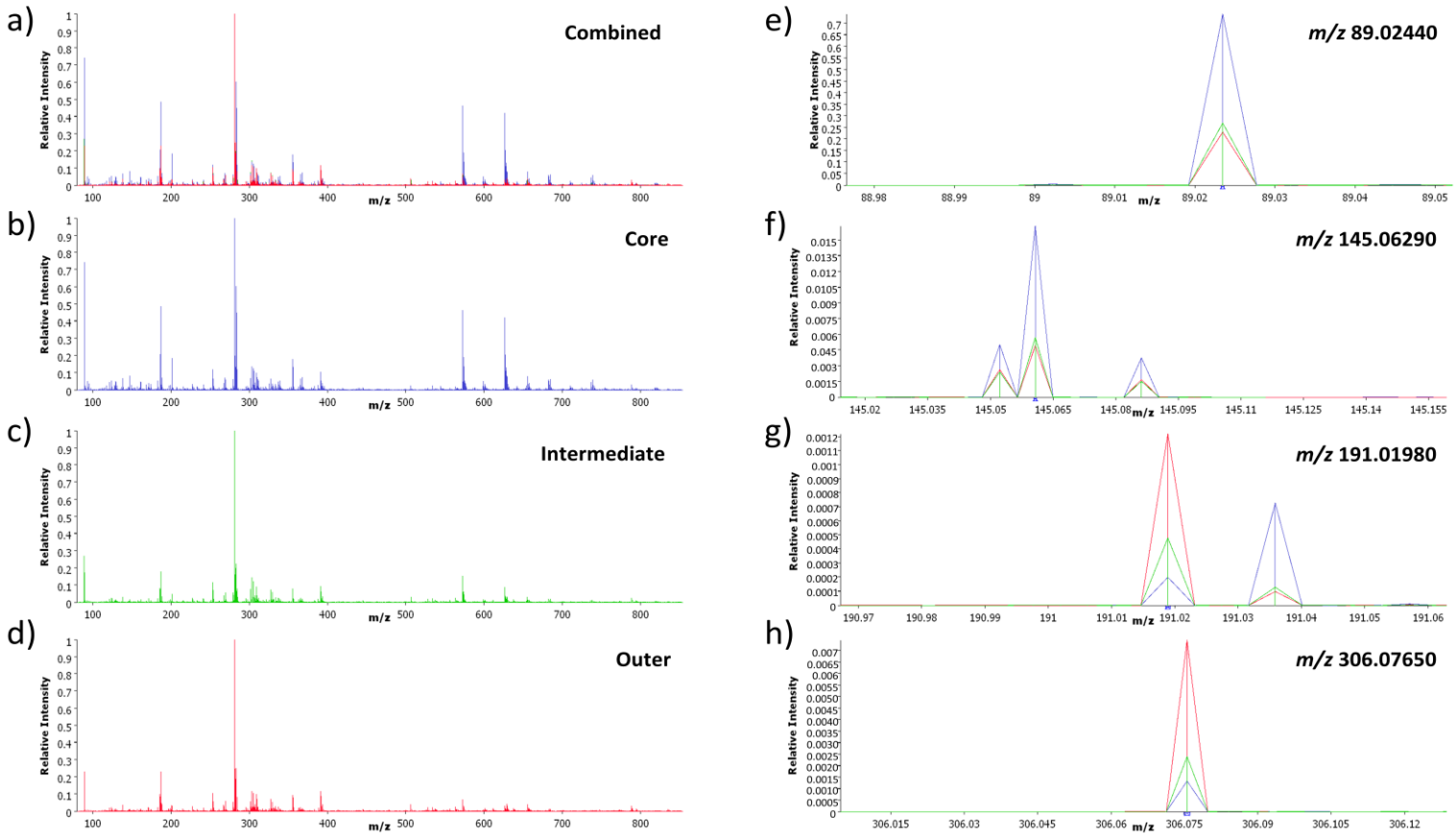

Figure 3.2 Average mean spectra of metabolites within the aggregoid regions extracted from SCiLS Lab software. a) Combined spectra of core, intermediate and outer region classified from bisecting k-means segmentation analysis. b) Core spectrum. c) Intermediate spectrum. d) Outer spectrum. Relative intensity of metabolites for each aggregoid region: e) Lactate, *m/z* 89.02440; f) Glutamine, *m/z* 145.06290; g) Citrate, *m/z* 191.01980; h) GSH, *m/z* 306.07650.

The image analysis identified an increased distribution of glutamine (*m/z* 145.06190) within the core of the aggregoid (Figure 3.3c). Glutamine is considered a major bioenergetic substrate that sources the TCA cycle by its metabolism to the intermediate α-ketoglutarate achieved by the glutaminolysis pathway (Fan *et al.*, 2013). The TCA cycle is described as the epicentre of cell metabolism due to the extensive supply of metabolic substrates that are utilised for energy production (Martínez-Reyes & Chandel, 2020). The localisation of glutamine within the core suggests the cells within the hypoxic environment are substituting for the lack of pyruvate sourcing the TCA cycle. Interestingly, glutamate (*m/z* 146.04590), an intermediate of glutaminolysis, is distributed towards the outer region of the aggregoid (Figure 3.3d). The TCA cycle is heavily utilised by proliferating cells for growth, the suppression of glutamine conversion to glutamate in the core therefore implies the presence of necrosis. Several spheroid studies have reported that the increase in diameter decreases the cell viability due to the reduced levels of oxygen and nutrients, thus the spheroid eventually develops an inner necrotic core (Curcio *et al.*, 2007; Grimes *et al.*, 2014). By examining the gene expression profiles, Däster *et al.*, (2017) identified the development of a necrotic region in multicellular spheroids larger than 500 µm. Since the diameter of the aggregoid model is ~ 1 mm the presence of an inner necrotic core is highly likely. Fluorescent staining of the aggregoid with propidium iodide, which only enters dead cells, confirms the presence of this necrotic region (Chapter 2.4.1, Figure 2.7) and additionally shows the large asymmetric hypoxic area opposed to the simple radial gradient in a typical spheroid model, which could explain the asymmetric metabolite distribution in Figure 3.3.

In contrast, the distributions of the major TCA cycle intermediates citrate (*m/z* 191.01980), malate (*m/z* 133.01430), and succinate (*m/z* 117.01940) were observed solely located with more annular features (Figure 3.3e-g), implying a surplus of oxygen and nutrients surrounding the aggregoid and the absence of cell proliferation in the core. By identifying the significant metabolites that drive cancer metabolism, it was possible to map the ion density images onto their corresponding pathways to associate the metabolic activity with specific regions of the aggregoid Figure 3.4.

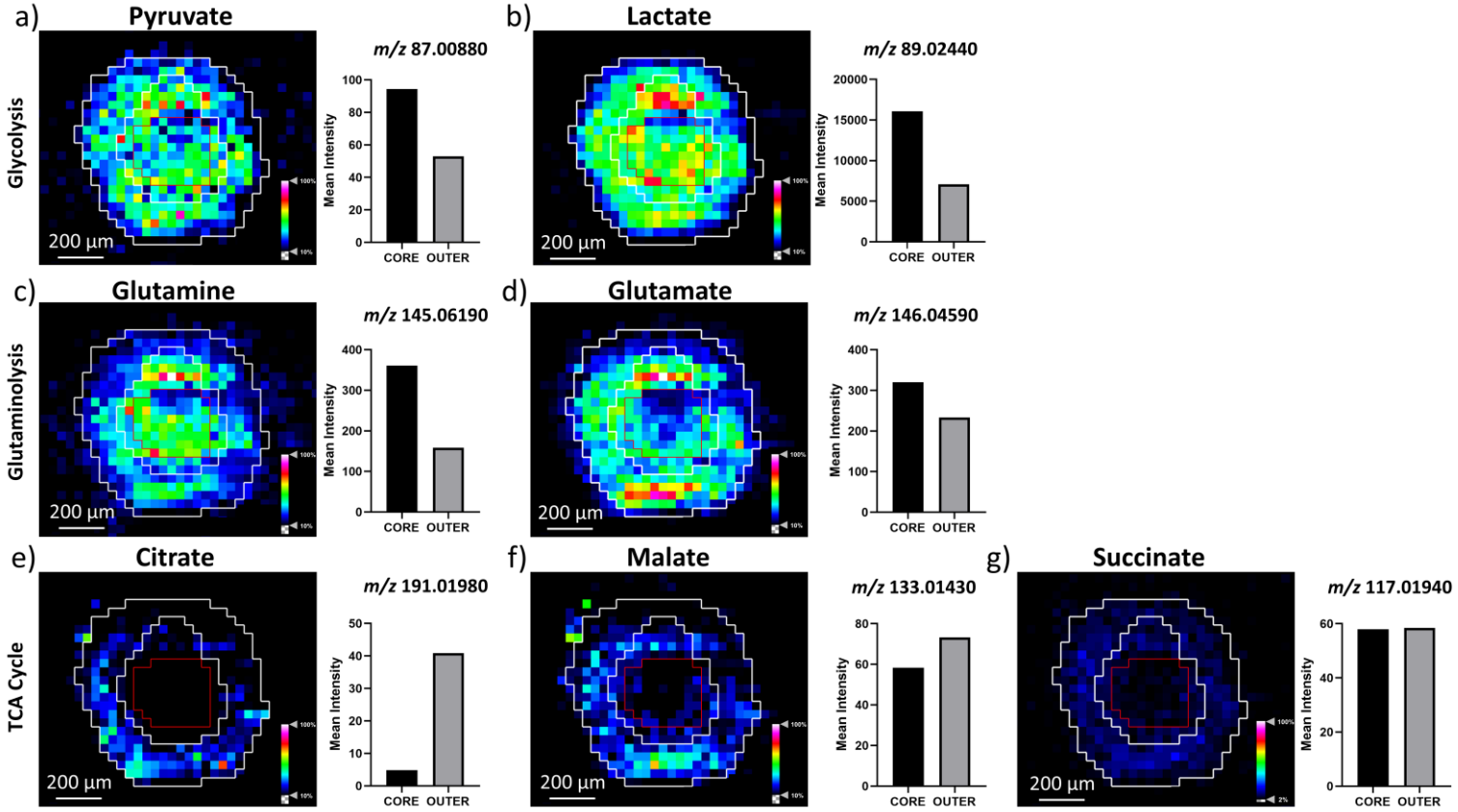

Figure 3.3 Distribution of metabolites regulating cancer growth and survival within the HCC827 aggregoid central section. Ion density maps of metabolites outlining the core and the outer area on the image. Mean intensity plotted on bar graph against the core and outer regions (n=1). Scale bar 200 µm. Intermediates of the glycolysis reaction: a) Pyruvate, *m/z* 87.00880; b) Lactate, *m/z* 89.02440. Glutaminolysis reaction: c) Glutamine, *m/z* 145.06190; d) Glutamate, *m/z* 146.04590. TCA cycle: e) Citrate, *m/z* 191.01980 f) Malate, *m/z* 133.01430; g) Succinate, *m/z* 117.01940.

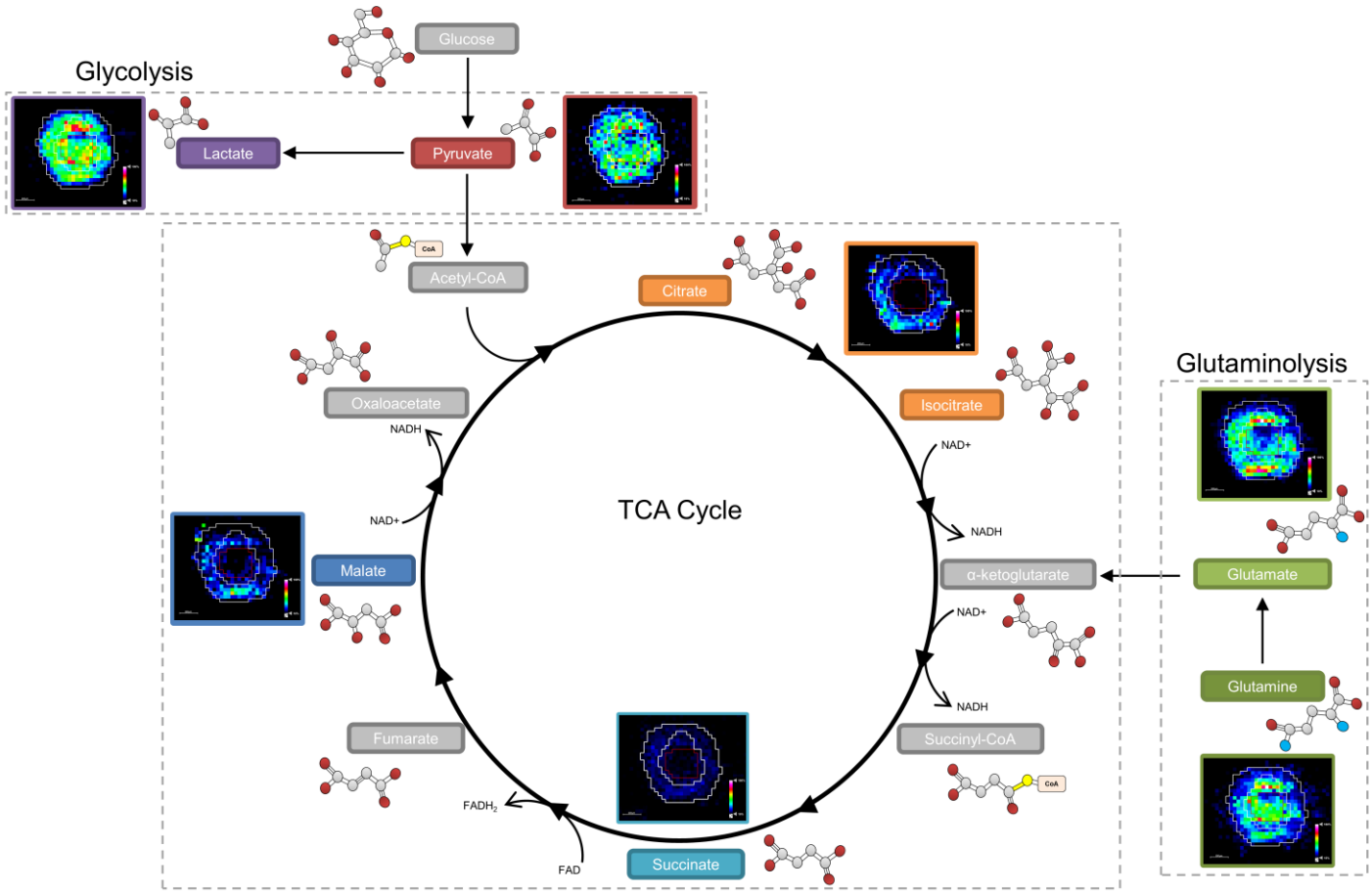

Figure 3.4 Mapping metabolites to biological pathways defined areas of tumour metabolism. The glycolysis reaction is highly expressed across the whole aggregoid section demonstrating the Warburg effect. Conversion of glutamine to glutamate is showing reduced expression in the core. The TCA intermediates present within the proliferative outer region. Intermediates acetyl-CoA, α-ketoglutarate, succinyl-CoA, fumarate, and oxaloacetate were not observed.

Proliferating cancer cells utilise fatty acids as they have essential roles as structural components of the membrane matrix, secondary messengers for signalling pathways, and sources for energy production (Beloribi-Djefaflia, Vasseur, & Guillaumond, 2016). Here fatty acid distribution was imaged and identified within the aggregoid with a mass error ≤ 0.7 ppm (Table 3.1). The image analysis demonstrated the presence of two polyunsaturated fatty acids, FA 18:2 e.g., linoleic acid at *m/z* 279.23280, and FA 20:4 e.g., arachidonic acid at *m/z* 303.23300 within the proliferative region (Figure 3.5a, b). Linoleic acid is a polyunsaturated fatty acid which is converted to arachidonic acid, a major metabolite involved in cellular proliferation and survival in cancer cells from which prostaglandins are synthesised via the cyclooxygenase (COX) pathway (Ding, Tong, & Adrian, 2000; Borin *et al.*, 2017). The accumulation of FA 20:4 (arachidonic acid) within the outer region of the aggregoid coincides with the distribution within the proliferative region of patient cancer tissue-originated spheroids of colorectal cancer (Hiraide *et al.*, 2016). It has also been reported that the metabolism of arachidonic acid is involved in the promotion of angiogenesis, cell invasion and metastasis by an alternative pathway, lipoxygenase (LOX) (Nie *et al.*, 2003). However, MS/MS profiling is required to confirm the identity of these fatty acids.

The metabolite glutathione (GSH) (*m/z* 306.07650) displayed a similar localisation to the fatty acids described with elevated levels surrounding the hotspot within the outer region (Figure 3.5c). GSH protects cells against reactive oxygen species (ROS), a normal product from cellular metabolism, through the oxidation of its sulfhydryl group to form glutathione disulphide (GSSG) (Armstrong *et al.*, 2002). The co-localisation of GSH with the fatty acids suggests an area of high metabolic activity. Interestingly, there was a lack of GSH in the core of the aggregoid, which is heavily associated with oxidative stress (Figure 3.5c). In hypoxia, the expression of antioxidant genes including genes involved in the glutathione biosynthesis are induced to allow cells to regulate ROS. However, it has been shown that in presence of excess ROS, GSH is depleted which leads to the activation of apoptosis and other forms of cell death such as necrosis and ferroptosis (Kipp *et al.*, 2017). The presence of GSH (or the lack of) can therefore be a potential measure of oxidative stress within the aggregoid model. Defining heterogeneity within the *in vitro* aggregoid model allows further

understanding of a realistic tumour microenvironment and the true metabolic behaviour of an *in vivo* cancer, which can then be utilised in applications of drug development.

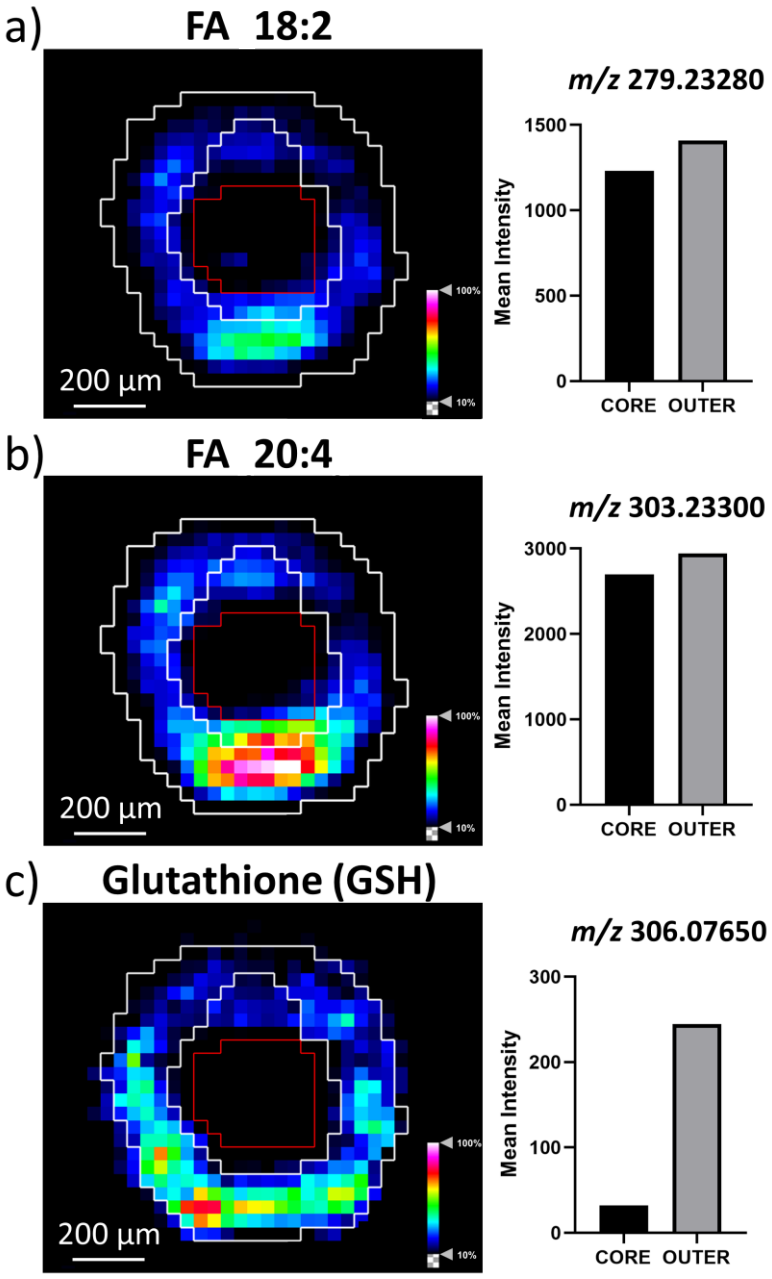

Figure 3.5 Fatty acid detection defines proliferative activity. Ion density maps of metabolites outlining the core and the outer area on the image. Mean intensity plotted on bar graph against the core and outer regions. Scale bar 200 µm. a) FA 18:2, *m/z* 279.23280; b) FA 20:4, *m/z* 303.23300; c) GSH, *m/z* 306.07650.

3.4.2 Single cell tumour characterisation

IMC is a novel, multiplex imaging platform capable of high-dimensional tissue phenotyping and the detection of signalling activities by the analysis of protein and protein modification markers at single-cell resolution (1 μm). The analysis of proteins within tissues can define essential cellular functions such as proliferation, metabolism, gene expression, organisation, and apoptosis (Downward, 2001). Modifications to such proteins can manipulate their spatial distribution, composition, and their function (Hoffman, Sniatynaski, & Kast, 2008), which can contribute to tumour progression. In the present study, IMC was employed for single-cell phenotyping of the HCC827 aggregoid model for an in-depth characterisation of the tumour microenvironment. Proteomic markers relevant to lung adenocarcinoma were selected to identify key components of cellular organisations, functions, and signalling.

Due to the complex heterogeneity of cancer tissues, morphological and structural components provide a navigational aid to determine the initial tissue organisation (Chang *et al.*, 2017). In this study, such cellular elements included DNA and epithelial tumour markers. The DNA intercalator selected was a generic marker, selected to identify the size and shape of the nucleus in individual cells within the aggregoid (Figure 3.7a). This data was used to spatially segment the image to calculate the percentage positive cells for each marker (HALO®, Indica Labs) (Figure 3.6).

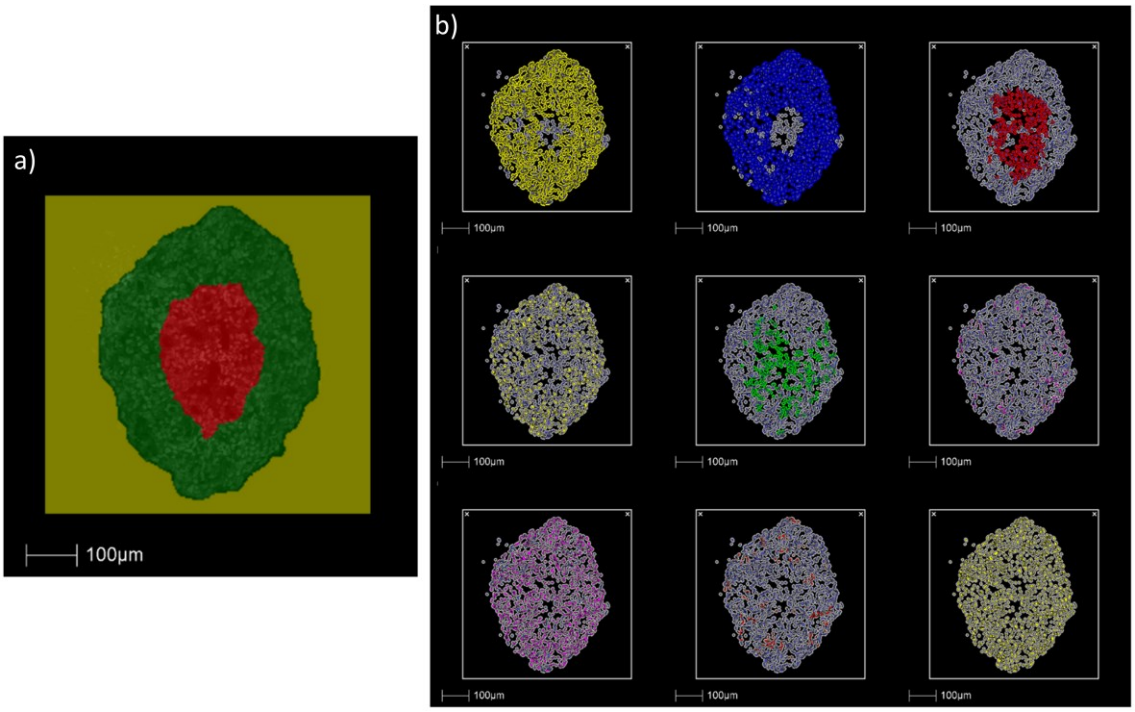

Figure 3.6 IMC classification and spatial bisecting k-means segmentation using HALO™ software. a) Regions of core, outer and background were classified from the IMC image analysis of aggregoid. Classification of aggregoid in reference to Glut1 distribution which is localised within the core. b) Spatial segmentation of each protein marker to determine percentage positive cells. From top left to bottom right: Pan-CK, E-Cadherin, Glut1, Ki-67, TNC, pS6, γH2AX, pHH3, DNA.

Tumour markers observed within the HCC827 aggregoid were epithelial cadherin (E-cadherin), and pan-cytokeratin (Pan-CK). The image analysis of both markers identified similar distributions with elevated expression levels within the outer region of the aggregoid (Figure 3.7b, c). In epithelial cells, E-cadherin and cytokeratin are responsible for mediating cell-cell adhesion and mechanical support via intermediate filaments, respectively. The absence of these markers within the core is possibly due to the breakdown of cell interactions as a result of necrosis. Simiantonaki *et al.*, (2007) reported a similar correlation with cellular necrosis and a lack of E-cadherin distribution in the core of HT-29 colorectal carcinoma spheroids via immunohistochemistry. Interestingly, the expression of both E-cadherin and cytokeratin can determine epithelial-mesenchymal transition (EMT), a process which promotes tumour progression and metastasis. In EMT, both epithelial markers are either downregulated or lost coupled with gain of

mesenchymal markers, N-cadherin and vimentin (Lamouille, Xu, & Derynck, 2014). Studies have demonstrated that EMT signalling can be induced by HIF-1α in tumour spheroids (Lehmann *et al.*, 2017; Essid, Chambard, & Elgaaïed, 2018). Unfortunately, N-cadherin was not a validated marker at the time the study was conducted, however, vimentin was included in the antibody panel, yet it was not detected within the aggregoid model. This suggests there is no mesenchymal phenotype present within the core and therefore the lack of E-cadherin is most likely due to necrosis. However, as necrosis and EMT have a crucial part in tumour progression, future tumour aggregoid analysis of other epithelial cancer types with IMC has potential for applications in drug development and resistance.

Alternatively, Tenascin C (TNC) is an ECM marker considered an active component of cancer. Relatively high expression of the marker was localised within the necrotic core of the aggregoid (Figure 3.7d). TNC is thought to promote survival and invasion by regulating the expression of proangiogenic factors such as vascular endothelial growth factor (VEGF) modulated by HIF-1α (Wang *et al.*, 2018). Additionally, TNC has been associated with inducing EMT changes with the downregulation of E-cadherin (Takahashi *et al.*, 2013). Thus, the TNC marker has an inverse correlation with the distribution of the E-cadherin marker (Figure 3.8).

To distinguish regions of the tumour microenvironment, and to complement the findings from the metabolite distributions, specific markers of proliferation and hypoxia were included. Ki-67 is a cellular marker, present in all stages of the cell cycle except for early G_1 and G_0 quiescent phases. The high expression of Ki-67 present within the outer region of the aggregoid therefore implies an active proliferative zone (Figure 3.7e). In addition, phosphorylated Histone H3 (pHH3) marker was identified in only a few specific cells, yet still located primarily in the outer region of the aggregoid (Figure 3.7f). HH3 is a nuclear core protein, and when phosphorylated at serine-10, is specifically involved in mitotic chromatin condensation (Kim *et al.*, 2017). Hence, the expression of pHH3 can identify cells undergoing mitosis. It can be concluded that the cells within the outer region of the aggregoid are highly proliferative implying a non-hypoxic area compared to the cells within the core, thus tightly corresponding to the distributions of the TCA cycle intermediates from the DESI-MSI analysis.

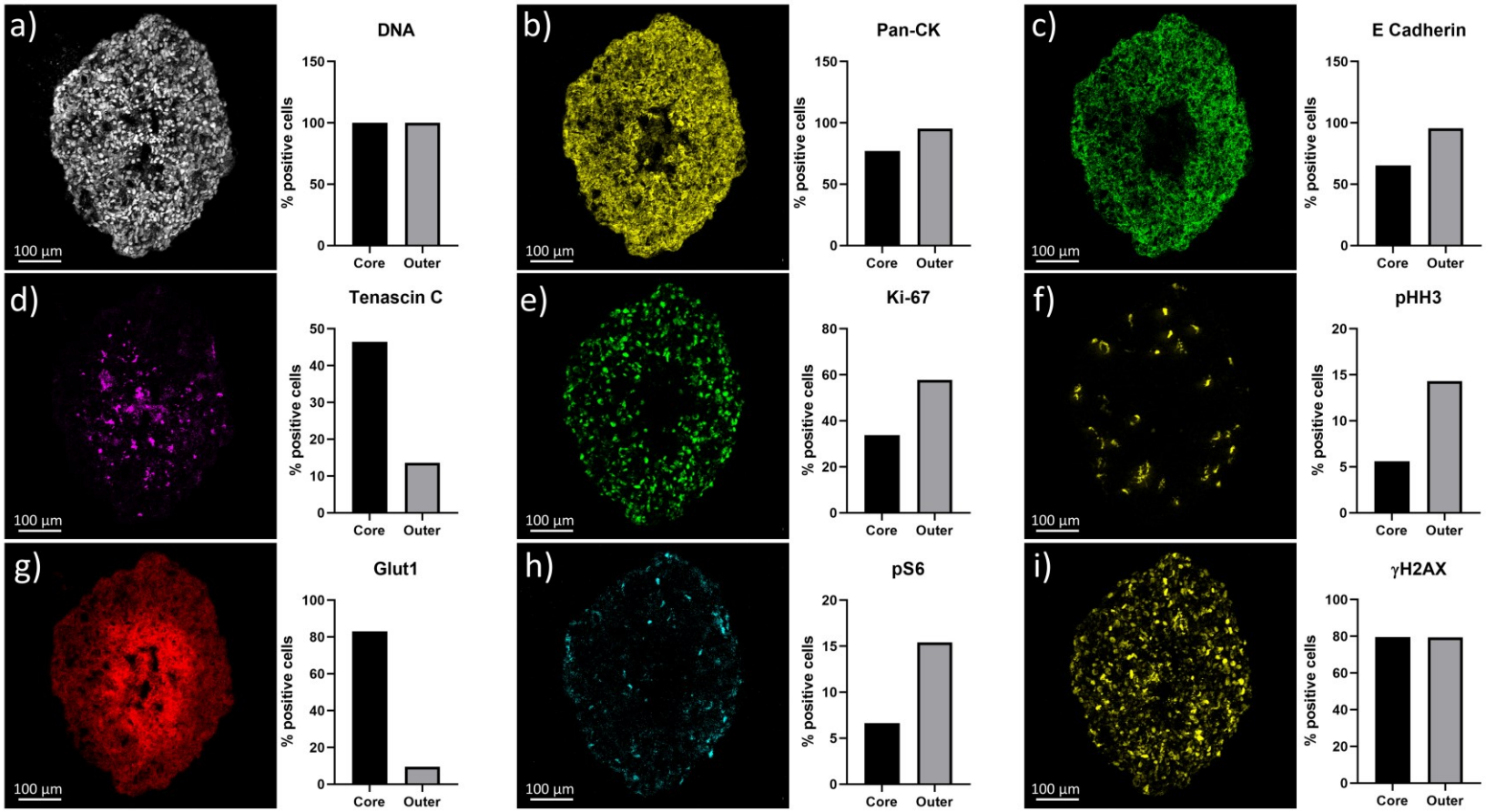

Figure 3.7 Representative IMC images of biological processes at subcellular detail in the HCC827 aggregoid model. Scale bar 100 µm. Percentage positive cells plotted on bar graph against the core and outer regions. a) DNA intercalator identified individual cells within the aggregoid section. Epithelial tumour markers: b) Pan-CK, c) E-Cadherin, and d) Tenascin C (TNC). Proliferation markers: e) Ki-67 and f) pHH3. Hypoxia influenced markers: g) Glut1, h) pS6. DNA damage marker: i) γH2AX.

On the other hand, Glut1 (glucose transporter 1) is a proxy hypoxia marker. Elevated levels of the marker were observed solely within the necrotic core of the aggregoid (Figure 3.7g). Glut1 is a hypoxia responsive gene, which is upregulated by HIF-1α to maintain an adequate energy supply in response to reduced oxidative phosphorylation (Ouiddir *et al.*, 1999). High levels of Glut1 complement the high lactate expression from the metabolite analysis, implying an increase in glucose transport into cells for lactate production via glycolysis. From the overlay image analysis, an inverse distribution of Ki-67 and Glut1 can distinguish the two major regions of the tumour microenvironment: proliferative outer, and hypoxic core (Figure 3.8). It is noted that some studies have challenged GLUT1 as a reliable marker for hypoxia (Sørensen *et al*., 2005) and therefore additional staining using pimonidazole, a routinely used hypoxia marker would be an appropriate validation method to confirm these findings. Phosphorylated S6 ribosomal protein (pS6), an active marker for mTOR signalling for cancer growth and metabolism associated with the PI3K/Akt/mTOR pathway, is also regulated by hypoxia. In contrast, the expression of pS6 was observed primarily within the outer region of the aggregoid, with high levels within specific cells (Figure 3.7h). In hypoxic conditions, the activity of the PI3K/Akt/mTOR pathway is reduced, negatively impacting on the pS6 expression (Schneider, Younis, & Gutkind, 2008). Both Glut1 and pS6 markers therefore identified metabolic signalling within the aggregoid that is affected by hypoxia.

Alternatively, phosphorylated Histone H2AX (γH2AX) is a marker for DNA damage and stress and can be indicative of cellular apoptosis (Rogakou Emmy *et al.*, 2000). This therefore explains the accumulation of γH2AX within the hypoxic core of the aggregoid (Figure 3.7i). From the image analysis however, high expression levels of γH2AX were also observed within the proliferative outer region (Figure 3.7i). Due to oxidative stress, induced by natural ROS from metabolic activity, proliferative cells are subjected to constant DNA damage (Tanaka *et al.*, 2006). Therefore, the distribution of γH2AX throughout the aggregoid is supported. In future, γH2AX marker has potential to be used for the detection of cellular stress within the aggregoid, with elevated levels when subject to therapeutic treatment.

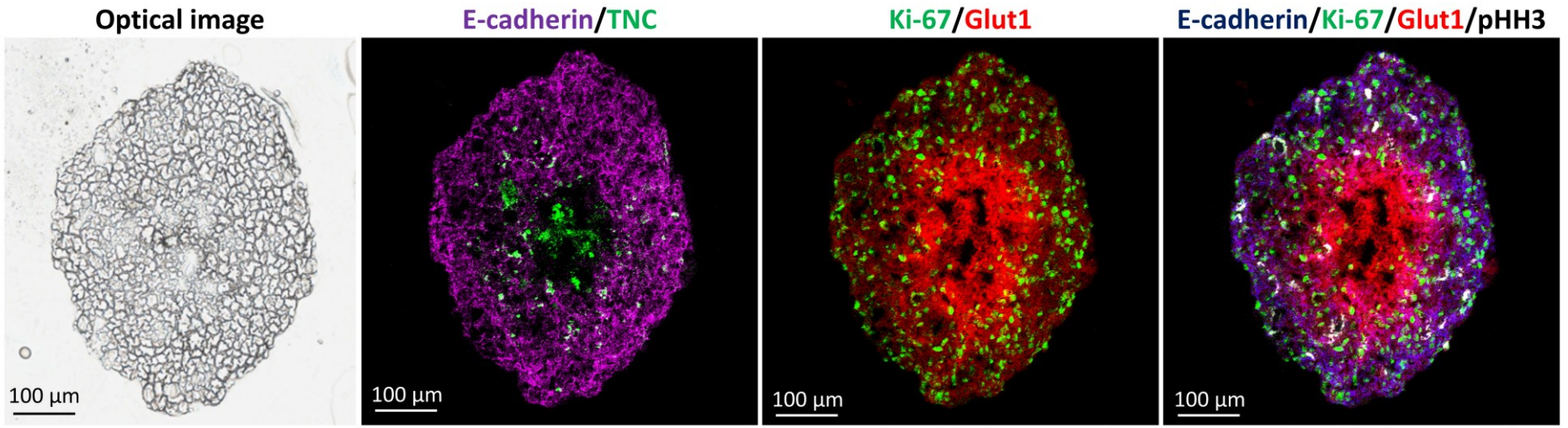

Figure 3.8 Structural organisation of biological processes for in-depth phenotyping of HCC827 aggregoid model. a) Optical image of aggregoid prior to staining with antibodies and image analysis. Scale bar 100 µm. Overlay of IMC markers displays representative images of b) Epithelial tumour markers: E-cadherin, TNC; c) Proliferation and hypoxia: Ki-67 and Glut1; d) Overlay image combining ECM, proliferation, hypoxia and mitosis: E-cadherin, Ki-67, Glut1, pHH3. Scale bar 100 µm.

This is the first report on the analysis of 3D cell culture models with IMC. The usage of IMC to characterize the HCC827 aggregoid model based on morphological and structural markers specific for epithelial tumour, growth and proliferation, and the hypoxia gradient of the tumour microenvironment has been demonstrated (Figure 3.8). Furthermore, with the single-cellular resolution capabilities of IMC it was possible to distinguish individual cells and the matrix surrounding based on the cellular localisation of such protein markers.

3.4.3 Endogenous elemental analysis

Deficiencies, defects, and accumulation of metal compounds within cells are known to be a hallmark of cancer and disease. Within tissues, metals have a heterogeneous distribution whereby high concentrations can be associated with high metabolic activity (Hare *et al.*, 2015). Therefore, visualising the metal composition within a tissue can provide essential information to understanding their key functions in different environments, such as hypoxia or nutrient rich areas. The composition of abundant metal isotopes ^{24}Mg, ^{66}Zn and ^{63}Cu were selected to analyse within the HCC827 aggregoid model. To measure the abundance of low mass range metal ions at high sensitivity LA-ICP-MSI was employed.

In the cell, Mg and Zn are essential components to drive cell growth, division, and proliferation (Vernon, 1988; MacDonald, 2000). Observations from the LA-ICP-MSI analysis localised both elements of high expression solely within the outer proliferative region of the aggregoid (Figure 3.9). Similar to Ki-67, Mg is involved in the cell cycle except for early G_1 and G_0 quiescent phases (Walker, 1986; Wolf & Trapani, 2008). The presence of Mg parallels with molecular control of cell proliferation and differentiation thus, the absence of Mg could be indicative of a non-proliferative region, or necrotic core. Zn on the other hand, has been directly linked to the proteasomal degradation of HIF-1α under normoxic conditions through the addition of excess Zn (Nardinocchi *et al.*, 2010). Whether endogenous Zn has the same impact on HIF-1α is unclear, however it is possible that the absence of Zn within the aggregoid core is associated with the activation of HIF-1α in hypoxia; whereby Zn is possibly exported to the proliferative zone where high levels are required for metabolic activity.

In contrast, the Cu levels in the aggregoid were elevated within the necrotic core (Figure 3.9). Increasing evidence has linked Cu with HIF-1α via the hypoxia signalling pathway as a response to oxidative stress to regulate Cu-dependent genes (Wenke Feng *et al.*, 2009; Wu, Zhang, & Kang, 2019). These include BNIP3, a cell death factor that induces necrosis (Sowter *et al.*, 2001), and VEGF which stimulates angiogenesis (Büchler *et al.*, 2003). Both of which are stimulating factors in hypoxia. In agreement with this, VEGF is also known to be regulated by TNC, which from the IMC analysis was also localised within the core of the aggregoid (Figure 3.9). In addition, HIF-1α accordingly promotes the upregulation of the Cu-efflux transporter, ATP7A (Zimnicka *et al.*, 2014), which tightly regulates levels of free Cu ions to prevent the formation of ROS. Thus, elevated Cu concentrations could imply an active export of free Cu ions into the ECM, accumulating in a less dense area of the aggregoid. As necrotic cells are unregulated the core therefore becomes the source of metabolic debris.

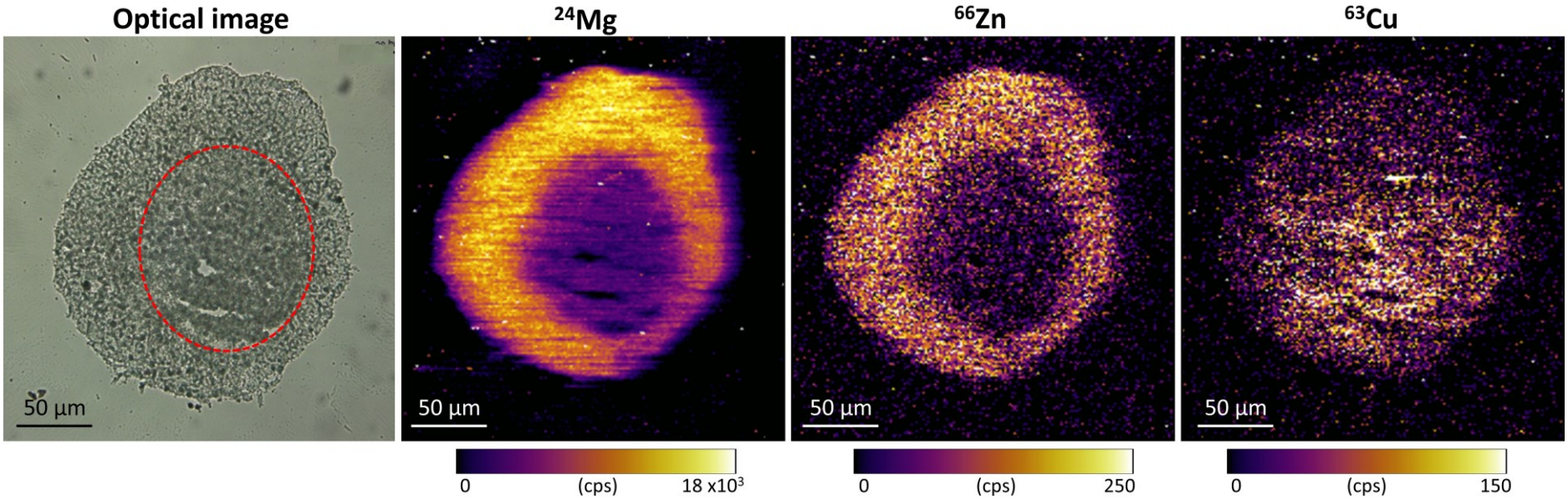

Figure 3.9 Elemental distributions within HCC827 aggregoid sections obtained using LA-ICP-MS. a) Optical image taken before acquisition; necrotic region outlined by red dotted line. Scale bar 50 µm. Elemental maps of b) ^{24}Mg, c) ^{66}Zn and d) ^{63}Cu within the section of aggregoid.

At present, there is only a limited amount of literature on the study of endogenous elemental compounds in 3D cultures by LA-ICP-MSI. Yet the analysis of tumour spheroids with this technique has had some interest regarding the localisation of platinum-based therapeutics and hypoxia-responsive drugs (Theiner *et al.*, 2016; O'Neill *et al.*, 2017). Theiner *et al.*, (2017) differentiated morphological characteristics of a necrotic core, quiescent zone, and proliferative outer region through the analysis of platinum accumulation within HCT116 colon cancer spheroids. However, the elemental compositions in this study are consistent with literature reported in studies employing X-ray fluorescence microscopy (XFM), an alternative analytical technique capable of elemental analysis at high sensitivity. Zhang *et al.*, (2012) reported similar distributions of Zn and Cu within DLD-1 colon carcinoma spheroids implying the accumulation of such compounds highlight regions of a proliferative outer zone and a necrotic core, respectively.

3.5 Concluding remarks

Advanced molecular imaging techniques have been applied for an in-depth phenotyping of a novel aggregated tumour model. This is the first example of an IMC application with a 3D cell culture model. Combining the IMC data with molecular information from DESI- and LA-ICP- MSI, a detailed characterisation of the tumour microenvironment within the aggregoid was possible. Distinct regions of a necrotic core and a proliferative outer were distinguished by each method. The localisation of metabolites including lactate, glutamine and citrate within the aggregoid highlighted the metabolic activity in relation to hypoxia. Mapping the ion density images onto the central biological pathways enabled a clearer understanding of the metabolite behaviour within the tumour microenvironment. IMC enabled single-cell phenotyping of protein signalling activity. The protein expression complemented the metabolite data including the expression of the Glut1 with elevated lactate levels in the core. In addition, the endogenous elemental compositions of Mg, Zn and Cu corresponded to the protein information and further validated the presence of heterogenous regions within the aggregoid model . This study improved the understanding of the molecular activity within the HCC827 3D cell culture tumour microenvironment. Therefore, demonstrating MSI analysis of tumour aggregoids a potential

methodology for *in vitro* studies in biomedical research and pre-clinical pharmaceutical development.

CHAPTER 4. CHARACTERISATION AND COMPARISON OF OSTEOSARCOMA AGGREGATED TUMOUR MODELS BY MULTIMODAL MSI

4.1 Introduction

OS is the most common primary bone malignancy and largely effects adolescents and young adults, with 60% of patients under the age of 25. Bone sarcomas are classified as a rare type of cancer with OS having an estimated incidence of approximately 7 in 100,000 persons, with 30,000 new cases a year (Ferguson & Turner, 2018). Despite improvements in treatment therapies over the recent years, the survival rate of bone sarcomas has remained unchanged with < 50% at 5 years (Stiller *et al.*, 2018). The aggressive tumoral behaviour of OS has challenged the development of an effective therapeutic treatment. Even with complete surgical resection of the primary tumour, approximately 90% of OS patients develop metastasis such as of the lung or breast (Ren *et al.*, 2015). Hence, there is still a great need for studying the molecular activity within the sarcoma in order to understand the metastatic behaviour and improve treatment therapies.

There are multiple cell models of OS described *in vitro* that express the specific genetic alterations of the sarcoma. The most common OS cell lines include the epithelial-like cells, SAOS-2 and the fibroblastic-like cells, MG63, both with a deficiency mutation in the tumour suppressor p53 gene. However, significant differences in the phenotypes of these cell lines have contributed to inconsistent results across studies. The SAOS-2 cells express a mature osteoblast phenotype with a high level of alkaline phosphatase (ALP) activity (Murray *et al.*, 1987); a gene associated with bone mineralisation. In contrast, the MG63 cell line represent the immature osteoblast phenotype with low ALP activity and matrix differentiation potential (Scheven, Marshall, & Aspden, 2002).

With differences in phenotypes, the expression of endogenous molecules would also be expected to vary, and thus impact the responses to treatment. Multiple studies have previously characterised the OS cell lines by DNA profiling and the expression of proteins through conventional methods, such as PCR analysis and immunostaining. For example, the detection of metastatic-related OS gene expressions, such as PHLDA1 enabled the categorisation of 18 OS cell lines from high to low metastatic potential, marking SAOS-2 and MG63 as relatively low metastatic cell lines (Ren *et al.*, 2015). In addition, heterogenous expressions of ECM proteins such as collagen I and III, and MMP-9 were used to differentiated SAOS-2 cells from MG63 cells (Paukte *et al.*, 2004). Untargeted LC-MS/MS

approaches have also been employed in metabolomics studies of both OS cell lines (Ren *et al.*, 2017; Wright Muelas *et al.*, 2020). The limitations of these studies, however, is the characterisation of the OS cell lines in 2D, which is not representative of *in vivo* behaviour. For instance, a significant change in the metabolite levels of lactate and alanine between 2D and 3D MG63 cultures was detected by high resolution nuclear magnetic resonance (NMR) (Santini *et al.*, 2004). Additionally, alterations in the proteome between monolayer and spheroid cultures of canine OS cells by differential gel electrophoresis (DIGE) MALDI-MS has also been reported (Gebhard *et al.*, 2018). However, the characterisation of OS 3D culture models has still been limited to PCR analysis or immunostaining techniques, which leads to loss of spatial information and/or requires target-specific analysis (Wang, Park, & Lin, 2009; Gebhard, Gabriel, & Walter, 2015; Bassi *et al.*, 2020).

In order to understand the wide molecular activity that drives OS and captures the heterogeneity of the tissue, a comprehensive analysis strategy is required. Palubeckaitė *et al.*, (2019) previously defined apoptotic and necrotic regions within the SAOS-2 spheroid aggregate model by detecting heterogeneous distributions of endogenous metabolites using MALD-MSI. As described in Chapter 3, employing multimodal MSI techniques demonstrated how obtaining a large amount of molecular information with a complementary nature can enhance the understanding of the biological processes within a tissue. The detection of metabolites, proteins and metals determined the interplay between molecules and established key pathways that defined the HCC827 lung adenocarcinoma aggregoid model (Flint *et al.*, 2020). A similar approach could therefore give a valuable insight into 3D tumour aggregoid models of OS, providing comprehensive information of biochemical pathways that influence the cancer pathogenesis. In addition to this, a recent paper demonstrated the combination of oesophageal cancer MCTS and clinical tissue with MALDI-MSI as an approach to determine the metabolic relevance of the models to *in vivo* (Zang *et al.*, 2021). With that in mind, detailed molecular characterisation of *in vitro* OS models and clinical tissue would improve the understanding of cancer metabolism within the 3D cultures and highlight biomarkers of patient outcome.

4.2 Aims of chapter

In this chapter, multiple MSI modalities were employed to characterise two OS aggregoid models, MG63 and SAOS-2, for the purposes of developing a potential *in vitro* methodology for cancer research and drug development. Firstly, the metabolic profiles of the models were determined by DESI-MSI and compared against the established tumour microenvironment of the HCC827 lung adenocarcinoma aggregoid. An investigation into the relevance of the OS aggregoid models with clinical OS patient samples was then conducted to determine the similarities in the metabolite levels that influenced tumour behaviour and potentially detect metastatic activity. In addition, IMC and LA-ICP-MSI were utilised to further establish the phenotypical characteristics of the tumour microenvironments of both aggregoid models through protein markers and metal compositions, respectively.

4.3 Materials and methods

4.3.1 Materials

Alginic acid, $CaCl_2$, casein solution, DPX mountant, eosin, EDTA, EtOH, haematoxylin, NaCl, PFA, PVP, sodium citrate, Triton™ X-100 and xylene substitute were purchased from Sigma-Aldrich (Gillingham, UK). HPMC was purchased from Alfa Aesar (Thermo Fisher Scientific, Heysham, UK).

4.3.2 3D cell culture growth

OS cell lines MG63 and SAOS-2 were cultured into 3D aggregated tumour models as described in Chapter 2.3.3.

4.3.3 Sample handling

Samples were prepared and processed following the protocol described in Chapter 2.3.4.

4.3.4 Tissue sample collection and handling

Two samples of human bone tissue biopsies which had been previously classified by conventional pathology as osteoblastic osteosarcoma were obtained from the Children's Cancer and Leukemia Group Tissue Bank. The samples were provided following ethical approval of this study (Project Reference 2017 BS 06). Samples were snap frozen and cryosectioned on a CM1950 cryostat (Leica

Biosystems, U.K.). Sections were cut at 10 µm thickness and n=3 sections of each sample from different depths of the tissues were thaw mounted onto positively charged X-tra® adhesive slides (Leica Biosystems, U.K.).

4.3.5 Small molecule analysis

Metabolite and lipid images were obtained by DESI-MSI on a Thermo Fisher Q-Exactive mass spectrometer (Thermo Fisher Inc, Germany) at 40 µm spatial resolution as reported in Chapter 2.3.5.3. The DESI-MSI data was analysed by SCiLS™ Lab MVS Premium 3D version 2020a (Bruker Daltonics, Germany) RMS normalization. Data was discriminated following as described in Chapter 3.3.4.2. Metabolites and biological pathways were identified by METASPACE (https://metaspace2020.eu). The peak list from each aggregoid section was exported into .csv files and grouped together. The data was then imported into MetaboAnalyst 5.0 (Xia *et al.*, 2009) to conduct multivariate analysis. PCA and PLS-DA were performed on the selected sample groups for each aggregoid model. The samples were normalised by the median, before applying log transformation and Pareto scaling on the data. The data was displayed in scores plots with 95% confidence regions to determine variance between groups. Loadings plots displayed the *m/z* values that profiled specific groups. The ion abundances for the *m/z* values were generated into histograms for comparison between regions using GraphPad™ Prism® software (La Jolla, USA).

4.3.6 Single-cell analysis

Proteins and protein modifications were detected by IMC analysis as performed and described in Chapter 3.3.5. All samples were prepared for staining and incubated with a cocktail of antibodies specific for markers relevant to osteosarcoma overnight at 4°C. Images were acquired on the Hyperion Imaging System (Fluidigm®) with the laser tuned to fully ablate the tissue. The imaging data was analysed using the MCD Viewer v1.0.560.2 software (Fluidgim®). Due to unavailability of the HALO® image analysis software (Indica Labs) during this study, the images were not spatially segmented, and therefore the percentage positivity of markers could not be quantified.

4.3.7 Elemental analysis

Metals within the aggregoid samples were detected using the method based on the protocol described in Chapter 3.3.6. Laser parameters were optimised to 6

μm spot size with, 25 μm/s scan speed, 0.07 Jcm^{-2} laser fluence, and 20 Hz repetition rate. Samples were ablated line by line with 6 μm raster spacing. Isotopes monitored were ^{24}Mg, ^{66}Zn and ^{63}Cu and the instrument was controlled using Syngistix software. Data analysis was achieved using Iolite Software on Igor Pro (WaveMetrics, USA).

4.3.8 Histology analysis

Aggregoid samples were stained with Haematoxylin and eosin as reported in Chapter 3.3.7.

4.4 Results and discussion

4.4.1 Metabolite imaging

4.4.1.1 Aggregoid phenotyping

To determine the metabolic profiles of the two OS aggregoid models, a comparative analysis was performed by employing DESI-MSI. In this study, the metabolic activity within three biological replicates of the MG63 and SAOS-2 aggregoid models were determined. Metabolite data of the lung adenocarcinoma model was also included as a reference to understand the phenotypes within the OS models.

Initially, the data was spatially segmented to determine phenotypical regions within the aggregoid sections. From the segmentation analysis, different phenotypical regions in each model were observed (Figure 4.1). As reported in Chapter 3.4.1, the segmented image of the HCC827 aggregoid model comprised three regions: a distinctive inner core, an annular zone and an outer region, which were also observable in the histological image. The segmentation of the MG63 model showed a similar pattern, where a core, two inner annular regions and a periphery were observable in the segmented MSI data. From the histology however, the MG63 model differed from the HCC827 aggregoid in that the cells were tightly compact throughout the section and although some condensing of DNA was observed, no significant apoptotic bodies were identified. This suggests that the core cluster within the MG63 aggregoid does not necessarily correspond to an obvious region of cellular stress due to hypoxia. Yet the segmentation analysis was still able to identify changes in metabolite activity effected by the lack of oxygen and nutrients towards the core of the aggregoid.

The SAOS-2 model showed significantly different features to the HCC827 and MG63 models in the segmentation analysis (Figure 4.1). Although a core was identified, the clustering pattern showed a lot of heterogeneity across the section, which was similar in each SAOS-2 sample (n = 3). Examination of the histological data indicated that a lot of fracturing was present. This has been noted across the SAOS-2 aggregoid samples throughout the experimental work conducted within this thesis and is potentially due to the nature of culturing the SAOS-2 cell line. A previous study reported a heterogenous capability to form 3D cultures between OS cell lines and noted that the SAOS-2 cells formed irregular spheroids, whereas the MG63 formed more spherical spheroids (Rimann *et al.*, 2014). Interestingly, from the histology data in the paper the SAOS-2 spheroids displayed a compact cellular distribution. However, the spheroids were significantly smaller (≤ 200 µm diameter) in comparison to the aggregoid model reported here (~ 1 mm diameter). The histology data in this study showed that a large area of apoptotic and necrotic activity within the SAOS-2 aggregoid was present. This is likely impacting the stability of the aggregoids. As this has been observed throughout the SAOS-2 samples, it is most likely due to the morphological nature of the cell line. Nevertheless, phenotypical regions within the SAOS-2 model were still observed and metabolite distributions were detected.

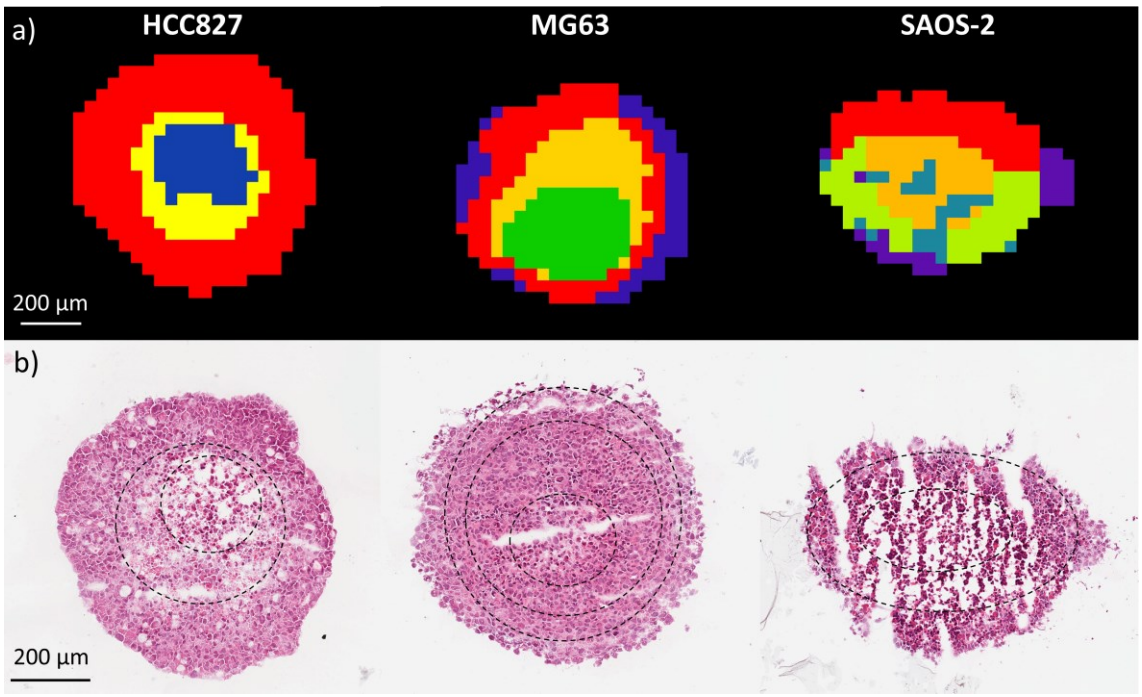

Figure 4.1 Spatial segmentation of a HCC827, MG63 and SAOS-2 aggregoid from metabolite data by DESI-MSI. a) Spatial segmentation identified heterogeneous clustering phenotypes between aggregoid models. Segmentation of each sample was performed independently and therefore the coloured clusters do not correspond between samples. b) H&E stain of same aggregoid sections from each model. Black dotted line were manually included to highlight different phenotypical regions on the H&E stain that were similar to the segmentation clustering analysis. Scale bar 200 µm.

PCA was conducted to determine the differences between the three aggregoid models. From the analysis, an obvious separation between the cell lines was observed with relatively tight 95% confidence grouping (Figure 4.2). The distribution of the OS models both located to the right of the scores plot and away from the HCC827 samples suggested more similarities in the metabolites compared to the lung model (Figure 4.2). However, from the PLS-DA, there was clear variance in separation on the scores plot from the detected metabolites between the MG63 and SAOS-2 aggregoid models (Figure 4.3). This is as expected, as the fibroblastic MG63 and epithelial SAOS-2 cell types will exhibit different metabolic behaviour. A summary of the key metabolites identified in the aggregoid models is reported in Table 4.1. Unfortunately, the metabolites involved in glycolysis and the TCA cycle, detected in the HCC827 aggregoid model in Chapter 3, were not detected in this study. This is likely due to the tuning of the DESI Thermo Fisher Q-Exactive mass spectrometer prior to acquisition which was performed externally by the AstraZeneca group. Due to time constraints, an additional image was not acquired. Nonetheless, a significant number of metabolites within the higher mass range including fatty acids and lipids were still detected and are discussed in this chapter.

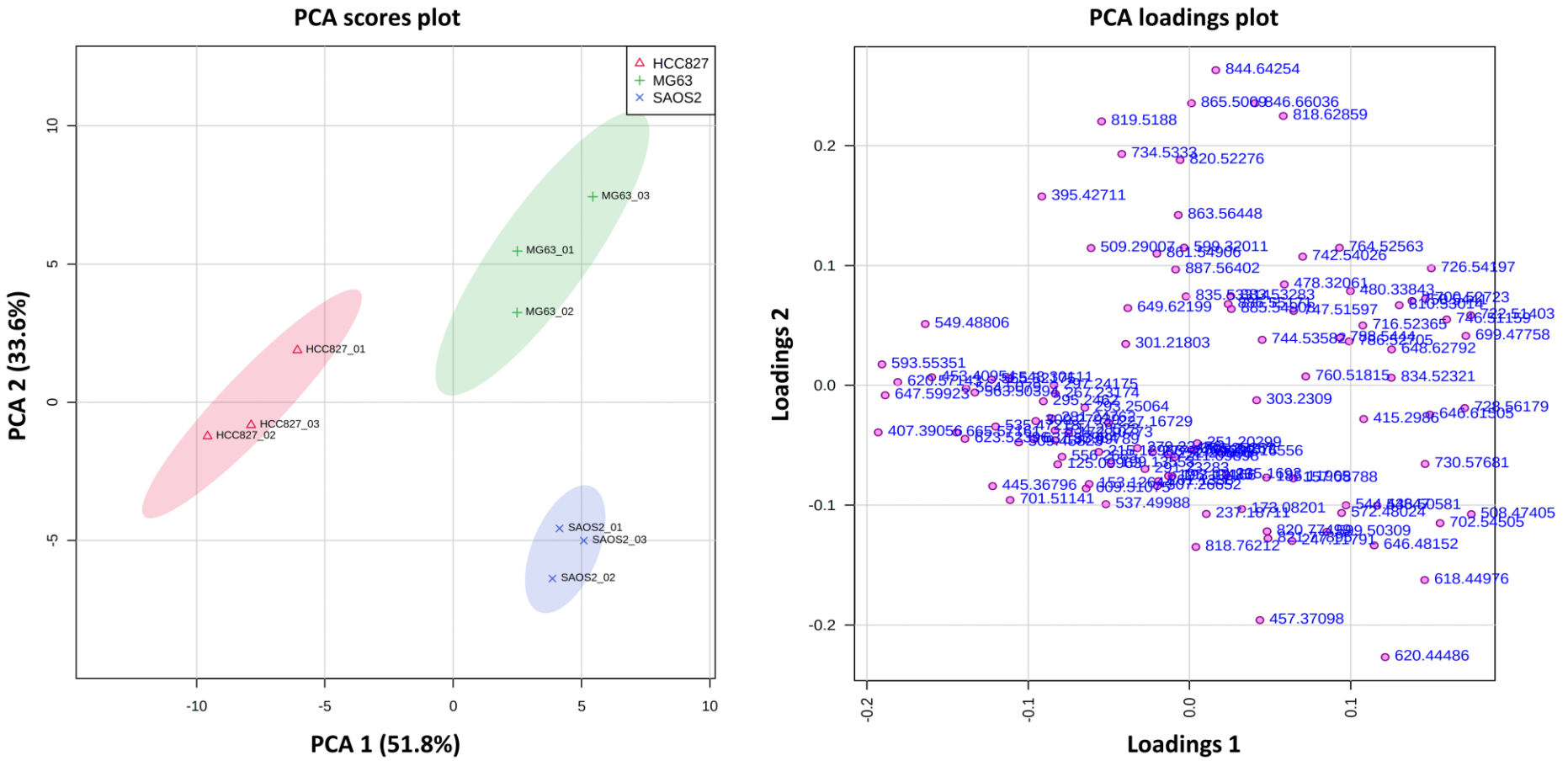

Figure 4.2 PCA scores and loadings plot show separation of the MG63 and SAOS-2 aggregoid models from the HCC827 aggregoid model. Principal components, PC 1 (51.8%) and PC 2 (33.6%) (% = the amount of variability) showed the best separation between sample groups. The discriminatory *m/z* values of interest were distributed separately from the cluster of peaks. Samples were grouped with 95% confidence, HCC827 (red), MG63 (green), and SAOS-2 (blue).

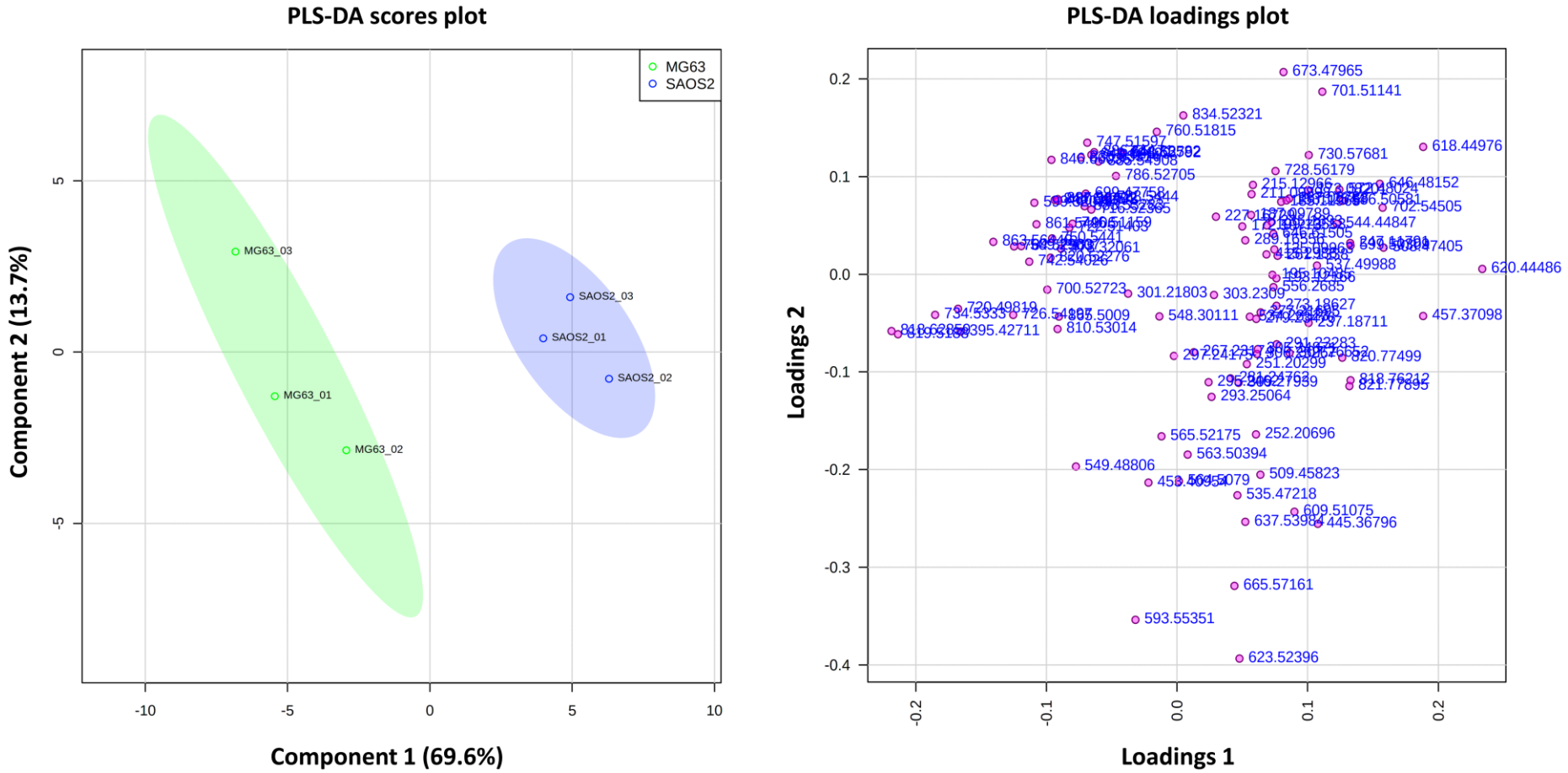

Figure 4.3 PLS-DA scores and loadings plot show variance between MG63 aggregoid model and the SAOS-2 aggregoid model. Component 1 (69.6%) and component 2 (13.7%) showed the best separation between samples. The discriminatory *m/z* values of interest were distributed separately from the cluster of peaks. Samples were grouped with 95% confidence, MG63 (green) and SAOS-2 (blue).

Metabolite	*m/z* (measured)	Accuracy (ppm error)	Aggregoid
FA 8:1;O2	173.082	0.0	OS: SAOS-2 *
FA 9:1;O2	187.098	0.0	All
FA 11:1;O	199.136	0.0	All
FA 17:1	267.232	0.0	All: HCC827 *
FA 18:5	273.186	1.0	All
FA 18:3	277.217	-0.4	OS
FA 18:2	279.235	6.3	All: OS
FA 18:1	281.248	-0.4	All: HCC827 *
FA 18:2;O	295.229	3.4	All: HCC827 *
FA 20:5	301.218	0.0	All: MG63 *
FA 20:4	303.231	-0.2	All: MG63 *
FOH 27:0	395.427	3.3	MG63 *
FA 20:4	457.371	5.0	SAOS-2 **
Cer 32:1;O2	508.474	1.1	SAOS-2 ***
FAHFA 34:2;O	535.472	-0.9	All: HCC827 *
Cer 34:1;O2	536.506	1.9	SAOS-2 ***
Cer 32:1;O2 $[M+Cl]^-$	544.449	-3.2	OS: SAOS-2 ***
FAHFA 36:2;O	563.504	-1.0	All: HCC827 ***
Cer 34:1;O2 $[M+Cl]^-$	572.480	-2.2	OS: SAOS-2 ***
PI 18:0	599.320	-0.2	MG63 *
PE O-28:1	618.450	-1.0	SAOS-2 **
PE O-30:1	646.482	-0.3	SAOS-2 ***
PE O-34:2	700.527	-2.1	OS: MG63 ***
PE 34:1	716.524	0.1	OS: MG63 *
PE O-36:6	720.498	1.1	MG63 **
PE O-36:2	728.562	2.5	OS ***
PC O-33:1	730.577	1.7	OS: SAOS-2 *
PS O-33:0	734.533	-1.2	MG63
PC 33:2	742.540	1.4	MG63 **
PG 34:1	747.516	-3.0	OS: MG63 *
PE O-38:5	750.544	-0.3	MG63 *
PS 34:1	760.518	7.0	OS *
PE O-38:6;O	764.526	2.7	MG63 **
PS 36:1	788.544	-0.4	OS: MG63 **
PS 38:4	810.530	1.3	MG63 **
PG 40:7	819.519	0.7	MG63 **
PS 40:6	834.523	-6.3	OS *
PI 38:4	885.549	-0.9	OS: MG63 *

Table 4.1 Assignments and errors for metabolites detected in specific aggregoid models. Metabolites were filtered by removal of isotope peaks and mass accuracy (< 7 ppm). Significant metabolite detection between tumour models was determined by mean intensities. Data is mean (n=3), one-way ANOVA * $p < 0.05$, ** $p < 0.01$, *** $p < 0.001$.

For the observed metabolites, differences in the detection levels across the tumour aggregoid models were observed. In particular, ceramide species Cer 32:1;O2, Cer 34:1;O2, and their chlorine adducts were significantly elevated in the SAOS-2 model (Table 4.1). From the image, the intensity of Cer 34:1;O2 $[M+Cl]^-$ at *m/z* 572.480 was localised across the aggregoid with highest concentrations within the core (Figure 4.4a). Some detection was observed in the MG63 aggregoid, and even less so in the HCC827 model. Ceramides are primarily associated with tumour suppressor activity by triggering anti-proliferative cellular processes such as apoptosis and autophagy (Galadari *et al.*, 2015). Activation of ceramides are typically induced by cellular stresses such as hypoxia or anti-cancer drug signalling (Haimovitz-Friedman, Kolesnick, & Fuks, 1997; Li, Feifei & Zhang, 2016). Equally, ceramides have also been associated with cell differentiation and bone development. Hill & Tumber (2010) detected ceramides in osteoblasts and determined low levels promoted cellular proliferation, as high levels induced apoptosis to promote bone reformation. From the histology images (Figure 4.1), a large area of apoptotic bodies was identified in the SAOS-2 model. Thus, the heterogenous ceramide levels within the SAOS-2 aggregoid could be an indicator of apoptotic activity within an inner hypoxic region and cellular differentiation in an outer proliferative zone. Though, as the ceramide detection within the apoptotic region of HCC827 aggregoids were significantly lower than the SAOS-2 model, it suggests ceramides are more associated with osteoblast-like cells. The discriminatory levels of ceramides between the OS models, however, implies these metabolites differentiate the mature osteoblast phenotype of the SAOS-2 model from the MG63 immature osteoblasts.

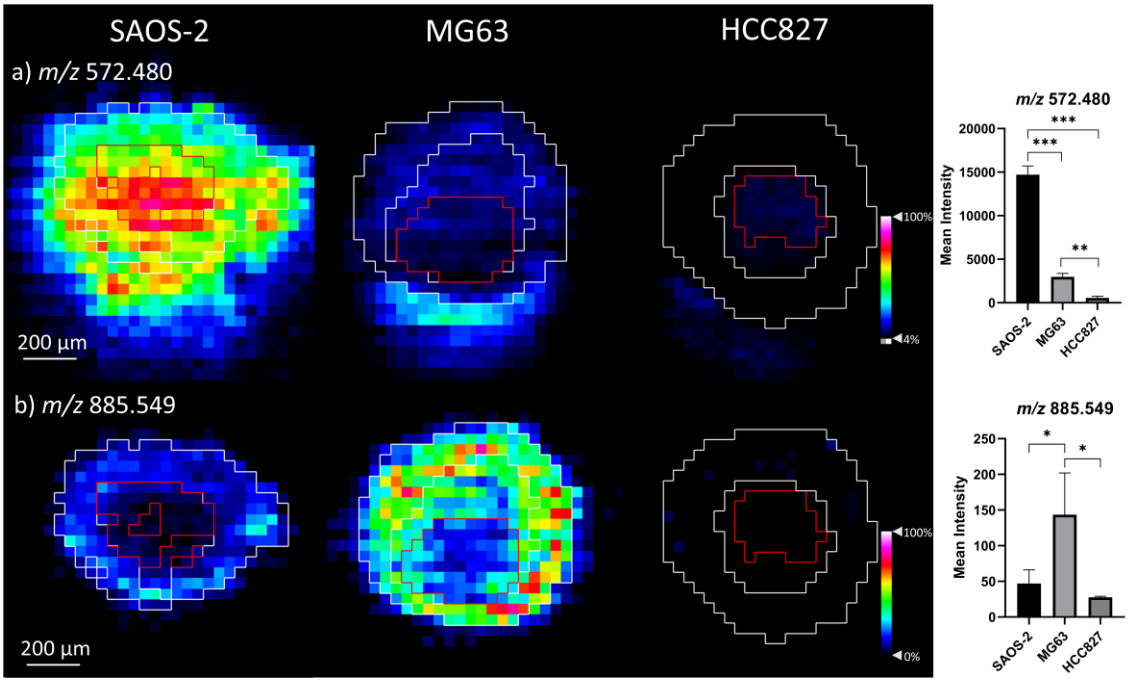

Figure 4.4 Distribution of metabolites detected in OS aggregoid models. Ion density maps of metabolites outlining the core and outer area on the image. Mean intensity plotted on bar graph against the SAOS-2, MG63 and HCC827 aggregoids. Data is mean ± SD (n=3), one-way ANOVA with Tukey post hoc test * $p < 0.05$, ** $p < 0.01$, *** $p < 0.001$. Scale bar 200 µm. Peaks identified a) *m/z* 572.480, Cer 34:1;O2 $[M+Cl]^-$; b) *m/z* 885.549, PI 38:4.

Within the MG63 aggregoid models, glycerophospholipid species, including PC, phosphatidylethanolamine (PE), phosphatidylserine (PS) and phosphatidylinositol (PI) were expressed considerably higher in comparison to the SAOS-2 and HCC827 models (Table 4.1). In highly proliferating cancer cells, phospholipid metabolism is altered to promote processes involved in the synthesis of signalling molecules, energy production and the formation of cellular membranes (Beloribi-Djefaflia *et al.*, 2016). From the histology image (Figure 4.1), the MG63 aggregoid displayed a high density of proliferative cells across the tissue and therefore could be reason for the higher detection of such phospholipids. In addition, the specific phospholipids have also been associated with aggressive properties of malignant cancer types (Luo *et al.*, 2017). Metabolites PS 38:4 at *m/z* 810.530 and PI 38:4 at *m/z* 885.549 were significant within the MG63 aggregoids, with some detection in the SAOS-2 aggregoids. PI 38:4 in particular was localised within the periphery of the MG63 aggregoid (Figure 4.4b). A previous study comparing the lipidomic profiles of low and high

metastatic breast cancer cell lines reported both PS 38:4 and PI 38:4 were markedly greater in the high metastatic cell type (Kim *et al.*, 2016). The presence of these lipids could suggest the MG63 aggregoid is exhibiting an aggressive tumoral behaviour, that is if the phospholipids have the same metastatic-promoting effects in OS as they do in breast cancer.

4.4.1.2 Characterisation of OS aggregoid models to OS human tissue

Initially, the MSI data of the OS human tissue samples was spatially segmented to classify the clusters with specific phenotypic regions. The spatial segmentation analysis showed complex clustering patterns within all tissue sections in comparison to the aggregoid models. This is due to the heterogeneity of the tissues comprising many cell types that form the tumorous tissue in addition to bone and cartilage. Figure 4.5a shows the spatial segmentation of a tissue section from OS patient_826 imaged by DESI-MSI and the histology stain after analysis (whole H&E image Figure 4.5b and enlarged regions Figure 4.5c-f). It was stated from the external pathology report, the sample had cancerous tumour regions identified throughout the tissue including the osteoid bone which was formed by tumour cells. Therefore, detection of different tumorous phenotypes throughout the whole tissue section was expected. From the segmentation analysis, a solid tumour region (yellow cluster) with an osteoid bone island (purple/blue clusters) was identified on the right of the tissue (Figure 4.5c). Similarities to this yellow tumour cluster were also detected throughout the sample (Figure 4.5d). A large area of mineralised bone within tumorous tissue was also detected and determined by the sage green cluster (Figure 4.5d, e). In addition, a significant area of dense osteoid bone with a filagree pattern was focally present and outlined by purple/blue clusters (Figure 4.5f).

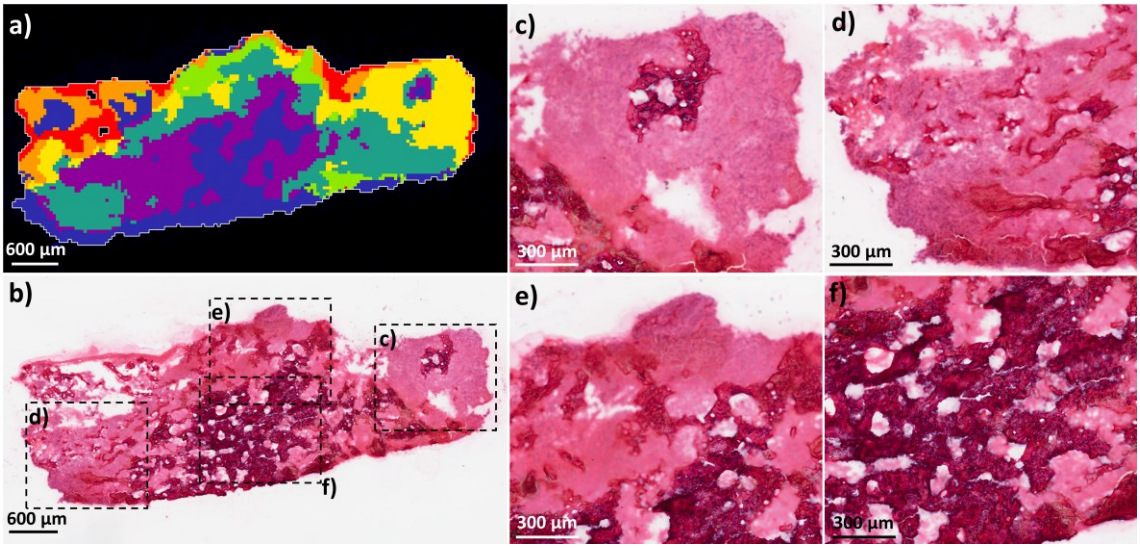

Figure 4.5 Spatial segmentation analysis of OS patient_826 tissue sample from metabolite data by DESI-MSI. a) spatial bisecting k-means segmentation of OS section highlighting heterogeneous clusters throughout tissue. Scale bar 600 µm. b) H&E of same OS tissue section after image analysis. Scale bar 600 µm. Magnification of ROIs: c) solid tumour (corresponding to the yellow cluster) with osteoid island (corresponding to the purple/blue clusters) at the right of the tissue; d) region of tumour and mineralised bone located to the left of tissue (corresponding to the yellow and sage green clusters); e) tumour and mineralised bone located at the top of the tissue (corresponding to the sage green cluster); f) Dense osteoid bone present focally (purple/blue cluster). Scale bar 300 µm.

Figure 4.6 shows the spatial segmentation analysis of a tissue section from OS patient_882 and the histological image. From the pathology report, typical osteoblastic osteosarcoma phenotypes were detected. Regions of lamellar bone were identified, the medullary space contained various cell types with irregular nuclei, and osteoid production by atypical mitotic cells was determined. From the DESI data, the different phenotypes could be identified by the segmentation analysis. A large region of solid tumour was identified on the right of the tissue (orange cluster) (corresponding enlarged H&E image Figure 4.6c). The medullary space (blue cluster) with osteoid regions (green cluster) was localised within the focal region of the tissue (corresponding enlarged H&E image Figure 4.6d). A region of lamellar bone (sage green) and a large area of osteoid formation were localised within the left of the tissue (corresponding enlarged H&E image Figure 4.6e). It is noted that the segmentation analysis was performed independently for

each patient sample and therefore the colour clusters do not correspond between groups.

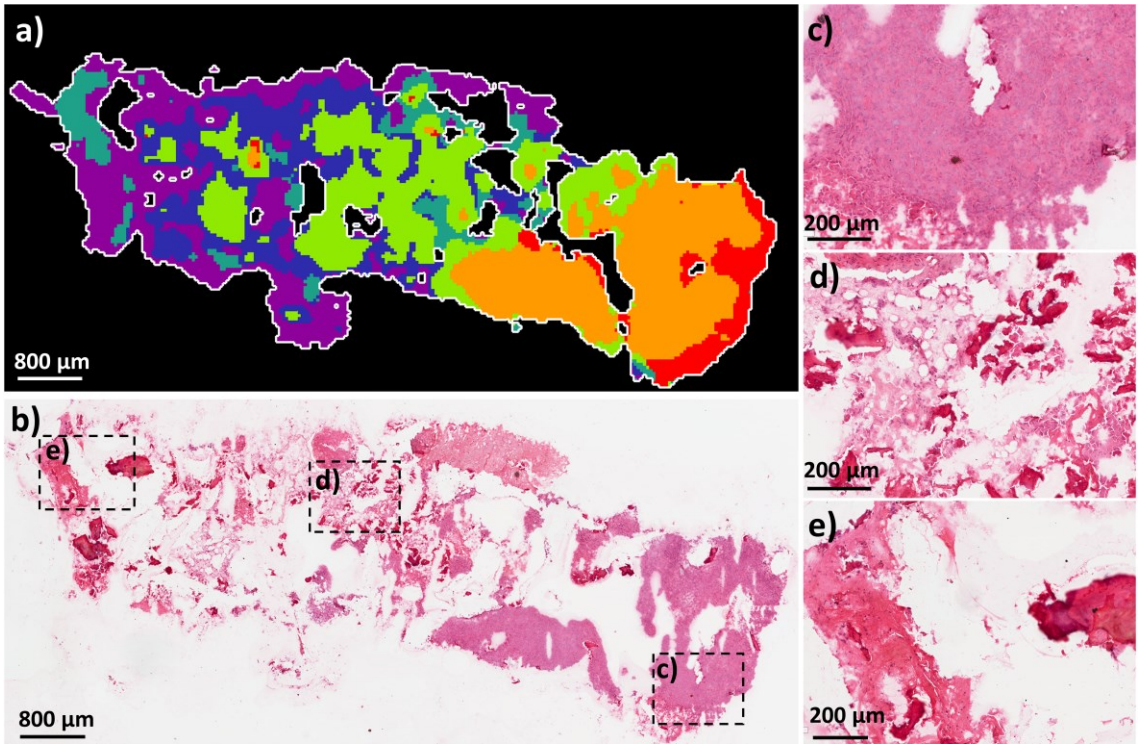

Figure 4.6 Spatial segmentation analysis of OS patient_882 tissue sample from metabolite data by DESI-MSI. a) spatial bisecting k-means segmentation of OS section highlighting heterogeneous clusters throughout tissue. Scale bar 800 µm. b) H&E of same OS tissue section after image analysis. Scale bar 800 µm. Magnification of ROIs in H&E image: c) solid tumour (corresponding to the orange cluster) at the right of the tissue; d) region of medullary space with osteoid bone located focally (corresponding to the green and blue clusters); e) lamellar bone located at the left of the tissue (corresponding to the sage green cluster). Scale bar 200 µm.

PCA was performed to determine the similarities and variances between the two OS aggregoid models with the two OS human tissue samples. It is stressed that the aggregoid data was acquired independently from the patient samples. Therefore, an indirect comparison of the samples from two individual imaging data sets has been performed in this study and thus the results are of a preliminary nature only. From the PCA scores plot, a clear separation of the aggregoid models from the OS human tissue samples was observed (Figure 4.7). As the human tissue is comprised of many heterogeneous regions and contains different cell types it was expected to have variance from the single-cell type aggregoid models. In addition, slight separation of the 95% confidence grouping of the two patient samples is also likely due to the heterogeneity between the tumour tissues. The MG63 aggregoid samples were relatively widely distributed which suggests some variability within the group. For each remaining sample type however, tight clustering between the samples was observed. A summary of the key metabolites within the OS patient samples and the OS aggregoid models is reported in Table 4.2. The significant metabolites detected within the samples highlighted the similarities that exist between the OS aggregoid models and the OS human tissue.

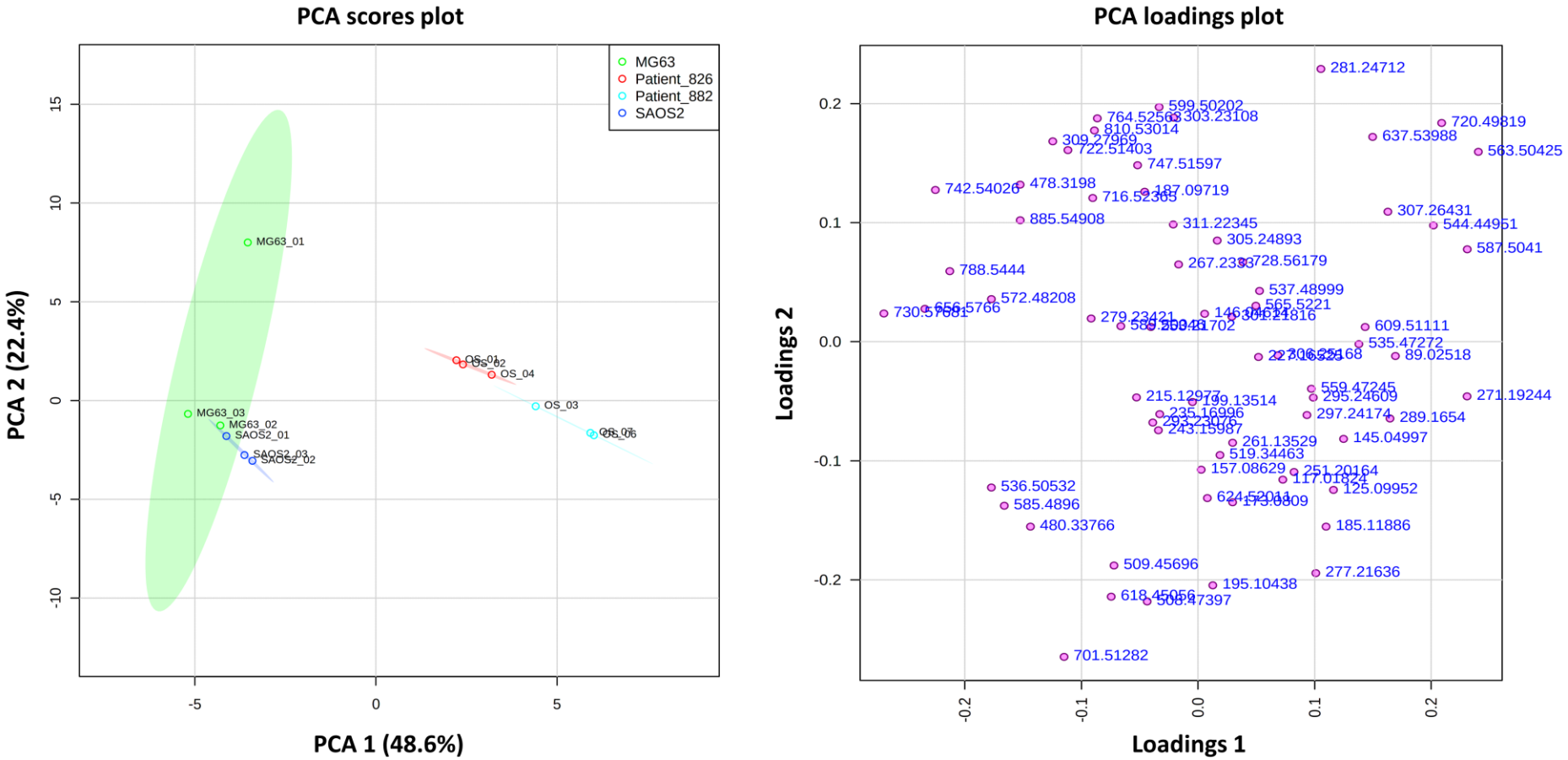

Figure 4.7 PCA scores and loadings plot show separation of the OS aggregoid models from the OS human tissue samples. Principal components, PC 1 (48.6%) and PC 2 (22.4%) showed the best separation between sample groups. The discriminatory m/z values of interest were distributed separately from the cluster of peaks. Samples were grouped with 95% confidence, MG63 (green), and SAOS-2 (blue), OS patient_826 (red) and OS patient_882 (light blue).

Metabolite	Osteosarcoma Tissue			Aggregoid		
	***m/z* (measured)**	**Accuracy (ppm error)**	**Patient sample**	***m/z* (measured)**	**Accuracy (ppm error)**	**Aggregoid model**
FA 9:1;O2	187.096	0.0	OS_882 ***	187.098	0.0	Both
FA 11:1;O	199.135	0.0	OS_882 **	199.136	0.0	Both
Phenol lipid	235.171	1.0	Both	235.169	-4.7	Both
FA 16:1	253.218	3.4	Both	253.216	-5.7	Both
FA 17:1	267.235	0.0	Both	267.232	0.0	Both
FA 18:3	277.216	0.0	Both	277.217	-0.4	Both
FA 18:2	279.234	2.4	Both	279.235	6.3	Both
FA 18:1	281.247	-0.4	Both	281.248	-0.4	Both
FA 18:2;O	295.229	2.9	OS_882 *	295.229	3.4	MG63 *
FA 18:1;O	297.242	-6.0	Both	297.242	-5.9	MG63 *
FA 20:5	301.218	0.3	OS_826 *	301.218	0.0	MG63 *
FA 20:4	303.231	0.2	OS_826 **	303.231	-0.2	Both
FA 18:2;O2	311.224	3.5	OS_882 *	311.223	0.7	Both
Cer 32:1;O2	508.474	0.7	OS_826 **	508.474	1.1	SAOS-2 ***
LPA(24:1)	519.345	-0.6	OS_882 *	519.345	-1.1	SAOS-2 *
FAHFA 34:2;O	535.473	1.1	Both	535.472	-0.9	Both
Cer 34:1;O2	536.505	0.0	OS_826 ***	536.506	1.9	SAOS-2 ***
Cer 32:1;O2 $[M+Cl]^-$	544.451	0.6	OS_826 **	544.448	-3.2	SAOS-2 ***
FAHFA 36:2;O	563.505	0.1	Both	563.504	-1.0	Both
FAHFA 36:1;O	565.522	4.2	Both	565.522	2.9	Both
Cer 34:1;O2 $[M+Cl]^-$	572.484	4.2	OS_826 ***	572.480	-2.2	SAOS-2 ***
PE O-28:1	618.451	1.6	OS_826 **	618.450	-1.0	SAOS-2 **
PE O-30:1	646.613	-2.1	OS_826 ***	646.615	1.0	Both
Cer 40:1;O2 $[M+Cl]^-$	656.578	3.5	OS_826 **	656.576	0.2	Both
PA 36:3	701.514	3.0	Both	701.511	-1.0	Both

PE 34:1	716.524	0.3	OS_826 *	716.524	0.1	MG63 *
PE O-36:2	728.560	-0.4	OS_826 *	728.562	2.5	Both
PC O-33:1	730.575	-0.8	Both	730.577	1.7	SAOS-2 *
PC 33:2	742.539	0.1	OS_826 *	742.540	1.4	MG63 *
PG 34:1	747.517	-1.1	OS_826 **	747.516	-3.0	MG63 *
PE O-38:5	750.542	-2.6	OS_826 *	750.544	-0.3	MG63 *
PE O-38:6;O	764.524	0.4	OS_826 *	764.526	2.7	MG63 **
PS 36:1	788.544	-1.3	OS_826 **	788.544	-0.4	MG63 **
PS 38:4	810.528	-1.5	OS_826 *	810.530	1.3	MG63 **
PS 40:4	838.559	-1.3	OS_826 **	838.562	2.2	Both
PI 38:4	885.550	0.5	OS_826 **	885.549	-0.9	MG63 *

Table 4.2 Assignments and errors for metabolites detected in both the OS human tissue samples and OS aggregoid models, MG63 and SAOS-2. Metabolites were filtered by removal of isotope peaks and mass accuracy (< 7 ppm). Significant metabolite detection between tumour models was determined by mean intensities. Data is mean (n=3), unpaired t test * $p < 0.05$, ** $p < 0.01$, *** $p < 0.001$.

The major similarities between the OS human tissue samples and the OS aggregoid models was the detection of fatty acid species, specifically related to the arachidonic metabolism pathway. Figure 4.8a-c shows FA 18:2, e.g., linoleic acid at *m/z* 279.234, FA 18:1, e.g., oleic acid at *m/z* 281.247 and FA 20:4, e.g., arachidonic acid at *m/z* 303.231 within the OS human tissues. Mean intensities for each metabolite detected in the OS patient tissues and OS aggregoid models are shown in Appendix Figure A.1. The localisations of the metabolites were concentrated within the solid tumour regions of the OS human tissues and distributed throughout the similar tumorous areas as identified by the clustering analysis. These species were also identified at high levels in SAOS-2 and MG63 aggregoid models (Figure 4.8e-f). Within the SAOS-2 model, the metabolites were distributed more within the periphery, compared to the MG63 model where the species were heavily distributed throughout the section. As discussed in Chapter 3, FA 18:1 and FA 20:4 were detected within the proliferation region of the HCC827 aggregoid model. The arachidonic acid metabolism has been associated with cellular proliferation and differentiation and the promotion of cancer growth and survival via the COX pathway (Ding *et al.*, 2000; Borin *et al.*, 2017). This correlates with the observations made in the OS aggregoid models, where proliferative cells were localised within the outer region of the SAOS-2 model, whereas from the histology of the MG63 model, proliferative cells were localised throughout the aggregoid. Therefore, this suggests that the localisation of the fatty acids within the OS human tissue samples are an indication of highly proliferative activity within the solid tumour regions.

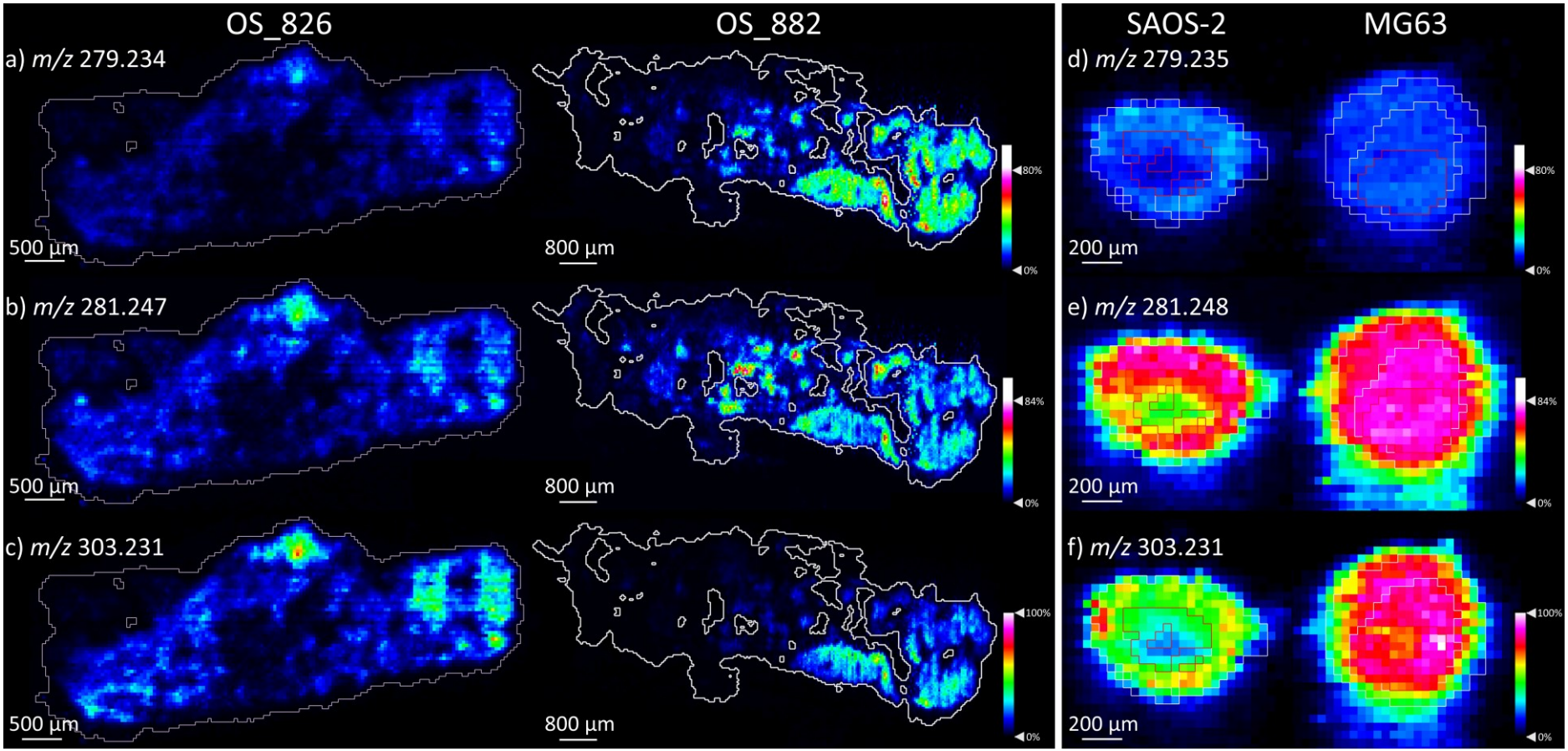

Figure 4.8 Fatty acid detection within OS human tissue and OS aggregoid models. Ion density maps of metabolites in OS patient_826 and OS patient_882. Scale bar 500 µm and 800 µm, respectively. Ion density maps of aggregoid models outlining the core and outer area. Scale bar 200 µm. Peaks identified in human tissue a) *m/z* 279.234, FA 18:2; b) *m/z* 281.247, FA 18:1; c) *m/z* 303.231, FA 20:4. Peaks identified in OS models d) *m/z* 279.235, FA 18:2; e) *m/z* 281.248, FA 18:1; f) *m/z* 303.231, FA 20:4.

Interestingly, the two aggregoid models follow a similar detection pattern of a lower FA 18:2 signal and elevated levels of FA 20:4 as OS patient_826. In contrast, OS patient_882 had higher intensities of FA 18:2. It has been reported that the metabolism of arachidonic acid is involved in the promotion of angiogenesis, cell invasion and metastasis by the LOX pathway (Nie *et al.*, 2003). From the pathology reports, a case of metastasis was reported from OS patient_826 and not in OS patient_882. The observation of an upregulation of FA 20:4, e.g., arachidonic acid, suggests the detection of a possible marker for metastatic potential, primarily within the solid tumour regions of OS patient_826 tissues. In contrast, a higher detection of FA 18:2 within OS patient_882 tissues indicates a slower metabolism to FA 20:4, and thus could identify a lower metastatic potential. The similar detection levels of the fatty acids within the OS aggregoids to the metastatic patient tissue therefore implies the tissue models could be exhibiting metastatic-like behaviour. In addition, the elevated levels of FA 20:4 within the MG63 aggregoid further suggests the cell type forms a higher metastatic tumour model compared to the SAOS-2 aggregoid.

To further analyse metabolites associated with metastatic potential within the aggregoid models, phospholipids PS 38:4 at *m/z* 810.528 and PI 34:4 at *m/z* 885.550, as discussed in section 4.4.1.1, were also detected significantly higher within the metastatic OS patient_826 tissues (Appendix Figure A.2). The localisations of both species were observed within the large tumorous regions identified by the yellow and sage green cluster of OS patient_826, as low amounts of *m/z* 810.528 and *m/z* 885.550 were distributed in the orange tumour cluster of OS patient_882 (Figure 4.9a, b). These specific metabolites could therefore correlate to high metastatic activity within osteosarcoma, as previously observed in highly metastatic breast cancer cell lines (Kim *et al.*, 2016). This supports the idea of the MG63 aggregoid model displaying a metastatic phenotype and demonstrates similarities to the OS patient_826 human tissue. On the other hand, the SAOS-2 samples expressed a lower signal for both phospholipid species and therefore suggests comparisons to a lower metastatic grade OS tissue, such as OS patient_882.

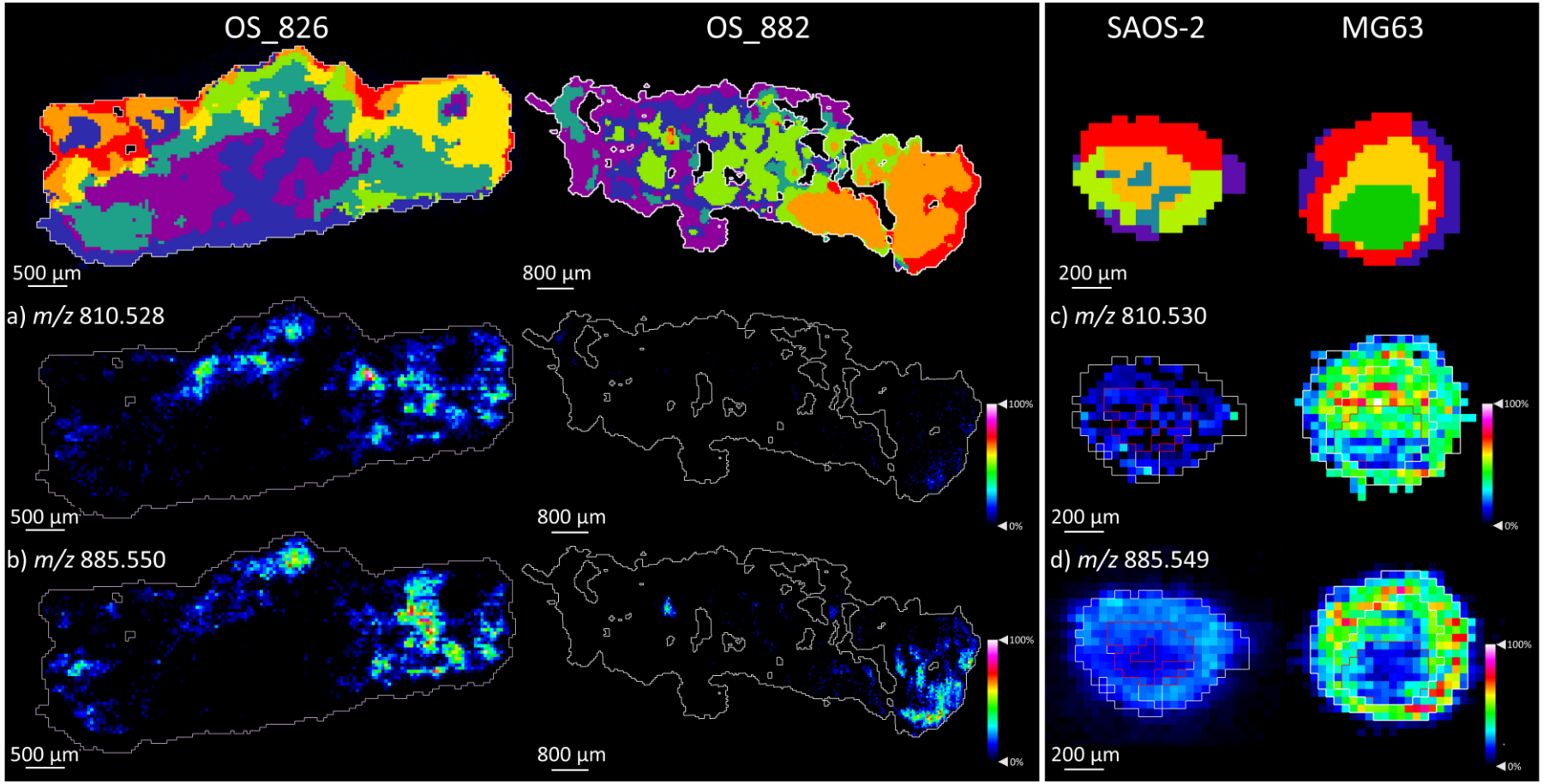

Figure 4.9 Potential metastasis-related phospholipid species detected within OS human tissue and OS aggregoid models. Ion density maps of metabolites in OS patient_826 and OS patient_882. Scale bar 500 µm and 800 µm, respectively. Ion density maps of aggregoid models outlining the core and outer area. Scale bar 200 µm. Peaks identified in human tissue a) *m/z* 810.528, PS 38:4; b) *m/z* 885.550, PI 38:4. Peaks identified in OS models d) *m/z* 810.530, PS 38:4; e) *m/z* 885.549, PI 38:4.

Conversely, the ceramide species that defined the SAOS-2 aggregoid model were significantly expressed within the metastatic OS patient_826 tissues. Cer 34:1;O2 at *m/z* 536.505 and its chlorine adduct at *m/z* 572.484 $[M+Cl]^-$ were localised within the tumorous regions that corresponded mainly to the sage green cluster of OS patient_826 (Figure 4.10 and Appendix Figure A.3). As discussed, the segmentation analysis highlighted this ROI with tumorous tissue and mineralised bone. The elevated ceramide levels within this region could be indicative of cellular differentiation and osteoid formation within the human tissues (Hill & Tumber, 2010). The comparison to the SAOS-2 aggregoid thus suggests the model exhibits similarities to regions in the OS tissue that express the mature differentiating osteoblast phenotype that mediates bone mineralisation. This contrasts with the MG63 model, which is determined as an immature osteoblast phenotype which could be the reason that it the lack of ceramide detection. Considering the differences in metabolic activity between the two OS aggregoid models and the processes within OS human tissue, it demonstrates how the 3D models can correspond to different phenotypes within the same tumour. This is significant in terms of drug development, as both models can be used to predict the cellular response within heterogeneous tissue.

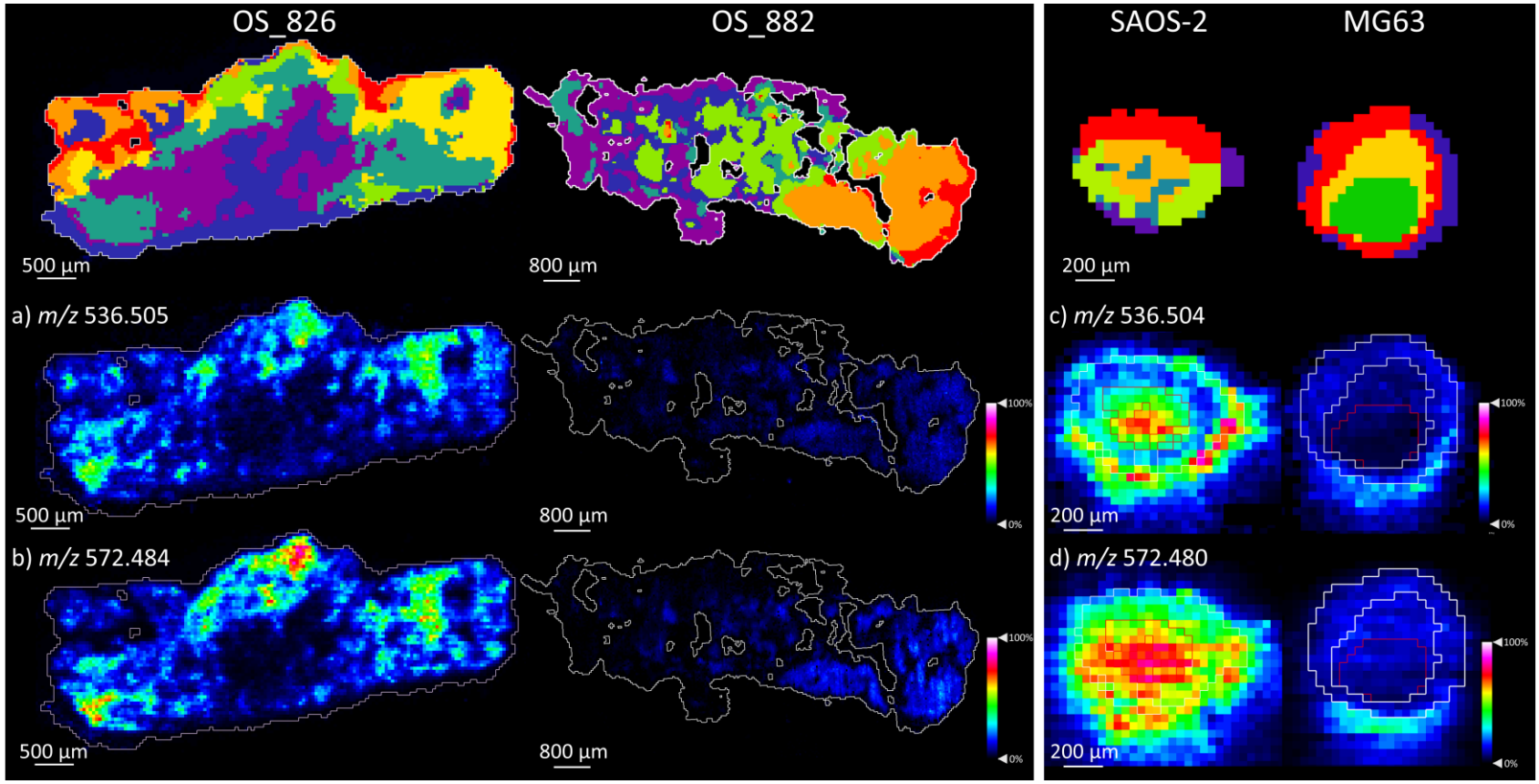

Figure 4.10 Ceramide species detected within OS human tissue and OS aggregoid models possibly identifies bone mineralisation. Ion density maps of metabolites in OS patient_826 and OS patient_882. Scale bar: 500 µm and 800 µm, respectively. Ion density maps of aggregoid models outlining the core and outer area. Scale bar: 200 µm. Peaks identified is human tissue a) *m/z* 536.505, Cer 34:1;O2; b) *m/z* 572.484, Cer 34:1;O2 $[M+Cl]^-$. Peaks identified in OS models c) *m/z* 536.504, Cer 34:1;O2; d) *m/z* 572.480, Cer 34:1;O2 $[M+Cl]^-$.

4.4.2 Protein localisations

To define the individual cellular organisation and tumour activity within the OS aggregoid models, IMC analysis was employed to detect protein and protein modification markers at 1 μm spatial resolution. Proteomic markers relevant to osteosarcoma were selected to identify structural and functional components that influence cancer metabolism.

A generic marker for DNA was used initially to determine the tissue organisation by identifying the nucleus in individual cells within the OS aggregoid models (Figure 4.11). From the DNA expression, differences between the MG63 and SAOS-2 sections can be immediately defined. Within the MG63 model, the DNA marker showed whole nuclei expressed homogenously throughout the section. When compared to the SAOS-2 model, a more heterogenous pattern was observed whereby the outer region of the aggregoid showed whole nuclei, as in the core the DNA was more condensed. This is a known indicator of nuclear disassembly and apoptotic bodies (Toné *et al.*, 2007), and implies a prevalent necrotic region within the SAOS-2 aggregoid compared to the MG63. This observation was consistent across OS aggregoid samples imaged with IMC and agreed with the metabolite data in section 4.4.1.1.

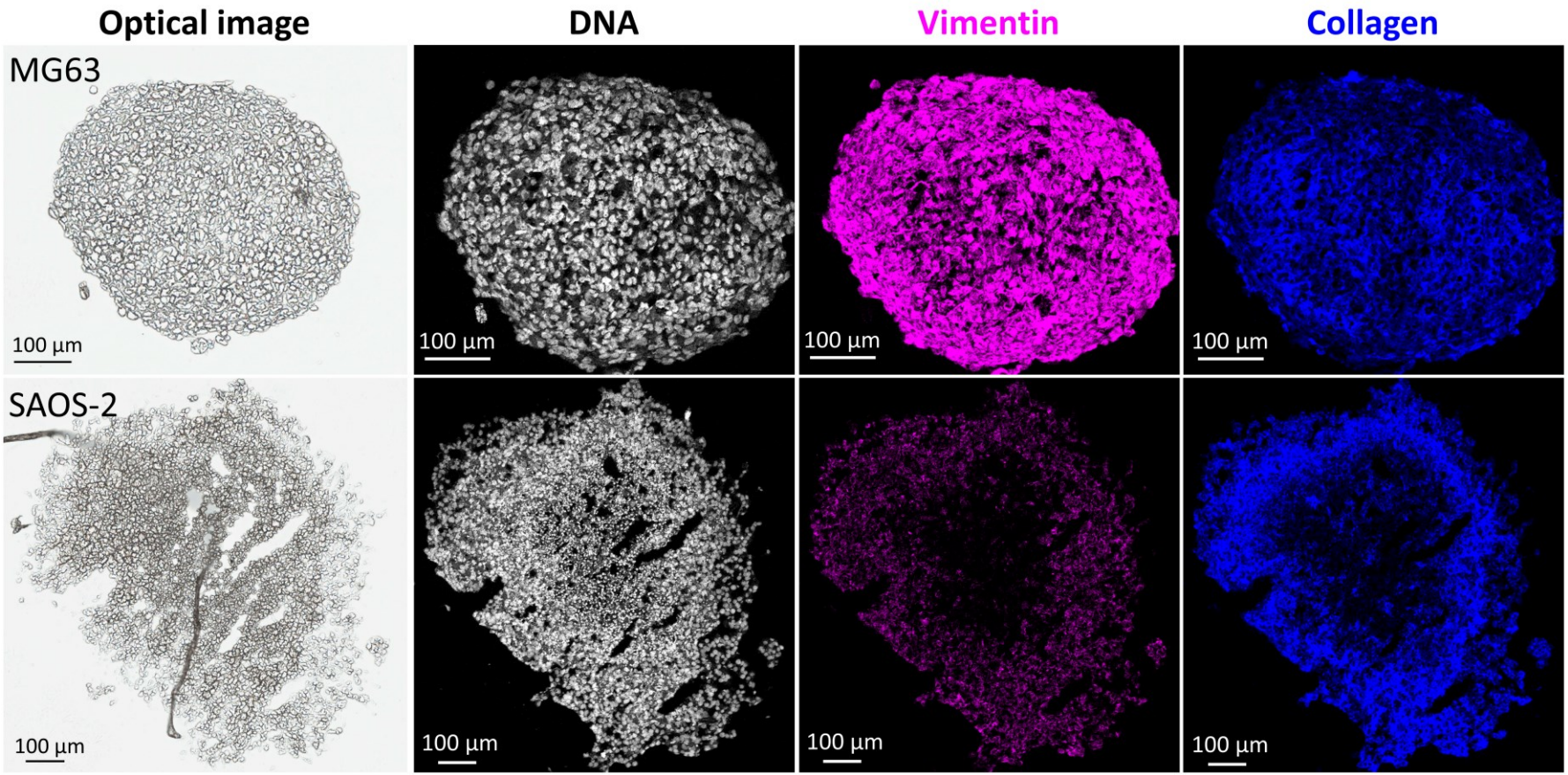

Figure 4.11 Representative IMC images of protein marker distributions within the OS aggregoid models. Scale bar: 100 µm. DNA intercalator identified individual cells within the aggregoid sections. Protein markers vimentin and collagen expressed identified structural components within the aggregoid tissue.

The differences between the two OS models are further confirmed by the expression of tumour markers, vimentin and collagen. Both structural components show similar co-localisations within the aggregoid sections (Figure 4.11). A homogeneous distribution of vimentin and collagen was detected throughout the MG63 aggregoid. As within the SAOS-2 aggregoid, the protein markers were prominently expressed within the outer region. Vimentin is known as a fibroblastic intermediate filament and a mesenchymal cell marker in differentiated cell types (Gebhard *et al.*, 2015). A higher expression of vimentin across the MG63 aggregoid compared to the lower expression in the periphery of the SAOS-2 aggregoid could be highlighting the differentiating mesenchymal cells within the models. In addition, an increase in vimentin has been associated with the overexpression of cyclooxygenase enzyme, COX-2 in MG63 cells (Zhang *et al.*, 2019). COX-2 is involved in the metabolism of arachidonic acid and promotes angiogenesis and migration. Therefore, the vimentin expression complements the metabolite data in section 4.4.1.2, where significantly high levels of FA 20:4 i.e., arachidonic acid was localised across the MG63 aggregoids, and only observed in the periphery of the SAOS-2 aggregoids.

The localisation of collagen suggests a similar expression as vimentin. Collagen is an important protein in bone when it is mineralised. The more differentiated the OS cells, the more collagen that is produced. Therefore, the levels of collagen could associate with tumour invasion by the nature of the differentiation status of the cells. The localisation of collagen within the periphery of the SAOS-2 aggregoid indicates an area of differentiation within the outer region, as the expression across the MG63 aggregoid suggests differentiated cells are present throughout (Figure 4.11). Without quantifying the percentage positivity of markers, differences in collagen expression levels between the two OS models cannot be determined by the images. One study reported a higher production of collagen type I in SAOS-2 cells in comparison to MG63 cells (Baumann & Hennet, 2016). The expression of collagen I has also been associated with ALP activity during bone mineralisation (Collin *et al.*, 1992), an activity that has been detected high in SAOS-2 cells (Murray *et al.*, 1987). In contrast, MG63 cells were reported to express higher levels of collagen III than collagen I (Jukkola *et al.*, 1993). Unfortunately, the marker used in this study detected all types of collagen, and therefore the specific type expressed in the aggregoid models was not

determined. However, the presence of different collagen types could also influence the heterogeneity between the models.

Interestingly, the markers that defined the distinctive proliferative outer region and hypoxic core phenotypes within the lung adenocarcinoma aggregoid (Chapter 3, Figure 3.8), are expressed differently between the two OS models. Similar to the HCC827 aggregoid, the SAOS-2 model showed the hypoxia marker, Glut1 localised within centre of the tissue surrounded by an annular expression of the proliferative marker, Ki-67 (Figure 4.12). The data appears to agree with the presence of cellular proliferation and differentiation within the periphery of the SAOS-2 model and identifies the core as a region of hypoxia. In the MG63 aggregoid however, a highly intense distribution of Glut1 with an expression of Ki-67 were both detected across the tissue (Figure 4.12). The purpose of Glut1 is to provide energy through the transport of glucose into cells that is converted into lactate for cancer to grow and survive in a severe microenvironment, such as hypoxia (Schneider *et al.*, 2008). High levels of Glut1 are therefore heavily associated with hypoxic tumours and has been correlated with metastatic outcome in some patients (Airley *et al.*, 2001). In OS, it was reported that the Glut1 gene is overexpressed in correlation with HIF-1α to promote tumour progression and is predictive of drug resistance and poor outcome in patients (Yang *et al.*, 2007). A higher Glut1 expression in MG63 cells compared to SAOS-2 cells has been previously reported (Cifuentes *et al.*, 2011), and a knockdown of the Glut1 gene showed inhibition of MG63 cell growth (Jian *et al.*, 2015). From the imaging data, the expression of Glut1 across the MG63 aggregoid suggests the gene is constantly switched on in all cells, regardless of the microenvironment. This in turn implies there is a constant stability of HIF-1α, consistent with a hypoxic environment but irrespective of oxygen levels in the MG63 model. This could give an indication of an aggressive hypoxic tumour model. This is supported by the Ki-67 expression across the MG63 aggregoid, whereby the cells are able to proliferate under severe hypoxic conditions due to high glucose concentrations imported by the overexpressed Glut1.

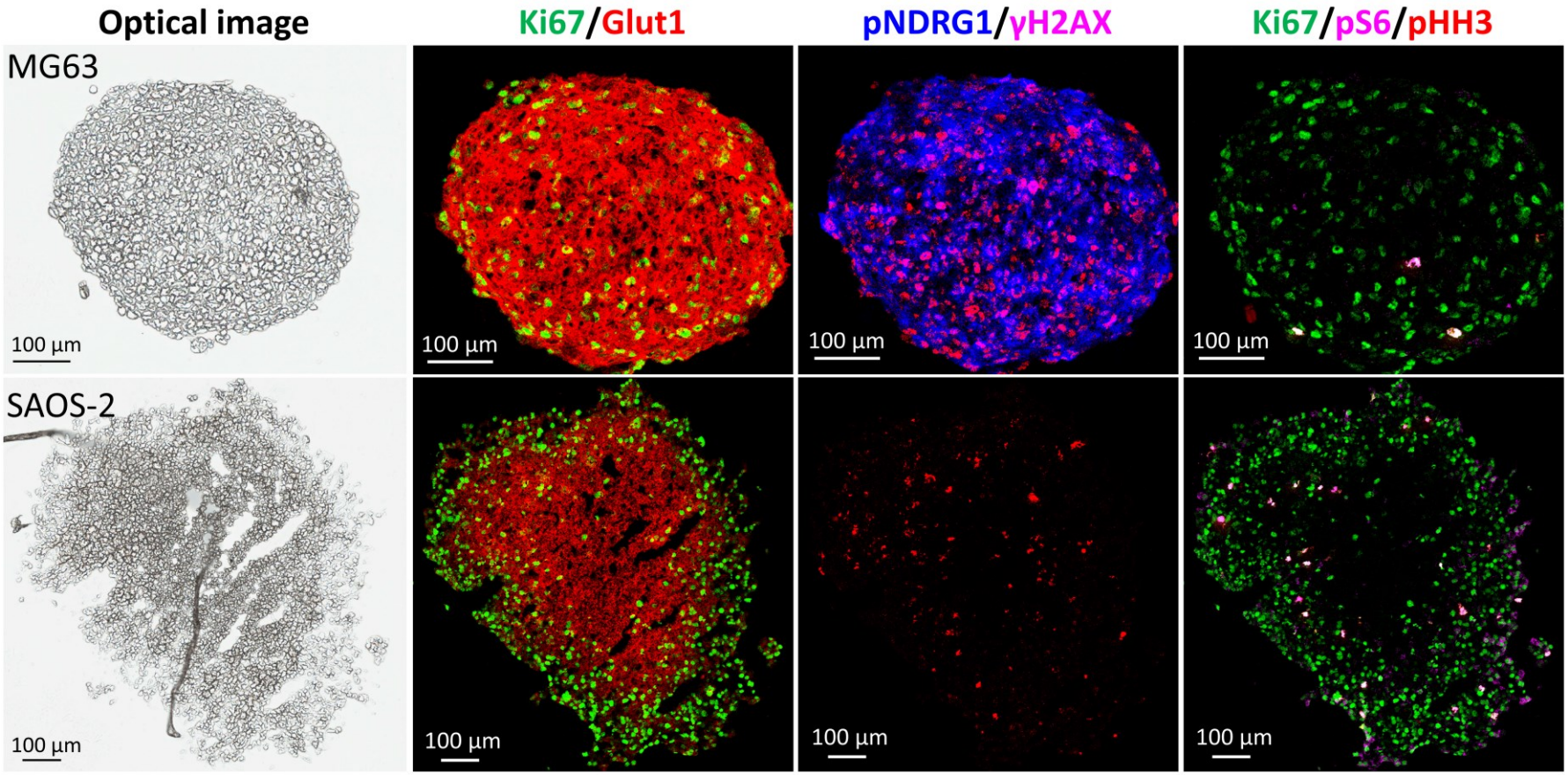

Figure 4.12 Representative IMC images of protein marker distributions highlight different tumour microenvironment phenotypes within the OS aggregoid models. Scale bar: 100 µm. Protein markers expressed identified the proliferative and hypoxic regions via Ki-67 and Glut1, respectively. Markers in response to DNA damage, pNDRG1 and γH2AX. Proliferative and differentiating phenotypes observed by pS6 and pHH3 markers.

The marker for phosphorylated N-myc downregulated gene 1 (pNDRG1) showed significant differences between the two OS models, with high expression in the MG63 aggregoid and no expression in the SAOS-2 aggregoid (Figure 4.12). NDRG1 is a stress responsive gene that can have both oncogenic and tumour suppressor roles involved in cellular differentiation, tumour progression and metastasis, hypoxia and DNA damage response (Taketomi *et al.*, 2003; Sun *et al.*, 2013; Wang *et al.*, 2013). It was reported an upregulation of NDRG1 was linked to an increase in hypoxia and HIF-1α expression (Cangul, 2004). This could therefore explain the co-localisation of pNDRG1 with Glut1 in the MG63 aggregoid, however no detection was observed in the core of the SAOS-2 aggregoid. Interestingly, Matsugaki *et al.*, (2010) reported the detection of pNDRG1 in the SAOS-2 cell line, however at significantly lower levels than in the MG63 cells. It was thought the decrease in pNDRG1 in the SAOS-2 cells was due to the differentiation state of the cells and the increased invasion potential. The group, however, noted the detection of pNDRG1 had no effect on the invasive properties of MG63 cells and therefore the role of pNDRG1 between the OS cell lines could be due to the differences in differentiation and cell phenotypes. In this study, growing the cells in 3D could have downregulated the NDRG1 gene, hence no detection of the protein marker, without comparing the expression to 2D cells this cannot be confirmed.

The expression of phosphorylated S6 ribosomal protein (pS6) and Histone H3 (pHH3) markers further confirm differences in the proliferation and differentiation activity between the two OS models. In the SAOS-2 aggregoid higher expression of pS6 and pHH3 were localised within the outer region, yet the limited expression within the MG63 aggregoid was randomly distributed (Figure 4.12). As previously discussed in Chapter 3.4.2, pS6 is an active marker for mTOR signalling which induces cancer growth and is downregulated in the presence of hypoxia (Schneider *et al.*, 2008). A low expression of the pS6 marker in the MG63 cells is therefore likely associated with the high levels of the Glut1 marker. The reverse expression of these markers is observed in the SAOS-2 model. This is a similar explanation for the pHH3 marker expression which identifies cells undergoing mitosis (Kim *et al.*, 2017).

4.4.3 Elemental compositions

The elemental analysis of the two OS aggregoid models conducted by LA-ICP-MSI, shows the typical tumour spheroid microenvironment phenotypes of an outer annular rim and inner core. However, there are slight differences between the metal distributions within the aggregoids. Firstly, Mg was highly expressed over a large area within the MG63 aggregoid compared to the SAOS-2 aggregoid, which was localised in a thin outer rim (Figure 4.13). From the discussion in Chapter 3.4.3, Mg is a component utilised in the cell cycle and is an indicator of an active energy metabolism suggesting an area of proliferation (Wolf & Trapani, 2008). From the IMC data, the Ki-67 proliferation marker showed the MG63 model expressed proliferative cells across the tissue, as the SAOS-2 model displayed a distinctive outer proliferative region. The elemental composition of Mg therefore correlates with the Ki-67 expression. In addition to this, it has been reported that Mg ions can promote the differentiation of mesenchymal stem cells to induce growth (Onder *et al.*, 2018; Qi *et al.*, 2021). The elevated levels within the aggregoids could therefore be indicative of the matrix differentiation process in the mesenchymal cells across the tissue.

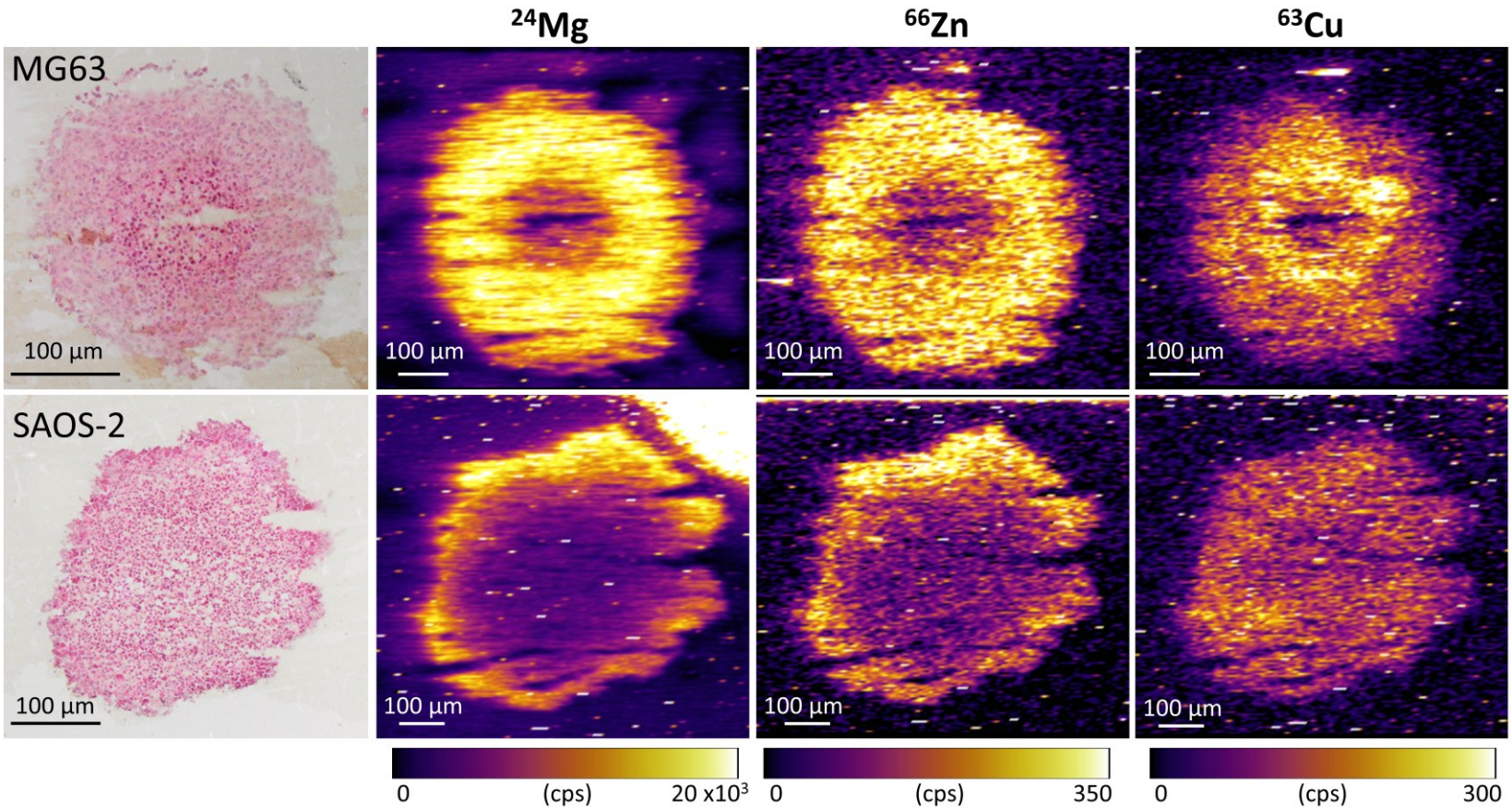

Figure 4.13 Elemental compositions within the OS aggregoid models identified the tumour microenvironment regions. H&E stain of serial sections of same aggregoid models imaged during LA-ICP-MSI analysis. Scale bar: 100 µm. Elemental maps of ^{24}Mg, ^{66}Zn and ^{63}Cu.

The co-localisation of Zn with Mg correlates with the areas of proliferation in the two OS models (Figure 4.13). From Chapter 3.4.3, it was suggested that the absence of Zn in the core of the HCC827 aggregoid could be associated with the activation of HIF-1α in hypoxia; as excess Zn was shown to induce proteasomal degradation of HIF-1α (Nardinocchi *et al.*, 2010). This theory coincides with the proliferative and hypoxic phenotype of the SAOS-2 model. The high Glut1 expression across the whole MG63 aggregoid would however disprove this, as elevated levels of Zn activity were detected. Alternatively, Zn has been linked to vimentin production, whereby the ions influence the assembly of vimentin in tissues (Monico *et al.*, 2021). Zn could be highlighting the formation of the structural component within the tissues due to the similar distributions of Zn and vimentin in the MG63 and SAOS-2 models. This would also correlate to the association of Mg with matrix differentiation in the mesenchymal cells.

In comparison, the Cu was localised more within the centre of both OS aggregoid models (Figure 4.13). As discussed in Chapter 3.4.3, the detection of Cu ions within the core of the aggregoid model could be due to an upregulation of Cu-efflux transporter, ATP7A induced by the activation of HIF-1α (Zimnicka *et al.*, 2014). A large area of Cu was detected within the SAOS-2 model, this is likely due to the large hypoxic region as observed in the H&E stain of the serial section, and in the Glut1 expression in the biological replicate from the IMC data. As for the MG63 H&E stain, it does show a small region of cells within the core that could be experiencing cellular damage, however apoptotic bodies were not present. This would suggest the MG63 aggregoid core is a less dense area due to the natural gradient of nutrients and oxygen and hence this is why Cu is accumulating within this region.

4.5 Concluding remarks

In this chapter, a multimodal imaging methodology was employed to characterise two models of osteosarcoma. Firstly, in-depth phenotyping of the metabolite activity within the two OS aggregoid models was achieved. A comparison of the metabolite data with OS human tissue samples revealed relevant fatty acid and phospholipid markers. Although, annotations of these species require MS/MS analysis for confident identification of the metabolites. From the putative assignments however, it was suggested that the MG63 aggregoids displayed an

aggressive tumour model that exhibited metastatic-like potential. Alternatively, the SAOS-2 aggregoids are more mature osteoblast-like phenotype that expressed characteristics of cellular differentiation and bone development. It was determined the two OS aggregoid models shared similarities of metabolic behaviour with different regions of OS human tissues, specifically of the higher metastatic grade. This is significant in terms of therapeutic research and development to target against aggressive *in vivo* OS tumours.

In addition, employing IMC showed significant differences in the distribution of protein markers within the OS aggregoid models. The SAOS-2 aggregoid displayed a typical tumour microenvironment with an inner hypoxic core (Glut1 marker) and an outer proliferative region (Ki-67 marker). Interestingly, the MG63 aggregoid protein expression distributions did not show the presence of such distinct regions. Furthermore, the elemental compositions within the aggregoid models corresponded to the protein distributions of proliferative activity and formation of structural components. The complementary nature of both the IMC and LA-ICP-MSI data validated the heterogeneity of metabolite distributions between the 3D models.

Overall, multimodal MSI determined the unique characteristics of two OS aggregoid models and improved the understanding of complex tumour microenvironments. MSI analysis of aggregoid models demonstrated a potential methodology to facilitate applications of cancer research and drug development for improved patient outcome.

CHAPTER 5. AN MSI STRATEGY TO DETERMINE THE CELLULAR RESPONSE TO BIOPHARMACEUTICAL TREATMENT

5.1 Introduction

An important part of pharmaceutical research and development is the determination of the maximum response achieved from treatment. Evaluating the cellular response during early pre-clinical drug development can later benefit the amount of therapeutics that pass the clinical stage. By studying the changes in levels of endogenous molecules and relating these to biochemical pathways, the efficacy of a drug and therapeutic resistance can be established.

Metabolomics is an area of increasing importance studied to determine drug action, variation in drug response and disease pathology (Kaddurah-Daouk, Kristal, & Weinshilboum, 2008). Metabolites are highly responsive molecules that interplay with gene and protein expression, and their surrounding environment. Changes to the cellular metabolism are therefore more detectable within the metabolome compared to the genome and proteome. Metabolites are also easier to detect within complex matrices due to their smaller molecular weight and size allowing for better ionisation. Small molecules and lipids are major components that drive cancer metabolism to promote tumour survival and growth (Hanahan & Weinberg, 2011). Alterations in metabolite compositions within tissues can therefore be markers of specific diseases and cancer types. In addition, metabolites serve as cofactors and signalling substrates for a multitude of proteins in numerous biological pathways that effect disease development. The analysis of metabolites within tissues can therefore give insight to the proteomic activity and highlight key biological pathways that are influenced by a therapeutic signal.

The study of metabolomics utilises analytical techniques which allow the simultaneous detection and quantitation of thousands of molecules within complex biological matrices. Robust techniques employed in metabolomics include gas chromatography mass spectrometry (GC-MS) (Fiehn, 2016), NMR (Zhang, Hatzakis, & Patterson, 2016), capillary electrophoresis mass spectrometry (CE-MS) (García *et al.*, 2017) and FT-ICR-MS (Brown, Kruppa, & Dasseux, 2005). LC-MS/MS is the primary method used in metabolic studies due to its capabilities to detect most compounds over a wide mass range (Li *et al.*, 2012; Lu *et al.*, 2019; Wang *et al.*, 2020). This technique allows for the separation of compounds with different polarities to analyse large metabolic profiles with high sensitivity and selectivity.

Metabolomics studies of biological tissues are conventionally conducted using cell lysates or plasma samples. Preparing samples in this way involves the breakdown of tissues through homogenisation, which inevitably results in the loss of spatial information. The localisation of endogenous metabolites within tissues is valued data as the detection of heterogeneous distributions can improve the understanding of specific metabolic activity within different phenotypic regions of an organism. In addition, the spatially resolved metabolites can highlight areas of therapeutic response and drug metabolism.

MSI, with high sensitivity and wide molecular coverage, can simultaneously detect multiple metabolites within tissues whilst maintaining its morphology. MALDI-MSI is the most used technique applied to metabolomics studies of disease characterisation and drug effects (Irie *et al.*, 2014; Swales *et al.*, 2018; Rzagalinski *et al.*, 2019). The study of metabolomics by MALDI-MSI has been extended to understand the pathophysiology of 3D cell cultures (Tucker *et al.*, 2019; Zang *et al.*, 2021). Additionally, the detection of drug metabolism and drug-induced metabolic changes within phenotypic regions of 3D models has also been demonstrated (Liu *et al.*, 2013; Palubeckaitė *et al.*, 2019). The use of MALDI-MSI in metabolomics studies has its limitations, however. The main challenge of MALDI is the addition of the required matrix, which can restrict the amount of lipid species detected within a single acquisition and potentially mask important small molecule signals by ion suppression effects (Holzlechner, Eugenin, & Prideaux, 2019). In addition, the application of matrix can directly affect the spatial resolution and sensitivity capabilities, as well as impacting the reproducibility of the application (Goodwin, 2012).

Ambient MSI techniques, including DESI and LESA, have increased in popularity for the study of metabolomics in cancer and treatment response (Eikel *et al.*, 2011; Lamont *et al.*, 2018; Dexter *et al.*, 2019; Henderson *et al.*, 2020). This is due to limited sample preparation that allows for rapid and direct analysis of various biological sample types. In addition, DESI-MSI, similar to LC-MS/MS, has a broader metabolite coverage due to the use of electrospray ionisation, and can also potentially generate multiply charged ions. This, therefore, provides an alternative imaging platform to analyse a wider range of compounds that is not possible with MALDI due to matrix-related interferences.

Current literature reporting metabolomic analysis of drug treatments in 3D cell culture models by ambient MSI techniques is limited. One study to date employed single-probe MSI to determine changes in metabolite distributions within irinotecan treated colon carcinoma spheroids (Tian *et al.*, 2019). In addition to this, there is a lack of literature reporting the metabolic responses to biologic treatment within tissues. This is likely due to the preference of analysing effective small molecule drugs that produce a rapid metabolic response; as well as the ability to detect the distribution of the compound and its metabolites simultaneously. The size and complexity of biopharmaceuticals, however, limits the application of ambient techniques for drug detection. Although, MALDI-MSI has demonstrated capabilities of detecting cetuximab in colon carcinoma MCTS and determined the change in ATP expression by targeted analysis (Liu *et al.*, 2018).

It is therefore clear there is a gap in research for studying a wide metabolomic response to biopharmaceuticals in 3D cell culture models. As demonstrated in Chapter 3 and Chapter 4, DESI-MSI analysis of the three aggregoid models provided a vital insight into the metabolic activity that drives their specific tumour microenvironment (Flint *et al.*, 2020). Therefore, using the same approach it could be possible to map changes in the metabolite distributions and identify key biological pathways activated in response to biopharmaceutical treatment.

5.1.1 Biologics of interest

5.1.1.1 Tumour necrosis factor-related apoptosis-inducing ligand (TRAIL)-based therapies

TRAIL is a member of the tumour necrosis factor (TNF) family of ligands that is an attractive anti-tumour agent due to its capability to extrinsically induce apoptosis through the engagement of its death receptors. TRAIL-based therapies can selectively target tumour cells, rather than normal cells, and are currently in the clinical stages of the drug development process against many cancers.

Apoptosis by TRAIL signalling is stimulated by the activation of the caspase cascade through the binding of death receptors, DR4 and DR5 (Pitti *et al.*, 1996) (Figure 5.1). Once bound, the apoptosis pathway is initiated via the activation of the carboxyl terminal death domain (DD). The ligand binding promotes receptor oligomerisation and recruitment of adapter protein, fas-associated protein with

death domain (FADD). Procaspase-8 and -10 are then recruited to form the death inducing signalling complex (DISC). During the formation of DISC, caspase-8 and -10 are cleaved and activated. From this signal, two types of cell death are stimulated: extrinsic and intrinsic pathways. The cell death extrinsic pathway follows onto the cleavage and activation of caspase-3, this in turn activates death inducing substrates and initiates apoptosis.

Subsequently, caspase-8 can induce the cell death intrinsic pathway, which typically triggers apoptosis in response to DNA damage, cell cycle checkpoint defects, hypoxia or other severe cellular stresses. In the intrinsic pathway, caspase-8 cleaves the proapoptotic Bcl-2 family member, Bid, forming truncated Bid (tBid). The translocation of tBid to the mitochondria targets anti-apoptotic Bcl-2 family members and promotes mitochondrial outer membrane permeabilization (MOMP) through release of Bax from anti-apoptotic Bcl-2 members and results in the release of cytochrome c into the cytosol. Following this, the binding of cytochrome c with APAF-1 adapter forms the apoptosome, which stimulates the apoptosis-initiating protease, capsase-9. This in turn, activates the cleavage of caspase-3 and other ‘executioner’ proteases such as caspases -6 and -7. In addition, the apoptogenic factor, DIABLO is also released during MOMP, and blocks protein inhibitors of apoptosis (IAP) such as cIAP1, cIAP2 and XIAP. The mechanistic link between extrinsic and intrinsic stimulation of cell death pathways is thought to amplify the apoptotic signal when TRAIL binds to its surface receptors (Fulda *et al.*, 2001).

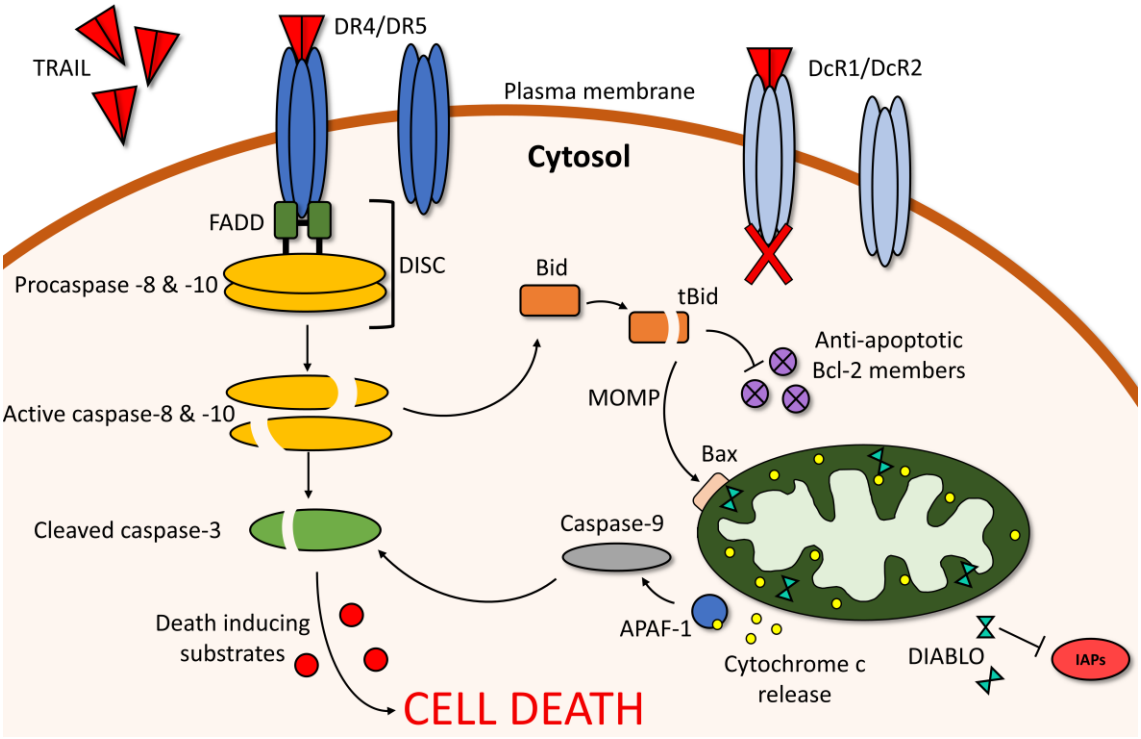

Figure 5.1 TRAIL signalling activates the intrinsic and extrinsic apoptotic signalling pathway.

Despite the effective signalling of both extrinsic and intrinsic apoptotic pathways, TRAIL-based therapies have still failed in clinical trials due to resistance in specific cancer types (Fuchs *et al.*, 2013; Reck *et al.*, 2013). One possible reason for this is the presence of decoy receptors (DcR1 and DcR2), which can inhibit death inducing signalling when TRAIL binds (Pan *et al.*, 1997). Therapeutic monoclonal antibodies (mAb) that are specific to DR4 and DR5 have been shown to bypass decoy receptors and induce apoptosis in cells insensitive to TRAIL (Locklin *et al.*, 2007). Conversely, engagement of death receptors can activate cell survival pathways. For instance, the TRAIL-induced anti-apoptotic factor, nuclear factor kappa B (NF-kB) has been shown to stimulate cellular proliferation and tumour promoting cytokines (Khanbolooki *et al.*, 2006). In addition, excessive stimulation of the PI3K/Akt/mTOR proliferation pathway by oncogenes and growth factors has shown to affect TRAIL sensitivity (Xu *et al.*, 2010).

TRAIL-based therapies as independent treatment or in combination with chemotherapeutics have been considered promising for OS treatment based on evidence from both *in vitro* and animal experiments (Hotta *et al.*, 2003; Suzuki *et al.*, 2003; Picarda *et al.*, 2010). However, differences in sensitivity to TRAIL and

agonistic mAb against the death receptors have been shown across OS cell lines (Locklin *et al.*, 2007; Phillips *et al.*, 2019). Literature reporting the effects of TRAIL treatment on 3D models of OS is limited. Therefore, it would be interesting to determine metabolite abundances in the OS aggregoids treated with TRAIL-based therapies and associate if the models exhibit pro-apoptotic or drug resistant responses.

5.1.1.2 Cetuximab

Cetuximab, otherwise known by its trade name Erbitux®, is an antagonistic mAb that selectively targets the epidermal growth factor receptor (EGFR). The immunotherapeutic has been FDA-approved for the use in treatment for oncogene EGFR addicted cancers including colorectal and head and neck (Goldberg & Kirkpatrick, 2005; Mehra, Cohen, & Burtness, 2008). Cetuximab is a recombinant chimeric human/mouse IgG1 monoclonal antibody generally used for personalised medicine. The mechanism of action is a competitive activity against ligands, such as the EGF and transforming growth factor-α (TGF-α) to bind to the EGFR and inhibit signalling.

The EGFR pathway (Figure 5.2) is an important process for cellular proliferation and growth and is overexpressed in cancers, such as NSCLC (Merrick *et al.*, 2006). The EGFR is a tyrosine kinase receptor that is phosphorylated when ligand bound. This in turn can activate multiple pathways such as the PI3K/Akt/mTOR pathway to promote cell cycle progression (Freudlsperger *et al.*, 2011). A critically important pathway activated by EGFR signalling is the Ras/Raf/MAPK pathway (Scaltriti & Baselga, 2006). Once the EGFR is phosphorylated through ligand binding, adapter proteins Grb2 and SOS bind directly onto the docking site of the receptor in the cytosol. This in turn leads to the modification of SOS to allow the binding of GTP to Ras. This process activates the Raf kinase that leads to the phosphorylation of mitogen-activate protein kinases (MAPK), MEK and ERK1/2. Consequently, MAPKs are then imported into the nucleus where they phosphorylate specific transcription factors that drive the cell cycle, such as increasing the production of cyclin D, which drives cells out of G_1 phase into DNA synthesis.

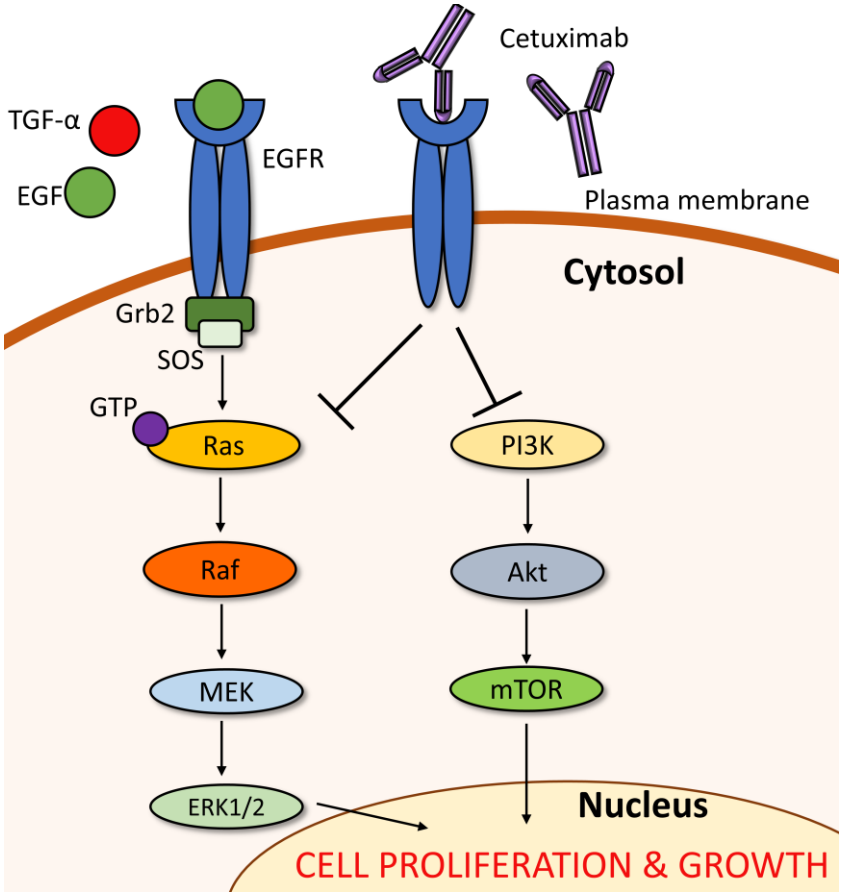

Figure 5.2 The EGFR signalling pathway promoting cell proliferation and growth is inhibited by cetuximab.

Cancers that are resistance to cetuximab treatment are considered to have genetic mutations in the signalling proteins of the Ras/Raf/MAPK pathway (Brand, Iida, & Wheeler, 2011). This means that even with the inhibition of the EGFR by cetuximab, the downstream proteins continue to signal for cellular proliferation. Despite the amplification of the EGFR gene in lung cancers, due to the highly mutated oncogene, K-Ras that leads to the overexpression of Ras, FDA-approval for cetuximab as an independent treatment was removed (Massarelli *et al.*, 2007; Sgambato *et al.*, 2014). Nonetheless, literature have still reported the success of cetuximab inhibiting proliferative activity in lung cancer, specifically in combination with therapeutic inhibitors that target signalling proteins downstream the EGFR pathways (Kurai *et al.*, 2007; Steiner *et al.*, 2007; Hasegawa *et al.*, 2019). With that in mind, by studying the metabolic changes it could be possible to determine a potential cellular response within the HCC827 aggregoid model treated with cetuximab.

5.2 Aims of chapter

In this study, an untargeted DESI-MSI approach was employed to observe the metabolome responses to three biologic treatments in the aggregoid models. The osteosarcoma aggregoids, MG63 and SAOS-2, were treated with TRAIL-based therapies, TRAIL and agonistic anti-Death Receptor 5 mAb (anti-DR5). The HCC827 lung adenocarcinoma aggregoid model was treated with antagonistic anti-EGFR mAb, cetuximab.

A multivariate statistical analysis approach was used to highlight specific metabolites of interest. PCA was used as an unsupervised method to identify variables with the most data variance and find potential outliers within treatment groups. PLS-DA was used for a supervised approach to identify differences between the control and the highest concentration treated groups for each biologic treatment.

5.3 Materials and methods

5.3.1 Materials

Recombinant Human sTRAIL/Apo2L (TRAIL) was purchased from PeproTech EC Ltd (London, UK). Human TRAIL R2/TNFRSF10B Antibody (anti-DR5) was purchased from R&D Systems (Abingdon, UK). Cetuximab (Erbitux®) was purchased from Merck (Darmstadt, Germany).

5.3.2 Cell culture

5.3.2.1 2D cell culture biologic treatment

Initial cell culture conditions for MG63 and SAOS-2 are reported in Chapter 2.3.2. Once confluent, cells were prepared for 2D experiments. Both cell lines were trypsinised and plated into 96-well plates at $5x10^4$ cells/mL and cultured for 24 h before treatment. Each cell line was treated in triplicate with either TRAIL at concentrations: 0 ng/mL, 50 ng/mL, 200 ng/mL; or anti-DR5 at concentrations: 0 ng/mL, 200 ng/mL, 1 µg/mL. Drug solutions were made up with DMEM supplemented with 10% FBS and 1% penicillin-streptomycin (Lonza Ltd, UK). Cells were cultured with treatment for 24 h before analysis. Cells were visualised with Hoechst 33342 and PI staining (10 µg/mL) using an Olympus IX81 microscope. Images were captured using Cell^F software.

5.3.2.2 3D cell culture biologic treatment

Aggregoids were cultured following the protocol described in Chapter 2.3.3. For the experiment, MG63 and SAOS-2 aggregoids were treated with TRAIL at concentrations: 0 ng/mL, 50 ng/mL, 200 ng/mL; or anti-DR5 at concentrations: 0 ng/mL, 200 ng/mL, 1 µg/mL. HCC827 aggregoids were treated with Cetuximab concentrations: 0 µg/mL, 5 µg/mL, 150 µg/mL and 1000 µg/mL. Drug solutions were made up with DMEM supplemented with 10% FBS and 1% penicillin-streptomycin (Lonza Ltd, UK). Samples were incubated for 24 h before harvesting.

HCC827 aggregoids were visualised in brightfield. Images were taken at 0 h and 24 h using a Cytation™ 5 Cell Imaging Multi-Mode Reader (BioTek, UK). The four cetuximab concentrations were imaged (n=2), and the diameter of each aggregoid sample was measured in triplicate.

5.3.3 Sample handling

Aggregoids were processed following the optimised method reported in Chapter 2.3.4.

5.3.4 Metabolite imaging

5.3.4.1 DESI-MSI analysis

Metabolite detection was performed on a Q-Exactive mass spectrometer (Thermo Fisher Inc, Germany) as described in Chapter 2.3.5.3. The images were collected in the mass range *m/z* 80-900 at a spatial resolution 40 µm and analysed by SCiLS Lab MVS Premium 3D Version 2020a (Bruker Daltonics, Germany) employing RMS normalization.

5.3.4.2 Discriminatory analysis

Data was processed following a similar method to that described in Chapter 3.3.4.2. ROIs containing the whole aggregoid sections were determined (SCiLS, Bruker Daltonics). The raw data file from the DESI-MSI were uploaded to METASPACE (https://metaspace2020.eu) for metabolite identification of the discriminated *m/z* values by employing HMDB and LIPIDMAPS®. The resulting peak list from each aggregoid section was exported into .csv files and grouped together by treatment conditions. The data was then imported into MetaboAnalyst 5.0 (Xia *et al.*, 2009) to conduct MVA following the method described in Chapter

4.3.5. PCA and PLS-DA were performed on the selected treatment groups for each aggregoid model. Peaks of interest from the loadings plots were corresponded to the *m/z* images. To determine discriminatory peaks, ROC analysis was performed to determine the AUC. Statistical analysis on the mean intensities of each sample group was performed using a parametric unpaired t-test, $p < 0.05$.

5.3.5 Histological analysis

Aggregoid samples were stained with Haematoxylin and eosin solutions as following method described in Chapter 3.3.7.

5.4 Results and discussion

5.4.1 Osteosarcoma treatment response

5.4.1.1 Sensitivity to TRAIL-based therapy

Initial assessment to determine the sensitivity of osteosarcoma cell lines, MG63 and SAOS-2 to TRAIL and anti-DR5 treatment was determined by Hoechst 33342 and PI nuclear staining. The percentage of apoptosis for each cell line was calculated (Figure 5.3). Monolayer cultures of MG63 showed a relatively high sensitivity to both biologic treatments. An induction of apoptosis was observed in > 50% of MG63 cells with 50 ng/mL TRAIL treatment. The sensitivity was reduced in response to anti-DR5 treatment with ~ 30% of MG63 cells displaying apoptotic activity at 200 ng/mL. It was, however, still significant in terms of observing a cellular reaction to the biologic treatment. The sensitivity of SAOS-2 to both TRAIL and anti-DR5 treatment was reduced in comparison. Less than 15% of cells displayed an induction of apoptosis with 50 ng/mL TRAIL treatment, as < 10% was observed in response to the highest concentration, 1000 ng/mL anti-DR5.

A similar pattern of sensitivity to TRAIL and anti-DR5 treatment was recently reported, whereby apoptotic activity was heightened in MG63 cells in comparison to SAOS-2 cells (Phillips *et al.*, 2019). This is likely due to an increased resistance to treatment in the SAOS-2 cell line. A number of publications have reported possible mechanisms of resistance in OS cell lines, including the expression of decoy receptors (DcR1 and DcR2) and osteoprotegerin (OPG), or activation of cellular proliferation via PI3K/Akt/mTOR pathway (Locklin *et al.*, 2007; Perry *et*

al., 2014). Based on this knowledge, the metabolic profiles of the OS aggregoid models treated with TRAIL and anti-DR5 were investigated to determine the detection of treatment response and resistance.

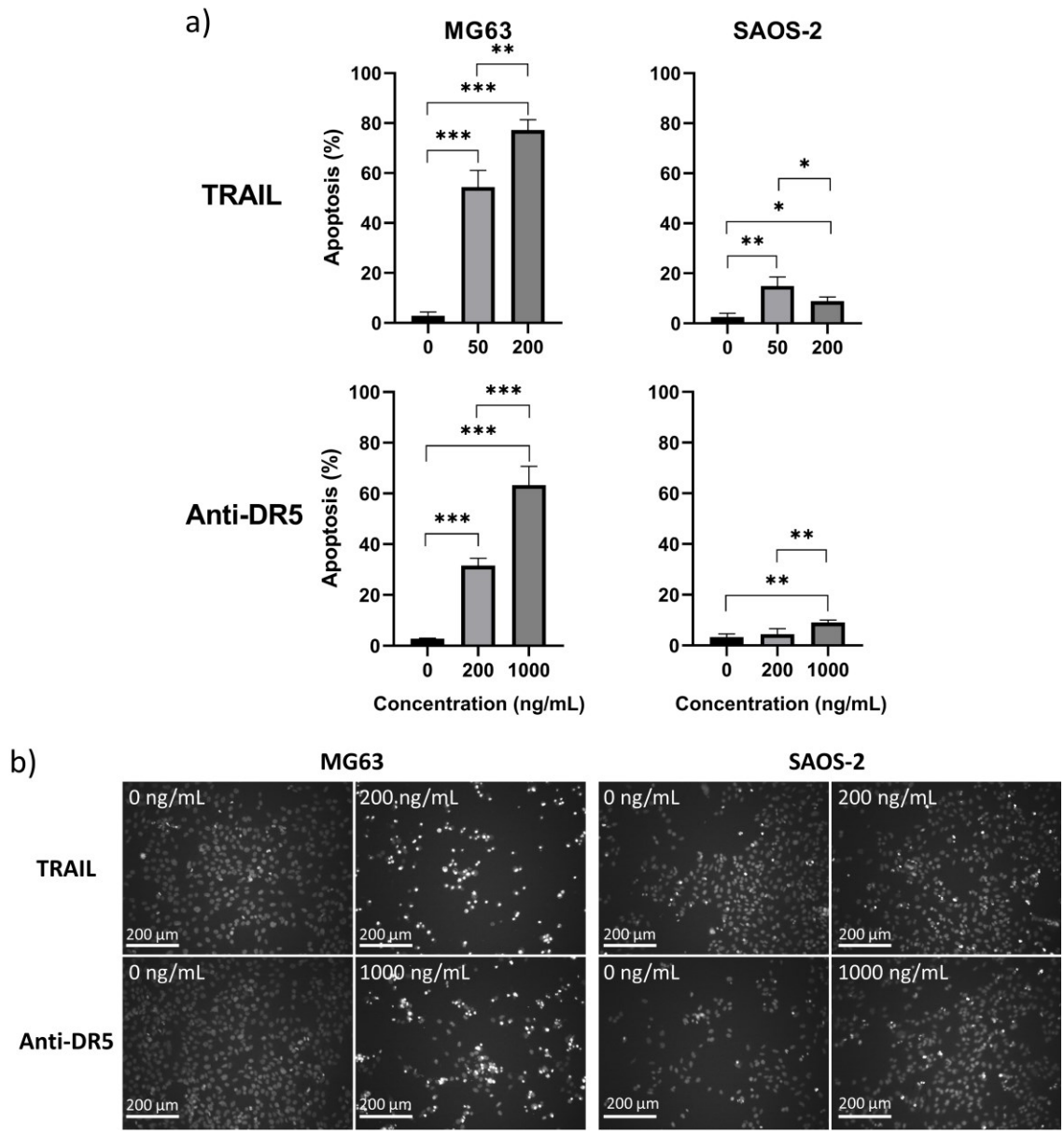

Figure 5.3 Apoptosis induction in osteosarcoma cell lines in response to TRAIL-based therapy. a) Percentage apoptosis after 24 h treatment with TRAIL or anti-DR5 in MG63 and SAOS-2 OS cell lines assessed by Hoechst 33342 and PI nuclear staining. Data is mean ± SD (n=3), one-way ANOVA with Tukey post hoc test * $p < 0.05$, ** $p < 0.01$, *** $p < 0.001$. b) Representative Hoechst 33342 and PI staining optical images of MG63 and SAOS-2 cells in response to TRAIL 0 ng/mL and 200 ng/mL, anti-DR5 0 ng/mL and 1000 ng/mL. Condensed nuclei are characteristic of apoptosis and are shown as brighter-stained nuclei.

5.4.1.2 Metabolic activity in response to TRAIL-based therapy

Based on the 2D experiment and the responses of the OS cell lines (MG63 and SAOS-2) on TRAIL-based therapies, the same doses were used to treat the OS aggregoid models. The metabolic response in the 3D models to TRAIL and anti-DR5 treatments were detected by DESI-MSI, and the H&E stains of the same section were used to determine the presence of apoptotic cellular morphology.

5.4.1.2.1 MG63 in response to TRAIL treatment

From the data of TRAIL-treated MG63 aggregoids, the PCA displayed significant variance of the 200 ng/mL samples from the control and 50 ng/mL treated groups, implying there is clear discrimination of *m/z* values towards the highest concentration of TRAIL treated aggregoids (Figure 5.4). The PLS-DA plot further demonstrates separation of the control samples from the 200 ng/mL treated samples (Figure 5.5). The 200 ng/mL samples were also closely clustered together within their group suggesting there is a strong similarity between the biological replicates. From the PLS-DA loadings plot, several *m/z* values identified in the right region of the plot correlated to specific lipid species that were more prevalent within the control group than the treated group. A summary of the main discriminatory metabolites detected are discussed and reported in Table 5.1.

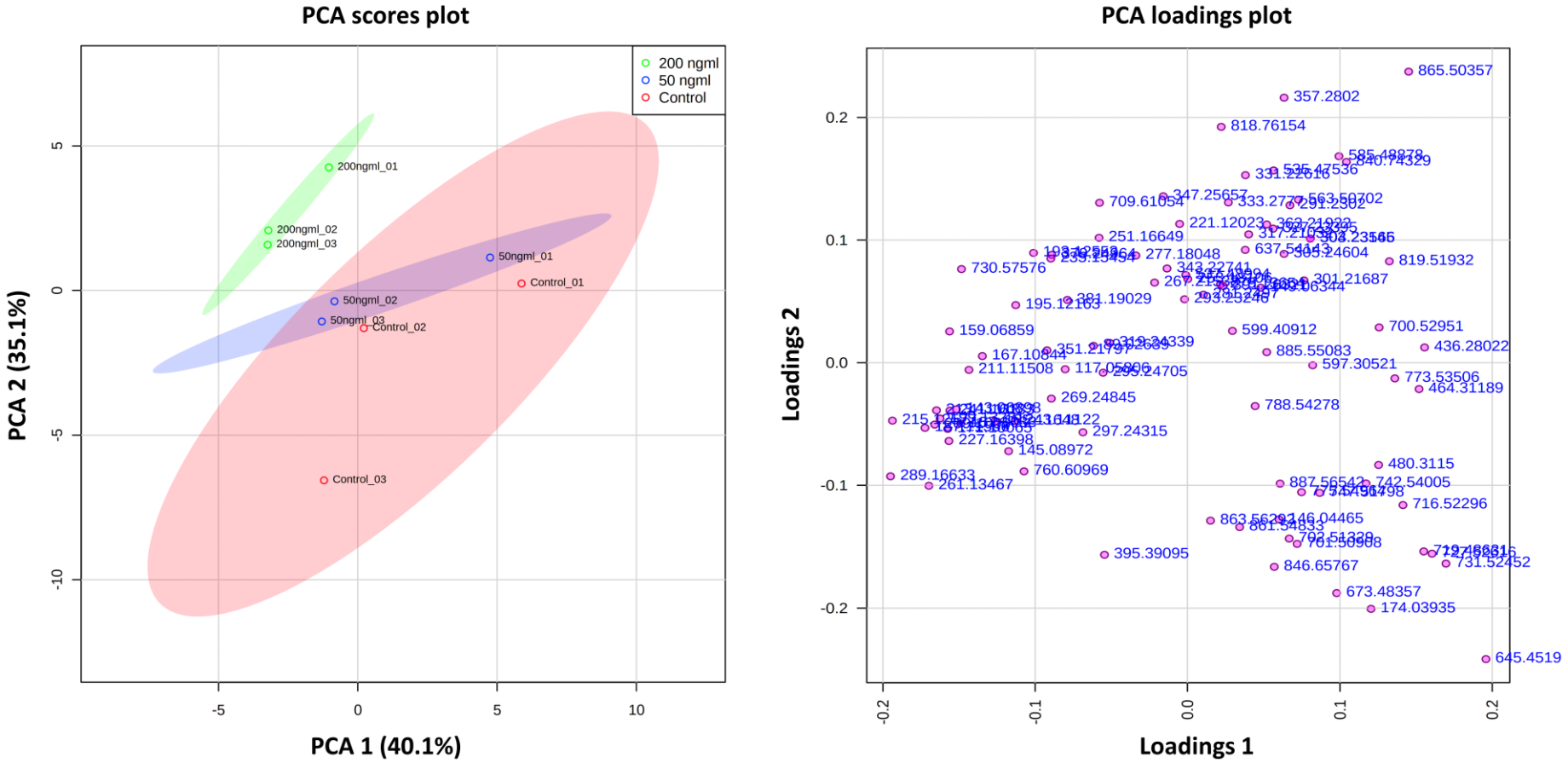

Figure 5.4 PCA scores and loadings plot show clear separation of control and TRAIL treated MG63 aggregoids. Principal components, PC 1 (40.1%) and PC 2 (35.1%) showed the best separation between sample groups. The discriminatory *m/z* values of interest were distributed separately from the cluster of peaks. Samples were grouped with 95% confidence, control (red), 50 ng/mL TRAIL (blue) and 200 ng/mL TRAIL (green).

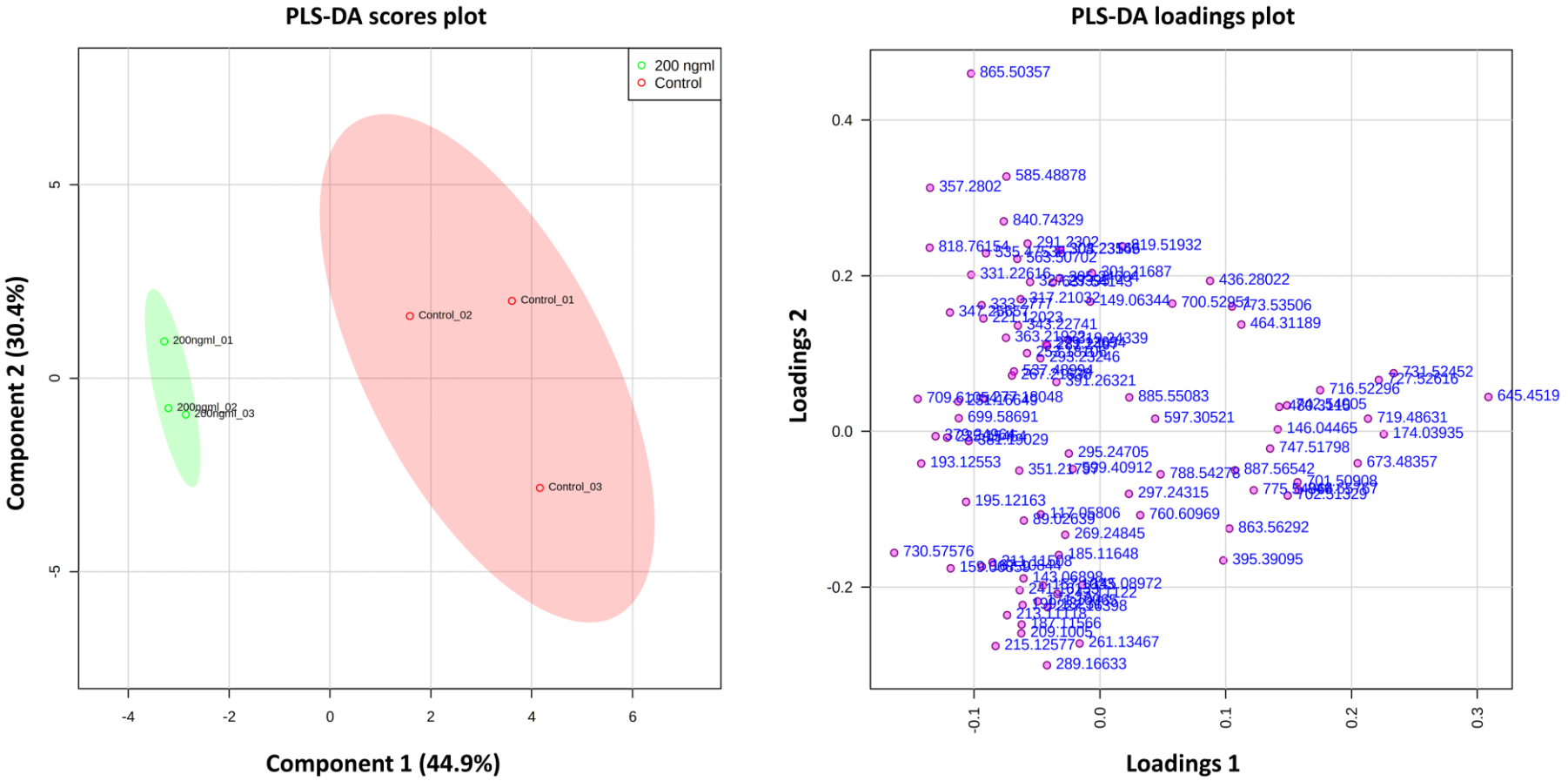

Figure 5.5 PLS-DA scores and loadings plot show variance between control and 200 ng/mL TRAIL treated MG63 aggregoids. Component 1 (44.9%) and component 2 (30.4%) showed the best separation between samples. The discriminatory *m/z* values of interest were distributed separately from the cluster of peaks. Samples were grouped with 95% confidence, control (red) and 200 ng/mL TRAIL (green).

A particular mass localised in the periphery of the MG63 control samples at *m/z* 645.452 (AUC = 0.604) was identified as glycerol 1-(9Z-octadecenoate) 2-tetradecanoate 3-phosphate, a glycerophospholipid (Figure 5.6b). Glycerophospholipids are continuously synthesised by highly proliferating cancer cells for membrane production, in addition to being used for energy through lipid modifications of proteins (Dolce *et al.*, 2011). Hence, this could explain the localisation of the metabolite in the outer proliferation region of the untreated aggregoids. A decrease in the metabolite in the TRAIL treated samples suggests a change in the glycerophospholipid metabolism. This is potentially due to a reduction in proliferation as a result of TRAIL treatment, which is known to inhibit cellular proliferation and stimulate apoptosis. This metabolite is also a product of 1,2-diacylglycerol-3-phosphate (DAG). DAG is a lipid species involved in inducing cellular proliferation through activation of protein kinase C (PKC) signalling (Black & Black, 2013). Therefore, a depletion of the DAG product could further indicate a reduced proliferation rate in the treated samples.

A high expression of *m/z* 730.576 within the core of the MG63 TRAIL treated samples (AUC = 0.247) was identified as PC O-33:1 (Figure 5.6c). PC is an abundant phospholipid in tissues, however a number of studies have reported that PC can inhibit growth and induce apoptosis through the assistance of death ligands, such as the TNF-α (Sakakima, Hayakawa, & Nakao, 2009; Li *et al.*, 2011). Elevated levels of PC O-33:1 in the treated samples could therefore be associated with apoptotic signalling induced by TRAIL. A contradictory report however, observed a depletion of specific PC species within HeLa and Jurkat cell lines treated with TRAIL due to the activation of PC-degrading enzymes (Sandra *et al.*, 2005). Comparing this finding to our results could suggest a signature of TRAIL resistance, and the high levels of PC might only be an indication of high apoptotic activity within the hypoxic region of the aggregoids. From the H&E stains, condensed DNA with potential apoptotic and necrotic cells were detected in all three 200 ng/mL treated samples. The control group consisted of cells with normal morphology with some cells condensed in the section displayed in Figure 5.6a, however no apoptosis was detected. The significant increase of the PC metabolite across the treated group therefore could imply a signal response to treatment rather than an activity stimulated by the tumour microenvironment.

In addition, a phosphatidic acid (PA) at *m/z* 673.480 (PA 34:1) was also localised within the outer region of the MG63 control samples (AUC = 0.645) (Figure 5.6d). PA lipid species are known to be responsible in the progression of cancer by stabilising mTOR to suppress apoptotic activity via the PI3K/Akt/mTOR pathway (Foster, 2009). This again explains the localisation of the PA species within the outer proliferative region of the aggregoids. A decrease in PA 34:1 in the treated samples could further indicate a signature of response in the MG63 aggregoids to TRAIL treatment, showing a reduced rate of proliferation.

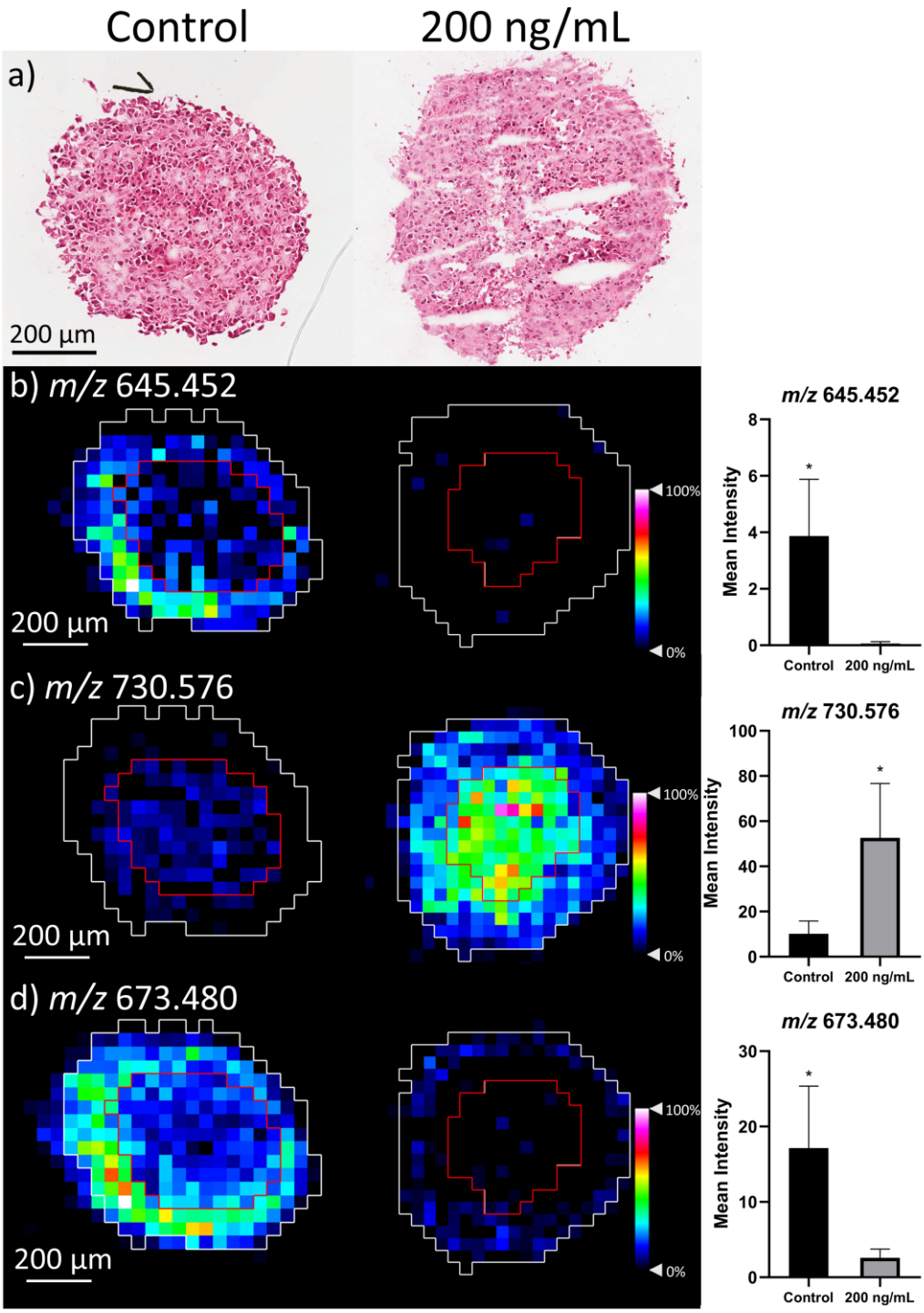

Figure 5.6 MG63 TRAIL treated aggregoid images identified from multivariate analysis. a) H&E images of MG63 aggregoids control and 200 ng/mL TRAIL treated. Scale bar 200 µm. Ion density maps of metabolites outlining the outer (white) and core (red) regions of the aggregoid sections. Mean intensity plotted on bar graph against the control and 200 ng/mL treated samples (n=3), unpaired t-test * $p < 0.05$. Scale bar 200 µm. Peaks identified b) *m/z* 645.452, glycerol 1-(9Z-octadecenoate) 2-tetradecanoate 3-phosphate; c) *m/z* 730.576, PC O-33:1; d) *m/z* 673.480, PA 34:1.

5.4.1.2.2 MG63 in response to anti-DR5 treatment

The PCA of the MG63 aggregoid samples treated with anti-DR5 showed less discrimination between the control and the treated groups in comparison to the TRAIL treated aggregoids (Figure 5.7). The 95% confidence grouping of 200 ng/mL treated samples showed overlay between the control and the 1000 ng/mL treated samples. This is potentially due to the lower sensitivity of MG63 to the anti-DR5 treatment which only targets DR5, as TRAIL targets both DR4 and DR5 (Locklin *et al.*, 2007). The PLS-DA however, showed slight variance of the 95% grouping between the control and the 1000 ng/mL samples (Figure 5.8). Though, from the PLS-DA scores plot, the samples for each treatment group were fairly distributed from one another suggesting some variability of the aggregoids within the groups. By looking at the imaging data for the differing peaks from the PLS-DA loadings plot and the ROC analysis results, little discrimination of the peaks of interest between groups was observed, this mainly due to variation of the metabolite expressions between samples. Therefore, either a limited response to anti-DR5 was detected or too much variation between samples has impacted the results. The potential metabolic markers of anti-DR5 response are discussed and summarised in Table 5.1.

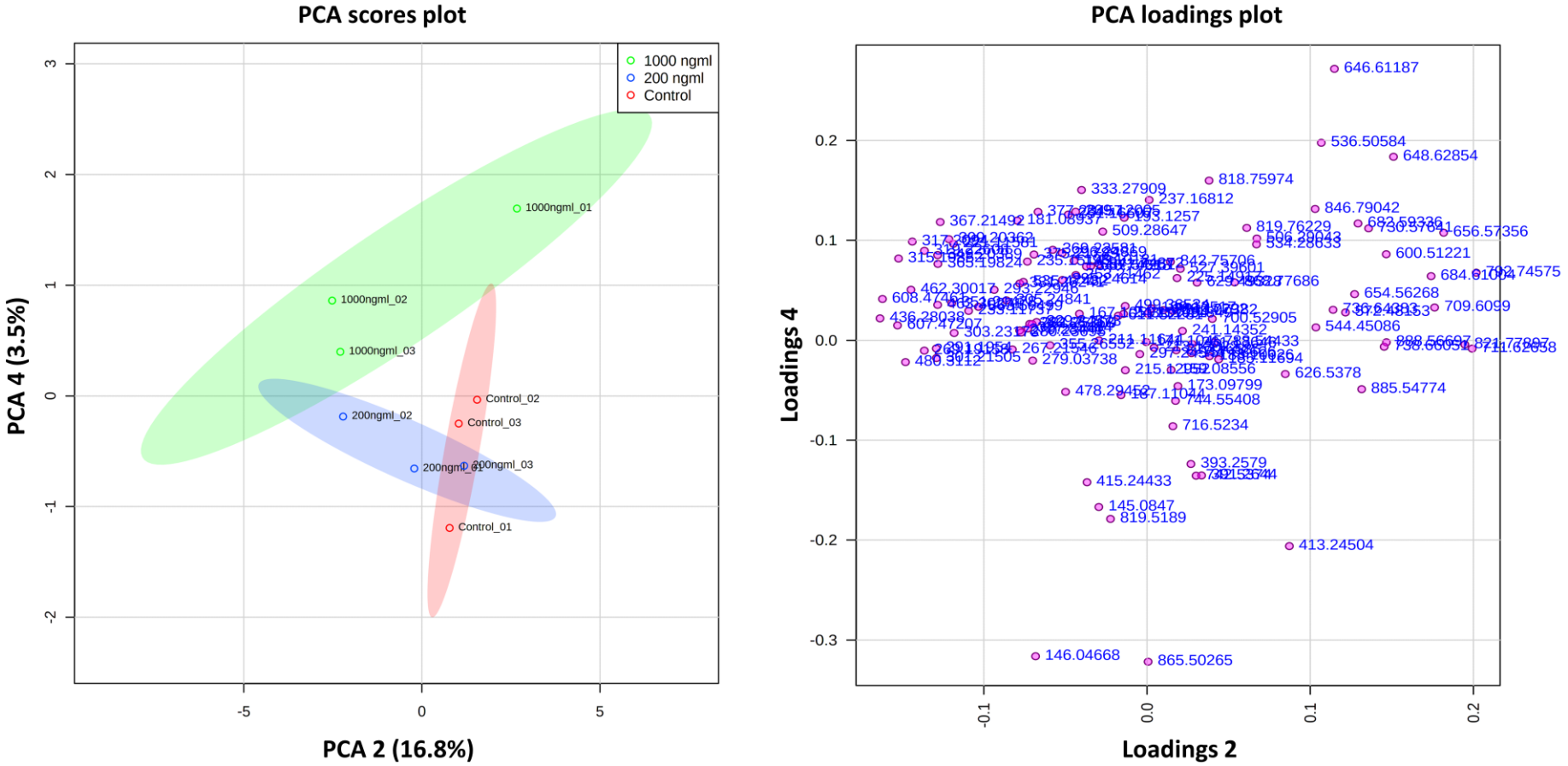

Figure 5.7 PCA scores and loadings plot show some separation of control and anti-DR5 treated MG63 aggregoids. Principal components, PC 2 (16.8%) and PC 4 (3.5%) showed the best separation between sample groups. The discriminatory *m/z* values of interest were distributed separately from the cluster of peaks. Samples were grouped with 95% confidence, control (red), 200 ng/mL anti-DR5 (blue) and 1000 ng/mL anti-DR5 (green).

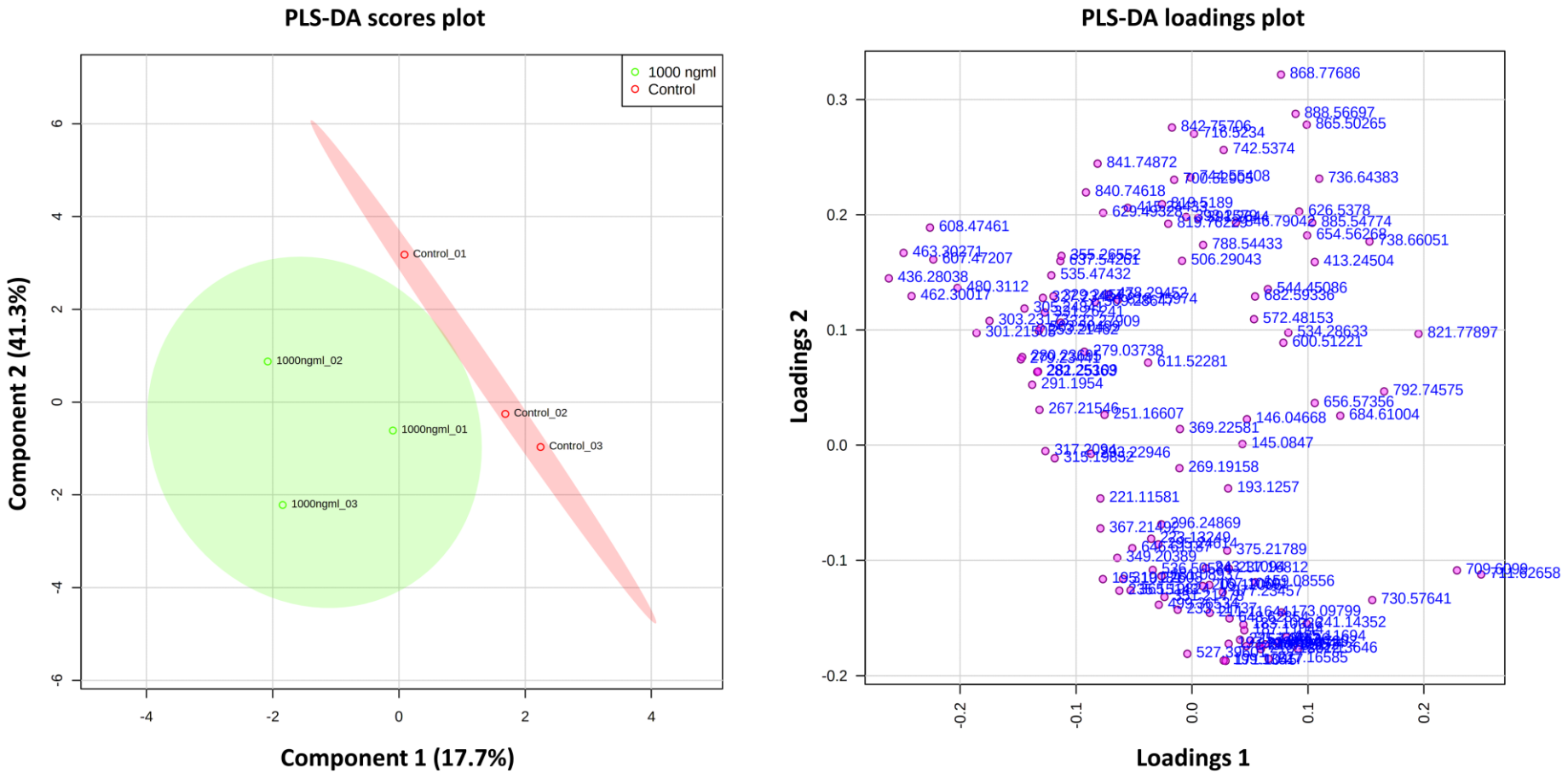

Figure 5.8 PLS-DA scores and loadings plot show variance between control and 1000 ng/mL anti-DR5 treated MG63 aggregoids. Component 1 (17.7%) and component 2 (41.3%) showed the best separation between samples. The discriminatory *m/z* values of interest were distributed separately from the cluster of peaks. Samples were grouped with 95% confidence, control (red) and 1000 ng/mL anti-DR5 (green).

The PC O-33:1 expression, as detected in the MG63 aggregoids treated with TRAIL, was observed in the data of the MG63 aggregoids treated with anti-DR5. The *m/z* value at 730.576 was separated slightly from the peak clusters on the PLS-DA loadings plot suggesting potential discrimination towards a specific sample group. From the imaging data, slightly higher levels of PC O-33:1 were detected in the control samples (AUC = 0.567), although was not significant (Figure 5.9b). This observation was contradictory to the elevated PC O-33:1 levels in the MG63 TRAIL treated samples. As previously discussed, PC species have been linked with apoptotic behaviour in response to death receptor activation (Sakakima *et al.*, 2009; Li *et al.*, 2011), and thus a potential increase in the metabolite could be expected if the MG63 aggregoids were highly sensitive to anti-DR5. In contrast, the similar levels of PC O-33:1 between the control and treated samples would suggest a lack of apoptotic response to anti-DR5. From the images, the localisation of the PC species within the core of the aggregoid samples is therefore more likely an indicator of cellular response to hypoxia.

On the other hand, metabolite PE P-16:0 at *m/z* 436.280 was localised across the aggregoids and expressed higher in the treated samples (AUC = 0.462) (Figure 5.9c). PE species, like PS species, are well-known lipids that are actively exposed on the outer membrane of cells during the early stages of apoptosis (Emoto *et al.*, 1997). However, due to the spatial resolution of the aggregoid cross-section image, the presence of the PE species on the outer membranes of the cells cannot be determined. The presence of the PE species could therefore be due to the normal abundance within tissues. By observing the histology stains, a lack of apoptotic bodies were identified across the treated aggregoid samples, even if some DNA condensing was present (Figure 5.9a). As H&E stained images provide information on the tissue morphology, it is possible early apoptotic changes were detected from the metabolite data. Due to the overall limited response and the variability between samples however, the MG63 aggregoid response to anti-DR5 cannot be determined. Thus, in order to establish the effect of anti-DR5 on the MG63 model further analysis is necessary.

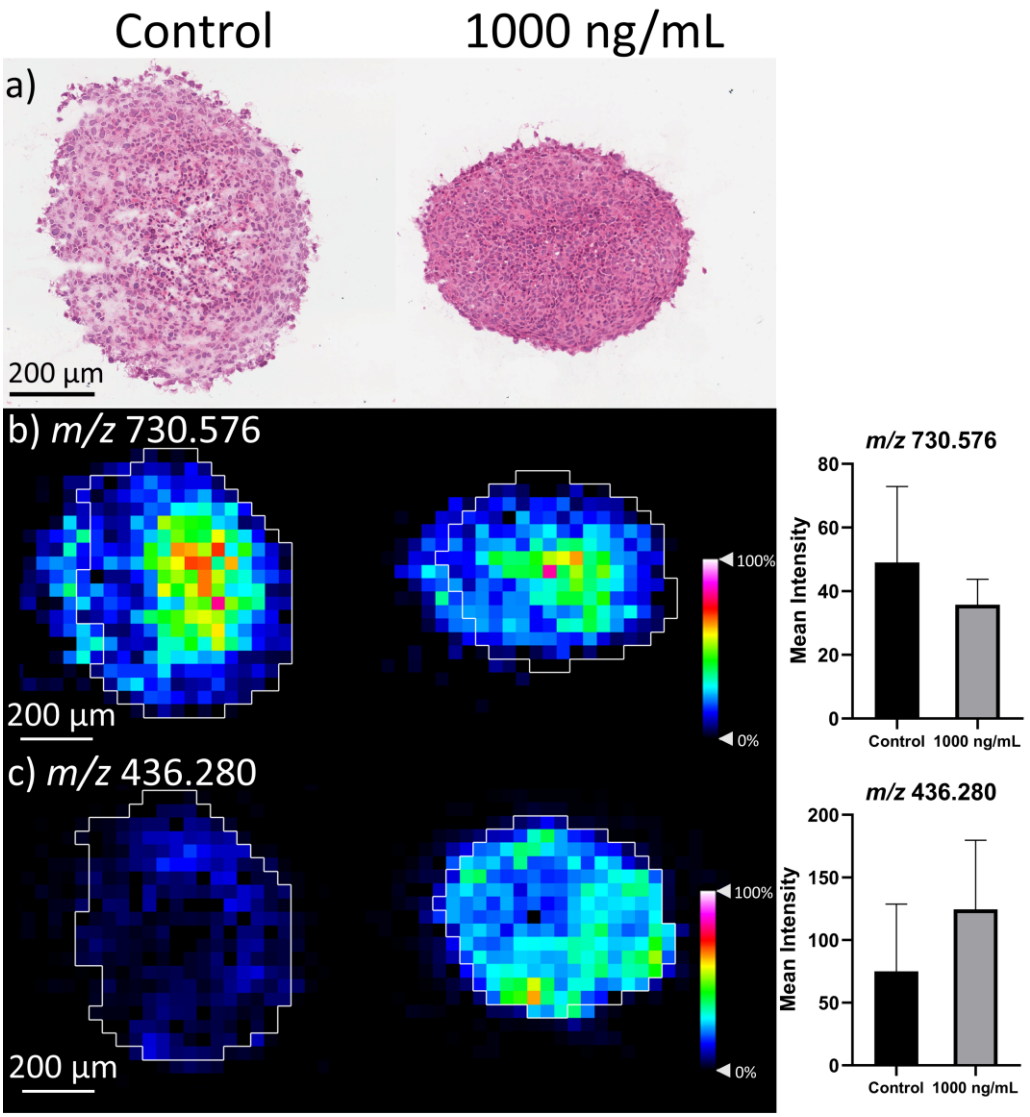

Figure 5.9 MG63 anti-DR5 treated aggregoid images identified from multivariate analysis. a) H&E images of MG63 aggregoids control and 1000 ng/mL TRAIL treated. Scale bar 200 µm. Ion density maps of metabolites outlining the outer (white) and core (red) regions of the aggregoid sections. Mean intensity plotted on bar graph against the control and 1000 ng/mL treated samples (n=3). Scale bar 200 µm. Peaks identified b) *m/z* 730.576, PC O-33:1; c) *m/z* 436.280, PE P-16:0.

5.4.1.2.3 SAOS-2 in response to TRAIL treatment

Both the PCA and PLS-DA of the SAOS-2 samples treated with TRAIL showed little variance between the control and the treated groups (Figure 5.10 and Figure 5.11). This is most likely due to the limited sensitivity of SAOS-2 to TRAIL-based therapies as demonstrated from the 2D experiment results. However, the samples of each group were relatively distributed throughout the scores plots and the imaging data observed variability between samples for specific *m/z* values. It was considered that potential sample outliers influenced the multivariate analysis as slight separation was observed between the control and 200 ng/mL treated samples in the PLS-DA scores plot (Figure 5.11). Nonetheless, by comparing ROC analysis some discriminatory *m/z* values were identified (Table 5.1), which suggested the presence of metabolic activity in response to treatment.

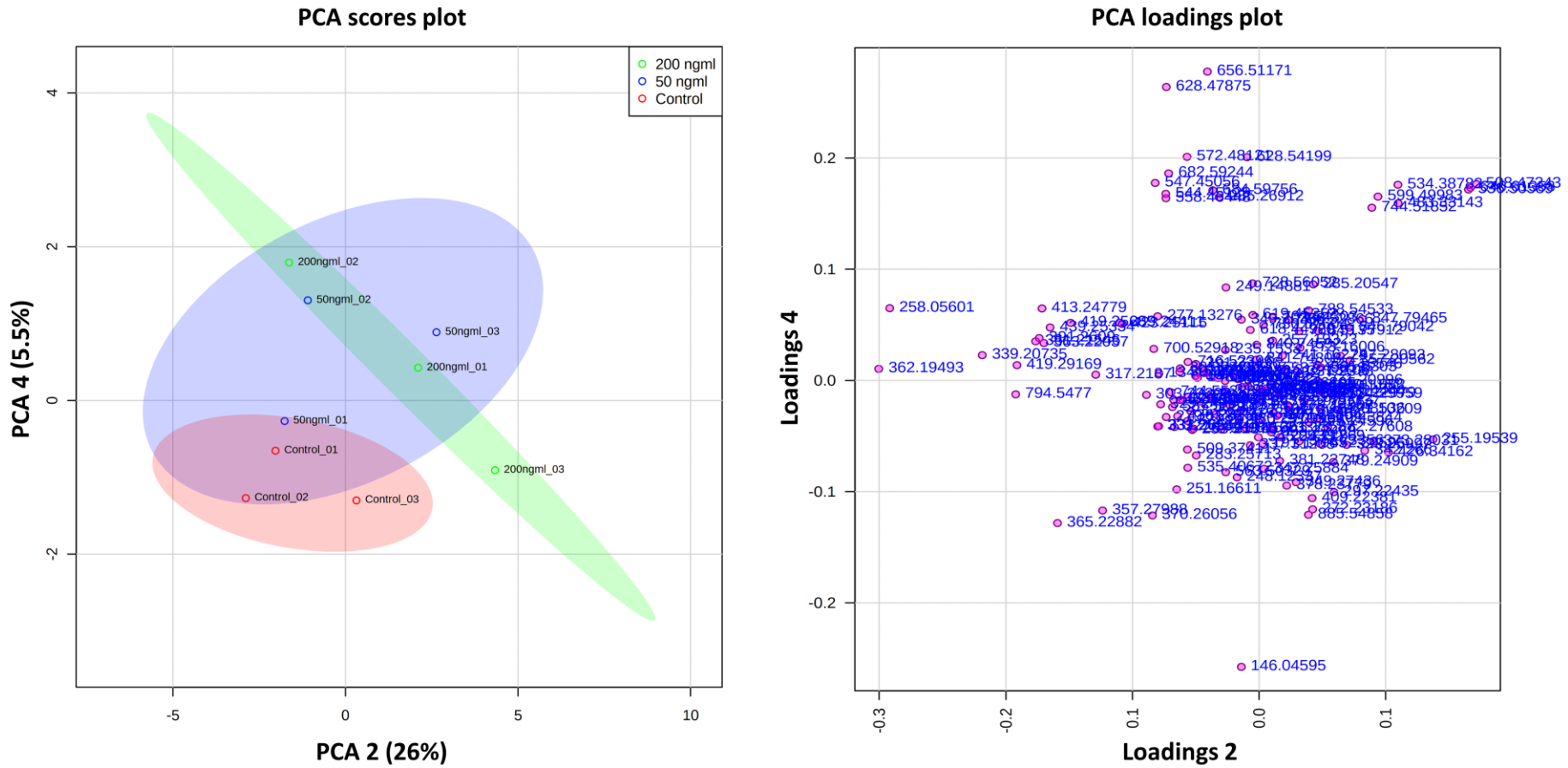

Figure 5.10 PCA scores and loadings plot of control and TRAIL treated SAOS-2 aggregoids. Principal components, PC 2 (26%) and PC 4 (5.5%) showed the most separation between samples. The discriminatory *m/z* values of interest were distributed separately from the cluster of peaks. Samples were grouped with 95% confidence, control (red), 50 ng/mL TRAIL (blue) and 200 ng/mL TRAIL (green).

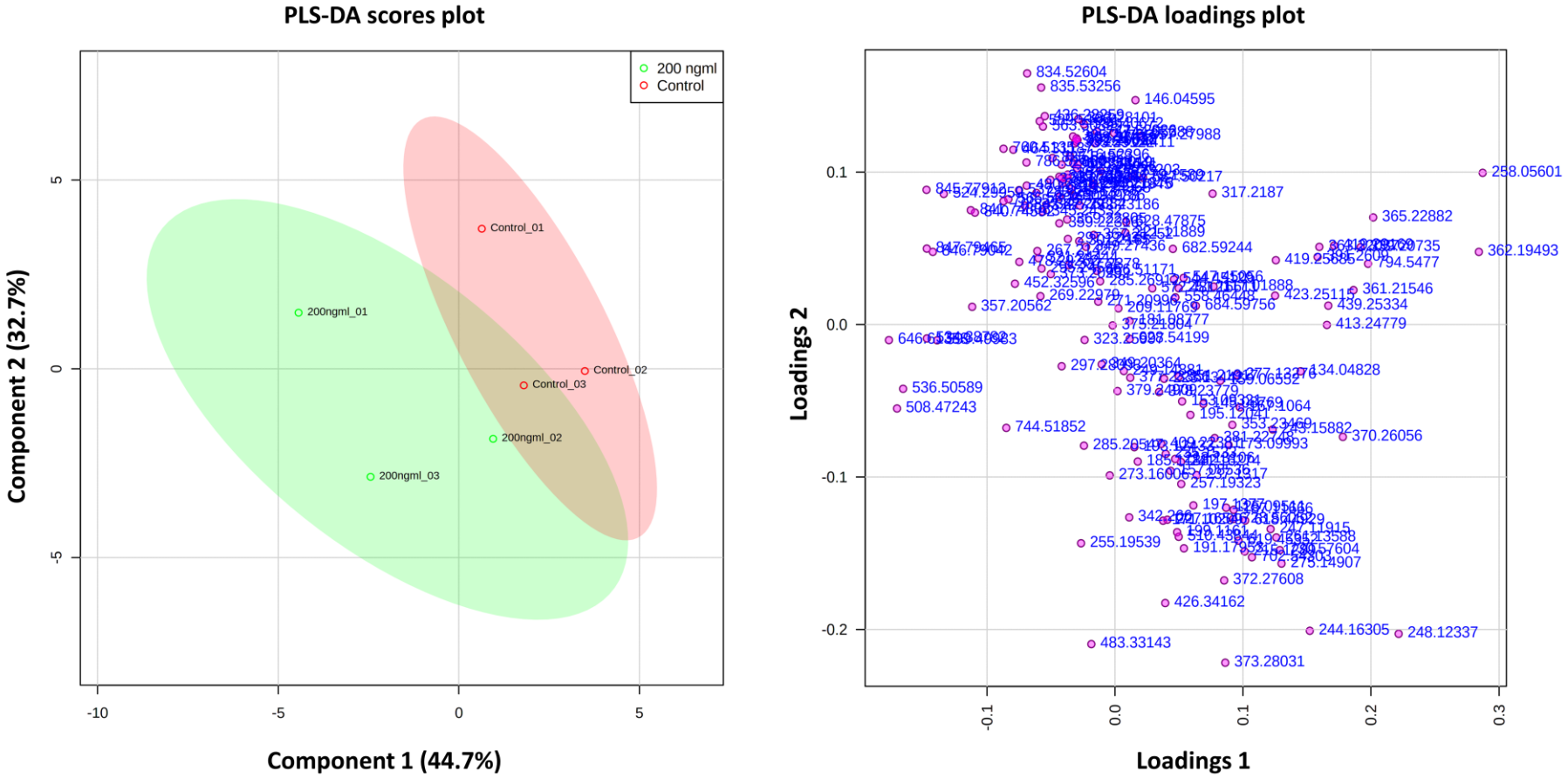

Figure 5.11 PLS-DA scores and loadings plot show some variance between control and 200 ng/mL TRAIL treated SAOS-2 aggregoids. Component 1 (44.7%) and component 2 (32.7%) showed the best separation between samples. The discriminatory *m/z* values of interest were distributed separately from the cluster of peaks. Samples were grouped with 95% confidence, control (red) and 200 ng/mL TRAIL (green).

Glutamate (*m/z* 146.046) was detected at lower levels within the SAOS-2 200 ng/mL treated samples (AUC = 0.652) (Figure 5.12b). As previously discussed (Chapter 3.4.1), cancer cells are relatively dependent on glutamate for tumour metabolism and proliferation. Glutamate is converted from glutamine within the mitochondria, which is either fed into the TCA cycle for proliferation (Martínez-Reyes & Chandel, 2020) or used as an intermediate to produce GSH for ROS regulation (Sappington *et al.*, 2016). As the images showed no differences in the GSH levels across samples (data not shown), it suggests that the reduced glutamate expression within the treated group could be due to a decrease in the rate of proliferation. The downstream effects of apoptotic signalling that induces MOMP and cell death would in theory have less need for glutamate.

Elevated levels of ceramide species at *m/z* 508.474 (Cer 32:1;O2) and *m/z* 536.506 (Cer 34:1;O2) were detected in the treated samples (AUC = 0.314; AUC = 0.310, respectively) (Figure 5.12c, d). As discussed previously, ceramides are well known secondary messengers that activate the apoptotic cascade, particularly stimulated through environmental stresses such as hypoxia (Haimovitz-Friedman *et al.*, 1997; Mullen & Obeid, 2012). From Chapter 4.4.1.2, high levels of ceramide species were detected within the SAOS-2 aggregoids, which correlated to the large hypoxia region within the models and also potentially detected metabolic activity associated with bone mineralisation in the OS clinical tissues. Therefore, it is interesting that the treated samples have a higher expression of the ceramide species compared to the control. Nevertheless, an accumulation of ceramides has also been linked to TNF-α induced apoptosis and is thought to assist cell death through the inhibition of the PI3K/Akt/mTOR pathway (Nam, Amoscato, & Lee, 2002; Gupta & Gollapudi, 2006). From the histology images (Figure 5.12a), all samples showed large regions of prevalent apoptotic cells in the tissue sections as was commonly observed within all SAOS-2 samples throughout the experimental work in thesis, previously explained in section 4.4.1.1. Therefore, it was challenging to determine the presence of an apoptotic response solely in relation to TRAIL treatment from the histology images. In order to understand the metabolite data, further experimental analysis with additional biological replicates would be required to improve the DESI data. In addition, alternative staining techniques could target the extrinsic apoptotic

pathway in an attempt to differentiate apoptotic bodies created from an external stimulus such as TRAIL or staining for TRAIL itself.

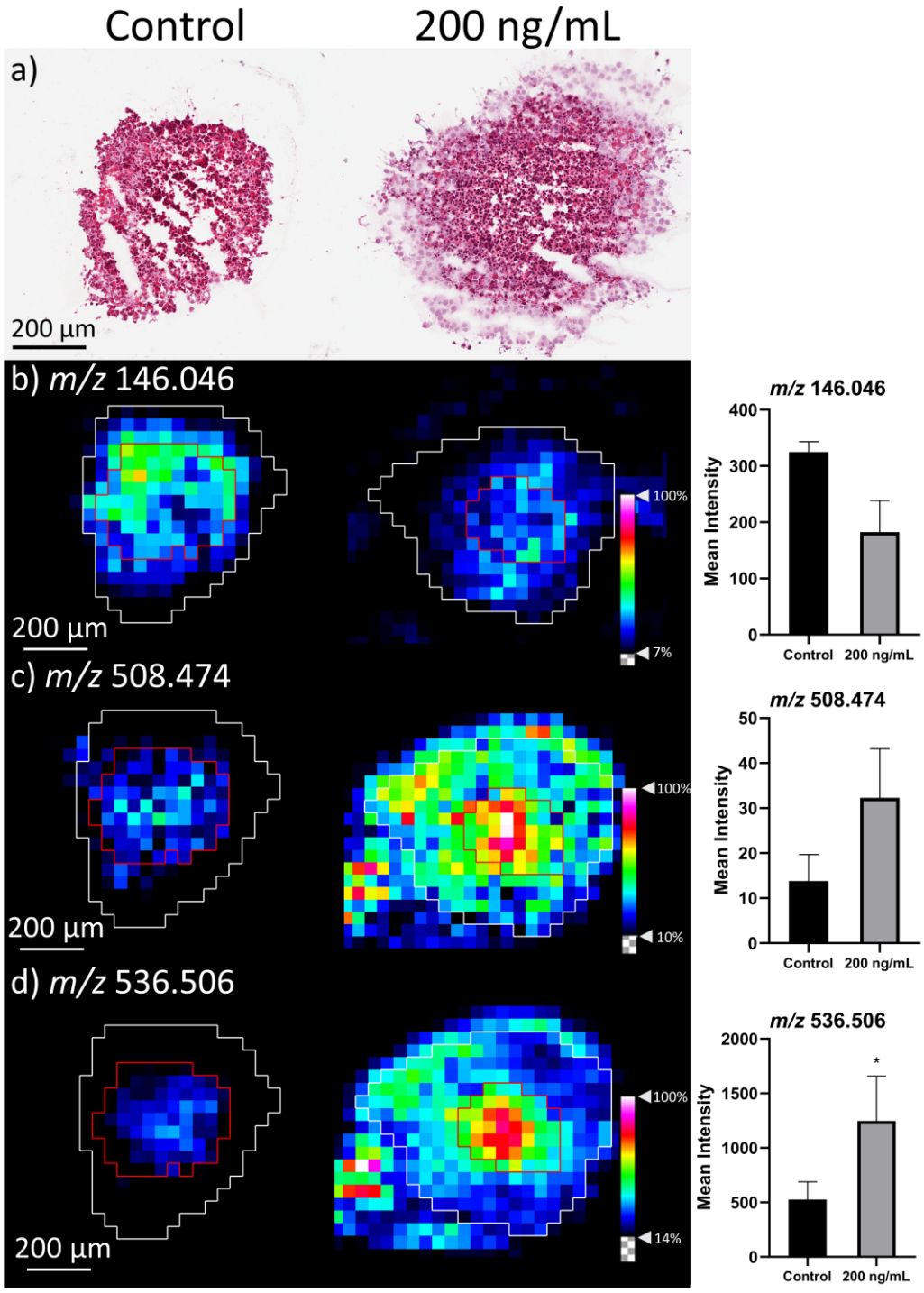

Figure 5.12 SAOS-2 TRAIL treated aggregoid images identified from multivariate analysis. a) H&E images of SAOS-2 aggregoids control and 200 ng/mL TRAIL treated. Scale bar 200 µm. Ion density maps of metabolites outlining the outer (white) and core (red) regions of the aggregoid sections. Mean intensity plotted on bar graph against the control and 200 ng/mL treated samples (n=3), unpaired t-test * $p < 0.05$. Scale bar 200 µm. Peaks identified b) *m/z* 146.046, glutamate; c) *m/z* 508.474, Cer 32:1;O2; d) *m/z* 536.506, Cer 34:1;O2.

5.4.1.2.4 SAOS-2 in response to anti-DR5 treatment

The PCA data of the anti-DR5 treated SAOS-2 samples showed little separation between the control and the treated groups (Figure 5.13). The loadings plot shows the *m/z* values closely clustered together suggesting there is little discrimination of the peaks. Separation between the groups was not expected for the anti-DR5 treated samples due to the low sensitivity of SAOS-2 cells in the 2D experiment. The PLS-DA plot, however, did display some variance between the control and the 1000 ng/mL treated samples allowing the identification of some discriminatory *m/z* values (Figure 5.14). The samples within the 95% confidence, however, were distributed widely for both groups. From the imaging data, variability between samples was observed and the ROC analysis of the peaks of interest showed little discrimination between groups. Therefore, it suggests again either a lack of metabolic shift within the SAOS-2 aggregoids in response to anti-DR5, or large variability between samples. Nevertheless, some identifications of potential metabolites of interest were determined and summarised in Table 5.1.

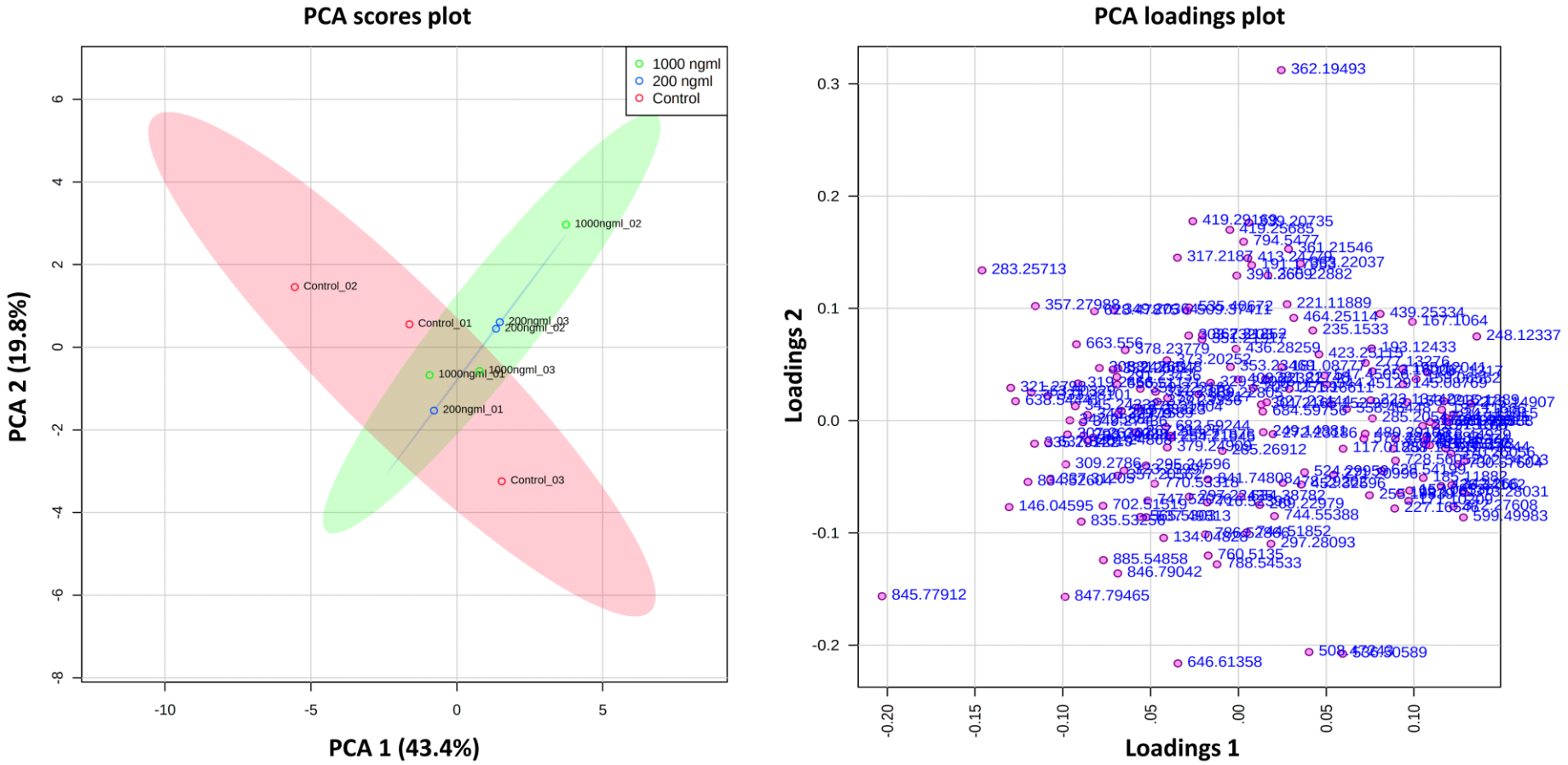

Figure 5.13 PCA scores and loadings plot of control and anti-DR5 treated SAOS-2 aggregoids. Principal components, PC 1 (43.3%) and PC 2 (19.8%) showed the best separation between samples. The discriminatory *m/z* values of interest were distributed separately from the cluster of peaks. Samples were grouped with 95% confidence, control (red), 200 ng/mL anti-DR5 (blue) and 1000 ng/mL anti-DR5 (green).

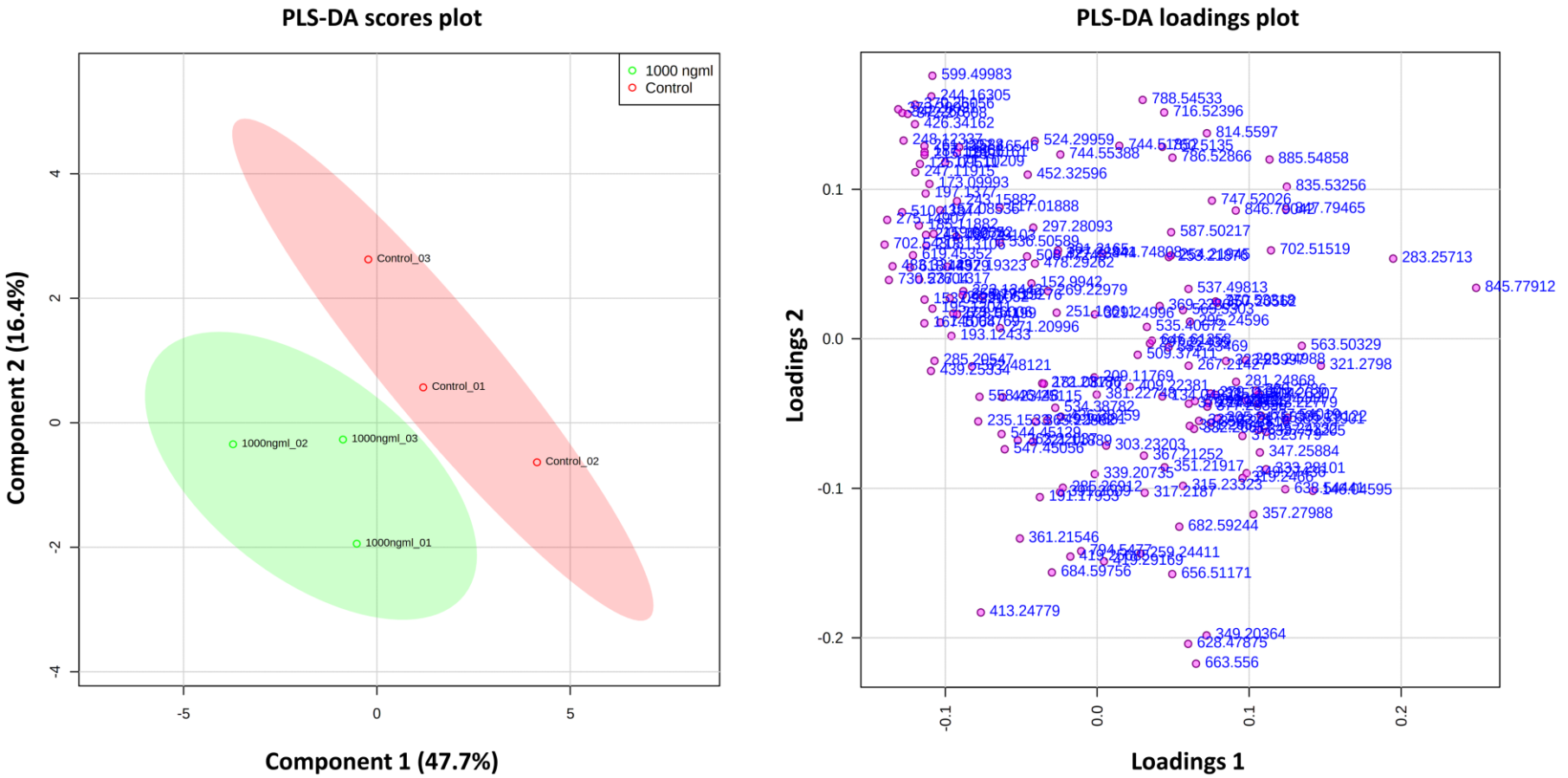

Figure 5.14 PLS-DA scores and loadings plot show some variance between control and 1000 ng/mL anti-DR5 treated SAOS-2 aggregoids. Component 1 (47.7%) and component 2 (16.4%) showed the best separation between samples. The discriminatory *m/z* values of interest were distributed separately from the cluster of peaks. Samples were grouped with 95% confidence, control (red) and 1000 ng/mL anti-DR5 (green).

Among the peaks of interest, a furan fatty acid (FA 20:3;O) and a product of the linoleic acid metabolism was identified within the periphery of the SAOS-2 aggregoid models at *m/z* 321.244 (Figure 5.15b). Although present in both groups, elevated levels were observed within the control samples (AUC = 0.604). As previously discussed (Chapter 3.4.1), fatty acids support cancer proliferation and confirmed the presence of cell growth within the outer region of the aggregoid. Linoleic acid in particular, has been associated with tumorigenesis via its metabolism to arachidonic acid, which is involved in the LOX pathway to promote angiogenesis and tumour survival (Ding *et al.*, 2000; Hanna & Hafez, 2018). Both fatty acids were detected a high intensity in the SAOS-2 aggregoid model in Chapter 4.4.1.2. From this data, slightly reduced levels of FA 18:2 (linoleic acid, *m/z* 279.232) (Figure 5.15c) and FA 20:4 (arachidonic acid, *m/z* 303.232) (data not shown) were observed within the treated samples (AUC = 0.598; AUC = 0.571, respectively), although no significant changes from the control samples were determined. A decrease in FA 20:3;O could therefore suggest the active metabolism of linoleic acid has been reduced. This implies a lower rate in proliferation within the treated samples, potentially as a response to anti-DR5.

In addition, *m/z* 835.534 was identified as PI 34:1 and detected higher within the control samples in comparison to the treated groups (AUC = 0.604) (Figure 5.15d). PI species are involved in multiple signalling pathways, including its phosphorylation to form phosphatidylinositol-(4,5)-bisphosphate (PIP2). PIP2 can be hydrolysed by phospholipase C (PLC) to form two secondary messengers, inositol triphosphate (IP3) and also DAG, which is used to activate PKC (Gamper & Shapiro, 2007). As previously mentioned, PKC signalling can promote cellular proliferation (Black & Black, 2013). However, PKC can also be responsible for promoting apoptosis through activation of an alternative isoform and thus it depends on the cellular signal (Zhu, Tsuji, & Chen, 2010). On the other hand, PIP2 can be further phosphorylated by phosphoinositide 3-kinase (PI3K) to PIP3. This process is heavily involved in tumour survival and growth as it initiates the PI3K/Akt/mTOR signalling pathway (Chalhoub & Baker, 2009). Therefore, a depletion of the PI molecule could imply the synthesis of PIP2. This can either produce a positive response to anti-DR5 through PKC-induced apoptosis or indicate resistance to treatment via growth-stimulating pathways. Unfortunately,

neither PIP2 nor PIP3 were detected within the imaging data so these findings cannot be further supported. Considering the role of the furan fatty acids, which were also depleted in the treated samples, a decrease in proliferative activity is implied. However, due to no significant changes in both metabolites and the high apoptotic activity across all samples within the histology stain analysis (Figure 5.15a), no definitive conclusions can be made.

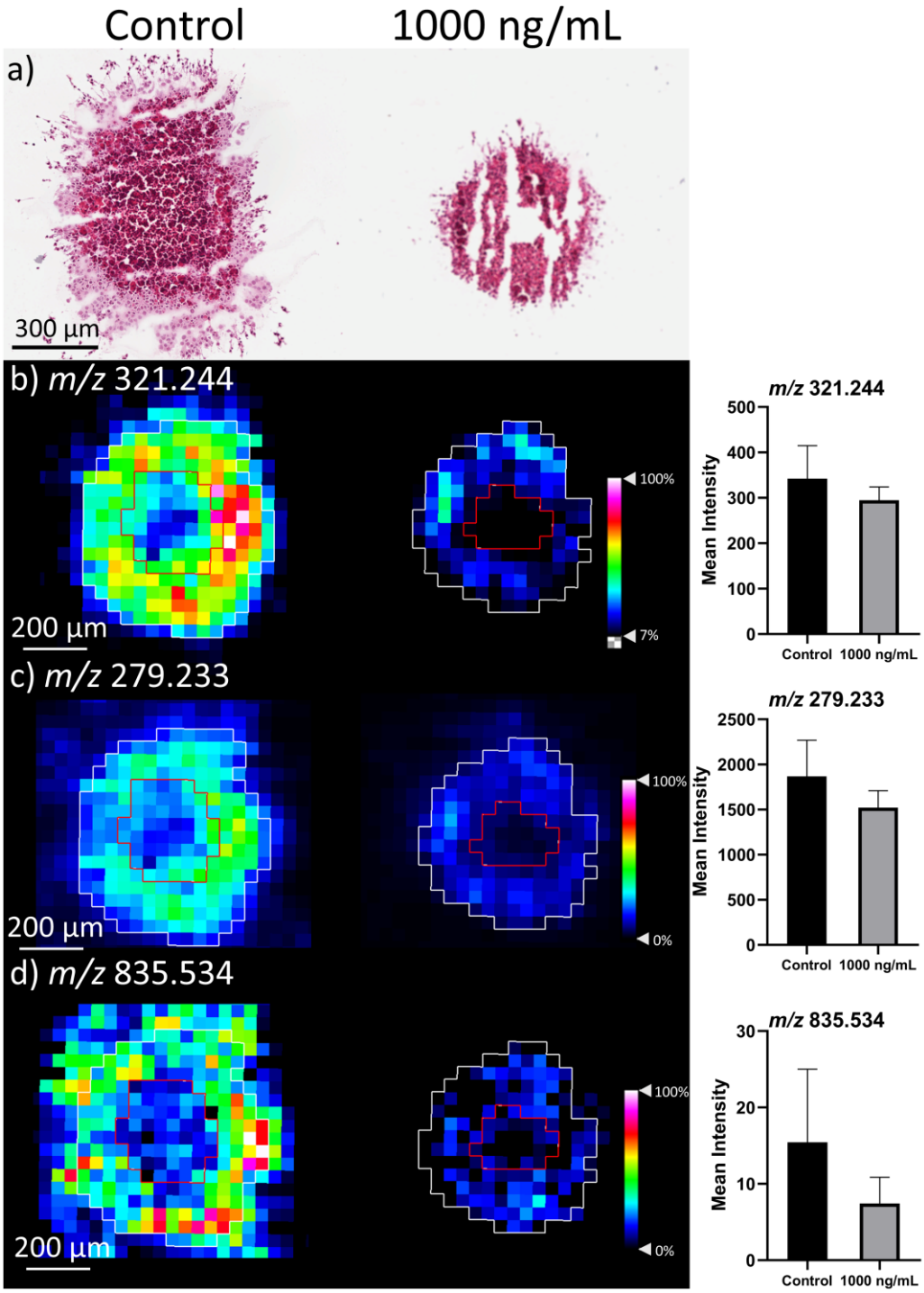

Figure 5.15 SAOS-2 anti-DR5 treated aggregoid images identified from multivariate analysis. a) H&E images of SAOS-2 aggregoids control and 1000 ng/mL TRAIL treated. Scale bar 200 µm. Ion density maps of metabolites outlining the outer (white) and core (red) regions of the aggregoid sections. Mean intensity plotted on bar graph against the control and 1000 ng/mL treated samples (n=3). Scale bar 200 µm. Peaks identified b) *m/z* 321.244, FA 20:3;O; c) *m/z* 279.233, FA 18:2; d) *m/z* 835.534, PI 34:1.

5.4.2 Lung adenocarcinoma treatment response

5.4.2.1 Cetuximab sensitivity

To determine the HCC827 response to cetuximab treatment, the growth of the aggregoid samples were analysed by measuring the diameter of each aggregoid at 0 h and 24 h. From the data, no significant changes were observed among the treatments between the two time points (Figure 5.16). The HCC827 cell line was reported to be highly sensitive to cetuximab treatment (Amann *et al.*, 2005; Mukohara *et al.*, 2005). It was suggested this was due to an amplification of the EGFR gene in the cell line, resulting in the receptor protein being highly expressed and therefore treatment with cetuximab (which targets EGFR) resulted in a considerable inhibition of cell growth (Amann *et al.*, 2005). However, the analysis of the effects of cetuximab treatment in these reports was carried out after a 72 h incubation on monolayer cells and therefore the experiment in this study is not comparable. Unfortunately, due to experimental time constraints of a 3-day laboratory rota as a result of covid-19, a 72 h incubation was unachievable in this study. Nonetheless, the metabolic profiles of the HCC827 aggregoid models treated with cetuximab after 24 h were investigated to determine if an initial treatment response could be detected.

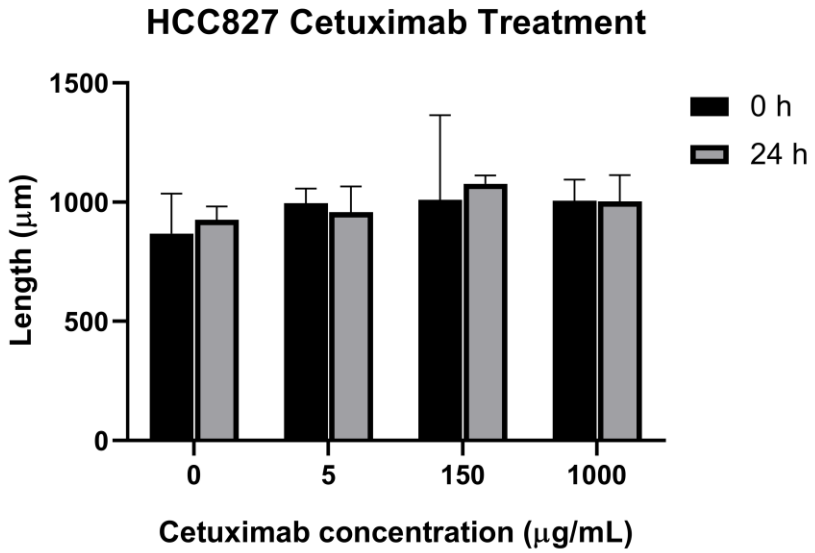

Figure 5.16 Growth of HCC827 aggregoids treated with cetuximab after 24 h. Data is mean length (n=3) of each aggregoid ± SD (n=2).

5.4.2.2 HCC827 metabolic activity in response to cetuximab

The PCA data from the HCC827 aggregoid samples treated with four concentrations of cetuximab, displayed minor separation of treatment groups (Figure 5.17). Overlay of the 5 µg/mL and 150 µg/mL treated samples was observed with 95% confidence grouping. The 1000 µg/mL samples, however, were closely clustered together suggesting a strong similarity between the aggregoid replicates. The PLS-DA scores plot of the control and the 1000 µg/mL treated samples showed clear variance between treatment groups (Figure 5.18). However, the control samples were dispersed suggesting some variance within the group. From the loadings plot, a few peaks of interest were identified from the images which are discussed and summarised in Table 5.1, however the ROC analysis showed low discrimination between groups. The low variance is likely due to the incubation period of the cetuximab treatment. With a longer treatment incubation, such as 72 h, a better metabolic response may have been detected.

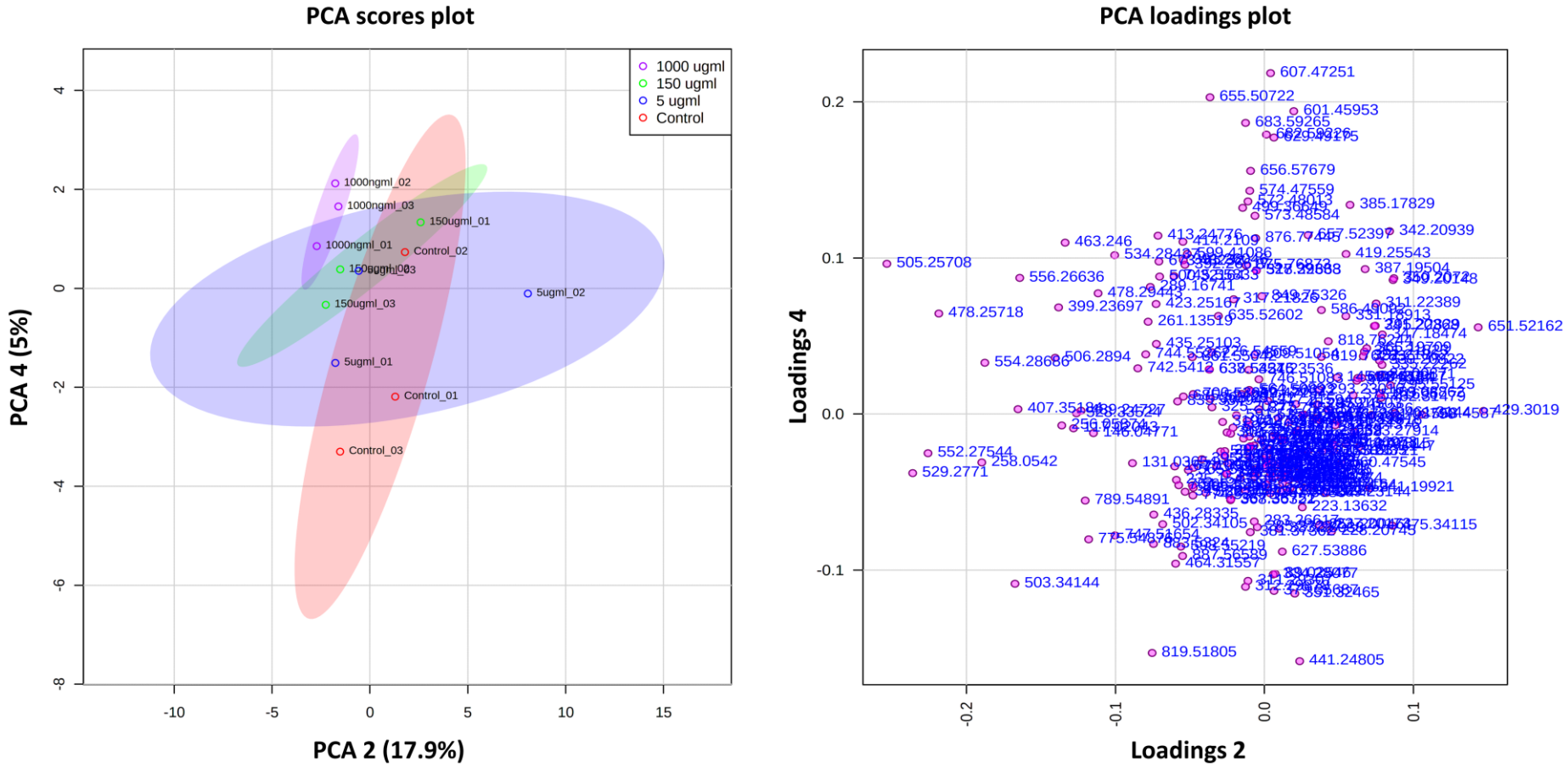

Figure 5.17 PCA scores and loadings plot of cetuximab treated HCC827 aggregoids. Principal components, PC 2 (17.9%) and PC 4 (5%) showed the best separation between samples. The discriminatory *m/z* values of interest were distributed separately from the cluster of peaks. Samples were grouped with 95% confidence, control (red), 5 µg/mL (blue), 150 µg/mL (green) and 1000 µg/mL (magenta) cetuximab.

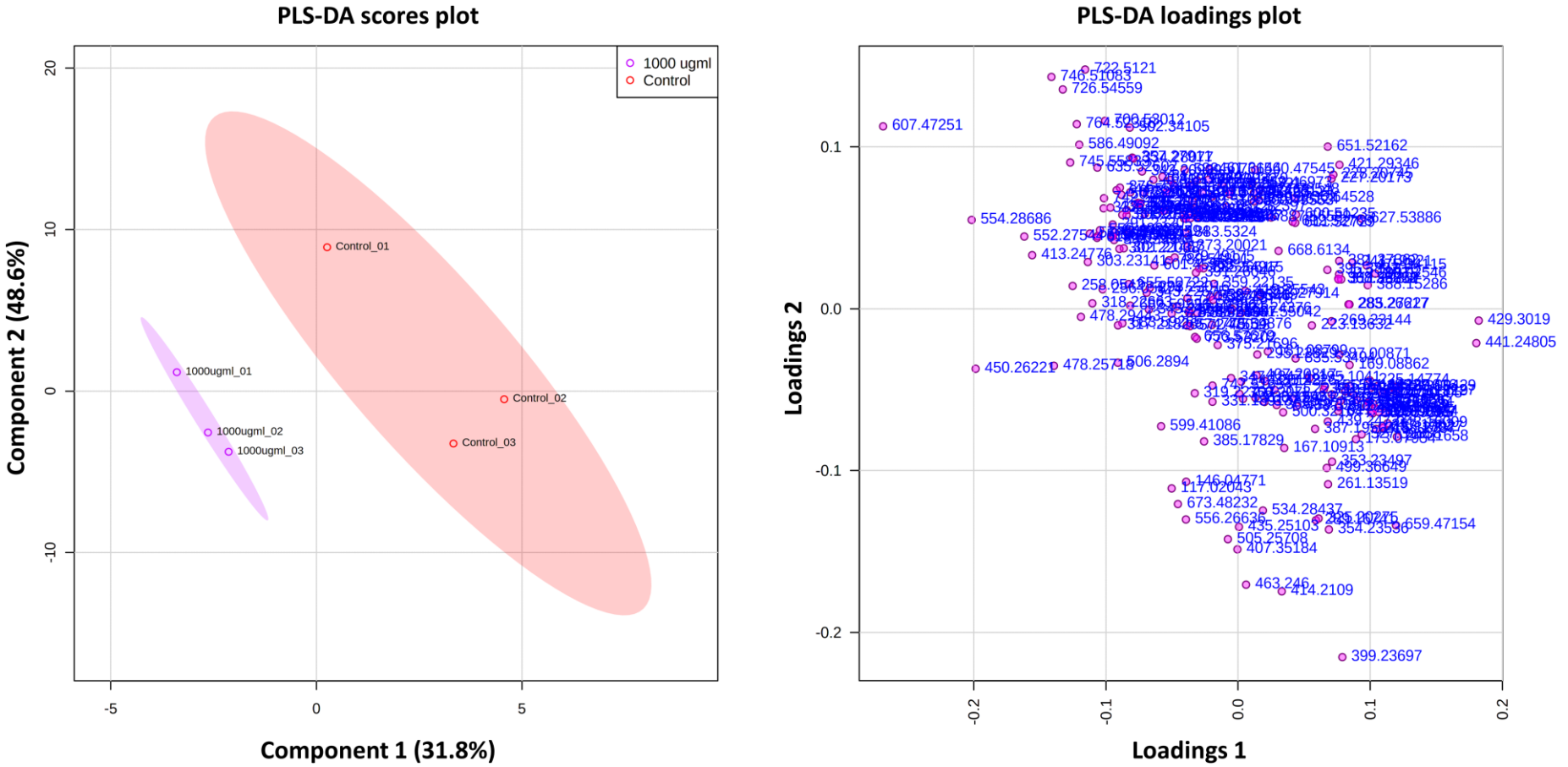

Figure 5.18 PLS-DA scores and loadings plot show variance between control and 1000 µg/mL cetuximab treated HCC827 aggregoids. Components, PC 1 (31.8%) and PC 2 (48.6%) showed the best separation between samples. The discriminatory *m/z* values of interest were distributed separately from the cluster of peaks. Samples were grouped with 95% confidence, control (red) and 1000 µg/mL (magenta) cetuximab.

Two peaks identified as lysophospholipid (LPL) species, LysoPE 18:1 at *m/z* 478.294 and LysoPC 15:0 at *m/z* 480.311, were expressed in the HCC827 cetuximab 1000 µg/mL treated samples (AUC = 0.430; AUC = 0.480) (Figure 5.19b, c). Interestingly, an upregulation of LPLs has been reported to stimulate the induction of apoptosis. It is thought that LysoPC in particular, induces apoptotic signalling through a p38-MAPK-dependent pathway, which inhibits extracellular signal-regulated kinases (ERK) in the EGFR stimulated Ras/Raf/MAPK pathway (Takahashi *et al.*, 2002). Therefore, the increase of LysoPC and potentially LysoPE could be due to a response to cetuximab treatment, inhibiting EGFR signalling. On the contrary, LPL expression has also been associated with tumour growth through stimulation of the same Ras/Raf/MAPK pathway (Kamphorst *et al.*, 2013). This would explain the localisation of the metabolites within the outer proliferative region of the HCC827 aggregoids and potentially an upregulation in LPLs is a signature of drug resistance due to a mutation in the Ras/Raf/MAPK pathway. By observing the histology images, a typical necrotic centre was determined however, no apoptotic bodies were identified within the periphery of the three treated aggregoids, similar to the control samples (Figure 5.19a). Therefore, the LPL expression is more likely associated with cellular proliferation, though as H&E staining can only determine morphology it is still a possibility that the metabolite data has detected early stage apoptotic signalling. With that in mind, if LPLs induced apoptosis their detection within the clear necrotic/apoptotic core would have also been expected.

In contrast, a sterol lipid species ST 27:3;O4 at *m/z* 429.302 was detected higher in the controls samples compared to the treated (AUC = 0.619) (Figure 5.19d). Cancer cells depend highly on sterols for active signalling and growth via the biosynthesis of cholesterol. High activity of oncogenic receptors, such as the EGFR, have been shown to accelerate sterol uptake as they are heavily involved in the EGFR pathway (Gabitova, Gorin, & Astsaturov, 2014; Gabitova *et al.*, 2015). More specifically, a high sterol activity has been reported in lung cancer cell lines (Howell *et al.*, 2020). It has been further shown that a depletion in specific sterols sensitised highly resistance cancer cells to the EGFR inhibitor, cetuximab (Sukhanova *et al.*, 2013). With a decrease of the sterol molecule in the treated samples, it suggests an associated signalling with EGFR pathway inhibition through the binding of cetuximab. This would coincide with the

increased LPL expression within the treated samples as a positive response to treatment. However, due to the overall limited response and slight variation between samples it is absolute that further investigations of the HCC827 response to cetuximab treatment are conducted. Nonetheless, identifying changes in specific metabolites in response to cetuximab treatment enabled the discovery of potential biological markers that could be used in future for a targeted approach either by further MSI experiments or the addition of higher accuracy techniques including LC-MS/MS.

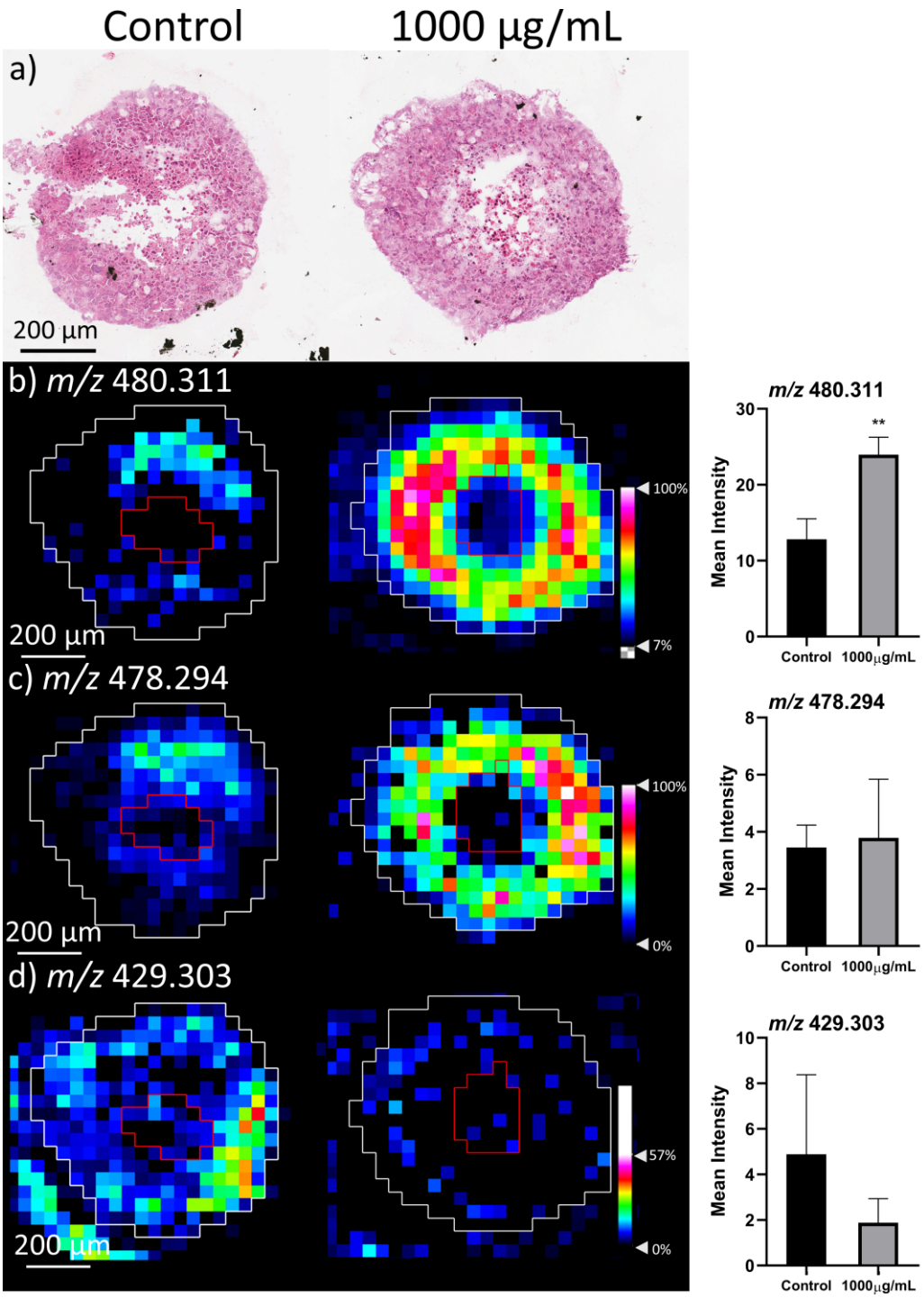

Figure 5.19 Cetuximab treated HCC827 aggregoid images identified from multivariate analysis. a) H&E images of HCC827 aggregoids control and 1000 µg/mL TRAIL treated. Scale bar 200 µm. Ion density maps of metabolites outlining the outer (white) and core (red) regions of the aggregoid sections. Mean intensity plotted on bar graph against the control and 1000 µg/mL treated samples (n=3), unpaired t-test ** $p < 0.01$. Scale bar 200 µm. Peaks identified a) *m/z* 478.294, LysoPE 18:1; b) *m/z* 480.311, LysoPC 15:0; c) *m/z* 429.303, ST 27:3;O4.

5.4.3 Summary of metabolites detected in response to biological treatment

Aggregoid	Treatment	Metabolite	*m/z* (measured)	Accuracy (ppm error)	Up/down regulated
MG63	TRAIL	Glycerol 1-(9Z-octadecenoate) 2-tetradecanoate 3-phosphate	645.452	3.7	↓ *
		PC O-33:1	730.576	0.2	↑ *
		PA 34:1	673.480	-1.8	↓ *
MG63	Anti-DR5	PC O-33:1	730.576	1.1	↓
		PE P-16:0	436.280	-6.9	↑
SAOS-2	TRAIL	Glutamate	146.046	0.5	↓
		Cer 32:1;O2	508.474	1.7	↑
		Cer 34:1;O2	536.506	2.0	↑ *
SAOS-2	Anti-DR5	FA 20:3;O	321.244	2.9	↓
		FA 18:2	279.233	-5.9	↓
		FA 20:4	303.232	-3.1	↓
		PI 34:1	835.534	-0.6	↓
HCC827	Cetuximab	LPE 18:1	478.294	1.1	↑ **
		LPC 15:0	480.311	3.3	↑
		ST 27:3;O4	429.302	2.1	↓

Table 5.1 A summary of metabolite changes detected in aggregoid models in response to biologic treatments. Mass accuracy < 7 ppm. Data is mean (n=3), unpaired t-test * $p < 0.05$, ** $p < 0.01$.

5.4.4 Possible biologic resistance in 3D cultures

Overall, the data suggests a limited metabolic response was detected within the three aggregoid models of cancer treated with biologics. For the MG63 aggregoid cultures, the response to TRAIL in comparison to anti-DR5 was similar to the data from the 2D experiment. A difference between TRAIL and the DR5 specific mAb could be due to the targeting of both death receptors (DR4 and DR5), which is more likely to stimulate an apoptotic response opposed to targeting DR5 only. The lack of metabolic response in the SAOS-2 aggregoid cultures on the other hand, was expected due to the limited sensitivity observed in the 2D experimental

data. A reason for the possible TRAIL-based therapy resistance in SAOS-2 has been reportedly due to the lack of TRAIL receptors on the cell surface of SAOS-2 cells (Locklin *et al.*, 2007), however Phillips *et al.*, (2019) showed that they do respond to TRAIL and anti-DR5 if treated with a TRAIL-sensitiser. Differences of TRAIL response between 2D to 3D cell cultures have previously been observed in breast cancer cells (Chandrasekaran *et al.*, 2014), in addition to prostate cancer cell lines, whereby a decrease in the expression of DR4 and DR5 was observed in spheroids (Grayson *et al.*, 2021). In the case of the HCC827 aggregoids treated with cetuximab, a limited response could simply be due to the incubation time of treatment. However, with the knowledge of cetuximab resistance in lung cancers, the efficacy of the antagonistic mAb could be affected by mutations downstream of the EGFR signalling pathways, such as the overexpression of Ras (Scaltriti & Baselga, 2006).

A major explanation to drug resistance is the presence of cancer stem cells (CSCs) within 3D cultures. Numerous studies have identified CSCs influencing key signalling pathways via self-renewal, quiescence, EMT and genetic modifications contributing to resistance against therapeutics (Prieto-Villa *et al.,* 2017; Phi *et al*., 2018). It is therefore highly likely that the presence of CSCs are playing an important role in the lack of metabolic response to biologic treatment of the aggregoid models. More specifically, evidence of resistance to a specific programmed cell death, known as anoikis has been established when monolayer cells are grown in 3D cultures. Anoikis is the induction of apoptosis in cells through both extrinsic and intrinsic pathways upon loss of attachment to the ECM (Frisch & Francis, 1994). The development of resistance to anoikis is essential for cancer cells to metastasise as they purposely detach from their ECM (Simpson, Anyiwe, & Schimmer, 2008). Such resistance has been directly linked to the expression of the phosphorylated tyrosine kinase Src (pSrc). The expression of pSrc correlated with E-cadherin expression in anoikis resistant spheroid cultures of lung adenocarcinoma, including the HCC827 cell line, and shown in intralymphatic lung adenocarcinoma patient tissues (Sakuma *et al.*, 2010). pSrc activity has also been associated with mediating the PI3K/Akt/mTOR pathway to promote anoikis resistance in SAOS-2 cells (Díaz-Montero, Wygant, & McIntyre, 2006). It is thought that such resistance to anoikis cell death can have a subsequent resistance to all apoptotic stimuli due to the alteration of the

apoptotic pathways, and thus leads to a resistance to apoptotic-inducing therapeutics (Kim *et al.*, 2012). Through the method of culturing the aggregoid models, cells are initially grown into spheroids from a single cell with no endogenous ECM, only alginate as a scaffold which is biologically inert. It is therefore possible this method has selected pSrc positive cells that have survived anoikis to form the aggregoid models and are thus consequently resistant to multiple forms of cell death, such as TRAIL signalling. A suitable method to test and determine anoikis resistance would be to treat the aggregoid models with Src inhibitors. Previous experiments have demonstrated success of reprogramming apoptosis with Src inhibitors, such as dasatinib (Johnson *et al.*, 2005; Araujo & Logothetis, 2010), and have shown dual inhibition of cancer growth in combination therapy, such as with cetuximab (Parseghian *et al.*, 2017).

Alternatively, a lack of metabolic response to treatment could also be due to the inefficiency of drug delivery within the aggregoid model. If a drug cannot penetrate through the tissue to its target or the amount of drug present is insufficient to cause a cellular effect, the efficacy of the drug is diminished. Therefore, a direct assessment of the biologic distribution within the aggregoid models could complement the metabolomics data to give a better understanding of the efficacy of the biopharmaceuticals. The development of a robust MSI strategy to detect cetuximab within the HCC827 aggregoid model is discussed in Chapter 6.

5.5 Concluding remarks

In this chapter, an unsupervised MVA in combination with DESI-MSI approach was employed to detect changes in the metabolome of the aggregoid models in response to biopharmaceutical treatment. The data from the two OS aggregoid models, suggested possible detection of metabolite changes in response to TRAIL-based therapy, specifically for the MG63 aggregoids treated with TRAIL. This was the same from the data of the cetuximab treated HCC827 lung adenocarcinoma aggregoids, where some changes in metabolites suggested a lower rate of proliferation through inhibition of EGFR signalling. Although, the overall limited response across the aggregoid models suggested possible drug-resistance. Therefore, further analysis is necessary to validate these findings and

determine if there is such resistance, whether it is due to a mechanistic or delivery issue.

On a technical note, no definitive conclusions on the annotations of each metabolite or the biological pathways discussed can be made at this point of the study. To support the findings, MS/MS profiling of each peak would be required to confirm the identities. Furthermore, employing LC-MS/MS analysis with additional biological replicates will allow for better sensitivity and accuracy of results to further support the validation of this method. It is clear that there is variation between aggregoid samples of the same model, therefore analysis of additional replicates would also be heavily suggested to decrease group variability and improve discrimination of metabolites. Nevertheless, significant changes in metabolite activity within treated aggregoids were detected and potential biomarkers have been identified, which could assist future aggregoid treatment research in a more targeted approach. Overall, the method to determine biologic response still requires optimisation, however, the preliminary work in this study demonstrates a potential strategy for analysing the efficacy of biologic treatment by the metabolome response in 3D cell culture models.

CHAPTER 6. OPTIMISATION OF STRATEGIES FOR MSI DETECTION OF A BIOPHARMACEUTICAL IN AN AGGREGATED 3D CELL CULTURE MODEL

6.1 Introduction

During the development of a pharmaceutical, it is necessary to study the delivery of the drug to understand its efficacy and toxicity. The quantitative measurement of a drug within tissue can provide essential information of its concentration and facilitate studies of its metabolism and the biological outcome. The direct assessment of drug distribution within tissues is technically challenging. Most methods have relied solely on the quantification of therapeutics in plasma or tissue homogenates by LC-MS/MS (Rönquist-Nii & Edlund, 2005; Punt *et al.*, 2019). As previously discussed, however, drug plasma concentrations do not provide an accurate representation of therapeutic levels in specific organs, and the homogenisation of tissues loses all spatial information.

Alternatively, the development of imaging techniques has promoted effective methods in research to which a drug's penetration and distribution can be assessed *in vivo*. Traditionally, the visualisation of compounds in tissues has been achieved using imaging techniques such as fluorescence microscopy (Hermsmeier *et al.*, 2018), PET (Piel *et al.*, 2014) and qWBA (Solon & Kraus, 2001). Such methodologies, however, are time consuming and costly. In addition, these techniques are targeted approaches which require the addition of fluorescent tags or radiolabels. These changes to the starting molecule can have a possible effect on therapeutic pathways or alter biological compositions, which can misrepresent the true distribution behaviour of the drug.

On the other hand, MSI techniques have the capabilities of detecting the localisation of therapeutics within a biological sample, without the use of labels. For that reason, MSI has emerged within pharmaceutical research and development as a valuable technique for drug efficacy and toxicity studies. Although many MSI techniques including DESI and LESA have demonstrated high capacity for drug distributional studies (Swales *et al.*, 2016; Dexter *et al.*, 2019), MALDI is the most predominantly used platform. The continuous advancements in spatial resolution, speed of acquisition and high-performance mass analysers with MALDI-MSI further the capabilities in pharmaceutical research (Swales *et al.*, 2019). The MALDI-MSI application has also had a significant impact on 3D cell culture models for assessing drug efficacy with great molecular detail, as previously discussed (Chapter 1.4).

Small molecule drugs have dominated the literature for MALDI-MSI applications in early stage drug development (Nilsson *et al.*, 2015; Aikawa *et al.*, 2016; Taylor, Dexter, & Bunch, 2018; Russo *et al.*, 2018; Handler *et al.*, 2021). Small molecule drugs are highly effective compounds as a treatment and have the ability to be administered by a variety of routes. Small molecules are also more readily ionisable compounds which are highly detectable during MALDI analysis. Although, current pharmaceutical applications are edging towards DESI due to the greater coverage in the detection of metabolites than MALDI, which is limited by matrix choice. In addition, DESI ionisation techniques are often coupled to mass analysers, such as orbitraps , for increased sensitivity and mass accuracy.

Over the recent years, biopharmaceuticals have received considerable attention, becoming one of the fastest growing sectors within the pharmaceutical industry. The rapid growth of biopharmaceuticals has thus challenged MSI to progress their detection with the same momentum. Due to its range of mass detection and resolution, MALDI is the superior ionisation technique for the detection of proteins (Hermann *et al.*, 2020). However, the detection of complex biologics ~ 40–150 kDa, presents issues associated with low ionisation efficiencies leading to poor sensitivity.

Attempts to detect biopharmaceuticals by MALDI-MSI have been previously reported, although the literature is limited. Ait-Belkacem *et al.*, (2014) exploited an in-source decay (ISD) top-down fragmentation approach to detect the monoclonal therapeutics, bevacizumab and palivizumab within the brain. The ISD technique has no limitation on mass range due to its ability to rapidly fragment proteins, therefore proved beneficial for biologic detection. However, limitations of in-source fragmentation include the lack of precursor ion selection and the low ion yield of fragments, which consequently creates issues in the accurate detection of biologic-specific peaks. The study, however, reported the use of a second fragmentation known as T3-sequencing, similar to MS/MS analysis, to assist the identification of specific peaks by determining the amino acid sequence.

Alternatively, Liu *et al.*, (2018) described a novel approach of an on-tissue reduction and alkylation for the detection of cetuximab in tumour spheroids and organoids. Reduction and alkylation are used to unfold structures by breaking and stabilising the disulphide bonds of proteins, this technique is typically used

prior to an in-solution or gel protein digestion. The use as an on-tissue approach in imaging studies has a limited amount of literature reporting this technique (Green-Mitchell *et al.*, 2011). In the biologic study, the method was used to separate the heavy and light chains of the antibody for the detection of cetuximab at a smaller mass range (from 150 kDa to ~ 20–50 kDa) (Liu *et al.*, 2018). Limitations of this practice can however result in low fragmentation efficiencies, which can impact the ability to accurately isolate the ion of interest from considerable signal of endogenous species. Initial profiling of the reduced mAb prior to imaging is also necessary to correctly identify the biologic.

A significant lack of publications in biopharmaceutical detection by MALDI imaging demonstrates the need for further method development. An alternative approach that has had extensive success in the detection of endogenous proteins by MALDI-MSI is an on-tissue bottom-up proteomics strategy (Lemaire *et al.*, 2007; Djidja *et al.*, 2009; Stauber *et al.*, 2010; Cole *et al.*, 2011). Bottom-up proteomics is a technique whereby proteins are digested *in situ* using specific enzymes, mainly trypsin, into smaller peptide fragments. These fragments are of a lower molecular weight and are more readily ionisable, allowing for the identification of proteins within a tissue.

A bottom-up proteomics approach has been previously demonstrated to be an accurate method to detect biologics in complex matrices such as plasma and tissue by direct LC-MS/MS analysis (Osaki, Tabata, & Oe, 2017; Shibata *et al.*, 2017). The LC-MS/MS method allowed for the identification of peptides derived from the variable chains of a mAb. The detection of such peptides also identified complementarity-determining regions (CDRs); these are hypervariable regions that are unique to the immunoglobulin gene sequence. The CDRs can be used as surrogate peptides to validate the identification of the therapeutic. Considering that the detection of a biologic was achievable following this proteomics method, an on-tissue imaging approach seems possible.

Currently, there is not a gold-standard on-tissue digestion protocol that has been established. This is in part due to the difficultly in developing one method that fits all sample types (Martin-Lorenzo *et al.*, 2014). Various papers have reported an “optimum methodology” for the detection of proteotypic peptides in biological tissues. An extensive review discussing existing on-tissue digestion methodology

from sample preparation and instrumentation to the identification and validation approaches has been published (Cillero-Pastor & Heeren, 2014).

Sample preparation is an important parameter in the proteomics workflow that not only influences the peptide yield, but can have a significant effect on the accuracy, sensitivity and reproducibility of the imaging data (Diehl *et al.*, 2015; Hermann *et al.*, 2020). In peptide MALDI-MSI experiments, sample preparation techniques include washing conditions, enzymatic digestion and matrix coating. A plethora of peptide imaging studies have followed a strategic approach to assess and optimise sample preparation parameters specific for their sample of interest (Lemaire *et al.*, 2006; Seeley *et al.*, 2008; Diehl *et al.*, 2015; Patel *et al.*, 2015; Hermann *et al.*, 2020). Yet, the outcome of each report differs and cannot be comparable due to a multitude of variables, including the analysis of different samples. It is therefore a necessary requirement to optimise various techniques for specific sample types and analytes of interest, such as in the case of detecting of a biopharmaceutical within the aggregoid model.

Alternatively, considering the principles of the IMC technique and following the successful application to analyse the aggregoid models (Chapter 3.4.2 and Chapter 4.4.2), a similar experimental approach could be designed for the detection of a biopharmaceutical; however, this is not a label-free method. The concept of IMC is to detect proteins and protein modifications by target specific antibodies that are tagged with a rare species of lanthanide metals exogenous to biological tissue. With that in mind, mAbs target a specific protein of interest. If the antibody is tagged prior to treatment, the distribution of the biologic could in theory be determined by imaging analysis. Van Acker *et al.*, (2019) reported a similar approach in which the group tagged cetuximab with a lanthanide (^{165}Ho) to detect the EGFR in 2D breast cancer cells by LA-ICP-MSI.

As previously reported (Chapter 3.4.3 and 4.4.3) LA-ICP-MSI is sensitive technique for the detection of endogenous metal isotopes at high spatial resolution within the aggregoid model (Flint *et al.*, 2020). Using LA-ICP-MSI, it would be possible to detect a metal-conjugated biologic simultaneously with endogenous elements to understand the distribution of the drug and the metabolic responses, without the use of additional labels for the metal isotopes.

6.2 Aims of chapter

In the following chapter, the aim was to employ a systematic approach to develop multimodal MSI strategies in which to detect the monoclonal antibody, cetuximab within the HCC827 aggregoid model.

Firstly, a bottom-up MALDI-MSI proteomics method was developed. Sample preparation parameters were optimised by the detection of endogenous proteins within the aggregoid model. The parameters evaluated included: trypsin solvent concentration and solvent composition, tissue washing methods, incubation conditions, and trypsin deposition. The optimised procedure was then employed to detect cetuximab based on its proteotypic peptides within the aggregoid model.

A second method of cetuximab detection by LA-ICP-MSI was also developed. Here, the approach used was to tag cetuximab with a rare lanthanide metal exogenous to the aggregoid tissue. The validation of tagging cetuximab was evaluated through LA-ICP-MS profiling. Following this, treatment of the aggregoid model with the tagged drug at therapeutic levels was evaluated by imaging analysis.

6.3 Materials and methods

6.3.1 Materials

α-CHCA, DHB, alginic acid, ammonium bicarbonate (NH_5CO_2), aniline, phosphorus red, potassium sulphate (K_2SO_4), and TFA were purchased from Sigma-Aldrich (Gillingham, UK). ACN, acetone (AcOH), Bond breaker neutral pH TCEP, chloroform ($CHCl_3$), EtOH, MeOH and isopropanol (IPA) were purchased from ThermoFisher Scientific (Loughborough, UK). Sequence grade modified trypsin (20 µg lyophilised) was purchased from Promega (Southampton, UK). RapiGest™ (1 mg lyophilised) was purchased from Waters (Manchester, UK). ^{151}Eu MaxPar® antibody labelling kit was purchased from Fluidigm® (Cambourne, UK). Antibody stabiliser PBS was purchased from Bioaxxess (Gloucestershire, UK).

6.3.2 ^{151}Eu antibody labelling protocol

Cetuximab was labelled with ^{151}Eu following the MaxPar® antibody labelling kit protocol (Fluidigm®, UK). Briefly, the MaxPar® X8 polymer was preloaded with the ^{151}Eu lanthanide metal solution (approximately equimolar ratio) and incubated

at 37°C. The protein concentration of Cetuximab was determined using the Nanodrop™ (ThermoFisher Scientific, UK) prior to reducing the antibody with TCEP at 37°C. The lanthanide-loaded polymer and the reduced antibody were purified using buffers provided by the labelling kit. Following this, the antibody was conjugated with the lanthanide-loaded polymer incubated at 37°C. The metal-conjugated antibody was washed with the provided buffer x3 before determining the yield of protein using the Nanodrop™. The antibody stabilising PBS buffer was added to obtain a final concentration of 0.5 mg/mL.

To validate the ^{151}Eu conjugation with cetuximab, a staining protocol similar to the IMC staining protocol described in Chapter 3.3.5.1 was followed. Briefly, aggregoid sections were fixed with 4% PFA (10 min) at RT. Prior to staining, tissues were permeabilized with 1x casein solution containing 0.1% Triton™ X-100 for 5 min at RT. Tissues were then incubated with blocking buffer (1x casein solution) for 30 min at RT. The conjugated antibody was made at different concentrations: 1:50, 1:100 and 1:200, with a control. Tissues were incubated with the conjugated antibody overnight at 4˚C. Washes with PBS were performed x3 between each step, with the last step washed in deionized water for 30 s. Slides were left to air-dry until analysis.

6.3.3 Cell culture

6.3.3.1 A cell plug for workflow optimisation

A cell pellet/plug was created for the purpose of optimising different parameters of the bottom-up proteomics workflow. Two T-175 flasks of HCC827 cell line were cultured in DMEM supplemented with 10% FBS and 1% penicillin-streptomycin (Lonza Ltd, UK) until 80% confluent. Cells were trypsinised, combined and centrifuged to create a non-homogenised cell pellet. The cell pellet was washed in PBS twice, centrifuging between each wash before flash freezing the pellet with the falcon tube in liquid nitrogen for approximately 1-2 min. Embedding media, 7.5% HPMC and 2.5% PVP, was coated within a mould. The cell pellet was slightly warmed to remove from the falcon, transferred into the mould and covered with additional HPMC & PVP. The cell plug was flash frozen in liquid nitrogen for 1-2 min and stored at - 80°C prior to sectioning. The cell plug was cryosectioned at 10 µm thickness and thaw mounted onto positively charged X-

tra® adhesive slides, desiccated and vacuum packed before storing at - 80°C until use.

6.3.3.2 3D culture growth and drug treatment

HCC827 lung adenocarcinoma aggregoids were cultured following the protocol described in Chapter 2.3.3.

For the bottom-up MALDI-MSI proteomics experiment, aggregoids were treated with Cetuximab concentrations: 0 µg/mL and 150 µg/mL. Drug solutions were made up with DMEM supplemented with 10% FBS and 1% penicillin-streptomycin (Lonza Ltd, UK). Samples were incubated for 24 h before harvesting.

For the LA-ICP-MSI metal detection experiment, aggregoids were treated with 0 µg/mL and 5 µg/mL ^{151}Eu-Cetuximab. Drug solutions were made up with DMEM supplemented with 10% FBS and 1% penicillin-streptomycin (Lonza Ltd, UK). Samples were incubated for 24 h before harvesting.

Aggregoids were processed following the optimised method reported in Chapter 2.3.4. Samples were sectioned at a thickness of 10 µm and thaw mounted onto either positively charged X-tra® adhesive slides or ITO-coated slides (Visiontek Systems Ltd, UK) dependant on the instrumentation used for analysis. Each section was desiccated, and slides were vacuum packed and stored at - 80°C until use.

6.3.4 Bottom-up MALDI-MSI proteomic workflow

6.3.4.1 In-solution digest

Firstly, varying solutions of trypsin were investigated for optimum digestion. Sequence grade modified trypsin (20 µg) was made up in either 25 mM or 50 mM NH_4HCO_3 and with 0.1% added or 0.1% final concentration of RapiGest™ (RG). The solutions were as follows: (1) 25 mM NH_4HCO_3 with 0.1% RG final; (2) 50 mM NH_4HCO_3 with 0.1% RG final; (3) 25 mM NH_4HCO_3 with 0.1% RG added; (4) 50 mM $NH_4HCO_3$with 0.1% RG added. The combinations of trypsin solution are shown in Table 6.1. Cetuximab (5 mg/mL) was digested with each trypsin solution and incubated for 1 h at 37°C. Solutions were placed on ice to stop the reaction. Sample clean-up was performed using C18 Milipore® Ziptips where digests were desalted and concentrated using the following procedure: 100% ACN wetting

solution (x2), 0.1% TFA equilibrium solution (x2), sample perfusion (x10), 0.1% TFA wash solution (x2), and 70% ACN:0.1% TFA elution buffer perfusion (x10). Digests were profiled using 5 mg/mL α-CHCA (70% ACN:0.1% TFA with equimolar amounts of aniline). Samples were manually spotted (0.5 µL) n=3 onto a MALDI target plate. Matrix (0.5 µL) was mixed with each spot on the target plate and allowed to dry at RT prior to analysis.

To determine the peptide mass fingerprint of cetuximab an in-solution digest was performed. Limit of detection of cetuximab peptides was performed by tryptic digestion of solutions ranging from 1 µg/mL to 5 mg/mL. Solutions were mixed 1:1 (v/v) with 0.2% RapiGest™ (0.1% final volume) and incubated at 37°C for 20 min prior to digesting the samples 1:25 (trypsin:protein, v/v) with optimum trypsin. The solutions were incubated for 1 h at 37°C. The digest was stopped on ice, and solutions were cleaned up using C18 Milipore® Ziptips. Digests (n=3) were profiled using 5 mg/mL α-CHCA.

6.3.4.2 Sample washing

Prior to washing, 0.5 µL of cetuximab (5 mg/mL) was spotted in one ROI onto each cell plug section and left to air-dry. Three washing protocols were assessed: (1) EtOH; (2) IPA; (3) Carnoy's fluid. A no wash was also included to compare the effects of the washes on the signal intensity of the acquired mass spectrometric data. Washes (1) and (2) were similar procedures whereby samples were washed subsequently in 70% and 95% ice-cold solvent for 45 s each. For the Carnoy's fluid (3) the sample was washed in 70%, 100% EtOH for 30 s, followed by 2 min wash in Carnoy's fluid (EtOH: $CHCl_3$: AcOH, 6:3:1 parts respectively), then 100% EtOH, H_2O, and 100% EtOH for 30 s. Slides were left to air-dry after each wash procedure. The washing conditions are shown in Table 6.1. Trypsin was spotted in three ROIs of each cell plug, including the cetuximab ROI, prior to incubation. α-CHCA was spotted on each region before to MALDI analysis.

6.3.4.3 Digestion incubation

The effect of incubation methods of the digested cell plug tissue sections on the signal intensity of the acquired mass spectrometric data was examined. Cell plug sections were spotted in one ROI with cetuximab (5 mg/mL), and then in three ROIs with trypsin. Three methods of incubation were investigated, and incubation

chambers were prepared as follows: (1) 50% H_2O: 50% MeOH within a silicone sealed container to ensure an air-tight environment; (2) Saturated K_2SO_4 within a silicon sealed container; (3) Wet paper within a tip box and sealed using parafilm. Each chamber was incubated at 37°C for 3 h. Incubation conditions are displayed in Table 6.1. Afterward, samples were spotted with 5 mg/mL α-CHCA prior to MALDI analysis.

6.3.4.4 Trypsin application for MSI analysis

Trypsin deposition onto aggregoid sections for the detection and localisation of proteotypic peptides was assessed by two methods. To assess the efficiency of the tryptic digestion protocol, rat brain sections (10 µm thickness) were included in the analysis. The two methods evaluated were spray-coat and micro-spotting. The spray-coat method conducted by the automated matrix TM Sprayer™ (HTX Technologies, USA). Trypsin was deposited onto tissue sections in 8 passes at a flow rate 0.06 mL/min using a nitrogen air pressure of 10 psi. The nozzle was set to a height of 40 mm and a temperature at 30°C. The micro-spotting technique was conducted using a BioSpot® TS Microarray (BioFluidiX Technologies, Germany). Trypsin was spotted at a volume of 50 nL, the droplet size was calibrated at a 0.2% variance. Trypsin deposition methods are reviewed in Table 6.1. Slides were digested in the optimum incubation chamber at 37°C for 3 h. Afterward, 37.5 mg/mL DHB matrix (50% MeOH: 0.1% TFA) was applied to the slides using a TM Sprayer in 8 passes. The nozzle height was 40 mm and temperature was set to 75°C with a backup flow of 50% MeOH: H_2O. The flow rate was 0.08 mL/min and nebulised with nitrogen at 10 psi.

Optimised Parameters	Optimal	Analysis
Trypsin solution	(1) 25 mM NH_4HCO_3; 0.1% (final) RapiGest™ (2) 50 mM NH_4HCO_3; 0.1% (final) RapiGest™ (3) 25 mM NH_4HCO_3; 0.1% (added) RapiGest™ (4) 50 mM NH_4HCO_3; 0.1% (added) RapiGest™	MALDI MS Profiling; α-CHCA
Washing conditions	(1) 70% EtOH, 95% EtOH; 45 s (2) 70% IPA, 95% IPA; 45 s (3) 70% EtOH, 100% EtOH; 30s. Carnoy's fluid (EtOH:CHCl3:AcOH, 6:3:1); 2 min. 100% EtOH, dH20, 100% EtOH; 30 s.	MALDI MS Profiling; α-CHCA
Digestion incubation	(1) 50% H_2O: 50% MeOH; silicon sealed container; 3 h (2) Saturated K2SO4; silicon sealed container; 3 h (3) Wet paper: tip box sealed with parafilm; 3 h	MALDI MS Profiling; α-CHCA
Trypsin application	(1) Spray-coat; HTX TM Sprayer™ (2) Micro-spotting; BioSpot® TS Microarray	MALDI MS Imaging; DHB

Table 6.1 An overview of the assessed parameters and conditions for the development of a bottom-up proteomics workflow by MALDI-MSI.

6.3.5 Instrumentation

6.3.5.1 MALDI analysis

6.3.5.1.1 MALDI-MS profiling

The MALDI-MS profiling spectra were acquired in positive mode using a Waters MALDI HDMS Synapt™ G2 mass spectrometer (Waters Corporation, UK), equipped with a Nd:YAG laser operated at 1 kHz. Instrument calibration was performed using phosphorus red. Spectra were acquired in full scan sensitivity mode within a *m/z* range 600-2500 at a resolution 10 000 FWHM. The laser energy was set to 350 arbitrary units. The ion mobility function was enabled to improve the separation of peaks.

MALDI-MS profiling data were converted to .txt file format using MassLynx™ software (Waters Corporation, UK) and analysed using mMass 3 open-source software (Strohalm *et al.*, 2010). Peak picking settings were set at a S/N threshold of 5 (unless stated in text), and the picking height was 100%. Both the absolute and relative intensity thresholds were set to 0 with baseline correction and smoothing applied. Amino acid sequences of abundant proteins were compiled into a library on mMass. Each sequence was *in silico* digested and matched against each mass spectra to annotate peaks. Identification of values were validated by using the PeptideMass tool from ExPASy:SIB bioinformatics resource portal (Artimo *et al.*, 2012). An *in silico* digest of specific protein sequences were cleaved and masses of generated peptides were computed.

6.3.5.1.2 MALDI-MSI

Initial sample preparation methods were evaluated using a MALDI rapifleX Tissuetyper (Bruker Daltonics, Germany) equipped with a 10 kHz Smartbeam 3D Nd:YAG laser. Images were acquired in positive ion-reflectron mode over a mass range of *m/z* 600-2500. Instrument calibration was performed using phosphorus red. Imaging data was collected at a spatial resolution of 20 µm, and 500 laser shots were summed per raster position.

MALDI-MSI data were initially processed using FlexImaging 5.0 software (Bruker Daltonics, Germany) to determine the quality of the data after acquisition. In-depth data processing was achieved using the SCiLS™ Lab MVS Version 2020a Core (Bruker Daltonics, Germany). Data was normalised to TIC and the peak list

was generated from the maximum 100 peaks per spectrum. Discrimination between samples was achieved by employing the ROC tool in SCiLS™ to calculate the AUC value.

6.3.5.2 LA-ICP-MSI analysis

Analysis of the metal tagged protein was performed following a similar method described in Chapter 3.3.6. Laser parameters were optimised to 6 µm spot size with laser power 46%, 25 µm/s scan speed, 0.07 Jcm^{-2} laser fluence, and 20 Hz repetition rate. Samples were ablated line by line with 6 µm raster spacing. Isotopes monitored included ^{24}Mg, ^{66}Zn, ^{63}Cu and ^{151}Eu. The instrument was controlled using Syngistix software. Data analysis was achieved using Iolite Software on Igor Pro (WaveMetrics, USA).

6.4 Results and discussion

6.4.1 A bottom-up MALDI-MSI proteomics strategy

6.4.1.1 Tryptic digestion

6.4.1.1.1 Optimisation of trypsin solution

First, the effect of an in-solution trypsinisation of cetuximab was investigated. Four combinations of trypsin solutions including concentrations of buffer, NH_4HCO_3, and surfactant, RapiGest™, were evaluated. The absolute intensity was determined by the most abundant peak *m/z* 1677.8, and the relative intensity calculated against the α-CHCA peak *m/z* 861.0 (Figure 6.1).

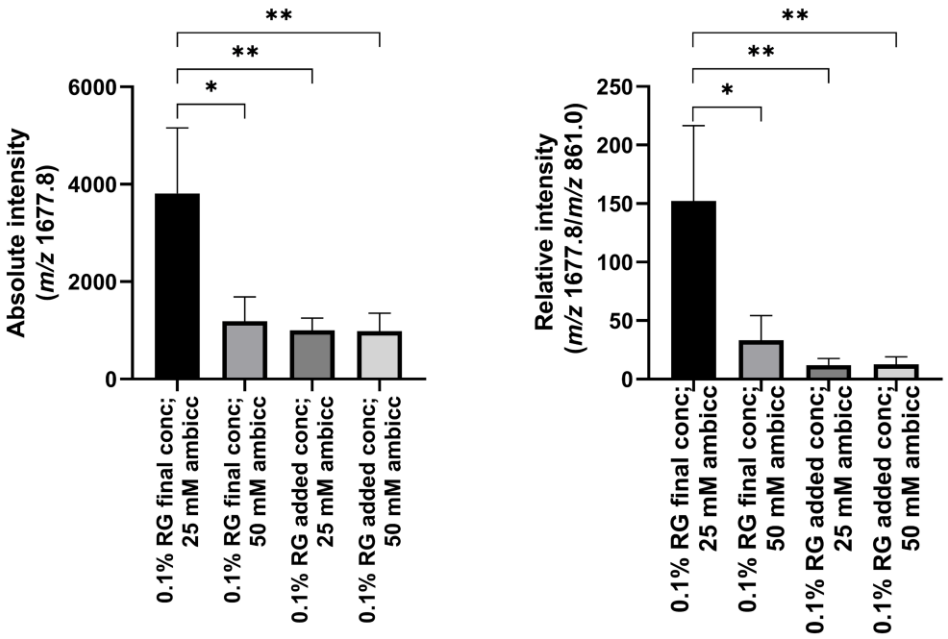

Figure 6.1 The absolute and relative intensity of the most abundant cetuximab peak *m/z* 1677.8 with several trypsin solvent solutions. For the relative intensity, *m/z* 1677.8 was normalised with the α-CHCA peak *m/z* 861.0. Data is mean (n=3) ± SD, statistical significance determined by one-way ANOVA with Tukey post hoc test * $p < 0.05$, ** $p < 0.01$.

NH_4HCO_3 is commonly used as a trypsin buffer. The slightly alkaline pH 7.7 is close to the optimum pH 8 for trypsin digestion to achieve optimum reaction (Link & LaBaer, 2011). Various publications have reported different concentrations of NH_4HCO_3 with trypsin ranging from 20 mM – 100 mM with successful peptide detection *in situ* (Ren *et al.*, 2009; Cole *et al.*, 2011; Ly *et al.*, 2019). From observing the absolute and relative intensity in this experiment there was no difference between 25 mM and 50 mM, when comparing 0.1% (added) RapiGest™.

Alternatively, the addition of 0.1% (final) RapiGest™ showed an increase in intensity for NH_4HCO_3 concentrations, particularly for the 25 mM solution. The optimum concentration of RapiGest™ therefore had an impact on the performance of trypsinisation. The purpose of a surfactant, or detergent, is to unfold the protein for more accessible enzymatic cleavage and effective solubilisation to increase the number of peptides and their intensity during analysis. RapiGest™ was used based on comparative studies that reported better performance to other detergents for in-solution digestions (Chen *et al.*,

2007; Chen *et al.*, 2008). Other typical surfactants include Octyl ß-D-glucopyranoside (OcGlu) and N-Octanoyl-N-methylglucamin (MEGA-8) which have been incorporated within in-solution and *in situ* digestion protocols (Djidja *et al.*, 2009; Patel *et al.*, 2015). The addition of RapiGest™ for *in situ* digestion, however, has limited literature with two studies reporting preliminary data profiling and imaging an ungroomed fingermark (Patel *et al.*, 2015; Deininger *et al.*, 2016).

Overall, a statistically significant difference in the relative intensity was observed from trypsin solution containing 25 mM NH_4HCO_3 with a 0.1% (final) RapiGest™ compared to the other trypsin solutions. It was therefore decided this solvent combination was the optimum for effective tryptic digestions.

6.4.1.1.2 Cetuximab peptide mass fingerprint

The tryptic peptide profile of cetuximab was determined to analyse and select specific peaks for the identification of the therapeutic within the aggregoid model. An *in silico* digest of cetuximab was used to assign the peaks within the acquired spectra. Table 6.2 reports the cetuximab peptides detected within the spectra, highlighting the variable chain location and the *m/z* values. Variable light chain (VL) peptides 49-YASESISGIPSR at *m/z* 1266.6 and 24-ASQSIGTNIHWYQQR at *m/z* 1788.8 were identified as signature peptides containing CDRs. These corresponded to existing literature (Li *et al.*, 2005; Shibata *et al.*, 2017) and were confirmed following the Kabat definition of CDR identification (Wu & Kabat, 1970; Kabat, Wu, & Bilofsky, 1977). These are unique sequences in the variable chains of cetuximab and therefore can be used as surrogate peptides for identification *in situ.* The CDR variable heavy chain (VH) peptide 44-GLEWLGVIWSGGNTDYNTPFTSR at *m/z* 2570.2 was also identified although at relatively low intensity.

Peptide *m/z*	Mass error (ppm)	Peptide sequence	Chain
755.4075	-1.5	SQVFFK	VH
835.4327	-1.8	DTLMISR	VH
838.5020	-1.5	ALPAPIEK	VH
1186.6509	3.6	GPSVFPLAPSSK	VH
1266.6439	9.0	YASESISGIPSR	VL
1677.8173	9.1	FNWYVDGVEVHNAK	VH
1788.8828	2.9	ASQSIGTNIHWYQQR	VL
1808.0089	1.3	VVSVLTVLHQDWLNGK	VH
1924.0779	1.5	DILLTQSPVILSVSPGER	VL
2082.9888	-8.2	TPEVTCVVVDVSHEDPEVK	VH
2570.2251	2.3	GLEWLGVIWSGGNTDYNTPFTSR	VH

Table 6.2 List of cetuximab tryptic peptides identified after in solution digestion by MALDI-MS analysis. Observed *m/z* values in positive ion mode, the mass error (ppm) and the variable chain are included. Underlined sequences highlight the CDRs. CDRs were determined following the Kabat definition.

A VH peptide 277-FNWYVDGVEVHNAK at *m/z* 1677.8 was observed as the most abundant peak present in the peptide mass fingerprint of cetuximab. The peak was validated by MS/MS analysis to confirm the sequence of the peak. Figure 6.2 displays the MS/MS spectra of *m/z* 1677.8 highlighting the y-ions of the sequence. A fragment ion calculator (Systems Biology) was used to identify a-, b-, y-, and z-ions and confirm the *de novo* sequencing.

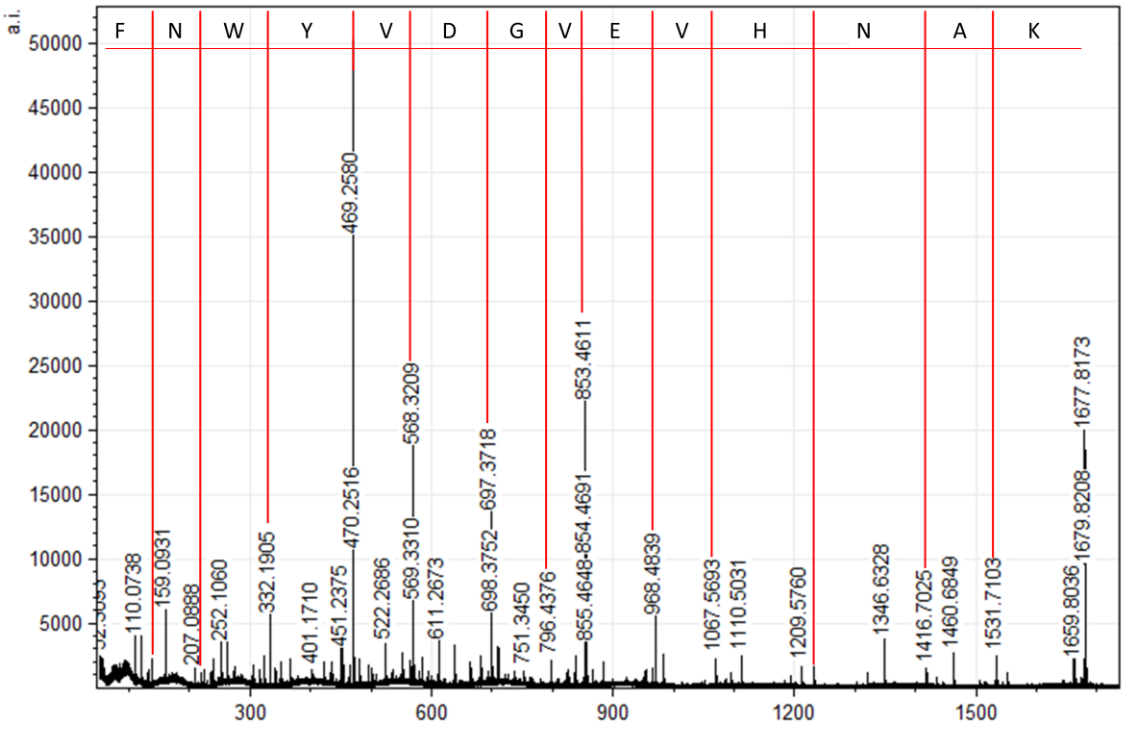

Figure 6.2 MALDI-MS/MS spectrum of the 5 mg/mL cetuximab tryptic peptide *m/z* 1677.8.

A range of cetuximab concentrations from 1 µg/mL to 5 mg/mL were digested to determine the limit of detection. The lowest concentration of cetuximab peptides detected was 5 µg/mL with a S/N of 3. The number of peptides detected, and their intensities were significantly reduced in comparison to 5 mg/mL, as expected. The VH *m/z* 1788.8 was the only CDR containing peptide identified (S/N 3) at this low concentration. Figure 6.3 displays spectra from the highest and lowest detected cetuximab peptides. Some peptides including *m/z* 1266.6 and *m/z* 1677.8 were detected within the lowest concentration, although at a S/N < 3.

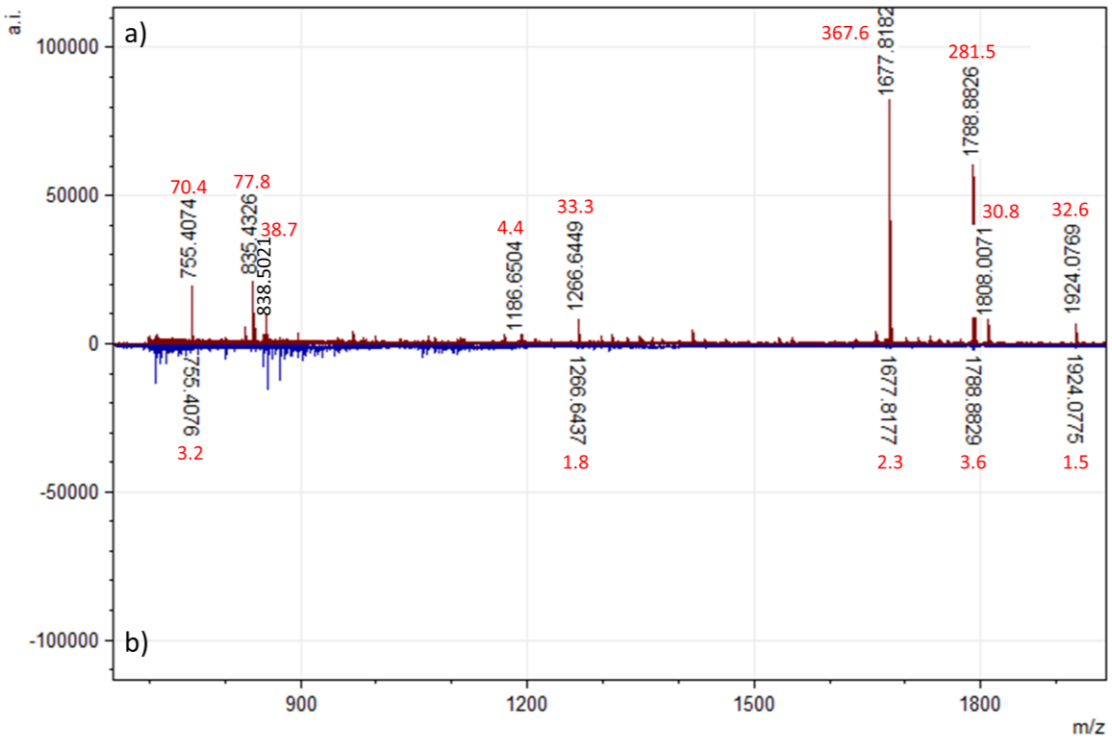

Figure 6.3 Peptide mass fingerprint of cetuximab by MALDI-MS. a) 5 mg/mL b) 5 µg/mL. S/N values (red) included for each detected peak in both spectra. Spectra display peaks within mass range 600-2000 Da**.**

6.4.1.1.3 *In situ* peptide mass fingerprint

Direct profiling of a HCC827 cell plug was performed to investigate the protein expression within the aggregoid samples. As the cell plug is created through the growth of HCC827 cell line, the protein profile would be similar to the aggregoid. This was achieved by following a standardised protocol for on-tissue tryptic digestion, prior to optimising a protocol for aggregoid peptide imaging analysis. Spectra were obtained within the peptide mass range of *m/z* 600-2500 and identification of peaks were made by putative assignments. Table 6.3 reports some of the detected peptides within the cell plug. Signals at *m/z* 944.5 (Histone H2A), *m/z* 1032.6 (Histone H3), *m/z* 1198.7 (actin) and *m/z* 1325.7 (Histone H4) were identified. These abundant peaks have been previously detected in tissues by MALDI-MSI (Djidja *et al.*, 2009; Cole *et al.*, 2011). It was therefore decided these peaks would be used for reference through the study for the evaluation of the bottom-up proteomics workflow conditions.

Protein	Peptide *m/z*	Mass error (ppm)	Peptide sequence	Protein function
Actin	1198.7123	5.7	AVFPSIVGRPR	Cell mobility
Cathepsin D	1601.8241	-5.1	LVDQNIFSFYLSR	Protease
GRP 78	1934.0120	-0.6	DNHLLGTFDLTGIPPAPR	Protein folding and quality control (HSP 70)
Histone H1	1438.7356	7.6	YSDMIVAAIQAEK	Condensation of nucleosome
Histone H2A	944.5358	4.9	AGLQFPVGR	Nuclear component
Histone H2B	816.4573	-0.1	EIQTAVR	Nuclear component
Histone H3	1032.6000	4.9	YRPGTVALR	Nuclear component
Histone H4	1325.7540	0.3	DNIQGITKPAIR	Nuclear component
HSP 70	1020.5420	-5.2	YLEAGAAGLR	Molecular chaperone
HSP 90	1513.7789	-4.4	SLSNDWEDHLAVK	Molecular chaperone
Lactate dehydrogenase B	959.5558	3.9	GLTSVINQK	Synthesis of lactate from pyruvate
Stathmin	1074.5730	4.9	DLSLEEIQK	Regulation of microtubule filaments
Vimentin	1121.5746	-8.1	EYQDLLNVK	Intermediate filaments

Table 6.3 List including some of the observed peptides after *in situ* digestion and MALDI-MS analysis. Observed *m/z* values in positive ion mode, the mass error (ppm) and the protein function are included.

6.4.1.2 Optimisation of an *in situ* bottom-up proteomic workflow

6.4.1.2.1 Washing protocol

Washing samples prior to trypsin application is a technique commonly used in peptide imaging experiments to remove lipids and salts from the tissue. The washing step improves peptide coverage by increasing the ion yields and the number of signals within the spectra.

Several washing procedures include combinations of organic solvents that extract small molecules and lipids from tissues. The most common method is increasing concentrations of EtOH (70%-100%) that has been demonstrated to significantly improve the signal intensity within the peptide mass range (Schwartz *et al.*, 2003; Taban *et al.*, 2007; Goodwin *et al.*, 2008). EtOH wash also improves the preservation of tissues, as it is a conventional method for fixing samples for staining analysis. Solvents including IPA, MeOH, AcOH and $CHCl_3$ have also been used in washing protocols. A comprehensive study conducted by Seeley *et al.*, (2008) evaluated these washing solvents to reveal IPA as the most effective solvent in terms of the MS signal of proteins and preservation of tissues. Alternatively, a combination of EtOH, $CHCl_3$ and AcOH, also known as Carnoy's fluid, used extensively in histology for tissue fixation, has been introduced into peptide imaging experiments. A recent study by Yang & Caprioli, (2011) developed a new washing protocol incorporating Carnoy's fluid that significantly improved the sensitivity of protein analysis in comparison to EtOH.

In this study, three washing protocols were evaluated, EtOH, IPA and Carnoy's fluid, for the peptide analysis in cell plug sections. Figure 6.4 shows the use of IPA as a wash was better in terms of the relative intensity of the peptide reference peaks *m/z* 944.5, *m/z* 1032.6 and *m/z* 1198.7. The use of EtOH however gave rise to a slightly reduced relative signal but a better absolute intensity for the peptides. No major statistical significance was observed between the three washes.

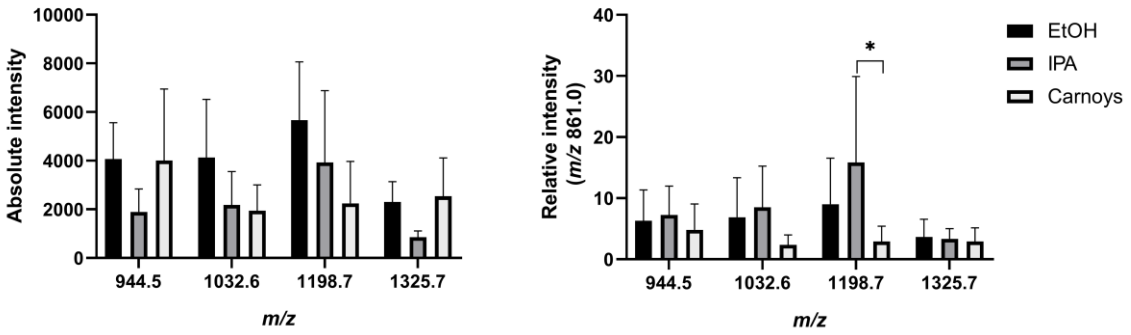

Figure 6.4 The absolute and relative intensities of the tryptic peptide reference peaks (*m/z* 944.5, *m/z* 1032.6, *m/z* 1198.7 and *m/z* 1325.7) with different wash protocols (EtOH, IPA and Carnoy's fluid). For the relative intensity, *m/z* values were normalised with the α-CHCA peak *m/z* 861.0. Data is mean (n=3) ± SD, statistical significance determined by one-way ANOVA with Tukey post hoc test * $p < 0.05$.

Figure 6.5 displays the spectra observed following the three washing protocols, including a no wash control. By observing the spectra, peaks within the lipid mass range (*m/*z 700-850) were still present within samples washed with IPA, although at reduced levels when compared to the control. The EtOH wash also showed this effect on the mass spectra, with a further reduction in the lipid signal in comparison to IPA. The Carnoy's fluid was the most successful in terms of diminishing the lipid intensity. This is most likely due to the addition of $CHCl_3$, which was demonstrated as an efficient lipid reduction method for protein analysis with MALDI-MSI (Lemaire *et al.*, 2006). In this study however, the Carnoy's fluid was not the most effective method to achieve a good peptide signal. From this conclusion, the EtOH wash was used for further experiments based on the absolute and relative sensitivity to detect peptide peaks, whilst suppressing a considerable lipid signal in comparison to IPA.

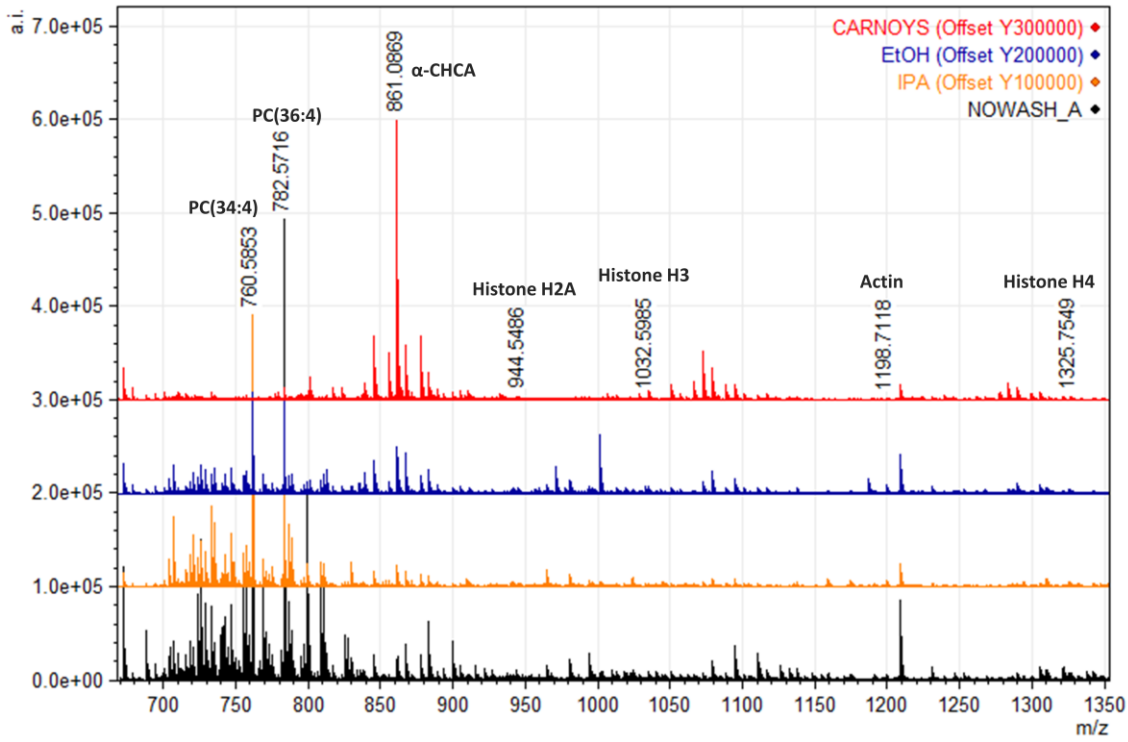

Figure 6.5 The effect of washing protocols on the mass spectra by direct MALDI-MS analysis. Annotations of lipid species PC 34:4, *m/z* 760.6 and PC 36:4, *m/z* 782.8; α-CHCA peak, *m/z* 861.1; tryptic peptide species Histone H2A, *m/z* 944.5, Histone H3, *m/z* 1032.6, Actin, *m/z* 1198.7 and Histone H4, *m/z* 1325.8**.**

6.4.1.2.2 Incubation methods

To maintain optimum enzymatic activity over a long period of time, on-tissue digestion protocols incubate samples within a humidity chamber typically at 37°C. Achieving a stable humidity at a high percentage (90-99%) is important to improve the quality of the digest (Ly *et al.*, 2019). Having an environment ≥ 100% humidity, otherwise known as supersaturation, can subsequently lead to condensation, compromising the digest and in turn increasing the risk of analyte delocalisation in imaging studies.

In this study, three methods of producing a humid environment were evaluated. Firstly, 50% H_2O: 50% MeOH (MeOH) within a sealed container is a common solution used previously in a range of peptide tissue imaging studies (Cole *et al.*, 2011; Patel *et al.*, 2015; Deininger *et al.*, 2016). In addition, the use of wet tissue paper with H_2O in an empty tip rack was also included due to its success of peptide detection in pig lung tissues by MSI (Do *et al.*, 2020). Alternatively, a

more recent paper stated the benefit of using saturated K_2SO_4 solution as a method for stable humidity at 96% for quality peptide analysis in clinical tissue microarrays (Ly *et al.*, 2019).

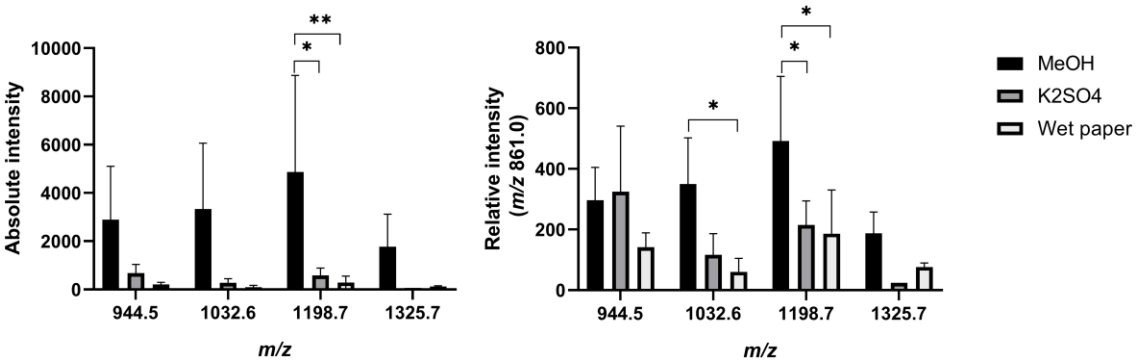

Figure 6.6 The absolute and relative intensities of the tryptic peptide reference peaks with different incubation methods: MeOH, K2SO4 and wet paper). For the relative intensity, *m/z* values (*m/z* 944.5, *m/z* 1032.6, *m/z* 1198.7 and *m/z* 1325.7) were normalised with the α-CHCA peak *m/z* 861.0. Data is mean (n=3) ± SD, statistical significance determined by one-way ANOVA with Tukey post hoc test * $p < 0.05$, ** $p < 0.01$.

By observing the absolute and relative intensity of the reference peaks, MeOH was a superior incubation method for increasing the sensitivity for peptide detection (Figure 6.6). Interestingly, the Histone H4 *m/z* 1325.7 peak had a relatively low intensity and could not be detected in all three ROIs of the cell plugs incubated by methods of K_2SO_4 and wet paper. The enzymatic activity during these incubation conditions was therefore impacted, most likely due to an unstable humidity.

6.4.1.2.3 Trypsin application

6.4.1.2.3.1 Spray-coat

Trypsin deposition is conventionally performed using a spray-coat technique to achieve a homogenous layer of enzyme over the tissue. Automated spraying systems are a preferred method over manual application to gain better reproducibility. Here, trypsin was applied using the TM-sprayer following the technical note #27 from HTX Technologies. In addition to the aggregoid sections, a section of rat brain tissue was included to determine the performance of the trypsin digestion. Two sets of samples were adhered onto one slide. One half of

the slide was prepared for digestion following the optimised washed protocol with EtOH, before depositing the trypsin solution.

Figure 6.7 shows the ion density maps for three of the reference peptides, *m/z* 944 (Histone H2A), *m/z* 1032 (Histone H3) and *m/z* 1198 (actin). From the data, the detection of peptides within the aggregoid section has poor sensitivity compared to the images from the rat brain section where detail of the cerebellum can be identified with high signal. Some peptide signal can be observed within the aggregoid region, although no specific detail on the localisation of these peaks can be determined, with potential delocalisation observed. The data suggests that the trypsin digestion was partly successful as these peaks were not detectable within the non-digested samples. The lack of sensitivity for peptides within the aggregoid sections implies the activity of the digestion was poor, or weak analyte extraction from the matrix. However, as the data from the rat brain displayed highly intense peptide images, it suggests specific issues with the technique for the aggregoid tissues.

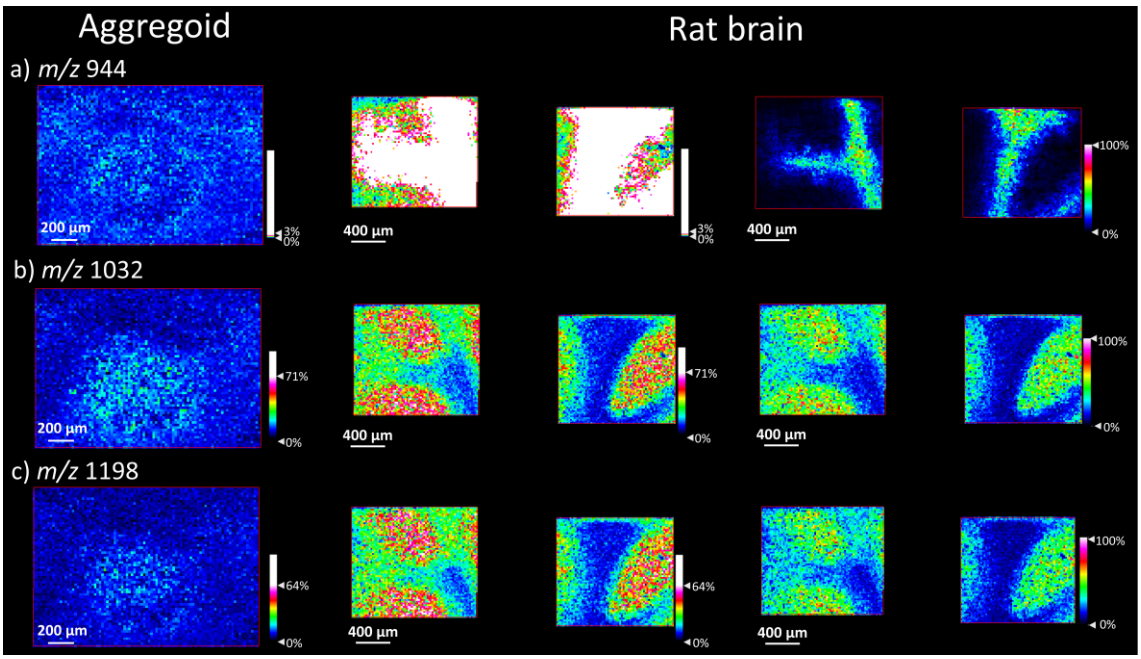

Figure 6.7 MALDI-MS images of tryptic peptides in an aggregoid section and rat brain section. Images of a) Histone H2A, b) Histone H3 and c) actin. Digestion achieved by trypsin spray-coat application. The left and middle panel of images have an altered intensity scale for the detection of peptide signals in the aggregoid section. The right panel displays the rat brain images at a normal intensity scale. Images were normalised using TIC. Scale bar 200 µm (aggregoid), 400 µm (rat brain cerebellum).

By studying the data further, some residual lipid peaks could be identified in the digested samples. A lot of delocalisation of lipid signals was observed within the aggregoid sections compared to the non-digested samples (Figure 6.8), this could be due to lipid migration as a result of the washing procedure. Although, another possible reason could be the high pressure and flow rate at which the trypsin was deposited onto the tissues, leading to molecular migration. It has also been reported that the combination of DHB matrix with TFA can cause significant hydrolysis of phospholipids (Schiller *et al.*, 2003), which could be a contributing factor. Since the non-digested samples showed no delocalisation, it suggests such effect is from the application of trypsin, and a could be reason for the lack of peptide signal.

An additional note, the analyte migration was only detected within the digested aggregoid sections and not in the digested rat brain section. This may be due to a delocalisation effect within tissue sections of a smaller size being more visible because it is off-tissue. An aggregoid sample is ~ 1 mm in diameter compared to larger tissues such as a rat brain section of ~ 20 mm in length.

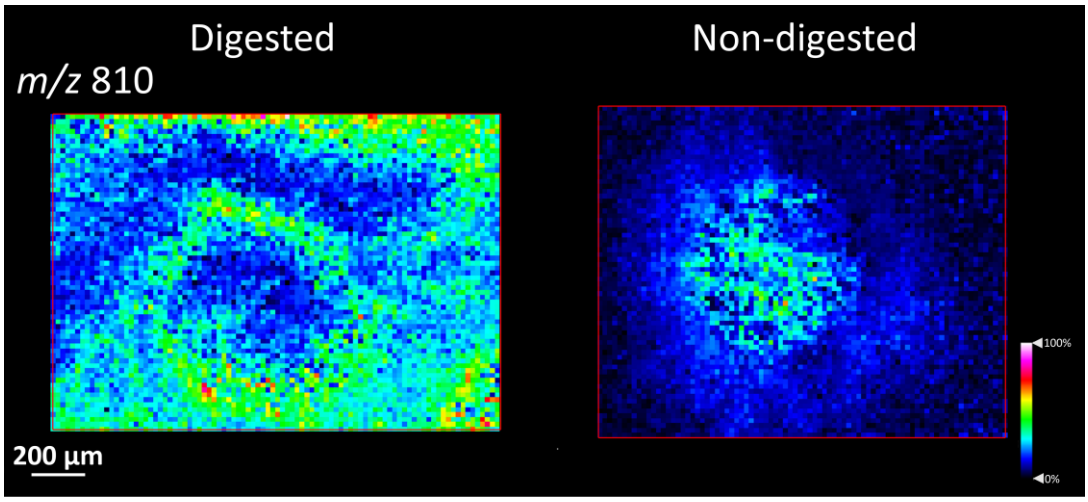

Figure 6.8 MALDI-MS images of lipid peak *m/z* 810 in a digested and non-digested aggregoid section. Digestion achieved by trypsin spray-coat application. Images were normalised using TIC. Scale bar 200 µm.

The spray technique requires further optimisation to increase the sensitivity of peptide detection within the aggregoid model. Reducing the pressure and flow rate would be the initial parameters to test for minimised analyte diffusion. Experimental work with the SunCollect™ sprayer, which allows for lower flow rate capabilities, has been performed. The detection of peptides at an increased intensity has been unsuccessful (data not shown). This data, however, cannot be compared to the data obtained by application of trypsin using the TM-sprayer due to different MALDI-MSI instrumentation used for analysis.

An alternative choice of matrix could also improve the sensitivity for peptide detection. The data reported was acquired with DHB as a matrix. Although DHB has previously demonstrated success in the detection of peptides for example in a mouse brain section (Schober *et al.,* 2012); α-CHCA is a more common matrix for peptide detection (< 2500 Da) and has demonstrated an effective matrix to extract peptide peaks during the optimisation of sample preparation in this study.

6.4.1.2.3.2 Micro-spotting

An alternative method of trypsin application is micro-spotting, this method allows for the deposition of trypsin within specific ROIs at nanolitre volumes. In this experiment, trypsin was deposited using a BioSpot® TS Microarray at 50 nL. The volume of the droplet was sufficient to cover a whole aggregoid section, as only specific spots of the rat brain were covered.

Figure 6.9 shows the detection of reference peptide peaks *m/z* 944, *m/z* 1032, m*/z* 1198 and *m/z* 1325 within the aggregoid sections at a relatively high intensity compared to the data obtained from the spray-coat technique. However, the spatial information using the micro-spotting technique has been impacted. Some images contained “water ring” marks where the droplet was deposited and displayed delocalisation of peptide signals. This is a major drawback; this means it is not a suitable method for spatial distribution studies as the localisation of analytes of interest cannot be determined.

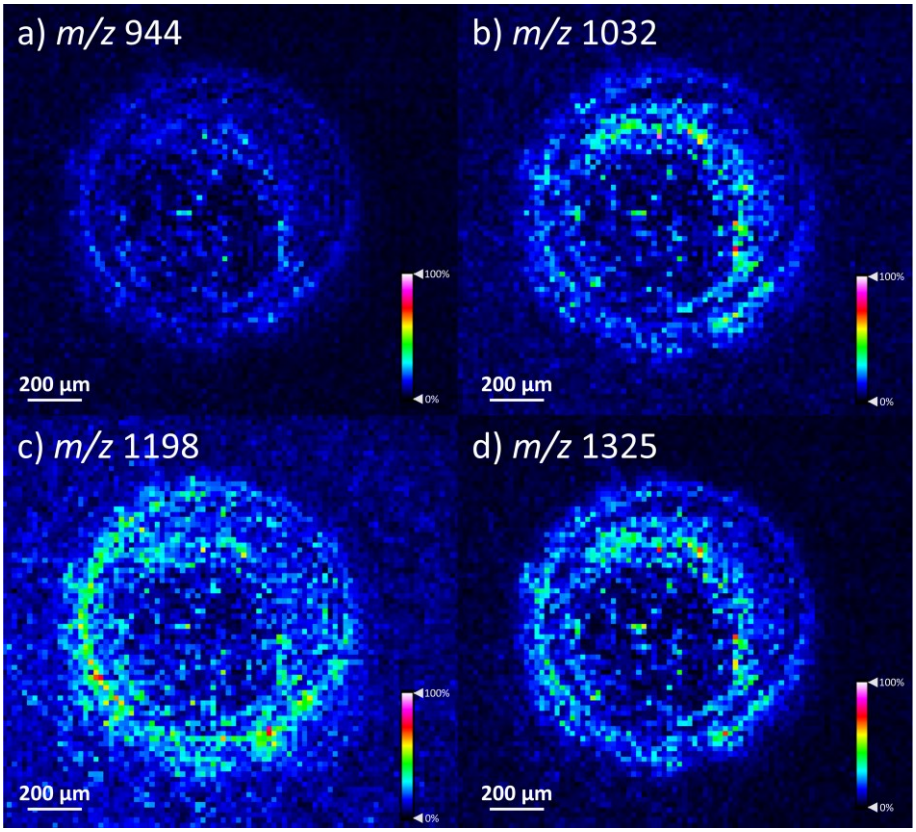

Figure 6.9 MALDI-MS images of tryptic peptides in an aggregoid section by micro-spotting trypsin application. Images of a) Histone H2A, b) Histone H3, c) actin and d) Histone H4. Images were normalised using TIC. Scale bar 200 µm.

Although the detection of peptides was achievable, further optimisation is required to retain the spatial information. Automated micro-spotting systems such as the Portrait™ 360 and CHIP-1000 have been reported as successful methods for peptide imaging studies (Djidja *et al.*, 2009; Cole *et al.*, 2011; Quanico *et al.*, 2013). These systems allow the deposition of droplets of trypsin at picolitre volumes within a predefined array size (~ 200 µm), which would be suitable for the size of the aggregoid model. Numerous concentrated areas of enzymatic digestion across the aggregoid tissue would allow for better detail whilst obtaining a relative peptide signal. Some experimental work, performed on the Portrait™ 360, detected a small number of peptides including *m/z* 1032 and *m/z* 1198 within the aggregoid model acquired using a different MALDI-MSI instrumentation (data not shown). The reproducibility of using the Portrait™ 360 for peptide detection in this study however was not satisfactory, although the capabilities of achieving

numerous enzymatic reactions for better spatial resolution demonstrates it is a promising technique for this specific application.

6.4.1.3 Preliminary detection of cetuximab within the aggregoid model

The purpose of this chapter was to develop an analytical method which could be employed to determine the localisation of a biopharmaceutical within the tumour aggregoid. Following the optimisation of the bottom-up proteomics workflow described, the micro-spotting technique was further utilised for the detection of cetuximab within the aggregoid model. The objective was to initially detect signal of cetuximab surrogate peptides within the aggregoid at the expense of the spatial information. This was primarily to establish the capabilities of detecting cetuximab *in situ* by MALDI-MSI.

In this experiment, the optimised protocol was as follows: slides were initially washed with increasing concentrations of EtOH. Control and treated cetuximab (150 µg/mL) HCC827 aggregoid sections were spotted with 50 nL trypsin (20 µg/mL in 25 mM NH_4HCO_3 with a 0.1% (final) RapiGest™). The sample was incubated within a 50% H_2O:50% MeOH humid environment at 37°C for 3 h before applying DHB matrix.

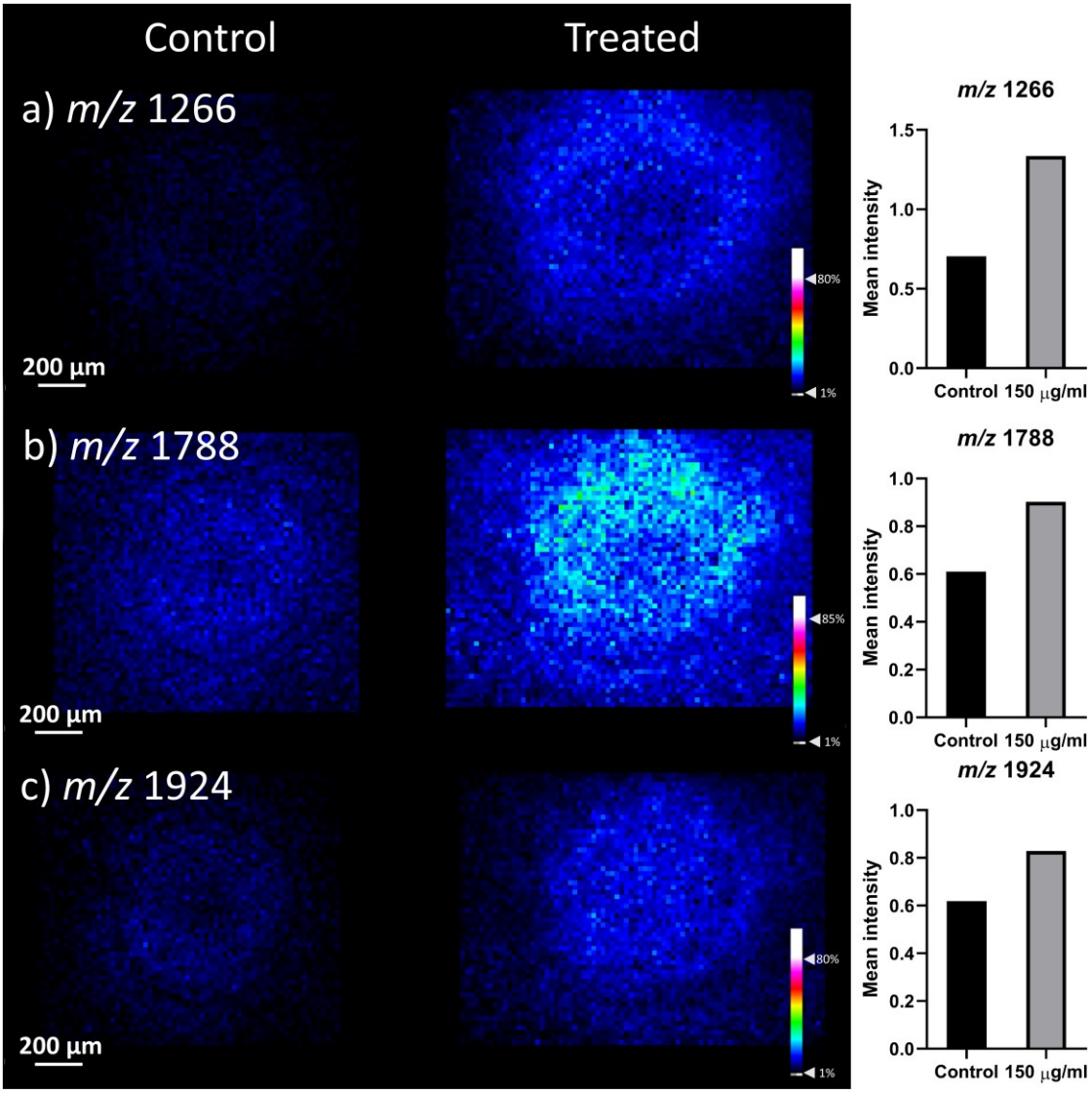

Figure 6.10 MALDI-MS images of cetuximab tryptic peptides in an aggregoid section. Surrogate peptides a) *m/z* 1266 (CDR L1), b) *m/z* 1788 (CDR L2) and c) *m/z* 1924. Images were normalised using TIC. Scale bar 200 µm. Box plot graphs displaying the medium signal intensity of each *m/z* value between the control and 150 µg/mL treated.

Figure 6.10 shows ion images of three surrogate cetuximab peaks *m/z* 1266 (CDR L1), *m/z* 1788 (CDR L2) and *m/z* 1924 within the aggregoid model. The detection of cetuximab peaks were confirmed with signal intensity present in the spotted cetuximab standard ROI. The intensities of each peak is low therefore optimisation is required to improve the sensitivity of detection. Further analysis using ROC to discriminate the *m/z* values between the control and treated samples was performed. For the three surrogate peaks, the AUC value from ROC

analysis was > 0.9 which defined the peaks as a variate in the treated sample and not in the control. This is promising in terms of the detection of unique cetuximab peptides containing the CDR sequence within the aggregoid model. However, the localisation of cetuximab within the aggregoid model cannot be determined due to the method of trypsin application.

An important note in this study is that the data reported are preliminary results. Only one set of samples was analysed due to experimental error during sample handling, in addition to the time constraints of instrument availability to conduct this experiment. Therefore, no definitive conclusions on the detection of cetuximab within the aggregoid model can be made. To validate the method, additional replicates are necessary; to determine biological variation and to define the expression levels of the cetuximab peaks more precisely. MS/MS profiling of the detected peaks could also be performed to confirm the identification of the surrogate peptides. Furthermore, analysis by LC-MS/MS for accurate detection of the reference peptides at high sensitivity should be employed to validate cetuximab detection within the aggregoids by MALDI-MSI, in addition to acquiring data for quantitative measurement.

6.4.2 LA-ICP-MSI detection of cetuximab by metal conjugation

6.4.2.1 Validation of metal-conjugated cetuximab

Prior to aggregoid treatment with ^{151}Eu-cetuximab, LA-ICP-MS profiling experiments were conducted to confirm the presence of the ^{151}Eu and validate the metal-conjugation with cetuximab. Initially, the detection of ^{151}Eu was determined by acquiring three line patterns through a 0.5 µL spot of the conjugated antibody solution on a glass slide. Figure 6.11 shows the ^{151}Eu intensity of each line as the laser acquires through the spot, confirming the presence of the metal within the solution.

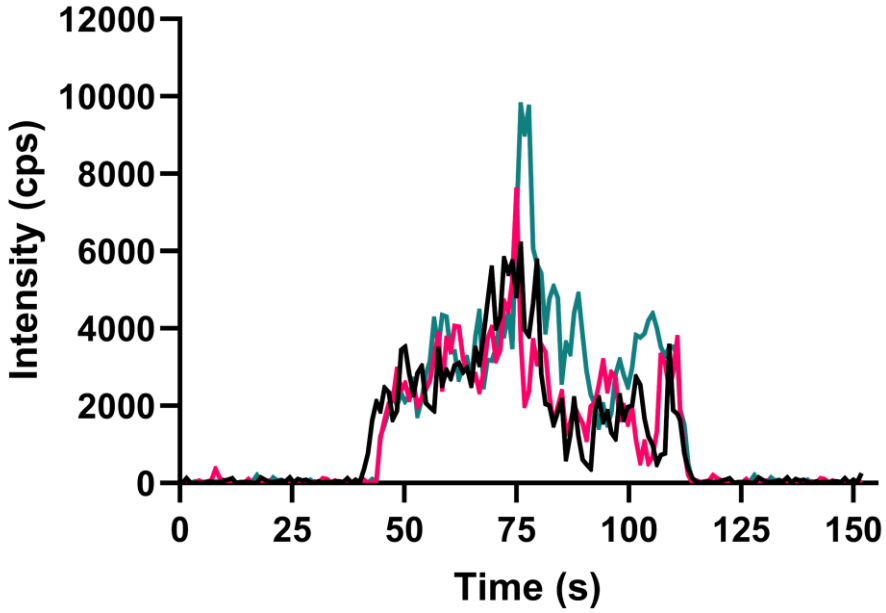

Figure 6.11 LA-ICP-MS profile of the ^{151}Eu-cetuximab solution. Three acquired ^{151}Eu intensity profiles through a spot of ^{151}Eu-cetuximab. Line patterns were extended approximately 40 s before and after the spotted solution.

To determine if the metal successfully conjugated to cetuximab, a staining protocol was employed. Four dilutions (control, 1:200, 1:100 and 1:50) of the ^{151}Eu-cetuximab solution were incubated onto sections of an aggregoid. Following this, five line patterns were acquired across each section. Figure 6.12 shows an increase in intensity with an increase of ^{151}Eu-cetuximab concentration within the aggregoid sections. A slight detection of ^{151}Eu within the control was due to signal interferences, therefore the data was normalised against the control. The presence of ^{151}Eu within the tissue sections was validated with the simultaneous detection of endogenous metals, ^{24}Mg, ^{66}Zn and ^{63}Cu (data not

shown). The detection of ^{151}Eu in the stained aggregoid sections therefore suggests the metal has conjugated to cetuximab; the antibody has bound to its EGFR target within the aggregoid and has been detected by its ^{151}Eu label. Any excess ^{151}Eu in the solution was expected to have been washed off during the staining procedure.

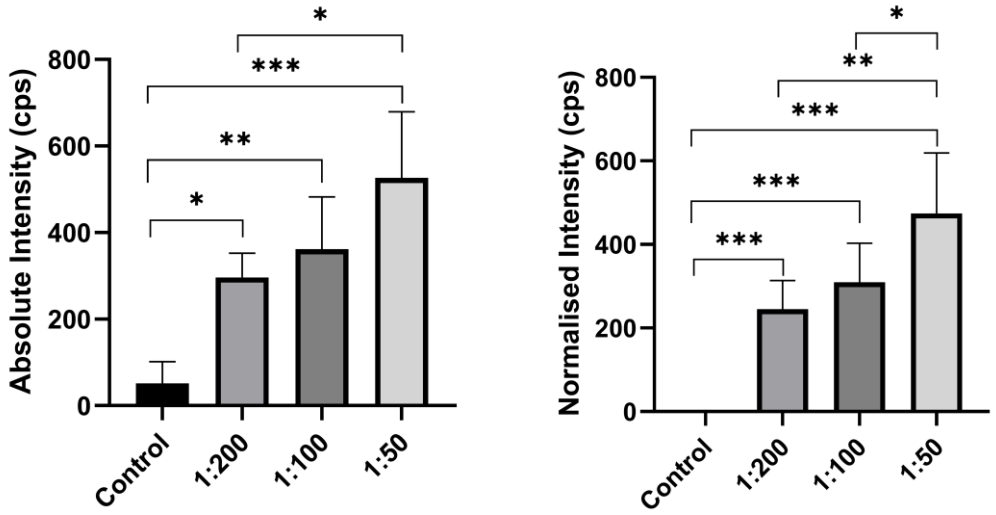

Figure 6.12 The absolute and normalised intensity of ^{151}Eu-cetuximab stained aggregoid sections. Average intensity of five acquisitions per tissue section. ^{151}Eu-cetuximab dilutions: control, 1:200, 1:100 and 1:50. Data is mean (n=3) ± SD, statistical significance determined by one-way ANOVA with Tukey post hoc test * $p < 0.05$, ** $p < 0.01$, *** $p < 0.001$.

6.4.2.2 Localisation of ^{151}Eu-cetuximab within the aggregoid model

To determine the localisation and distribution of cetuximab within the aggregoid model, the main experiment was to image aggregoid samples treated with therapeutic levels of ^{151}Eu-cetuximab in culture by LA-ICP-MSI. The composition of endogenous metals, ^{24}Mg, ^{66}Zn and ^{63}Cu were selected to identify the phenotypical regions of the HCC827 aggregoid model, as previously demonstrated in Chapter 3.4.3 (Flint *et al.*, 2020).

Figure 6.13 demonstrates the successful detection of ^{151}Eu signal within the treated aggregoid; no signal was observed in the corresponding control sample. The distribution of ^{151}Eu was localised at a higher signal intensity within the core of the treated aggregoid, suggesting this is where cetuximab is localised. This was validated through the contrast in distribution of ^{24}Mg and ^{66}Zn, which are both

highly expressed within the outer proliferative region. The detection of ^{151}Eu-cetuximab within the core implies the drug efficiently diffused through peripheral regions of tissue, as lower levels of ^{151}Eu can be observed within the surrounding areas.

Conversely, another possible reason of the heterogenous distribution of ^{151}Eu-cetuximab is due to the expression of the EGFR within the aggregoid model. Liu *et al.*, (2018) reported that the EGFR expression was distributed differently between two spheroid models of colon cancer (in the core of the HT 29 and in the periphery of DLD-1 MCTS), and therefore the localisation of cetuximab also differed. This suggests that the HCC827 aggregoid model highly expresses the EGFR within its core compared to the outer region. The EGFR has also been associated with hypoxia. In NSCLC, an increase in hypoxia is thought to induce the expression of the EGFR transmembrane protein in order to stimulate the expression of HIF-1α for tumour survival (Swinson & O'Byrne, 2006). Interestingly, a recent study reported hypoxia sensitises cancer cells to EGFR inhibitors (Mamo *et al.*, 2020). Therefore, the detection of cetuximab in the core of the aggregoid may correlate with a positive cellular response from metabolomics results (Chapter 5.4.2.2). Staining for the EGFR, by immunofluorescence or IMC, would be carried out in further work in order to determine its presence and confirm the co-localisation of the ^{151}Eu-cetuximab within the aggregoid model.

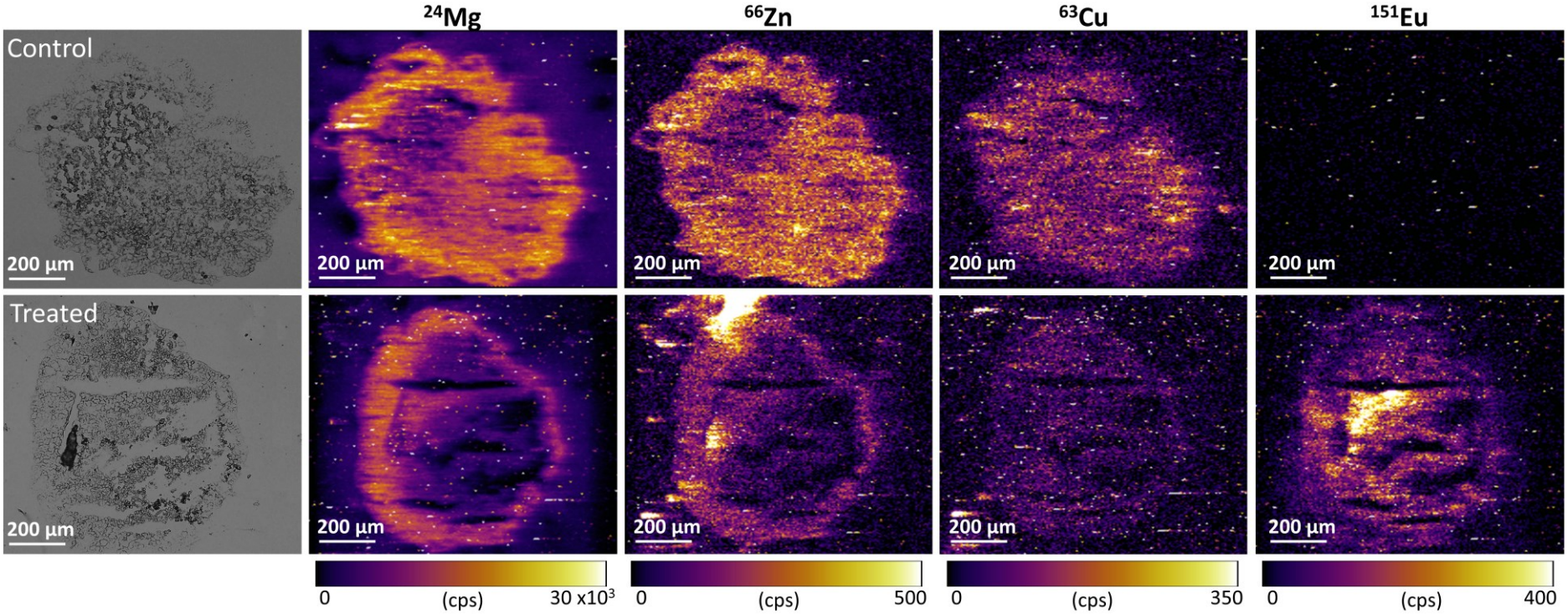

Figure 6.13 The detection of ^{151}Eu-cetuximab within a HCC827 aggregoid by LA-ICP-MSI after 24 h. Optical images of control and treated aggregoid sections. Scale bar 200 µm. Elemental distributions of ^{24}Mg, ^{66}Zn, ^{63}Cu and ^{151}Eu, intensity recorded in counts per second (cps). Slight fissures can be observed in tissues formed during sectioning.

6.5 Concluding remarks

In this chapter, two MSI strategies were developed for the detection of a biopharmaceutical, cetuximab, within the HCC827 aggregoid model.

Firstly, for a bottom-up MALDI-MSI proteomics method, a number of different workflow parameters were assessed. An optimised protocol was developed for the analysis of tryptic peptides within an aggregoid model by MALDI-MSI. Methods tested included buffer and surfactant concentrations for a suitable trypsin solution, washing solvents, incubation techniques and methods of on-tissue trypsin application.

From the data, a trypsin solution containing 25 mM NH_4HCO_3 with 0.1% (final) RapiGest™ showed a significantly higher intensity of peptide signals. Washing slides with increasing concentrations of EtOH reduced the presence of lipids within the spectra and subsequently amplified the peptide intensity. Furthermore, the use of 50% H_2O: 50% MeOH created an ideal humid environment to maintain efficient trypsin activity.

Both the spray-coat and micro-spotting methods of trypsin application require further optimisation to improve the sensitivity of the method and improve the detection of peptides. The use of alternative automated devices are likely more suitable for trypsin application in order to retain the spatial information within the aggregoid model (necessary for analyte localisation).

Following the current optimised protocol, preliminary work in the detection of cetuximab within the aggregoid model by MALDI-MSI was achieved. Additional experimental work is necessary for the validation of the method to ensure the reproducibility of the data, as well as improving the spatial capabilities of the sample preparation. Nonetheless, there has been progress towards the development of a robust proteomic imaging strategy for applications studying biopharmaceutical efficacy.

The second imaging approach by LA-ICP-MS was successful in the detection of cetuximab by a metal labelling technique. ^{151}Eu-cetuximab was localised primarily within the core of the aggregoid which demonstrated significance for determining drug delivery.

A comparison of the two methods developed in this study would indicate that the detection of a metal-labelled drug allows for a more sensitive approach to detect a biopharmaceutical within the 3D model. Though, this conflicts with the purpose of using label-free MSI techniques for drug detection in pre-clinical studies. The more favourable approach would be the bottom-up MALDI-MSI proteomics method due to the capabilities of detecting the biologic closer to its natural behaviour. In addition, MALDI-MSI allows for the simultaneous detection of the proteomic response to the treatment. The lack of a standardised protocol however, has hindered its ability for biopharmaceutical applications thus far.

Overall, using multimodal MSI techniques it was possible to detect and visualise cetuximab within the aggregoid model. This demonstrates great potential for applications in early stage biopharmaceutical development and assessing drug efficacy and toxicity.

CHAPTER 7. CONCLUSIONS AND FUTURE WORK

7.1 Overview

The analysis of 3D cell culture models by MSI has revolutionised pre-clinical drug testing. In particular, tumour spheroids have been demonstrated to have value for studying cancer metabolism and drug pharmacology in many MSI applications. Tumour spheroids offer a more accurate representation of the tumour microenvironment compared to 2D cultures, they can be produced for high throughput drug analysis without ethical implications, and they represent a valid attempt to respond to the societal requirements to implement the 3Rs – reduction, replacement and refinement – for the use of animals in such research. Whilst extensive applications of MSI in combination with tumour spheroids existed when this research started, there were still significant areas yet to be explored. Firstly, to address the conflicting arguments of whether the tumour spheroid model fully replicates the complex morphological, phenotypic and genetic characteristics of *in vivo* tumours, continuous advancements in model development is required to ensure that pharmaceutical analyses conducted using them is relevant to the *in vivo* situation. The work presented in this thesis aimed to address conflicting issues of tumour spheroids through the development a novel aggregated tumour spheroid model, termed as an aggregoid, in order to create higher levels of molecular heterogeneity. Following from this, it was important to examine the cellular metabolism that drives cancer growth within these 3D cultures in order to understand and highlight additional biomarkers that could facilitate the prediction of drug behaviour. The use of multimodal MSI techniques has previously been demonstrated as a methodology for extracting large amounts of molecular information with a complementary nature. Multimodal MSI was therefore employed in this study to enable an in-depth characterisation of the aggregoid models. In addition, a multimodal MSI strategy in combination with the aggregoid model was developed for the use as a pre-clinical *in vitro* tool for biopharmaceutical testing in order to address the increasing demands for advancements in this field in pharmaceutical industry.

7.2 Aggregoid optimisation for MSI analysis

The development of three aggregoid models of cancer was achieved, two osteosarcoma models: one from the epithelial-like cell line SAOS-2 and one from the fibroblast-like cell line MG63; and a HCC827 lung adenocarcinoma model.

The purpose of developing a novel 3D culture model was to enhance the molecular heterogeneity to establish a more accurate representation of *in vivo*. The method in which the aggregoid models were cultured allowed for the development of single-cell populations to grow into individual spheroid colonies of different sizes and genetic variability. Therefore, once aggregated together, they created a tissue comprised of clonal spheroids that exhibit different genetic phenotypes which are easier to detect and interpret than a heterogeneous single cell within an conventional MCTS model. It is suggested aggregoid model represents the tumour microenvironment by displaying phenotypical regions of a hypoxic/necrotic core and a proliferative outer region developed through the gradient of oxygen and nutrients. The expression of these tumour environments was an important attribute in order to the study a drug's behaviour and efficacy in heterogenous regions of the *in vitro* model.

In order to efficiently analyse the aggregoid model, it was a requirement to optimise sample handling methods for universal application across MSI techniques. The use of an embedding media, HPMC & PVP, enabled preservation of the aggregoid tissues and created ease of handling samples throughout the imaging workflow. The addition of immediate desiccation of tissue sections followed by vacuum packing samples prior to storage effectively minimised delocalisation effects of analytes within the aggregoids allowing for quality imaging analysis. The spray-coat application of matrix gave a better sensitivity for the detection of lipid species in heterogenous distributions that corresponded to the hypoxic core and outer proliferative zone. Further investigations to improve the quality of the images and reduced delocalisation of lipids during matrix deposition is still required, such as optimising the spraying parameters and solvent concentrations, or an investigation of a recrystallisation step following from matrix application by sublimation.

7.3 Multimodal MSI: Characterisation of a lung adenocarcinoma aggregoid

The use of different MSI techniques enabled an in-depth characterisation of the tumour microenvironment within the lung adenocarcinoma model, allowing detailed molecular phenotyping based on the endogenous metabolite, protein and metal content. An untargeted DESI-MSI method highlighted the metabolic

activity of central biological pathways including the TCA cycle and glycolysis in relation to proliferative activity and the hypoxic core. The first application of IMC with a 3D cell culture was reported which enabled single-cell phenotyping of proteins and protein modifications including the detection of Glut1 expression which highlighted the hypoxic core and corresponded to the lactate distribution. The use of LA-ICP-MSI detected endogenous metals including Mg, Zn and Cu and complemented the DESI and IMC data. As this was an initial study, additional biological replicates and technical repeats imaging different slides of the same samples are now required to validate this methodology of characterising the aggregoid model. Nevertheless, this work still improved the understanding of the molecular activity that influences the tumour microenvironment. Following on from this study, further data processing of the untargeted DESI-MSI data could be performed to highlight all detected metabolites within the lung model to obtain a larger metabolic prolife.

7.4 Multimodal MSI: Comparison of OS aggregoid models to sarcoma tissue

It is important to ensure that any 3D cell culture model aimed to be used in pre-clinical drug analysis exhibits similar molecular characteristics to *in vivo* tumours. A comparison between the two OS models and clinical OS patient tissue was performed using an untargeted DESI-MSI approach. In these experiments metabolic similarities were observed. MG63 exhibited metastatic-like potential due to the detection of fatty acid and phospholipid species that were also detected at high concentrations in the metastatic patient tissue. SAOS-2, on the other hand, showed potential characteristics of cellular differentiation and bone development, which were identified within specific regions of bone mineralisation in the OS patient tissue. To validate these findings further work involving direct imaging analysis of the aggregoid models and OS patient tissue within the same acquisition is essential. In addition, imaging MS/MS analysis and/or LC-MS/MS is required for confident identification of metabolite species detected in this study.

The IMC and LA-ICP-MSI techniques were also employed to enhance the characterisation of the models and showed heterogeneity in the expression of proteins and metal compositions. The SAOS-2 model displayed the typical outer proliferative region (Ki-67) within an inner hypoxic core (Glut1), similar to the lung

adenocarcinoma model, as the MG63 model did not show the presence of such distinct regions. The phenotypical differences demonstrated the need for characterising the aggregoids by multimodal imaging techniques to validate the unique molecular distributions across OS tumour models and to understand how these differences could influence drug behaviour.

7.5 Aggregoid response to biopharmaceutical treatment

To establish the use of the aggregoid model as a pre-clinical tool for biopharmaceutical testing by MSI, the metabolic response to biologic treatment in each model was studied using DESI-MSI. The use of multivariate statistics (PCA and PLS-DA) allowed for the identification of potential biomarkers that showed changes in detection levels in response to treatment. However, the overall response of the aggregoids was limited suggesting a potential drug resistance. As this limited response was observed across all three models it suggested that the potential resistance is due to the method in which the aggregoids are cultured. Increasing evidence has showed the development of spheroid cultures promoted resistance to cell death via anoikis, which leads to alterations in the apoptotic extrinsic and intrinsic pathways and thus subsequently leads to the resistance to drug-induced cell death such as treatment with TRAIL-based therapies or Cetuximab. Future work would investigate this mechanism of resistance through the treatment of specific inhibitors that re-establish anoikis s and to use inhibitors in combination with biologic therapies to determine the metabolic response.

Following the untargeted DESI-MSI approach, LC-MS/MS is a necessary requirement for the confident identification of metabolites detected and to validate the method as a suitable pre-clinical biopharmaceutical analysis tool. In addition, due to the variability between aggregoid samples it is essential to include more biological replicates to improve the discrimination of metabolites. The overall study however still demonstrated a potential strategy for the analysis of biologic treatment in the aggregoid model by MSI from the detection of significant metabolic changes in the preliminary data.

7.6 Development of a multimodal MSI strategy for biopharmaceutical detection

A lack of metabolic response to treatment could be due to the inefficiency of drug delivery within the aggregoid model. In an attempt to understand the potential drug resistance within the aggregoid model, a MSI strategy to detect the biopharmaceutical, cetuximab within the lung adenocarcinoma model was developed. The ability to detect a drug within tissues by imaging techniques allows for the direct assessment of how a therapeutic penetrates, distributes and metabolises and is thus essential for early stage pre-clinical drug analysis.

In chapter 6, two MSI techniques were developed. Firstly, a bottom-up MALDI-MSI proteomics strategy was used to detect cetuximab's constituent proteotypic peptides that contained unique CDRs for valid identification. This approach involved the optimisation of trypsin solution, sample washing, incubation techniques, and methods of trypsin application. Further investigations in the trypsin deposition is required in order to improve the sensitivity of peptide detection whilst retaining the spatial information. However, by using the micro-spotting technique preliminary data showed small amounts of cetuximab peptides were detected within the lung adenocarcinoma aggregoid model at the expense of spatially localising the therapeutic. Additional experimental work is required to ensure reproducibility of the method with the aim of utilising this approach for a quantitative application in future analysis.

The second method of biologic detection employed a targeted approach based on the principles of IMC using metal-tagged antibodies for the detection of proteins. In this study, cetuximab was tagged with ^{151}Eu which was then used to treat the aggregoids in culture. Following the standard LA-ICP-MSI workflow, the detection of ^{151}Eu-cetuximab localised within the core of the HCC827 aggregoid model was achieved. Although this method conflicts with the purpose of using a label-free MSI approach for drug detection, it is an example of the use of multimodal imaging techniques to validate and complement data of the MALDI-MSI method which lacks a current standardised protocol for proteotypic peptide detection. The detection of cetuximab within the HCC827 aggregoid model also suggests that the potential drug resistance observed from the metabolomics study is not related to a delivery issue, although further investigations into the

detection of TRAIL-based therapies within the OS aggregoid models would be required to confirm this.

7.7 Final conclusions

The aim of this thesis was to develop a multimodal MSI approach to analyse a novel aggregated tumour model for applications in pre-clinical biopharmaceutical testing. The work reported here shows the culture and development of the aggregoid model for the universal use across various MSI techniques. It demonstrated the importance of characterising the wide molecular content within the tissues for knowledge of the biological processes that drive their unique cancer metabolism. The combination of multimodal MSI with the aggregoid model showed capacity of spatially resolving metabolite changes in response to biologic treatment, in addition to the detection of a biopharmaceutical through the development of novel methods that could be used to understand biologic efficacy and toxicity.

APPENDIX I

Figure A.1. Mean intensity plotted on bar graph of fatty acid detection within OS human tissue and OS aggregoid models. Data is mean ± SD (n=3), unpaired t-test * $p < 0.05$, ** $p < 0.01$. Peaks identified in human tissue a) *m/z* 279.234, FA 18:2; b) *m/z* 281.247, FA 18:1; c) *m/z* 303.231, FA 20:4. Peaks identified in OS models d) *m/z* 279.235, FA 18:2; e) *m/z* 281.248, FA 18:1; f) *m/z* 303.231, FA 20:4.

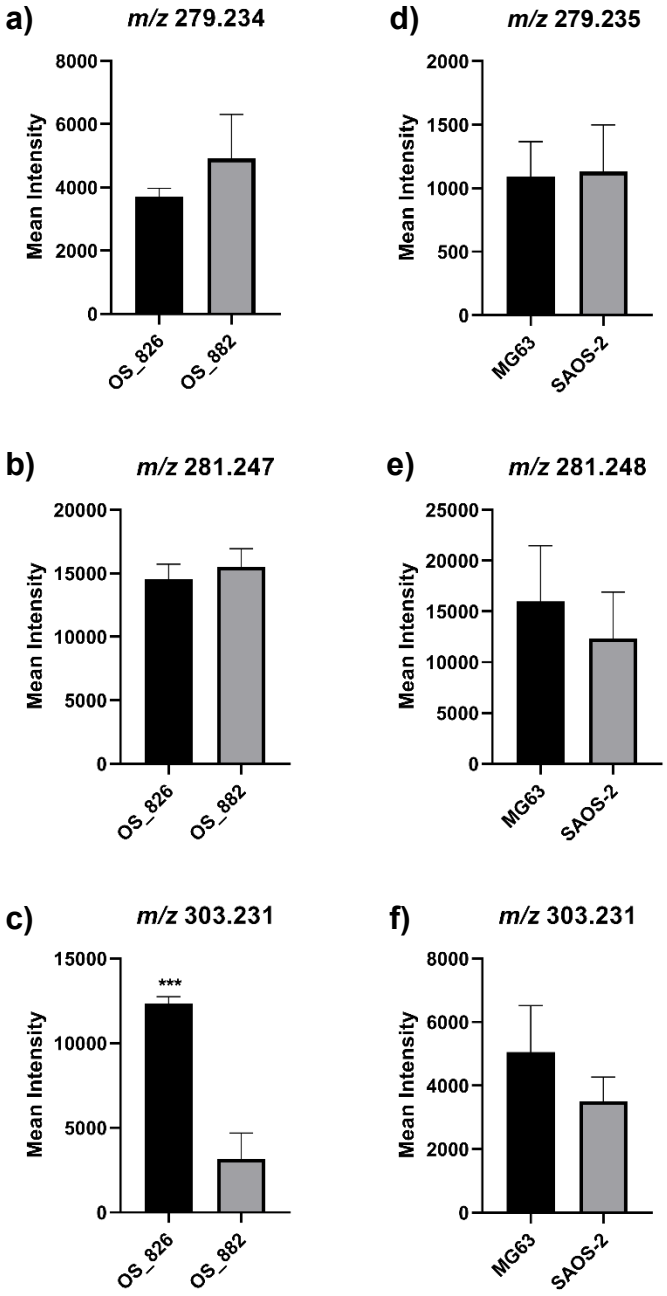

Figure A.2. Mean intensity plotted on bar graph of metastasis-related phospholipid species within OS human tissue and OS aggregoid models. Data is mean ± SD (n=3), unpaired t-test * $p < 0.05$, ** $p < 0.01$. Peaks identified in human tissue a) *m/z* 810.528, PS 38:4; b) *m/z* 885.550, PI 38:4. Peaks identified in OS models d) *m/z* 810.530, PS 38:4; e) *m/z* 885.549, PI 38:4.

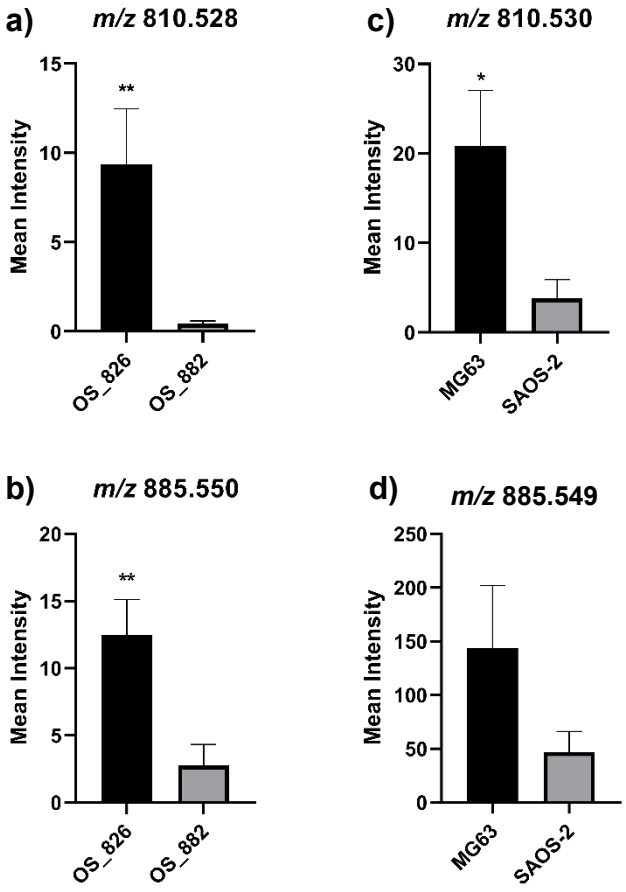

Figure A.3. Mean intensity plotted on bar graph of ceramide species detected within OS human tissue and OS aggregoid models. Data is mean ± SD (n=3), unpaired t-test * $p < 0.05$, ** $p < 0.01$, *** $p < 0.001$. Peaks identified is human tissue a) *m/z* 536.505, Cer 34:1;O2; b) *m/z* 572.484, Cer 34:1;O2 $[M+Cl]^-$. Peaks identified in OS models c) *m/z* 536.504, Cer 34:1;O2; d) *m/z* 572.480, Cer 34:1;O2 $[M+Cl]^-$.

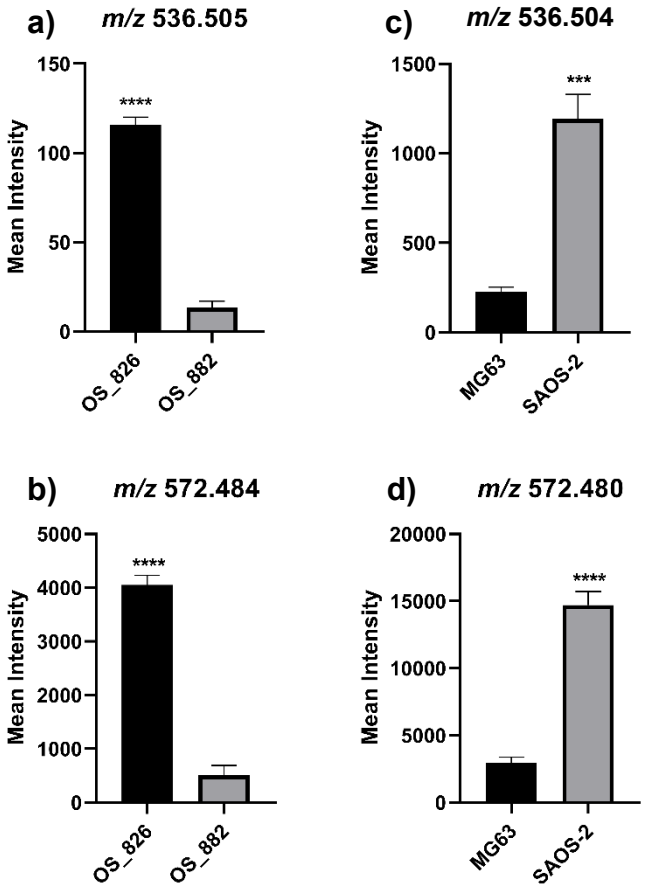

APPENDIX II

Scientific publications

Spencer, C. E; **Flint, L. E**; Duckett, C. J; Cole, L. M; Cross, N; Smith, D. P; Clench, M. R. Role of MALDI-MSI in Combination with 3D Tissue Models for Early Stage Efficacy and Safety Testing of Drugs and Toxicants. (2021). *Expert Rev. Proteomics.* 17 (11-12) 827-841. doi: 10.1080/14789450.2021.1876568

Flint, L. E; Hamm, G., Ready, J. D.; Ling, S.; Duckett, C. J.; Cross, N. A.; Cole, L. M.; Smith, D. P.; Goodwin, R. J. A.; Clench, M. C. The Characterisation of an Aggregated Three-Dimensional Cell Culture Model by Multimodal Mass Spectrometry Imaging. (2020). *Anal. Chem.* 92 (18) 12538–12547. doi: 10.1021/acs.analchem.0c02389

Russo, C; Heaton, C; **Flint, L**; Voloaca, O; Haywood-Small, S; Clench, M. R; Francese, S; Cole, L. M. Emerging applications in mass spectrometry imaging; enablers and roadblocks. (2020). *J. Spectral Imaging.* 9 a13. doi.org/10.1255/jsi.2020.a13

Russo, C.; Lewis, E. E. L.; **Flint, L.**; Clench, M. R. Mass Spectrometry Imaging of 3D Tissue Models. (2018). *Proteomics.* 18, e1700462. doi: 10.1002/pmic.201700462

Oral Presentations

Multimodal MSI: A Method to Characterise a Novel Aggregated 3D Cell Culture Model for Potential Biopharmaceutical Applications. *24h International Mass Spectrometry Imaging, virtual conference (2020)*

Progress in Biopharmaceutical Detection in An Aggregated 3D Model by Mass Spectrometry Imaging. *40th BMSS Annual Conference, Manchester, UK (2019)*

Progress in Biopharmaceutical Detection in An Aggregated 3D Model by Mass Spectrometry Imaging. *6th BMSS Imaging Symposium, Sheffield, UK (2019)*

Detection of Bevacizumab in a 3D Osteosarcoma Model using Mass Spectrometry Imaging. *4th RSC DMDG/DMG New perspectives in DMPK, London, UK (2018)*

Poster Presentations

Multimodal MSI: A Method to Characterise a Novel Aggregated 3D Cell Culture Model for Potential Biopharmaceutical Applications. *I2RI Winter poster event, Sheffield Hallam University, Sheffield, UK (2020)* ***(1st Poster Prize & Public Vote Prize)***

Multimodal MSI: A Method to Characterise a Novel Aggregated 3D Cell Culture Model for Potential Biopharmaceutical Applications. *24h International Mass Spectrometry Imaging Poster Gala, virtual conference (2020)*

The Characterisation of an Aggregated Three-Dimensional Cell Culture Model by Multimodal Mass Spectrometry Imaging. *BMRC/MERI Winter poster event, Sheffield Hallam University, Sheffield, UK (2019)* ***(3rd Poster Prize)***

Progress in Biopharmaceutical Detection in An Aggregated 3D Model by Multimodal Mass Spectrometry Imaging. *67th ASMS Annual Conference, Atlanta, USA (2019)*

Progress in Biopharmaceutical Detection in An Aggregated 3D Model by Mass Spectrometry Imaging. *6th BMSS Imaging Symposium, Sheffield, UK (2019)*

Progress in Biopharmaceutical Detection in An Aggregated 3D Model by Mass Spectrometry Imaging. *39th BMSS Annual Meeting, Cambridge, UK (2018)*

Progress in Biopharmaceutical Detection in An Aggregated 3D Model by Mass Spectrometry Imaging. *66th ASMS Annual Conference, San Diego, USA (2018)*

Detection of Bevacizumab in a 3D Osteosarcoma Model using Mass Spectrometry Imaging. *4th RSC DMDG/DMG New perspectives in DMPK, London, UK (2018)*

Laboratory visits

MSI Laboratory, AstraZeneca, Cambridge, UK: 4-weeks March 2019; 4-weeks September 2019; 1-week February 2020

Workshops

BMSS Introduction to Mass Spectrometry 2018

REFERENCES

Aerni, H-R., Cornett, D. S., & Caprioli, R. M. (2006). Automated acoustic matrix deposition for MALDI sample preparation. *Analytical Chemistry, 78(3),* 827-834. doi.org/10.1021/ac051534r

Ahlf Wheatcraft, D. R., Liu, X., & Hummon, A. B. (2014). Sample preparation strategies for mass spectrometry imaging of 3D cell culture models. *Journal of Visualized Experiments,* (94). doi:10.3791/52313

Ahlf, D. R., Masyuko, R. N., Hummon, A. B., & Bohn, P. W. (2014). Correlated mass spectrometry imaging and confocal raman microscopy for studies of three-dimensional cell culture sections. *Analyst, 139*(18), 4578-4585. doi:10.1039/C4AN00826J

Aikawa, H., Hayashi, M., Ryu, S., Yamashita, M., Ohtsuka, N., Nishidate, M., Yasuhiro, F., & Hamada, A. (2016). Visualizing spatial distribution of alectinib in murine brain using quantitative mass spectrometry imaging. *Scientific Reports, 6*(1), 23749. doi:10.1038/srep23749

Airley, R., Loncaster, J., Davidson, S., Bromley, M., Roberts, S., Patterson, A., Hunter, R., Stratford, R., & West, C. (2001). Glucose transporter glut-1 expression correlates with tumor hypoxia and predicts metastasis-free survival in advanced carcinoma of the cervix. *Clinical Cancer Research, 7*(4), 928-934.

Ait-Belkacem, R., Berenguer, C., Villard, C., Ouafik, L., Figarella-Branger, D., Beck, A., Chinot, O., & Lafitte, D. (2014). Monitoring therapeutic monoclonal antibodies in brain tumor. *mAbs, 6*(6), 1385-1393. doi:10.4161/mabs.34405

Akeda, K., Nishimura, A., Satonaka, H., Shintani, K., Kusuzaki, K., Matsumine, A., Kasai, Y.,, Masuda., & Uchida, A. (2009). Three-dimensional alginate spheroid culture system of murine osteosarcoma. *Oncology Reports, 22*(5), 997-1003. doi:10.3892/or_00000527

Akizuki, R., Maruhashi, R., Eguchi, H., Kitabatake, K., Tsukimoto, M., Furuta, T., Matsunaga, T., Endo, S., & Ikari, A. (2018). Decrease in paracellular permeability and chemosensitivity to doxorubicin by claudin-1 in spheroid culture models of human lung adenocarcinoma A549 cells. *BBA - Molecular Cell Research, 1865*(5), 769-780. doi:10.1016/j.bbamcr.2018.03.001

Amann, J., Kalyankrishna, S., Massion, P. P., Ohm, J. E., Girard, L., Shigematsu, H., Peyton, M., Juroske, D., Huang, Y., Salmon., Young, K. H., Pollack, J. R., KYanagisawa, K., Gazdar,A., Minna, J. D., Kurie, J. M., & Carbone, D. P. (2005). Aberrant epidermal growth factor receptor signaling and enhanced sensitivity to EGFR inhibitors in lung cancer. *Cancer Research, 65*(1), 226-235.

Angel, P. M., Spraggins, J. M., Baldwin, H. S., & Caprioli, R. (2012). Enhanced sensitivity for high spatial resolution lipid analysis by negative ion mode matrix assisted laser desorption ionization imaging mass spectrometry. *Analytical Chemistry, 84*(3), 1557-1564. doi:10.1021/ac202383m

Araujo, J., & Logothetis, C. (2010). Dasatinib: A potent SRC inhibitor in clinical development for the treatment of solid tumors. *Cancer Treatment Reviews, 36*(6), 492-500. doi:10.1016/j.ctrv.2010.02.015

Armstrong, J. S., Steinauer, K. K., Hornung, B., Irish, J. M., Lecane, P., Birrell, G. W., Peehl, D. M., & Knox, S. J. (2002). Role of glutathione depletion and reactive oxygen species generation in apoptotic signaling in a human B lymphoma cell line. *Cell Death and Differentiation, 9*(3), 252-263. doi:10.1038/sj.cdd.4400959

Artimo, P., Jonnalagedda, M., Arnold, K., Baratin, D., Csardi, G., de Castro, E., Duvaud, S., Flegel, V., Fortier, A., Gasteiger, E., Grosdidier, A., Hernandez, C., Ioannidis, V., Kuznetsov, D., Liechti R., Moretti, S., Mostaguir, K., Redaschi, N., Rossier, G., Xeanrios, I., & Stockinger, H. (2012). ExPASy: SIB bioinformatics resource portal. *Nucleic Acids Research, 40*, W597-W603. doi:10.1093/nar/gks400

Avery, J. L., McEwen, A., Flinders, B., Francese, S., & Clench, M. R. (2011). Matrix-assisted laser desorption mass spectrometry imaging for the examination of imipramine absorption by straticell-RHE-EPI/001 an artificial model of the human epidermis. *Xenobiotica, 41*(8), 735-742. doi:10.3109/00498254.2011.573015

Barré, F. P. Y., Paine, M. R. L., Flinders, B., Trevitt, A. J., Kelly, P. D., Ait-Belkacem, R., Garcia, J. P., Creemer, L. B., Stauber, J., Vreeken, R. J., Cillero-Pastor, B., Ellis, S. R., & Heeren, R. M. A. (2019). Enhanced sensitivity using MALDI imaging coupled with laser postionization (MALDI-2) for pharmaceutical

research. *Analytical Chemistry, 91*(16), 10840-10848. doi:10.1021/acs.analchem.9b02495

Bartosh, T. J., Ylöstalo, J. H., Mohammadipoor, A., Bazhanov, N., Coble, K., Claypool, K., Hwa Lee, R., Choi, H., & Prockop, D. J. (2010). Aggregation of human mesenchymal stromal cells (MSCs) into 3D spheroids enhances their antiinflammatory properties. *Proceedings of the National Academy of Sciences of the United States of America, 107*(31), 13724-13729. doi:10.1073/pnas.1008117107

Bassi, G., Panseri, S., Dozio, S. M., Sandri, M., Campodoni, E., Dapporto, M., Sprio, S., Tampieri, A., & Montesi, M. (2020). Scaffold-based 3D cellular models mimicking the heterogeneity of osteosarcoma stem cell niche. *Scientific Reports, 10*(1), 22294. doi:10.1038/s41598-020-79448-y

Baumann, S., & Hennet, T. (2016). Collagen accumulation in osteosarcoma cells lacking GLT25D1 collagen galactosyltransferase. *The Journal of Biological Chemistry, 291*(35), 18514-18524. doi:10.5167/uzh-130488

Becker, J. S. (2013). Imaging of metals in biological tissue by laser ablation inductively coupled plasma mass spectrometry (LA–ICP–MS): State of the art and future developments. *Journal of Mass Spectrometry., 48*(2), 255-268. doi:10.1002/jms.3168

Beloribi-Djefaflia, S., Vasseur, S., & Guillaumond, F. (2016). Lipid metabolic reprogramming in cancer cells. *Oncogenesis, 5*(1), e189. doi:10.1038/oncsis.2015.49

Bergmann, S., Lawler, S. E., Qu, Y., Fadzen, C. M., Wolfe, J. M., Regan, M. S., Pentelute, B. L., Agar, N. Y. R., & Cho, C. (2018). Blood–brain-barrier organoids for investigating the permeability of CNS therapeutics. *Nature Protocols, 13*(12), 2827-2843. doi:10.1038/s41596-018-0066-x

Black, A. R., & Black, J. D. (2013). Protein kinase C signaling and cell cycle regulation. *Frontiers in Immunology, 3*, 423. doi:10.3389/fimmu.2012.00423

Borin, T. F., Angara, K., Rashid, M. H., Achyut, B. R., & Arbab, A. S. (2017). Arachidonic acid metabolite as a novel therapeutic target in breast cancer metastasis. *International Journal of Molecular Sciences, 18*(12), 2661. doi:10.3390/ijms18122661

Bouzekri, A., Esch, A., & Ornatsky, O. (2019). Multidimensional profiling of drug-treated cells by imaging mass cytometry. *FEBS Open Bio, 9*(9), 1652-1669. doi:10.1002/2211-5463.12692

Brand, T. M., Iida, M., & Wheeler, D. L. (2011). Molecular mechanisms of resistance to the EGFR monoclonal antibody cetuximab. *Cancer Biology & Therapy, 11*(9), 777-792. doi:10.4161/cbt.11.9.15050

Bresciani, G., Hofland, L., Dogan, F., Giamas, G., Gagliano, T., & Zatelli, M. C. (2019). Evaluation of spheroid 3D culture methods to study a pancreatic neuroendocrine neoplasm cell line. *Frontiers in Endocrinology, 10*, 682. doi:10.3389/fendo.2019.00682

Brown, S. C., Kruppa, G., & Dasseux, J. (2005). Metabolomics applications of FT-ICR mass spectrometry. *Mass Spectrometry Reviews, 24*(2), 223-231. doi:10.1002/mas.20011

Buchberger, A. R., DeLaney, K., Johnson, J., & Li, L. (2018). Mass spectrometry imaging: A review of emerging advancements and future insights. *Analytical Chemistry, 90*(1), 240-265. doi:10.1021/acs.analchem.7b04733

Büchler, P., Reber, H. A., Büchler, M., Shrinkante, S., Büchler, M. W., Friess, H., Semenza, G. L., & Hines, O. J. (2003). Hypoxia-inducible factor 1 regulates vascular endothelial growth factor expression in human pancreatic cancer. *Pancreas, 26*(1), 56-64. doi:10.1097/00006676-200301000-00010

Cangul, H. (2004). Hypoxia upregulates the expression of the NDRG1 gene leading to its overexpression in various human cancers. *BMC Genetics, 5*(1), 27. doi:10.1186/1471-2156-5-27

Chalhoub, N., & Baker, S. J. (2009). PTEN and the PI3-kinase pathway in cancer. *Annual Review of Pathology, 4*(1), 127-150. doi:10.1146/annurev.pathol.4.110807.092311

Chambers, M. C., Maclean, B., Burke, R., Amodei, D., Ruderman, D. L., Neumann, S., Gatto, L., Fischer, B., Pratt, B., Egertson, J., Hoff, K., Kessner, D., Tasman, N. Shulman, N., Frewen, B., Baker, T. A., Brukmiak, M-Y., Paulse, C., Creasy, D., Flashner, L., Kani, K., Moulding, C., Seymour, S. L., Nuwaysir, L. M., Lefebrve, B., Kuhlmann, F., Roark, J., Rainer, P., Detlev, S., Hemenway, T., Huhmer, A., Langridge, J., Connolly, B., Chadick, R., Holly, K., Eckels, J.,

Deutsch, E. W., Moritz, R. L., Katz, J. E., Agus, D. B., MacCoss, M., Tabb, D. L., & Mallick, P. (2012). A cross-platform toolkit for mass spectrometry and proteomics. *Nature Biotechnology, 30*(10), 918-920. doi:10.1038/nbt.2377

Chandrasekaran, S., Marshall, J. R., Messing, J. A., Hsu, J., & King, M. R. (2014). TRAIL-mediated apoptosis in breast cancer cells cultured as 3D spheroids. *PloS One, 9*(10), e111487. doi:10.1371/journal.pone.0111487

Chang, Q., Ornatsky, O. I., Siddiqui, I., Loboda, A., Baranov, V. I., & Hedley, D. W. (2017). Imaging mass cytometry. *Cytometry Part A, 91*(2), 160-169. doi:10.1002/cyto.a.23053

Chang, Q., Ornatsky, O. I., Siddiqui, I., Straus, R., Baranov, V. I., & Hedley, D. W. (2016). Biodistribution of cisplatin revealed by imaging mass cytometry identifies extensive collagen binding in tumor and normal tissues. *Scientific Reports, 6*(1), 36641. doi:10.1038/srep36641

Chen, E. I., Cociorva, D., Norris, J. L., & Yates, J. R. (2007). Optimization of mass spectrometry-compatible surfactants for shotgun proteomics. *Journal of Proteome Research, 6*(7), 2529-2538. doi:10.1021/pr060682a

Chen, E. I., McClatchy, D., Park, S. K., & Yates III, J. R. (2008). Comparisons of mass spectrometry compatible surfactants for global analysis of the mammalian brain proteome. *Analytical Chemistry, 80*(22), 8694-8701. doi:10.1021/ac800606w

Chen, H., Talaty, N. N., Takáts, Z., & Cooks, R. G. (2005). Desorption electrospray ionization mass spectrometry for high-throughput analysis of pharmaceutical samples in the ambient environment. *Analytical Chemistry, 77*(21), 6915-6927. doi:10.1021/ac050989d

Chen, J., Hsieh, Y., Knemeyer, I., Crossman, L., & Korfmacher, W. A. (2008). Visualization of first-pass drug metabolism of terfenadine by MALDI-imaging mass spectrometry. *Drug Metabolism Letters, 2*(1), 1.

Chen, L., Randtke, E., Jones, K., Moon, B., Howison, C., & Pagel, M. (2015). Evaluations of tumor acidosis within in vivo tumor models using parametric maps generated with AcidoCEST MRI. *Molecular Imaging and Biology, 17*(4), 488-496. doi:10.1007/s11307-014-0816-2

Chen, Q., Wu, J., Zhang, Y., & Lin, J. (2012). Qualitative and quantitative analysis of tumor cell metabolism via stable isotope labeling assisted microfluidic chip electrospray ionization mass spectrometry. *Analytical Chemistry, 84*(3), 1695-1701. doi:10.1021/ac300003k

Cheng, M., Bhujwalla, Z. M., & Glunde, K. (2016). Targeting phospholipid metabolism in cancer. *Frontiers in Oncology, 6*, 266. doi:10.3389/fonc.2016.00266

Chiu, D. T., deMello, A. J., Di Carlo, D., Doyle, P. S., Hansen, C., Maceiczyk, R. M., & Wootton, R. C. R. (2017). Small but perfectly formed? Successes, challenges, and opportunities for microfluidics in the chemical and biological sciences. *Chem, 2*(2), 201-223. doi:10.1016/j.chempr.2017.01.009

Chughtai, S., Chughtai, K., Cillero-Pastor, B., Kiss, A., Agrawal, P., MacAleese, L., & Heeren, R. M. A. (2012). A multimodal mass spectrometry imaging approach for the study of musculoskeletal tissues. *International Journal of Mass Spectrometry, 325-327*, 150-160. doi:10.1016/j.ijms.2012.07.008

Cifuentes, M., García, M. A., Arrabal, P. M., Martínez, F., Yañez, M. J., Jara, N., Weil, B., Dominguez, D., Medina, R.A., & Nualart, F. (2011). Insulin regulates GLUT1-mediated glucose transport in MG-63 human osteosarcoma cells. *Journal of Cellular Physiology, 226*(6), 1425-1432. doi:10.1002/jcp.22668

Cillero-Pastor, B., & Heeren, R. M. A. (2014). Matrix-assisted laser desorption ionization mass spectrometry imaging for peptide and protein analyses: A critical review of on-tissue digestion. *Journal of Proteome Research, 13*(2), 325-335. doi:10.1021/pr400743a

Cole, L. M., Djidja, M., Bluff, J., Claude, E., Carolan, V. A., Paley, M., Tozer, G., M., & Clench, M. R. (2011). Investigation of protein induction in tumour vascular targeted strategies by MALDI MSI. *Methods, 54*(4), 442-453. doi:10.1016/j.ymeth.2011.03.007

Collin, P., Nefussi, J. R., Wetterwald, A., Nicolas, V., Boy-Lefevre, M., Fleisch, H., & Forest, N. (1992). Expression of collagen, osteocalcin, and bone alkaline phosphatase in a mineralizing rat osteoblastic cell culture. *Calcified Tissue International, 50*(2), 175-183. doi:10.1007/BF00298797

Comi, T. J., Do, T. D., Rubakhin, S. S., & Sweedler, J. V. (2017). Categorizing cells on the basis of their chemical profiles: Progress in single-cell mass spectrometry. *Journal of the American Chemical Society, 139*(11), 3920-3929. doi:10.1021/jacs.6b12822

Coroller, T. P., Grossmann, P., Hou, Y., Rios Velazquez, E., Leijenaar, R. T. H., Hermann, G., Lambin, P., Haibe-Kains, B., Mak, R. H., & Aerts, Hugo J. W. L. (2015). CT-based radiomic signature predicts distant metastasis in lung adenocarcinoma. *Radiotherapy and Oncology, 114*(3), 345-350. doi:10.1016/j.radonc.2015.02.015

Costa, E. C., Gaspar, V. M., Coutinho, P., & Correia, I. J. (2014). Optimization of liquid overlay technique to formulate heterogenic 3D co-cultures models. *Biotechnology and Bioengineering, 111*(8), 1672-1685. doi:10.1002/bit.25210

Crespo, M., Vilar, E., Tsai, S., Chang, K., Amin, S., Srinivasan, T., Zhang, T., Pipalia, N. H., Chen, H. J., Witherspoon, M., & Gordillo, M. (2017). Colonic organoids derived from human induced pluripotent stem cells for modeling colorectal cancer and drug testing. *Nature Medicine, 23*(7), 878-884. doi:10.1038/nm.4355

Cui, X., Han, Z., He, S., Wu, X., Chen, T., Shao, C., Chen, D-L., Su, N., Chen, Y-M., Wang, T., Wang J., Song, D-W., Yan, W-J., Yang, X-H., Liu, T., Wei., & Xiao, J. (2017). HIF1/2α mediates hypoxia-induced LDHA expression in human pancreatic cancer cells. *Oncotarget, 8*(15), 24840-24852. doi:10.18632/oncotarget.15266

Curcio, E., Salerno, S., Barbieri, G., De Bartolo, L., Drioli, E., & Bader, A. (2007). Mass transfer and metabolic reactions in hepatocyte spheroids cultured in rotating wall gas-permeable membrane system. *Biomaterials, 28*(36), 5487-5497. doi:10.1016/j.biomaterials.2007.08.033

Dannhorn, A., Kazanc, E., Ling, S., Nikula, C., Karali, E., Serra, M. P., Vorng, J-L., Inglese, P., Maglennon, G., Hamm, G., Swales, J., Strittmatter, N., Barry S. T., Sansom, O. J., Poulogiannis, G., Bunch, J., Goodwin, R. J. A., & Takats, Z. (2020). Universal sample preparation unlocking multimodal molecular tissue imaging. *Analytical Chemistry,* doi:10.1021/acs.analchem.0c00826

Das, V., Fürst, T., Gurská, S., Džubák, P., & Hajdúch, M. (2017). Evaporation-reducing culture condition increases the reproducibility of multicellular spheroid formation in microtiter plates. *Journal of Visualized Experiments,* (121). doi:10.3791/55403

Däster, S., Amatruda, N., Calabrese, D., Ivanek, R., Turrini, E., Droeser, R. A., Zajac, P., Fimognaria, C., Spagnoli, G. C., Iezzi, G., Mele, V., & Muraro, M. G. (2017). Induction of hypoxia and necrosis in multicellular tumor spheroids is associated with resistance to chemotherapy treatment. *Oncotarget, 8*(1), 1725-1736. doi:10.18632/oncotarget.13857

David, B. P., Dubrovskyi, O., Speltz, T. E., Wolff, J. J., Frasor, J., Sanchez, L. M., & Moore, T. W. (2018). Using tumor explants for imaging mass spectrometry visualization of unlabeled peptides and small molecules. *ACS Medicinal Chemistry Letters, 9*(7), 768-772. doi:10.1021/acsmedchemlett.8b00091

Deininger, L., Patel, E., Clench, M. R., Sears, V., Sammon, C., & Francese, S. (2016). Proteomics goes forensic: Detection and mapping of blood signatures in fingermarks. *Proteomics, 16*(11-12), 1707-1717. doi:10.1002/pmic.201500544

Denti, V., Piga, I., Guarnerio, S., Clerici, F., Ivanova, M., Chinello, C., Paglia, G., Magni, F., & Smith, A. (2020). Antigen retrieval and its effect on the MALDI-MSI of lipids in formalin-fixed paraffin-embedded tissue. *Journal of the American Society for Mass Spectrometry, 31*(8), 1619-1624. doi:10.1021/jasms.0c00208

Dexter, A., Race, A. M., Styles, I. B., & Bunch, J. (2016). Testing for multivariate normality in mass spectrometry imaging data: A robust statistical approach for clustering evaluation and the generation of synthetic mass spectrometry imaging data sets. *Analytical Chemistry, 88*(22), 10893-10899. doi:10.1021/acs.analchem.6b02139

Dexter, A., Steven, R. T., Patel, A., Dailey, L. A., Taylor, A. J., Ball, D., Klapwijk, J., Forbers, B., Page, C. P., & Bunch, J. (2019). Imaging drugs, metabolites and biomarkers in rodent lung: A DESI MS strategy for the evaluation of drug-induced lipidosis. *Analytical and Bioanalytical Chemistry, 411*(30), 8023-8032. doi:10.1007/s00216-019-02151-z

Díaz-Montero, C. M., Wygant, J. N., & McIntyre, B. W. (2006). PI3-K/akt-mediated anoikis resistance of human osteosarcoma cells requires src activation.

European Journal of Cancer (1990), 42(10), 1491-1500. doi:10.1016/j.ejca.2006.03.007

Diehl, H. C., Beine, B., Elm, J., Trede, D., Ahrens, M., Eisenacher, M., Marcus, K., Meyer, H. E., & Henkel, C. (2015). The challenge of on-tissue digestion for MALDI MSI - a comparison of different protocols to improve imaging experiments. *Analytical and Bioanalytical Chemistry, 407*(8), 2223-2243. doi:10.1007/s00216-014-8345-z

Dill, A., Eberlin, L., Costa, A., Ifa, D., & Cooks, R. (2011). Data quality in tissue analysis using desorption electrospray ionization. *Analytical and Bioanalytical Chemistry, 401*(6), 1949-1961. doi:10.1007/s00216-011-5249-z

Ding, X. Z., Tong, W. G., & Adrian, T. E. (2000). Blockade of cyclooxygenase-2 inhibits proliferation and induces apoptosis in human pancreatic cancer cells. *Anticancer Research, 20*(4), 2625.

Djidja, M., Claude, E., Snel, M., Francese, S., Scriven, P., Carolan, V., & Clench, M. (2010). Novel molecular tumour classification using MALDI–mass spectrometry imaging of tissue micro-array. *Anal Bioanal Chem, 397*(2), 587-601. doi:10.1007/s00216-010-3554-6

Djidja, M., Francese, S., Loadman, P. M., Sutton, C. W., Scriven, P., Claude, E., Snel, M. F., Franck, J., Salzet, M., & Clench, M. R. (2009). Detergent addition to tryptic digests and ion mobility separation prior to MS/MS improves peptide yield and protein identification for in situ proteomic investigation of frozen and formalin-fixed paraffin-embedded adenocarcinoma tissue sections. *Proteomics, 9*(10), 2750-2763. doi:10.1002/pmic.200800624

Djidja, M., Claude, E., Scriven, P., Allen, D. W., Carolan, V. A., & Clench, M. R. (2017). Antigen retrieval prior to on-tissue digestion of formalin-fixed paraffin-embedded tumour tissue sections yields oxidation of proline residues. *Biochimica Et Biophysica Acta. Proteins and Proteomics, 1865*(7), 901-906. doi:10.1016/j.bbapap.2016.11.019

Do, T., Guran, R., Jarosova, R., Ondrackova, P., Sladek, Z., Faldyna, M., Vojtech, A., & Zitka, O. (2020). MALDI MSI reveals the spatial distribution of protein markers in tracheobronchial lymph nodes and lung of pigs after respiratory infection. *Molecules, 25*(23), 5723. doi:10.3390/molecules25235723

Dolce, V., Rita Cappello, A., Lappano, R., & Maggiolini, M. (2011). Glycerophospholipid synthesis as a novel drug target against cancer. *Current Molecular Pharmacology, 4*(3), 167-175. doi:10.2174/1874467211104030167

Donovan, L., Welford, S., Haaga, J., LaManna, J., & Strohl, K. (2010). Hypoxia—implications for pharmaceutical developments. *Sleep Breath, 14*(4), 291-298. doi:10.1007/s11325-010-0368-x

Downward, J. (2001). The ins and outs of signalling. *Nature, 411*(6839), 759-762. doi:10.1038/35081138

Duval, K., Grover, H., Han, L., Mou, Y., Pegoraro, A. F., Fredberg, J., & Chen, Z. (2017). Modeling physiological events in 2D vs. 3D cell culture. *Physiology, 32*(4), 266-277. doi:10.1152/physiol.00036.2016

Dye, B. R., Hill, D. R., Ferguson, M. A. H., Tsai, Y., Nagy, M. S., Dyal, R., Wells. J. M., Mayhew, C. N., Nattiv, R., Klein, O. D., White, E. S., Deutsch, G. H., & Spence, J. R. (2015). In vitro generation of human pluripotent stem cell derived lung organoids. *eLife, 4.* doi:10.7554/eLife.05098

Edmondson, R., Broglie, J. J., Adcock, A. F., & Yang, L. (2014). Three-dimensional cell culture systems and their applications in drug discovery and cell-based biosensors. *ASSAY and Drug Development Technologies, 12*(4), 207-218. doi:10.1089/adt.2014.573

Eikel, D., Vavrek, M., Smith, S., Bason, C., Yeh, S., Korfmacher, W. A., & Henion, J. D. (2011). Liquid extraction surface analysis mass spectrometry (LESA-MS) as a novel profiling tool for drug distribution and metabolism analysis: The terfenadine example. *Rapid Communications in Mass Spectrometry, 25*(23), 3587-3596. doi:10.1002/rcm.5274

Ekert, J. E., Johnson, K., Strake, B., Pardinas, J., Jarantow, S., Perkinson, R., & Colter, D. C. (2014). Three-dimensional lung tumor microenvironment modulates therapeutic compound responsiveness in vitro–implication for drug development. *PloS One, 9*(3), e92248. doi:10.1371/journal.pone.0092248

Ellis, S. R., Soltwisch, J., Paine, M. R. L., isewerd, K., & Heeren, R. M. A. (2017). Laser post-ionisation combined with a high resolving power orbitrap mass spectrometer for enhanced MALDI-MS imaging of lipids. *Chemical Communications, 53*(53), 7246-7249. doi:10.1039/C7CC02325A

Emoto, K., Toyama-Sorimachi, N., Karasuyama, H., Inoue, K., & Umeda, M. (1997). Exposure of phosphatidylethanolamine on the surface of apoptotic cells. *Experimental Cell Research, 232*(2), 430-434. doi:10.1006/excr.1997.3521

Endo, H., Okami, J., Okuyama, H., Kumagai, T., Uchida, J., Kondo, J., Takehara, T., Nishizawa, Y., Imamura, F., Higashiyama, M., & Inoue, M. (2013). Spheroid culture of primary lung cancer cells with neuregulin 1/HER3 pathway activation. *Journal of Thoracic Oncology, 8*(2), 131-139. doi:10.1097/JTO.0b013e3182779ccf

Essid, N., Chambard, J. C., & Elgaaïed, A. B. (2018). Induction of epithelial-mesenchymal transition (EMT) and Gli1 expression in head and neck squamous cell carcinoma (HNSCC) spheroid cultures. *Bosnian Journal of Basic Medical Sciences, 18*(4), 336-346. doi:10.17305/bjbms.2018.3243

Fan, J., Kamphorst, J. J., Mathew, R., Chung, M. K., White, E., Shlomi, T., & Rabinowitz, J. D. (2013). Glutamine-driven oxidative phosphorylation is a major ATP source in transformed mammalian cells in both normoxia and hypoxia. *Molecular Systems Biology, 9*(1), 712. doi:10.1038/msb.2013.65

Feist, P. E., Sidoli, S., Liu, X., Schroll, M. M., Rahmy, S., Fujiwara, R., Garcia, B. A., & Hummon, A. B. (2017). Multicellular tumor spheroids combined with mass spectrometric histone analysis to evaluate epigenetic drugs. *Analytical Chemistry, 89*(5), 2773-2781. doi:10.1021/acs.analchem.6b03602

Ferguson, J. L., & Turner, S. P. (2018). Bone cancer: Diagnosis and treatment principles. *American Family Physician, 98*(4), 205-213.

Fiehn, O. (2016). Metabolomics by gas chromatography-mass spectrometry: The combination of targeted and untargeted profiling. *Current Protocols in Molecular Biology, 114,* 30.4.1-30.4.32. doi:10.1002/0471142727.mb3004s114

Fischbach, C., Polverini, P. J., Chen, R., Brugge, J. S., Mooney, D. J., Matsumoto, T., & Schmelzle, T. (2007). Engineering tumors with 3D scaffolds. *Nature Methods, 4*(10), 855-860. doi:10.1038/nmeth1085

Flint, L. E., Hamm, G., Ready, J. D., Ling, S., Duckett, C. J., Cross, N. A., Cole, L. M., Smith, D. P., Goodwin, R. J. A., & Clench, M. R. (2020). Characterization of an aggregated three-dimensional cell culture model by multimodal mass

spectrometry imaging. *Analytical Chemistry, 92*(18), 12538-12547. doi:10.1021/acs.analchem.0c02389

Fong, E. L. S., Harrington, D. A., Farach-Carson, M. C., & Yu, H. (2016). Heralding a new paradigm in 3D tumor modeling. *Biomaterials, 108*, 197-213. doi:10.1016/j.biomaterials.2016.08.052

Foster, D. A. (2009). Phosphatidic acid signaling to mTOR: Signals for the survival of human cancer cells. *Biochimica Et Biophysica Acta. Molecular and Cell Biology of Lipids, 1791*(9), 949-955. doi:10.1016/j.bbalip.2009.02.009

Francese, S., Bradshaw, R., Flinders, B., Mitchell, C., Bleay, S., Cicero, L., & Clench, M. R. (2013). Curcumin: A multipurpose matrix for MALDI mass spectrometry imaging applications. *Analytical Chemistry, 85*(10), 5240-5248. doi:10.1021/ac4007396

Freudlsperger, C., Burnett, J. R., Friedman, J. A., Kannabiran, V. R., Chen, Z., & Van Waes, C. (2011). EGFR-PI3K-AKT-mTOR signaling in head and neck squamous cell carcinomas: Attractive targets for molecular-oriented therapy. *Expert Opinion on Therapeutic Targets, 15*(1), 63-74. doi:10.1517/14728222.2011.541440

Frisch, S. M., & Francis, H. (1994). Disruption of epithelial cell-matrix interactions induces apoptosis. *The Journal of Cell Biology, 124*(4), 619-626. doi:10.1083/jcb.124.4.619

Fuchs, C. S., Fakih, M., Schwartzberg, L., Cohn, A. L., Yee, L., Dreisbach, L., Kozloff, M., F., Hei, Y-J., Galimi, F., Pan, Y., Haddad, V., Hsu, C-P., Sabin, A., & Saltz, L. (2013). TRAIL receptor agonist conatumumab with modified FOLFOX6 plus bevacizumab for first-line treatment of metastatic colorectal cancer. *Cancer, 119*(24), 4290-4298. doi:10.1002/cncr.28353

Fulda, S., Meyer, E., Friesen, C., Susin, S. A., Kroemer, G., & Debatin, K. (2001). Cell type specific involvement of death receptor and mitochondrial pathways in drug-induced apoptosis. *Oncogene, 20*(9), 1063-1075. doi:10.1038/sj.onc.1204141

Gabitova, L., Gorin, A., & Astsaturov, I. (2014). Molecular pathways: Sterols and receptor signaling in cancer. *Clinical Cancer Research, 20*(1), 28-34. doi:10.1158/1078-0432.CCR-13-0122

Gabitova, L., Restifo, D., Gorin, A., Manocha, K., Handorf, E., Yang, D., Cai, K. Q., Klein-Szanto, A. J., Cunningham, D., Kratz, L. E., Herman, G. E., Golemis, E. A., & Astsaturov, I. (2015). Endogenous sterol metabolites regulate growth of EGFR/KRAS-dependent tumors via LXR. *Cell Reports, 12*(11), 1927-1938. doi:10.1016/j.celrep.2015.08.023

Galadari, S., Rahman, A., Pallichankandy, S., & Thayyullathil, F. (2015). Tumor suppressive functions of ceramide: Evidence and mechanisms. *Apoptosis, 20*(5), 689-711. doi:10.1007/s10495-015-1109-1

Gamper, N., & Shapiro, M. S. (2007). Target-specific PIP2 signalling: How might it work? *The Journal of Physiology, 582*(3), 967-975. doi:10.1113/jphysiol.2007.132787

García, A., Godzien, J., López-Gonzálvez, Á, & Barbas, C. (2017). Capillary electrophoresis mass spectrometry as a tool for untargeted metabolomics. *Bioanalysis, 9*(1), 99-130. doi:10.4155/bio-2016-0216

Gebhard, C., Gabriel, C., & Walter, I. (2015). Morphological and immunohistochemical characterization of canine osteosarcoma spheroid cell cultures.*45*(3), 219-230. doi: 10.1111/ahe.12190

Gebhard, C., Miller, I., Hummel, K., nee Ondrovics, M. N., Schlosser, S., & Walter, I. (2018). Comparative proteome analysis of monolayer and spheroid culture of canine osteosarcoma cells. *Journal of Proteomics, 177*, 124-136. doi:10.1016/j.jprot.2018.01.006

Gencoglu, M. F., Barney, L. E., Hall, C. L., Brooks, E. A., Schwartz, A. D., Corbett, D. C., . . . Peyton, S. R. (2018). Comparative study of multicellular tumor spheroid formation methods and implications for drug screening. *ACS Biomaterials Science & Engineering, 4*(2), 410-420. doi:10.1021/acsbiomaterials.7b00069

Giesen, C., Wang, H. A. O., Schapiro, D., Zivanovic, N., Jacobs, A., Hattendorf, B., Schuffler, P. J., Grolimun, D., Buhmann, J. M., Brant, S., Varga, Z., Wild, P. J., Gunther, D., & Bodenmiller, B. (2014). Highly multiplexed imaging of tumor tissues with subcellular resolution by mass cytometry. *Nature Methods, 11*(4), 417-422. doi:10.1038/nmeth.2869

Gill, E. L., Yost, R. A., Vedam-Mai, V., & Garrett, T. J. (2017). Precast gelatin-based molds for tissue embedding compatible with mass spectrometry imaging. *Analytical Chemistry, 89*(1), 576-580. doi:10.1021/acs.analchem.6b04185

Gilmore, I. S. (2013). SIMS of organics—Advances in 2D and 3D imaging and future outlook. *Journal of Vacuum Science & Technology. A, Vacuum, Surfaces, and Films, 31*(5), 50819. doi:10.1116/1.4816935

Goldberg, R., & Kirkpatrick, P. (2005). Cetuximab. *Nature Reviews. Drug Discovery, 4*(5), S10-S11. doi:10.1038/nrd1728

Gong, X., Lin, C., Cheng, J., Su, J., Zhao, H., Liu, T., Wen, X., & Zhao, P. (2015). Generation of multicellular tumor spheroids with microwell-based agarose scaffolds for drug testing. *PloS One, 10*(6), e0130348. doi:10.1371/journal.pone.0130348

Goodwin, R. J. A. (2012). Sample preparation for mass spectrometry imaging: small mistakes can lead to big consequences. *Journal of Proteomics, 75*(16), 4893. doi: 10.1016/j.jprot.2012.04.012

Goodwin, R. J. A., Dungworth, J. C., Cobb, S. R., & Pitt, A. R. (2008). Time-dependent evolution of tissue markers by MALDI-MS imaging. *Proteomics, 8*(18), 3801-3808. doi:10.1002/pmic.200800201

Goodwin, R. J. A., Takats, Z, & Bunch, J. (2020). A critical and concise review of mass spectrometry applied to imaging in drug discovery. *SLAS Discov., 25(9)*, 963-976. doi: 10.1177/2472555220941843

Grayson, K. A., Jyotsana, N., Ortiz-Otero, N., & King, M. R. (2021). Overcoming TRAIL-resistance by sensitizing prostate cancer 3D spheroids with taxanes. *PloS One, 16*(3), e0246733. doi:10.1371/journal.pone.0246733

Green-Mitchell, S. M., Cazares, L. H., Semmes, O. J., Nadler, J. L., & Nyalwidhe, J. O. (2011). On-tissue identification of insulin: In situ reduction coupled with mass spectrometry imaging. *Proteomics. Clinical Applications, 5*(7-8), 448-453. doi:10.1002/prca.201000152

Grimes, D. R., Kelly, C., Bloch, K., & Partridge, M. (2014). A method for estimating the oxygen consumption rate in multicellular tumour spheroids. *Journal of the Royal Society, Interface, 11*(92), 20131124. doi:10.1098/rsif.2013.1124

Guenther, S., Muirhead, L. J., Speller, A. V. M., Golf, O., Strittmatter, N., Ramakrishnan, R., Goldin, R. D., Jones, E., Veselkov, K., Nicholson, J., Darzi, A., & Takats, Z. (2015). Spatially resolved metabolic phenotyping of breast cancer by desorption electrospray ionization mass spectrometry. *Cancer Research, 75*(9), 1828-1837. doi:10.1158/0008-5472.CAN-14-2258

Guenther, S., Römpp, A., Kummer, W., & Spengler, B. (2011). AP-MALDI imaging of neuropeptides in mouse pituitary gland with 5 µm spatial resolution and high mass accuracy. *International Journal of Mass Spectrometry, 305*(2), 228-237. doi:10.1016/j.ijms.2010.11.011

Gupta, S., & Gollapudi, S. (2006). Molecular mechanisms of TNF-α-induced apoptosis in naïve and memory T cell subsets. *Autoimmunity Reviews, 5*(4), 264-268. doi:10.1016/j.autrev.2005.09.007

Haimovitz-Friedman, A., Kolesnick, R. N., & Fuks, Z. (1997). Ceramide signaling in apoptosis. *British Medical Bulletin, 53*(3), 539-553. doi:10.1093/oxfordjournals.bmb.a011629

Hanahan, D., & Weinberg, R. (2011). Hallmarks of cancer: The next generation. *Cell, 144*(5), 646-674. doi:10.1016/j.cell.2011.02.013

Handler, A. M., Pommergaard Pedersen, G., Troensegaard Nielsen, K., Janfelt, C., Just Pedersen, A., & Clench, M. R. (2021). Quantitative MALDI mass spectrometry imaging for exploring cutaneous drug delivery of tofacitinib in human skin. *European Journal of Pharmaceutics and Biopharmaceutics, 159*, 1-10. doi:10.1016/j.ejpb.2020.12.008

Hankin, J. A., Barkley, R. M., & Murphy, R. C. (2007). Sublimation as a method of matrix application for mass spectrometric imaging. *Journal of the American Society for Mass Spectrometry, 18*(9), 1646-1652. doi:10.1016/j.jasms.2007.06.010

Hanna, V. S., & Hafez, E. A. A. (2018). Synopsis of arachidonic acid metabolism: A review. *Journal of Advanced Research, 11*, 23-32. doi:10.1016/j.jare.2018.03.005

Hare, D. J., New, E. J., de Jonge, M. D., & McColl, G. (2015). Imaging metals in biology: Balancing sensitivity, selectivity and spatial resolution. *Chemical Society Reviews, 44*(17), 5941-5958. doi:10.1039/c5cs00055f

Harvey, A., Cole, L. M., Day, R., Bartlett, M., Warwick, J., Bojar, R., Smith, D., Cross, N., & Clench, M. R. (2016). MALDI-MSI for the analysis of a 3D tissue-engineered psoriatic skin model. *Proteomics, 16*(11-12), 1718-1725. doi:10.1002/pmic.201600036

Hasegawa, H., Yasuda, H., Hamamoto, J., Masuzawa, K., Tani, T., Nukaga, S., Hirano, T., Kobayashi, K., Manabe, T., Terai, H., Ikemura, S., Kawada, I., Naoki, K., & Soejima, K. (2019). Efficacy of afatinib or osimertinib plus cetuximab combination therapy for non-small-cell lung cancer with EGFR exon 20 insertion mutations. *Lung Cancer, 127*, 146-152. doi:10.1016/j.lungcan.2018.11.039

Hayashi, M., Sakata, M., Takeda, T., Yamamoto, T., Okamoto, Y., Sawada, K., Kimura, A., Minekawa, R., Tahara, M., Tasaka, K., & Murata, Y. (2004). Induction of glucose transporter 1 expression through hypoxia-inducible factor 1alpha under hypoxic conditions in trophoblast-derived cells. *The Journal of Endocrinology, 183*(1), 145.

Henderson, F., Jones, E., Denbigh, J., Christie, L., Chapman, R., Hoyes, E., Claude, E., Williams, K. J., Roncaroli, F., & McMahon, A. (2020). 3D DESI-MS lipid imaging in a xenograft model of glioblastoma: A proof of principle. *Scientific Reports, 10*(1), 16512. doi:10.1038/s41598-020-73518-x

Hermann, J., Noels, H., Theelen, W., Lellig, M., Orth-Alampour, S., Boor, P., Jankowski, V., & Jankowski, J. (2020). Sample preparation of formalin-fixed paraffin-embedded tissue sections for MALDI-mass spectrometry imaging. *Analytical and Bioanalytical Chemistry, 412*(6), 1263-1275. doi:10.1007/s00216-019-02296-x

Hermsmeier, M., Jeong, S., Yamamoto, A., Chen, X., Nagavarapu, U., Evans, C. L., & Chan, K. F. (2018). Characterization of human cutaneous tissue autofluorescence: Implications in topical drug delivery studies with fluorescence microscopy. *Biomedical Optics Express, 9*(11), 5400-5418. doi:10.1364/BOE.9.005400

Hess, S. T., Girirajan, T. P. K., & Mason, M. D. (2006). Ultra-high resolution imaging by fluorescence photoactivation localization microscopy. *Biophysical Journal, 91*(11), 4258-4272. doi:10.1529/biophysj.106.091116

Hill, P. A., & Tumber, A. (2010). Ceramide-induced cell death/survival in murine osteoblasts. *Journal of Endocrinology, 206*(2), 225-233. doi:10.1677/JOE-10-0068

Hiraide, T., Ikegami, K., Sakaguchi, T., Morita, Y., Hayasaka, T., Masaki, N., Waki, M., Sugiyama, E., Shinriki, S., Takeda, M., Shibasaki, E., Miyazaki, S., Kikuchi, H., Okuyama, H., Inoune, M., Setou, M., & Konno, H. (2016). Accumulation of arachidonic acid-containing phosphatidylinositol at the outer edge of colorectal cancer. *Scientific Reports, 6*(1), 29935. doi:10.1038/srep29935

Hirschhaeuser, F., Menne, H., Dittfeld, C., West, J., Mueller-Klieser, W., & Kunz-Schughart, L. A. (2010). Multicellular tumor spheroids: An underestimated tool is catching up again. *Journal of Biotechnology, 148(1)*, 3-15. doi: 10.1016/j.jbiotec.2010.01.012

Hoffman, M. D., Sniatynaski, M. J., & Kast, J. (2008). Current approaches for global post-translational modification discovery and mass spectrometric analysis. *Analytical Chimica Atca, 627*(1), 50-61.

Holzlechner, M., Eugenin, E., & Prideaux, B. (2019). Mass spectrometry imaging to detect lipid biomarkers and disease signatures in cancer. *Cancer Reports, 2*(6), e1229-n/a. doi:10.1002/cnr2.1229

Hooijmans, C. R., Leenaars, M., & Ritskes-Hoitinga, M. (2010). A gold standard publication checklist to improve the quality of animal studies, to fully integrate the Three Rs, and to make systematic reviews more feasible. *Altern. Lab. Amin. 38*(2), 167-182. doi: 10.1177/026119291003800208.

Hosokawa, Y., Masaki, N., Takei, S., Horikawa, M., Matsushita, S., Sugiyama, E., Ogura, H., Shiiya, N., & Setou, M. (2017). Recurrent triple-negative breast cancer (TNBC) tissues contain a higher amount of phosphatidylcholine (32:1) than non-recurrent TNBC tissues. *PloS One, 12*(8), e0183724. doi:10.1371/journal.pone.0183724

Hotta, T., Suzuki, H., Nagai, S., Yamamoto, K., Imakiire, A., Takada, E., Itoh, M., & Mizuguchi, J. (2003). Chemotherapeutic agents sensitize sarcoma cell lines to tumor necrosis factor-related apoptosis-inducing ligand-induced caspase-8 activation, apoptosis and loss of mitochondrial membrane potential. *Journal of Orthopaedic Research, 21*(5), 949-957. doi:10.1016/S0736-0266(03)00062-7

Howat, W. J., & Wilson, B. A. (2014). Tissue fixation and the effect of molecular fixatives on downstream staining procedures. *Methods, 70*(1), 12-19. doi:10.1016/j.ymeth.2014.01.022

Howell, M. C., Green, R., Khalil, R., Foran, E., Quarni, W., Nair, R., Stevens, S., Grinchuk, A., Hanna, A., Mohapatra, S., & Mohapatra, S. (2020). Lung cancer cells survive epidermal growth factor receptor tyrosine kinase inhibitor exposure through upregulation of cholesterol synthesis. *FASEB bioAdvances, 2*(2), 90-105. doi:10.1096/fba.2019-00081

Huang, L., Holtzinger, A., Jagan, I., Begora, M., Lohse, I., Ngai, N., Nostro, C., & Wang, R. (2015). Ductal pancreatic cancer modeling and drug screening using human pluripotent stem cell– and patient-derived tumor organoids. *Nature Medicine, 21*(11), 1364-1371. doi:10.1038/nm.3973

Huizing, L. R. S., Ellis, S. R., Beulen, Bart W. A. M. M, Barre, F. P. Y., Kwant, P. B., Vreeken, R. J., & Heeren, R. M. A. (2019). Development and evaluation of matrix application techniques for high throughput mass spectrometry imaging of tissues in the clinic. *Clinical Mass Spectrometry, 12*, 7-15. doi:10.1016/j.clinms.2019.01.004

Irie, M., Fujimura, Y., Yamato, M., & Wariishi, H. (2014). Integrated MALDI-MS imaging and LC–MS techniques for visualizing spatiotemporal metabolomic dynamics in a rat stroke model. *Metabolomics, 10*(3), 473-483. doi:10.1007/s11306-013-0588-8

Jacobi, N., Seeboeck, R., Hofmann, E., Schweiger, H., Smolinska, V., Mohr, T., Boyer, A., Sommergruber, W., Lechner, P., Pichler-Huebschmann, C., Onder, K., Hundsberger, H., Wiesner, C., & Eger, A. (2017). Organotypic three-dimensional cancer cell cultures mirror drug responses in vivo : Lessons learned from the inhibition of EGFR signaling. *Oncotarget, 8*(64), 107423-107440. doi:10.18632/oncotarget.22475

Jian, F., Yuan, F., Jiong, M., Zhu, X., Yu, G., & Lu, D. (2015). Silencing of glucose transporter protein-1 by RNA interference inhibits human osteosarcoma Mg63 cells growth in vivo. *Technology in Cancer Research & Treatment, 14*(2), 243-248. doi:10.7785/tcrt.2012.500412

Jiang, L., Chughtai, K., Purvine, S. O., Bhujwalla, Z. M., Raman, V., Paša-Tolić, L., Heeren, R. M. A., & Glunde, K. (2015). MALDI-mass spectrometric imaging revealing hypoxia-driven lipids and proteins in a breast tumor model. *Analytical Chemistry, 87*(12), 5947-5956. doi:10.1021/ac504503x

Jing, X., Yang, F., Shao, C., Wei, K., Xie, M., Shen, H., & Shu, Y. (2019). Role of hypoxia in cancer therapy by regulating the tumor microenvironment. *Mol. Cancer, 18*, 157. doi: 10.1186/s12943-019-1089-9

Jo, K., Heien, M. L., Thompson, L. B., Zhong, M., Nuzzo, R. G., & Sweedler, J. V. (2007). Mass spectrometric imaging of peptide release from neuronal cells within microfluidic devices. *Lab on a Chip, 7*(11), 1454-146. doi:10.1039/b706940e

Johnson, F. M., Saigal, B., Talpaz, M., & Donato, N. J. (2005). Dasatinib (BMS-354825) tyrosine kinase inhibitor suppresses invasion and induces cell cycle arrest and apoptosis of head and neck squamous cell carcinoma and Non–Small cell lung cancer cells. *Clinical Cancer Research, 11*(19), 6924-6932. doi:10.1158/1078-0432.CCR-05-0757

Johnson, J., Sharick, J. T., Skala, M. C., & Li, L. (2020). Sample preparation strategies for high-throughput mass spectrometry imaging of primary tumor organoids. *Journal of Mass Spectrometry., 55*(4), e4452. doi:10.1002/jms.4452

Jukkola, A., Risteli, L., Melkko, J., & Risteli, J. (1993). Procollagen synthesis and extracellular matrix deposition in MG-63 osteosarcoma cells. *Journal of Bone and Mineral Research, 8*(6), 651-657. doi:10.1002/jbmr.5650080602

Kabat, E. A., Wu, T. T., & Bilofsky, H. (1977). Unusual distributions of amino acids in complementarity-determining (hypervariable) segments of heavy and light chains of immunoglobulins and their possible roles in specificity of antibody-combining sites. *The Journal of Biological Chemistry, 252*(19), 6609-6616.

Kaddurah-Daouk, R., Kristal, B. S., & Weinshilboum, R. M. (2008). Metabolomics: A global biochemical approach to drug response and disease. *Annual Review of Pharmacology and Toxicology, 48*(1), 653-683. doi:10.1146/annurev.pharmtox.48.113006.094715

Källback, P., Nilsson, A., Shariatgorji, M., & Andrén, P. E. (2016). msIQuant – quantitation software for mass spectrometry imaging enabling fast access,

visualization, and analysis of large data sets. *Analytical Chemistry, 88*(8), 4346-4353. doi:10.1021/acs.analchem.5b04603

Kamphorst, J. J., Cross, J. R., Fan, J., Stanchina, E. d., Mathew, R., White, E. P., Thompson, C. B., & Rabinowitz, J. D. (2013). Hypoxic and ras-transformed cells support growth by scavenging unsaturated fatty acids from lysophospholipids. *Proceedings of the National Academy of Sciences - PNAS, 110*(22), 8882-8887. doi:10.1073/pnas.1307237110

Kapałczyńska, M., Kolenda, T., Przybyła, W., Zajączkowska, M., Teresiak, A., Filas, V., Ibbs, M., Bliźniak, R., Łuczewski, Ł., & Lamperska, K. (2018). 2D and 3D cell cultures – a comparison of different types of cancer cell cultures. *Arch. Med. Sci., 14*(4), 910-919. doi: 10.5114/aoms.2016.63743Kertesz, V., & Van Berkel, G. J. (2010). Fully automated liquid extraction-based surface sampling and ionization using a chip-based robotic nanoelectrospray platform. *Journal of Mass Spectrometry, 45*(3), 252-260. doi:10.1002/jms.1709

Khanbolooki, S., Nawrocki, S. T., Arumugam, T., Andtbacka, R., Pino, M. S., Kurzrock, R., Logsdon, C. D., Abbruzzese, J. L., & McConkey, D. J. (2006). Nuclear factor-kappaB maintains TRAIL resistance in human pancreatic cancer cells. *Molecular Cancer Therapeutics, 5*(9), 2251-2260. doi: 10.1158/1535-7163.MCT-06-0075

Kim, H., Lee, K., Kim, S., Kwon, Y., Chun, Y., & Choi, H. (2016). Comparative metabolic and lipidomic profiling of human breast cancer cells with different metastatic potentials. *Oncotarget, 7*(41), 67111-67128. doi:10.18632/oncotarget.11560

Kim, J., Jeong, H. S., Chung, T., Kim, M., Lee, J. H., Jung, W. H., & Koo, J. S. (2017). The value of phosphohistone H3 as a proliferation marker for evaluating invasive breast cancers: A comparative study with Ki67. *Oncotarget, 8*(39), 65064-65076. doi:10.18632/oncotarget.17775

Kim, J., Tchernyshyov, I., Semenza, G. L., & Dang, C. V. (2006). HIF-1-mediated expression of pyruvate dehydrogenase kinase: A metabolic switch required for cellular adaptation to hypoxia. *Cell Metabolism, 3*(3), 177-185. doi:10.1016/j.cmet.2006.02.002

Kim, Y., Koo, K. H., Sung, J. Y., Yun, U., & Kim, H. (2012). Anoikis resistance: An essential prerequisite for tumor metastasis. *International Journal of Cell Biology, 2012*, 306879-11. doi:10.1155/2012/306879

Kipp, A. P., Deubel, S., Arnér, E. S. J., & Johansson, K. (2017). Time- and cell-resolved dynamics of redox-sensitive Nrf2, HIF and NF-κB activities in 3D spheroids enriched for cancer stem cells. *Redox Biology, 12*, 403-409. doi:10.1016/j.redox.2017.03.013

Krasny, L., Hoffmann, F., Ernst, G., Trede, D., Alexandrov, T., Havlicek, V., Guntinas-Lichius, O., von Eggeling, F., & Crecelius, A. (2015). Spatial segmentation of MALDI FT-ICR MSI data: A powerful tool to explore the head and neck tumor in situ lipidome. *J. Am. Soc. Mass Spectrom, 26*(1), 36-43. doi:10.1007/s13361-014-1018-5

Krohn, K. A., O'Sullivan, F., Crowley, J., Eary, J. F., Linden, H. M., Link, J. M., Mankoff, D. A., Muzi, M., Rajendran, J. G., Spence, A. M., & Swanson, K. R. (2007). Challenges in clinical studies with multiple imaging probes. *Nucl. Med. Biol. 34*(7), 879-885. doi:10.1016/j.nucmedbio.2007.07.014.

Kurai, J., Chikumi, H., Hashimoto, K., Yamaguchi, K., Yamasaki, A., Sako, T., Touge, H., Makino, H., Takata, M., Miyata, M., Natamoto, M., Burioka, N., & Shimizu, E. (2007). Antibody-dependent cellular cytotoxicity mediated by cetuximab against lung cancer cell lines. *Clinical Cancer Research, 13*(5), 1552-1561. doi:10.1158/1078-0432.CCR-06-1726

LaBonia, G. J., Ludwig, K. R., Mousseau, C. B., & Hummon, A. B. (2018). iTRAQ quantitative proteomic profiling and MALDI–MSI of colon cancer spheroids treated with combination chemotherapies in a 3D printed fluidic device. *Analytical Chemistry, 90*(2), 1423. doi: 10.1021/acs.analchem.7b04969

Lamont, L., Eijkel, G. B., Jones, E. A., Flinders, B., Ellis, S. R., Porta Siegel, T., Heeren, R. M. A., & Vreeken, R. J. (2018). Targeted drug and metabolite imaging: Desorption electrospray ionization combined with triple quadrupole mass spectrometry. *Analytical Chemistry, 90*(22), 13229-13235. doi:10.1021/acs.analchem.8b03857

Lamouille, S., Xu, J., & Derynck, R. (2014). Molecular mechanisms of epithelial–mesenchymal transition. *Nature Reviews. Molecular Cell Biology, 15*(3), 178-196. doi:10.1038/nrm3758

Lehmann, S., te Boekhorst, V., Odenthal, J., Bianchi, R., van Helvert, S., Ikenberg, K., Ilina, O., Stoma, S., Xandry, J., Jiang, L., Grenman, R., Rudin, M., & Friedl, P. (2017). Hypoxia induces a HIF-1-dependent transition from collective-to-amoeboid dissemination in epithelial cancer cells. *Current Biology, 27*(3), 392-400. doi:10.1016/j.cub.2016.11.057

Lemaire, R., Desmons, A., Tabet, J. C., Day, R., Salzet, M., & Fournier, I. (2007). Direct analysis and MALDI imaging of formalin-fixed, paraffin-embedded tissue sections. *Journal of Proteome Research, 6*(4), 1295-1305. doi:10.1021/pr060549i

Lemaire, R., Wisztorski, M., Desmons, A., Tabet, J. C., Day, R., Salzet, M., & Fournier, I. (2006). MALDI-MS direct tissue analysis of proteins: Improving signal sensitivity using organic treatments. *Analytical Chemistry, 78*(20), 7145-7153. doi:10.1021/ac060565z

Lewis, E. E. L., Barrett, M. R. T., Freeman-Parry, L., Bojar, R. A., & Clench, M. R. (2018). Examination of the skin barrier repair/wound healing process using a living skin equivalent model and matrix-assisted laser desorption-ionization-mass spectrometry imaging. *International Journal of Cosmetic Science, 40*(2), 148-156. doi:10.1111/ics.12446

Li, F., & Zhang, N. (2016). Ceramide: Therapeutic potential in combination therapy for cancer treatment. *Current Drug Metabolism, 17*(1), 37-51. doi:10.2174/1389200216666151103120338

Li, F., Gonzalez, F. J., & Ma, X. (2012). LC–MS-based metabolomics in profiling of drug metabolism and bioactivation. *Acta Pharmaceutica Sinica. B, 2*(2), 118-125. doi:10.1016/j.apsb.2012.02.010

Li, H., Lee, J., Kim, S. Y., Yun, H., Baek, K. J., Kwon, N. S., Yoon, Y., Jeong, J. H., & Kim, D. (2011). Phosphatidylcholine induces apoptosis of 3T3-L1 adipocytes. *Journal of Biomedical Science, 18*(1), 91. doi:10.1186/1423-0127-18-91

Li, H., & Hummon, A. B. (2011). Imaging mass spectrometry of three-dimensional cell culture systems. *Analytical Chemistry, 83*(22), 8794-8801. doi:10.1021/ac202356g

Li, S., Schmitz, K. R., Jeffrey, P. D., Wiltzius, J. J. W., Kussie, P., & Ferguson, K. M. (2005). Structural basis for inhibition of the epidermal growth factor receptor by cetuximab. *Cancer Cell, 7*(4), 301-311. doi:10.1016/j.ccr.2005.03.003

Li, Y., & Kumacheva, E. (2018). Hydrogel microenvironments for cancer spheroid growth and drug screening. *Science Advances, 4*(4), eaas8998. doi:10.1126/sciadv.aas8998

Link, A. J., & LaBaer, J. (2011). Solution protein digest. *Cold Spring Harbor Protocols, 2011*(2), pdb.prot5569. doi:10.1101/pdb.prot5569

Liu, X., Flinders, C., Mumenthaler, S., & Hummon, A. (2018). MALDI mass spectrometry imaging for evaluation of therapeutics in colorectal tumor organoids. *J. Am. Soc. Mass Spectrom, 29*(3), 516-526. doi:10.1007/s13361-017-1851-4

Liu, X., & Hummon, A. B. (2015). Mass spectrometry imaging of therapeutics from animal models to three-dimensional cell cultures. *Analytical Chemistry, 87*(19), 9508. doi:10.1021/acs.analchem.5b00419

Liu, X., & Hummon, A. B. (2015). Quantitative determination of irinotecan and the metabolite SN-38 by nanoflow liquid chromatography-tandem mass spectrometry in different regions of multicellular tumour spheroids. *Journal of the American Society for Mass Spectrometry, 26(4),* 577-586. doi: 10.1007/s13361-014-1071-0

Liu, X., & Hummon, A. B. (2016). Chemical imaging of platinum-based drugs and their metabolites. *Scientific Reports, 6*, 38507. doi:10.1038/srep38507

Liu, X., Lukowski, J. K., Flinders, C., Kim, S., Georgiadis, R. A., Mumenthaler, S. M., & Hummon, A. B. (2018). MALDI-MSI of immunotherapy: Mapping the EGFR-targeting antibody cetuximab in 3D colon-cancer cell cultures. *Analytical Chemistry, 90*(24), 14156-14164. doi:10.1021/acs.analchem.8b02151

Liu, X., Weaver, E. M., & Hummon, A. B. (2013). Evaluation of therapeutics in three-dimensional cell culture systems by MALDI imaging mass spectrometry. *Analytical Chemistry, 85*(13), 6295-6302. doi:10.1021/ac400519c

Locklin, R. M., Federici, E., Espina, B., Hulley, P. A., Russell, R. G. G., & Edwards, C. M. (2007). Selective targeting of death receptor 5 circumvents resistance of MG-63 osteosarcoma cells to TRAIL-induced apoptosis. *Molecular Cancer Therapeutics, 6*(12), 3219-3228. doi:10.1158/1535-7163.MCT-07-0275

Lu, Y., Zhao, X., Hu, Z., Wang, L., & Li, F. (2019). LC–MS-based metabolomics in the study of drug-induced liver injury. *Current Pharmacology Reports, 5*(1), 56-67. doi:10.1007/s40495-018-0144-3

Lukowski, J. K., Weaver, E. M., & Hummon, A. B. (2017). Analyzing liposomal drug delivery systems in three-dimensional cell culture models using MALDI imaging mass spectrometry. *Analytical Chemistry, 89*(16), 8453-8458. doi:10.1021/acs.analchem.7b02006

Luo, X., Cheng, C., Tan, Z., Li, N., Tang, M., Yang, L., & Cao, Y. (2017). Emerging roles of lipid metabolism in cancer metastasis. *Molecular Cancer, 16*(1), 76. doi:10.1186/s12943-017-0646-3

Ly, A., Buck, A., Balluff, B., Sun, N., Gorzolka, K., Feuchtinger, A., Jansses, K-P., Kuppen, P. J. K., van de Velde, C. J. H., Weirich, G., Erlmeier, F., Langer, R., Aubele, M., Zitzelsberger, H., McDonnell, L., Aichler, M., & Walch, A. (2016). High-mass-resolution MALDI mass spectrometry imaging of metabolites from formalin-fixed paraffin-embedded tissue. *Nature Protocols, 11*(8), 1428-1443. doi:10.1038/nprot.2016.081

Ly, A., Longuespée, R., Casadonte, R., Wandernoth, P., Schwamborn, K., Bollwein, C., Marsching, C., Kriegsmann, K., Hopf, C., Weichert, W., Kreigsmann, J., Schirmacher, P., Kriegsmann, M., & Deininger, S. (2019). Site-to-Site reproducibility and spatial resolution in MALDI–MSI of peptides from Formalin-Fixed Paraffin-Embedded samples. *PROTEOMICS – Clinical Applications, 13*(1), e1800029-n/a. doi:10.1002/prca.201800029

Ly, A., Schöne, C., Becker, M., Rattke, J., Meding, S., Aichler, M., Suckau, D., Walch, A., Hauck, A. M., & Ueffing, M. (2015). High-resolution MALDI mass

spectrometric imaging of lipids in the mammalian retina. *Histochem Cell Biol, 143*(5), 453-462. doi:10.1007/s00418-014-1303-1

Ma, H., Hung, S., Lin, S., Chen, Y., & Lo, W. (2003). Chondrogenesis of human mesenchymal stem cells encapsulated in alginate beads. *Journal of Biomedical Materials Research Part A, 64A*(2), 273-281. doi:10.1002/jbm.a.10370

MacDonald, R. S. (2000). The role of zinc in growth and cell proliferation. *The Journal of Nutrition, 130*(5S Suppl), 1500S-1508S. doi:10.1093/jn/130.5.1500S

Machálková, M., Pavlatovská, B., Michálek, J., Pruška, A., Štěpka, K., Nečasová, T., Radaszkiewicz, K. A., Kozubek, M., Šmarda, J., Preisler, J., & Navrátilová, J. (2019). Drug penetration analysis in 3D cell cultures using fiducial-based semiautomatic coregistration of MALDI MSI and Immunofluorescence images. *Analytical Chemistry, 91*(21), 13475-13484. doi:10.1021/acs.analchem.9b02462

Mallah, K., Quanico, J., Trede, D., Kobeissy, F., Zibara, K., Salzet, M., & Fournier, I. (2018). Lipid changes associated with traumatic brain injury revealed by 3D MALDI-MSI. *Analytical Chemistry, 90*(17), 10568-10576. doi:10.1021/acs.analchem.8b02682

Mamo, M., Ye, I. C., DiGiacomo, J. W., Park, J. Y., Downs, B., & Gilkes, D. M. (2020). Hypoxia alters the response to anti-EGFR therapy by regulating EGFR expression and downstream signaling in a DNA methylation-specific and HIF-dependent manner. *Cancer Research, 80*(22), 4998-5010. doi:10.1158/0008-5472.CAN-20-1232

Martínez-Reyes, I., & Chandel, N. S. (2020). Mitochondrial TCA cycle metabolites control physiology and disease. *Nature Communications, 11*(1), 102-11. doi:10.1038/s41467-019-13668-3

Martin-Lorenzo, M., Balluff, B., Sanz-Maroto, A., van Zeijl, R. J. M., Vivanco, F., Alvarez-Llamas, G., & McDonnell, L. A. (2014). 30μm spatial resolution protein MALDI MSI: In-depth comparison of five sample preparation protocols applied to human healthy and atherosclerotic arteries. *Journal of Proteomics, 108*, 465-468. doi:10.1016/j.jprot.2014.06.013

Maschmeyer, I., Lorenz, A. K., Schimek, K., Hasenberg, T., Ramme, A. P., Hübner, J., Lindner, M., Drewell, C., Bauer, S., Thomas, A., Sambo, N. S., Sonntag, F., Lauster, R., & Marx, U. (2015). A four-organ-chip for interconnected

long-term co-culture of human intestine, liver, skin and kidney equivalents. *Lab on a Chip, 15*(12), 2688-2699. doi:10.1039/c5lc00392j

Massarelli, E., Varella-Garcia, M., Tang, X., Xavier, A. C., Ozburn, N. C., Liu, D. D., Bekele, B. N., Herbst, R. S., & Wistuba, I. I. (2007). KRAS mutation is an important predictor of resistance to therapy with epidermal growth factor receptor tyrosine kinase inhibitors in Non–Small-cell lung cancer. *Clinical Cancer Research, 13*(10), 2890-2896. doi:10.1158/1078-0432.CCR-06-3043

Massonnet, P., & Heeren, R. M. A. (2019). A concise tutorial review of TOF-SIMS based molecular and cellular imaging. *Journal of Analytical Atomic Spectrometry, 34*(11), 2217-2228. doi:10.1039/c9ja00164f

Matsugaki, T., Zenmyo, M., Hiraoka, K., Fukushima, N., Shoda, T., Komiya, S., ono, M., Kuwano, M., & Nagata, K. (2010). N-myc downstream-regulated gene 1/Cap43 expression promotes cell differentiation of human osteosarcoma cells. *Oncology Reports, 24*(3), 721-725. doi:10.3892/or_00000913

McMahon, K. M., Volpato, M., Chi, H. Y., Musiwaro, P., Poterlowicz. K., Peng, Y., Scally, a. J., Patterson, L. H., Phillips, R. M., & Sutton, C. W. (2012). Characterisation of changes in the proteome in different regions of 3D multicell tumour spheroids. *Journal of Proteome Research, 11(5),* 2863-2875. doi: 10.1021/pr2012472

Mehra, R., Cohen, R. B., & Burtness, B. A. (2008). The role of cetuximab for the treatment of squamous cell carcinoma of the head and neck. *Clinical Advances in Hematology & Oncology, 6*(10), 742-750.

Merrick, D. T., Kittelson, J., Winterhalder, R., Kotantoulas, G., Ingeberg, S., Keith, R. L., Kennedy, T. C., Miller, y. E., Franklin, W. A., & Hirsch, F. R. (2006). Analysis of c-ErbB1/epidermal growth factor receptor and c-ErbB2/HER-2 expression in bronchial dysplasia: Evaluation of potential targets for chemoprevention of lung cancer. *Clinical Cancer Research, 12*(7), 2281-2288. doi:10.1158/1078-0432.CCR-05-2291

Michálek, J., Štěpka, K., Kozubek, M., Navrátilová, J., Pavlatovská, B., Machálková, M., Preisler, J., & Pruška, A. (2019). Quantitative assessment of anti-cancer drug efficacy from coregistered mass spectrometry and fluorescence

microscopy images of multicellular tumor spheroids. *Microscopy and Microanalysis, 25*(6), 1311-1322. doi:10.1017/S1431927619014983

Mignini, L. E., & Khan, K. S. (2006). Methodological quality of systematic reviews of animal studies: A survey of reviews of basic research. *BMC Medical Research Methodology, 6*(1), 10. doi:10.1186/1471-2288-6-10

Mitchell, C., Long, H., Donaldson, M., Francese, S., & Clench, M. R. (2015). Lipid changes within the epidermis of living skin equivalents observed across a time-course by MALDI-MS imaging and profiling. *Lipids in Health and Disease, 14,* 84-96. doi: 10.1186/s12944-015-0089-z

Mitchell, C., Donaldson, M., Francese, S., & Clench, M. R. (2016). MALDI MSI analysis of lipid changes in living skin equivalents in response to emollient creams containing palmitoylethanolamide. *Methods, 104,* doi: 93-100. 10.1016/j.ymeth.2016.02.001

Mittal, P., Price, Z. K., Lokman, N. A., Ricciardelli, C., Oehler, M. K., Klingler-Hoffmann, M., & Hoffmann, P. (2019). Matrix assisted laser desorption/ionization mass spectrometry imaging (MALDI MSI) for monitoring of drug response in primary cancer spheroids. *Proteomics, 19*(21-22), e1900146.

Molinier, O., Goupil, F., Debieuvre, D., Auliac, J. -., Jeandeau, S., Lacroix, S., Martin, F., & Grivaux, M. (2020). Five-year survival and prognostic factors according to histology in 6101 non-small-cell lung cancer patients. *Respiratory Medicine and Research, 77*, 46-54. doi:10.1016/j.resmer.2019.10.001

Monico, A., Guzman-Caldentey, J., Pajares, M. A., Martin-Santamaria, S., & Perez-Sala, D. (2021). Elucidating vimentin interaction with zinc ions and its interplay with oxidative modifications through crosslinking assays and molecular dynamics simulations. [preprint]. doi:10.1101/2021.02.12.430929

Mukohara, T., Engelman, J. A., Tenen, D. G., Johnson, B. E., Janne, P. A., Hanna, N. H., Yeap, B. Y., Kobayashi, S., Lindeman, N., Halmos, B., Pearlberg, J., Tsuchihasti, Z., & Cantley, L. C. (2005). Differential effects of gefitinib and cetuximab on non–small-cell lung cancers bearing epidermal growth factor receptor mutations. *JNCI : Journal of the National Cancer Institute, 97*(16), 1185-1194. doi:10.1093/jnci/dji238

Mullen, T. D., & Obeid, L. M. (2012). Ceramide and apoptosis: Exploring the enigmatic connections between sphingolipid metabolism and programmed cell death. *Anti-Cancer Agents in Medicinal Chemistry, 12*(4), 340-363. doi:10.2174/187152012800228661

Murray, E., Provvedini, D., Curran, D., Catherwood, B., Sussman, H., & Manolagas, S. (1987). Characterization of a human osteoblastic osteosarcoma cell line (SAOS-2) with high bone alkaline phosphatase activity. *Journal of Bone and Mineral Research, 2*(3), 231-238. doi:10.1002/jbmr.5650020310

Muz, B., de la Puente, P., Azab, F., & Azab, A. K. (2015). The role of hypoxia in cancer progression, angiogenesis, metastasis, and resistance to therapy. *Hypoxia, 3*(1), 83-92. doi:10.2147/hp.s93413

Nagelkerke, A., Bussink, J., Sweep, F. C. G. J., & Span, P. N. (2013). Generation of multicellular tumor spheroids of breast cancer cells: How to go three-dimensional. *Analytical Biochemistry, 437*(1), 17-19. doi:10.1016/j.ab.2013.02.004

Nam, S. Y., Amoscato, A. A., & Lee, Y. J. (2002). Low glucose-enhanced TRAIL cytotoxicity is mediated through the ceramide-Akt-FLIP pathway. *Oncogene, 21*(3), 337-346. doi:10.1038/sj.onc.1205068

Nardinocchi, L., Pantisano, V., Puca, R., Porru, M., Aiello, A., Grasselli, A., D'Orazi, G. (2010). Zinc downregulates HIF-1α and inhibits its activity in tumor cells in vitro and in vivo. *PloS One, 5*(12), e15048. doi:10.1371/journal.pone.0015048

Nie, D., Nemeth, J., Qiao, Y., Zacharek, A., Li, L., Hanna, K., Tang, K., Hillman, G., Cher, M., Grignon, D., & Honn, K. (2003). Increased metastatic potential in human prostate carcinoma cells by overexpression of arachidonate 12-lipoxygenase. *Clin Exp Metastasis, 20*(7), 657-663. doi:10.1023/A:1027302408187

Nilsson, A., Goodwin, R. J. A., Shariatgorji, M., Vallianatou, T., Webborn, P. J. H., & Andrén, P. E. (2015). Mass spectrometry imaging in drug development. *Analytical Chemistry, 87*(3), 1437-1455. doi:10.1021/ac504734s

Nilsson, A., Goodwin, R. J. A., Swales, J. G., Gallagher, R., Shankaran, H., Sathe, A., Pradeepan, S., Xue, A., Keirstead, N., Saski, J. C., Andren, P. E., &

Gupta, A. (2015). Investigating nephrotoxicity of polymyxin derivatives by mapping renal distribution using mass spectrometry imaging. *Chemical Research in Toxicology, 28*(9), 1823-1830. doi:10.1021/acs.chemrestox.5b00262

Onder, S., Calikoglu-Koyuncu, A. C., Kazmanli, K., Urgen, M., Kok, F. N., & Torun-Kose, G. (2018). Magnesium doping on TiN coatings affects mesenchymal stem cell differentiation and proliferation positively in a dose-dependent manner. *Bio-Medical Materials and Engineering, 29*(4), 427-438. doi:10.3233/BME-181000

O'Neill, E. S., Kaur, A., Bishop, D. P., Shishmarev, D., Kuchel, P. W., Grieve, S. M., Figtree, G. A., Renfrew, A. K., Bonnitcha, P.D., & New, E. J. (2017). Hypoxia-responsive cobalt complexes in tumor spheroids: Laser ablation inductively coupled plasma mass spectrometry and magnetic resonance imaging studies. *Inorganic Chemistry, 56*(16), 9860-9868. doi:10.1021/acs.inorgchem.7b01368

O'Rourke, M. B., Raymond, B. B. A., Djordjevic, S. P., & Padula, M. P. (2015). A versatile cost-effective method for the analysis of fresh frozen tissue sections via matrix-assisted laser desorption/ionisation imaging mass spectrometry. *Rapid Communications in Mass Spectrometry, 29*(7), 637-644. doi:10.1002/rcm.7138

Osaki, F., Tabata, K., & Oe, T. (2017). Quantitative LC/ESI-SRM/MS of antibody biopharmaceuticals: Use of a homologous antibody as an internal standard and three-step method development. *Anal Bioanal Chem, 409*(23), 5523-5532. doi:10.1007/s00216-017-0488-2

Ouiddir, A., Planes, C., Fernandes, I., VanHesse, A., & Clerici, C. (1999). Hypoxia upregulates activity and expression of the glucose transporter GLUT1 in alveolar epithelial cells. *American Journal of Respiratory Cell and Molecular Biology, 21*(6), 710-718. doi:10.1165/ajrcmb.21.6.3751

Palubeckaite, I. (2018). *Analysis of three dimensional cell cultures using mass spectrometry imaging.* PhD Thesis, Sheffield Hallam University. Sheffield.

Palubeckaitė, I., Crooks, L., Smith, D. P., Cole, L. M., Bram, H., Le Maitre, C., Clench, M. R., & Cross, N. A. (2019). Mass spectrometry imaging of endogenous metabolites in response to doxorubicin in a novel 3D osteosarcoma cell culture model. *Journal of Mass Spectrometry, 55*(4), e4461. doi:10.1002/jms.4461

Pan, G., Ni, J., Wei, Y., Yu, G., Gentz, R., & Dixit, V. M. (1997). An antagonist decoy receptor and a death domain-containing receptor for TRAIL. *Science, 277*(5327), 815-818. doi:10.1126/science.277.5327.815

Parseghian, C. M., Parikh, N. U., Wu, J. Y., Jiang, Z., Henderson, L., Tian, F., Pastor, B., Ychou, M., Raghav, K., Dasari, A., Fogelman, D. R., Katsiampoura, A. D., Menter, D. G., Wolff, R. A., Eng, C., Overman, M. J., Thierry, A. R., Gallick, G. E., & Kopetz, S. (2017). Dual inhibition of EGFR and c-src by cetuximab and dasatinib combined with FOLFOX chemotherapy in patients with metastatic colorectal cancer. *Clinical Cancer Research, 23*(15), 4146-4154. doi:10.1158/1078-0432.CCR-16-3138

Passarelli, M. K., & Ewing, A. G. (2013). Single-cell imaging mass spectrometry. *Current Opinion in Chemical Biology, 17*(5), 854-859. doi:10.1016/j.cbpa.2013.07.017

Passarelli, M. K., Newman, C. F., Marshall, P. S., West, A., Gilmore, I. S., Bunch, J., Alexander, M. R., & Dollery, C. T. (2015). Single-cell analysis: Visualizing pharmaceutical and metabolite uptake in cells with label-free 3D mass spectrometry imaging. *Analytical Chemistry, 87*(13), 6696-6702. doi:10.1021/acs.analchem.5b00842

Patel, E., Clench, M., West, A., Marshall, P., Marshall, N., & Francese, S. (2015). Alternative surfactants for improved efficiency of in situ tryptic proteolysis of fingermarks. *J. Am. Soc. Mass Spectrom, 26*(6), 862-872. doi:10.1007/s13361-015-1140-z

Paton, C., Hellstrom, J., Paul, B., Woodhead, J., & Hergt, J. (2011). Iolite: Freeware for the visualisation and processing of mass spectrometric data. *Journal of Analytical Atomic Spectrometry, 26*(12), 2508. doi:10.1039/c1ja10172b

Paukte, C., Schieker, M., Tischer, T., Kolk, A., Neth, P., Mutschler, W., & Milz, S. (2004). Characterization of osteosarcoma cell lines MG-63, saos-2 and U-2 OS in comparison to human osteoblasts. *Anticancer Research, 24*(6), 3743-3748.

Perry, J. A., Kiezun, A., Tonzi, P., Van Allen, E. M., Carter, S. L., Baca, S. C., Cowley, G. S., Bhatt, A. S., Getz, G., & Janeway, K. A. (2014). Complementary genomic approaches highlight the P13K/mTOR pathway as a common

vulnerability in osteosarcoma. *Proceedings of the National Academy of Sciences - PNAS, 111*(51), 18111.

Phillips, K. L., Wright, N., McDermott, E., & Cross, N. A. (2019). TRAIL responses are enhanced by nuclear export inhibition in osteosarcoma. *Biochemical and Biophysical Research Communications, 517*(2), 383-389. doi:10.1016/j.bbrc.2019.07.047

Picarda, G., Lamoureux, F., Geffroy, L., Delepine, P., Montier, T., Laud, K., Tirode, F., Delattre, O., Heymann Rédini, F. (2010). Preclinical evidence that use of TRAIL in ewing's sarcoma and osteosarcoma therapy inhibits tumor growth, prevents osteolysis, and increases animal survival. *Clinical Cancer Research, 16*(8), 2363-2374. doi:10.1158/1078-0432.CCR-09-1779

Phil, L. T. H., Sari, I. N., Yang, Y-G., Lee, S-H., Jun, N., Kim, K. S., Lee, Y. K., & Kwon, H. Y. (2018). Cancer Stem Cells (CSCs) in Drug Resistance and their Therapeutic Implications in Cancer Treatment. *Stem Cells Int.* (2018). 5416923. doi: 10.1155/2018/5416923

Piel, M., Vernaleken, I., & Rösch, F. (2014). Positron emission tomography in CNS drug discovery and drug monitoring. *Journal of Medicinal Chemistry, 57*(22), 9232-9258. doi:10.1021/jm5001858

Pirman, D. A., Reich, R. F., Kiss, A., Heeren, R. M. A., Yost, R. A. (2013). Quantitative MALDI tandem mass spectrometric imaging of cocaine from brain tissue with a deuterated internal standard. *Analytical Chemistry, 85(2),* 1081-1089. doi:10.1021/ac302960j

Pitti, R. M., Marsters, S. A., Ruppert, S., Donahue, C. J., Moore, A., & Ashkenazi, A. (1996). Induction of apoptosis by apo-2 ligand, a new member of the tumor necrosis factor cytokine family. *The Journal of Biological Chemistry, 271*(22), 12687-12690. doi:10.1074/jbc.271.22.12687

Porta Siegel, T., Hamm, G., Bunch, J., Cappell, J., Fletcher, J. S., & Schwamborn, K. (2018). Mass spectrometry imaging and integration with other imaging modalities for greater molecular understanding of biological tissues. *Molecular Imaging and Biology: The Official Publication of the Academy of Molecular Imaging, 20*(6), 888-901. doi:10.1007/s11307-018-1267-y

Potchoiba, M. J., Tensfeldt, T. G., Nocerini, M. R., & Silber, B. M. (1995). A novel quantitative method for determining the biodistribution of radiolabeled xenobiotics using whole-body cryosectioning and autoradioluminography. *Journal of Pharmacology and Experimental Therapeutics, 272*(2), 953-962.

Pozebon, D., Scheffler, G. L., Dressler, V. L., & Nunes, M. A. G. (2014). Review of the applications of laser ablation inductively coupled plasma mass spectrometry (LA-ICP-MS) to the analysis of biological samples.*29*(12), 224-2228. doi:10.1039/c4ja00250d

Prideaux, B., Staab, D., & Stoeckli, M. (2010). Applications of MALDI-MSI to pharmaceutical research. *Methods in molecular biology,* 656, 405-413. doi:10.1007/978-1-60761-746-4_23

Prieto-Vila, M., Takahashi, R-U., Usuba, W., Kohama, I., & Ochiya, T. (2017). Drug Resistance Driven by Cancer Stem Cells and Their Niche. *Int. J. Mol. Sci. 18*(2), 2574. doi: 10.3390/ijms18122574

Punt, A. M., Stienstra, N. A., van Kleef, M. E. A., Lafeber, M., Spiering, W., Blankestijn, P. J., Bots, M. L., & van Maarseveen, E. M. (2019). Screening of cardiovascular agents in plasma with LC-MS/MS: A valuable tool for objective drug adherence assessment. *Journal of Chromatography. B, Analytical Technologies in the Biomedical and Life Sciences, 1121*, 103-110. doi:10.1016/j.jchromb.2019.05.013

Qi, T., Weng, J., Yu, F., Zhang, W., Li, G., Qin, H., Tan, Z., & Zeng, H. (2021). Insights into the role of magnesium ions in affecting osteogenic differentiation of mesenchymal stem cells. *Biological Trace Element Research, 199*(2), 559-567. doi:10.1007/s12011-020-02183-y

Quanico, J., Franck, J., Dauly, C., Strupat, K., Dupuy, J., Day, R., Salzat, M., Fournier, I., & Wisztorski, M. (2013). Development of liquid microjunction extraction strategy for improving protein identification from tissue sections. *Journal of Proteomics, 79*, 200-218. doi:10.1016/j.jprot.2012.11.025

Race, A. M., Palmer, A. D., Dexter, A., Steven, R. T., Styles, I. B., & Bunch, J. (2016). SpectralAnalysis: Software for the masses. *Analytical Chemistry, 88*(19), 9451-9458. doi:10.1021/acs.analchem.6b01643

Reck, M., Krzakowski, M., Chmielowska, E., Sebastian, M., Hadler, D., Fox, T., Wang, Q., Greenberg, J., Beckmam, R. A., & von Pawel, J. (2013). A randomized, double-blind, placebo-controlled phase 2 study of tigatuzumab (CS-1008) in combination with carboplatin/paclitaxel in patients with chemotherapy-naïve metastatic/unresectable non-small cell lung cancer. *Lung Cancer, 82*(3), 441-448. doi:10.1016/j.lungcan.2013.09.014

Ren, D., Pipes, G. D., Liu, D., Shih, L., Nichols, A. C., Treuheit, M. J., Bondarenko, P. V. (2009). An improved trypsin digestion method minimizes digestion-induced modifications on proteins. *Analytical Biochemistry, 392*(1), 12-21. doi:10.1016/j.ab.2009.05.018

Ren, L., Hong, E. S., Mendoza, A., Issaq, S., Tran Hoang, C., Lizardo, M., LeBlanc, A., & Khanna, C. (2017). Metabolomics uncovers a link between inositol metabolism and osteosarcoma metastasis. *Oncotarget, 8*(24), 38541-38553. doi:10.18632/oncotarget.15872

Ren, L., Mendoza, A., Zhu, J., Briggs, J. W., Halsey, C., Hong, E. S., Burkett, A. A., Morrow, J., lizard, M. M., Osbourne, T., Li, S. Q., Luu, H. H., Meltzer, P., & Khanna, C. (2015). Characterization of the metastatic phenotype of a panel of established osteosarcoma cells. *Oncotarget, 6*(30), 29469-29481. doi:10.18632/oncotarget.5177

Reynolds, D. S., Tevis, K. M., Blessing, W. A., Colson, Y. L., Zaman, M. H., & Grinstaff, M. W. (2017). Breast cancer spheroids reveal a differential cancer stem cell response to chemotherapeutic treatment. *Scientific Reports, 7*(1), 10382-12. doi:10.1038/s41598-017-10863-4

Reyzer, M. L., Hsieh, Y., Ng, K., Korfmacher, W. A., & Caprioli, R. M. (2003). Direct analysis of drug candidates in tissue by matrix-assisted laser desorption/ionization mass spectrometry. *Journal of Mass Spectrometry., 38*(10), 1081-1092. doi:10.1002/jms.525

Rheinwald, J. G., & Green, H. (1975). Serial cultivation of strains of human epidermal keratinocytes: The formation of keratinizing colonies from single cells. *Cell, 6*(3), 331.

Rimann, M., Laternser, S., Gvozdenovic, A., Muff, R., Fuchs, B., Kelm, J. M., & Graf-Hausner, U. (2014). An in vitro osteosarcoma 3D microtissue model for drug

development. *Journal of Biotechnology, 189*, 129-135. doi:10.1016/j.jbiotec.2014.09.005

Roach, P. J., Laskin, J., & Laskin, A. (2010). Nanospray desorption electrospray ionization: An ambient method for liquid-extraction surface sampling in mass spectrometry. *Analyst, 135*(9), 2233-2236. doi:10.1039/c0an00312c

Robison, H. M., Chini, C. E., Comi, T. J., Ryu, S. W., Ognjanovski, E., & Perry, R. H. (2020). Identification of lipid biomarkers of metastatic potential and gene expression (HER2/p53) in human breast cancer cell cultures using ambient mass spectrometry. *Analytical and Bioanalytical Chemistry, 412*(12), 2949-2961. doi:10.1007/s00216-020-02537-4

Rogakou Emmy, P., Nieves-Neira Wilberto, Boon Chye, Pommier Yves, & Bonner William, M. (2000). Initiation of DNA fragmentation during apoptosis induces phosphorylation of H2AX histone at serine 139. *Journal of Biological Chemistry, 275*(13), 9390-9395. doi:10.1074/jbc.275.13.9390

Römpp, A., Schramm, T., Hester, A., Klinkert, I., Both, J., Heeren, R. M. A., Stöckli, M., & Spengler, B. (2010). imzML: Imaging mass spectrometry markup language: A common data format for mass spectrometry imaging. *Data mining in proteomics, 696,* 205-224. doi:10.1007/978-1-60761-987-1_12

Rönquist-Nii, Y., & Edlund, P. O. (2005). Determination of corticosteroids in tissue samples by liquid chromatography–tandem mass spectrometry. *Journal of Pharmaceutical and Biomedical Analysis, 37*(2), 341-350. doi:10.1016/j.jpba.2004.10.044

Russo, C., Heaton, C., Flint, L., Voloaca, O., Haywood-Small, S., Clench, M. R., Francese, S., & Cole, L. M. (2020). Emerging applications in mass spectrometry imaging; enablers and roadblocks. *Journal of Spectral Imaging, 9*(a13) doi:10.1255/jsi.2020.a13

Russo, C., Brickelbank, N., Duckett, C., Mellor, S., Rumbelow, S., & Clench, M. R. (2018). Quantitative investigation of terbinafine hydrochloride absorption into a living skin equivalent model by MALDI-MSI. *Analytical Chemistry, 90*(16), 10031-10038. doi:10.1021/acs.analchem.8b02648

Russo, C., Lewis, E. E. L., Flint, L., & Clench, M. R. (2018). Mass spectrometry imaging of 3D tissue models. *Proteomics, 18*(14). doi:10.1002/pmic.201700462

Rzagalinski, I., Hainz, N., Meier, C., Tschernig, T., & Volmer, D. (2019). Spatial and molecular changes of mouse brain metabolism in response to immunomodulatory treatment with teriflunomide as visualized by MALDI-MSI. *Analytical and Bioanalytical Chemistry, 411*(2), 353-365. doi:10.1007/s00216-018-1444-5

Sakakima, Y., Hayakawa, A., & Nakao, A. (2009). Phosphatidylcholine induces growth inhibition of hepatic cancer by apoptosis via death ligands. *Hepato-Gastroenterology, 56*(90), 481-484.

Sakuma, Y., Takeuchi, T., Nakamura, Y., Yoshihara, M., Matsukuma, S., Nakayama, H., Ohgane, N., Yokose, T., Kameda, Y., Tsuchiya, E., & Miyagi, Y. (2010). Lung adenocarcinoma cells floating in lymphatic vessels resist anoikis by expressing phosphorylated src. *The Journal of Pathology, 220*(5), 574-585.

Sammour, D. A., Marsching, C., Geisel, A., Erich, K., Schulz, S., Guevara, C. R., Rabe, J-H., Marx, A., Findeisen, P., Hohenberger, P., & Hopf, C. (2019). Quantitative mass spectrometry imaging reveals mutation status-independent lack of imatinib in liver metastases of gastrointestinal stromal tumors. *Scientific Reports, 9,* 10698. doi:10.1038/s41598-019-47089-5

Sandra, F., Degli Esposti, M., Ndebele, K., Gona, P., Knight, D., Rosenquist, M., & Khosravi-Far, R. (2005). Tumor necrosis factor-related apoptosis-inducing ligand alters mitochondrial membrane lipids. *Cancer Research, 65*(18), 8286-8297. doi:10.1158/0008-5472.CAN-04-1913

Santbergen, J. C., Zande, v. d., M, Gerssen, A., Bouwmeester, H., & Nielen, M. W. F. (2020). Dynamic in vitro intestinal barrier model coupled to chip-based liquid chromatography mass spectrometry for oral bioavailability studies. *Analytical and Bioanalytical Chemistry, 412*(5), 1111-1122. doi:10.1007/s00216-019-02336-6

Santini, M. T., Rainaldi, G., Romano, R., Ferrante, A., Clemente, S., Motta, A., & Indovina, P. L. (2004). MG-63 human osteosarcoma cells grown in monolayer and as three-dimensional tumor spheroids present a different metabolic profile: A 1H NMR study. *FEBS Letters, 557*(1), 148-154. doi:10.1016/S0014-5793(03)01466-2

Sappington, D. R., Siegel, E. R., Hiatt, G., Desai, A., Penney, R. B., Jamshidi-Parsian, A., Griffin, R. J., & Boysen, G. (2016). Glutamine drives glutathione synthesis and contributes to radiation sensitivity of A549 and H460 lung cancer cell lines. *Biochimica Et Biophysica Acta. General Subjects, 1860*(4), 836-843. doi:10.1016/j.bbagen.2016.01.021

Scaltriti, M., & Baselga, J. (2006). The epidermal growth factor receptor pathway: A model for targeted therapy. *Clinical Cancer Research, 12*(18), 5268-5272. doi:10.1158/1078-0432.CCR-05-1554

Scheven, B. A. A., Marshall, D., & Aspden, R. M. (2002). In vitro behaviour of human osteoblasrs on dentin and bone. *Cell Biology International, 26*(4), 337-346. doi:10.1006/cbir.2002.0860

Schiller, J., Müller, K., Süß, R., Arnhold, J., Gey, C., Herrmann, A., Leßig, J., Arnold, K., & Müller, P. (2003). Analysis of the lipid composition of bull spermatozoa by MALDI-TOF mass spectrometry—a cautionary note. *Chemistry and Physics of Lipids, 126*(1), 85-94. doi:10.1016/S0009-3084(03)00097-5

Schneider, A., Younis, R. H., & Gutkind, J. S. (2008). Hypoxia-induced energy stress inhibits the mTOR pathway by activating an AMPK/REDD1 signaling axis in head and neck squamous cell carcinoma. *Neoplasia, 10*(11), 1295-1302. doi:10.1593/neo.08586

Schober, Y., Guenther, S., Spengler, B., & Römpp, A. (2012). High-resolution matrix-assisted laser desorption/ionization imaging of tryptic peptides from tissue. *Rapid Communications in Mass Spectrometry, 26*(9), 1141-1146. doi:10.1002/rcm.6192

Schober, Y., Guenther, S., Spengler, B., & Römpp, A. (2012). Single cell matrix-assisted laser desorption/ionization mass spectrometry imaging. *Analytical Chemistry, 84*(15), 6293-6297. doi:10.1021/ac301337h

Schramm, T., Hester, Z., Klinkert, I., Both, J., Heeren, R. M. A., Brunelle, A., Laprevote, O., Desbenoit, N., Robbe, M-F., Stoeckli, M., Spengler, B., & Römpp, A. (2012). imzML — A common data format for the flexible exchange and processing of mass spectrometry imaging data. *Journal of Proteomics, 75*(16), 5106-5110. doi:10.1016/j.jprot.2012.07.026

Schulz, S., Becker, M., Groseclose, M. R., Schadt, S., & Hopf, C. (2019). Advanced MALDI mass spectrometry imaging in pharmaceutical research and drug development. *Current Opinion in Biotechnology, 55*, 51-59. doi:10.1016/j.copbio.2018.08.003

Schwartz, S. A., Reyzer, M. L., & Caprioli, R. M. (2003). Direct tissue analysis using matrix-assisted laser desorption/ionization mass spectrometry: Practical aspects of sample preparation. *Journal of Mass Spectrometry., 38*(7), 699-708. doi:10.1002/jms.505

Seeley, E. H., Oppenheimer, S. R., Mi, D., Chaurand, P., & Caprioli, R. M. (2008). Enhancement of protein sensitivity for MALDI imaging mass spectrometry after chemical treatment of tissue sections. *J Am Soc Mass Spectrom, 19*(8), 1069-1077. doi:10.1016/j.jasms.2008.03.016

Seok, J., Warren, H. S., Cuenca, A. G., Mindrinos, M. N., Baker, H. V., Xu, W., Richards, D. R., McDonald-Smith, G. P., Geo, H., & Hennessy, L. (2013). Genomic responses in mouse models poorly mimic human inflammatory diseases. *Proceedings of the National Academy of Sciences of the United States of America, 110*(9), 3507-3512. doi:10.1073/pnas.1222878110

Sgambato, A., Casaluce, F., Maione, P., Rossi, A., Ciardiello, F., & Gridelli, C. (2014). Cetuximab in advanced non-small cell lung cancer (NSCLC): The showdown? *Journal of Thoracic Disease, 6*(6), 578-580. doi:10.3978/j.issn.2072-1439.2014.06.14

Shah, A. T., Heaster, T. M., & Skala, M. C. (2017). Metabolic imaging of head and neck cancer organoids. *PloS One, 12*(1), e0170415. doi:10.1371/journal.pone.0170415

Shibata, K., Naito, T., Okamura, J., Hosokawa, S., Mineta, H., & Kawakami, J. (2017). Simple and rapid LC-MS/MS method for the absolute determination of cetuximab in human serum using an immobilized trypsin. *Journal of Pharmaceutical and Biomedical Analysis, 146*, 266-272. doi:10.1016/j.jpba.2017.08.012

Simiantonaki, N., Kurzik-Dumke, U., Karyofylli, G., Jayasinghe, C., & Kirkpatrick, C. (2007). Loss of E-cadherin in the vicinity of necrosis in colorectal carcinomas:

Association with NFκB expression. *International Journal of Oncology,* doi:10.3892/ijo.31.2.269

Simpson, C. D., Anyiwe, K., & Schimmer, A. D. (2008). Anoikis resistance and tumor metastasis. *Cancer Letters, 272*(2), 177-185. doi:10.1016/j.canlet.2008.05.029

Sjövall, P., Johansson, B., & Lausmaa, J. (2006). Localization of lipids in freeze-dried mouse brain sections by imaging TOF-SIMS. *Applied Surface Science, 252*(19), 6966-6974. doi:10.1016/j.apsusc.2006.02.126

Smith, A., L'Imperio, V., Denti, V., Mazza, M., Ivanova, M., Stella, M., Denti, V., Del Puppo, M., & Magni, F. (2019). High spatial resolution MALDI-MS imaging in the study of membranous nephropathy. *Proteomics. Clinical Applications, 13*(1), e1800016-n/a. doi:10.1002/prca.201800016

Solon, E. G., & Kraus, L. (2001). Quantitative whole-body autoradiography in the pharmaceutical industry: Survey results on study design, methods, and regulatory compliance. *Journal of Pharmacological and Toxicological Methods, 46*(2), 73-81. doi:10.1016/S1056-8719(02)00161-2

Soltwisch, J., Kettling, H., Vens-Cappell, S., Wiegelmann, M., Müthing, J., & Dreisewerd, K. (2015). Mass spectrometry imaging with laser-induced postionization. *Science (American Association for the Advancement of Science), 348*(6231), 211-215. doi:10.1126/science.aaa1051

Soo-Hyun, K., Hyo-Jeong, K., & Crispin, D. R. (2011). The reciprocal interaction: Chemotherapy and tumor microenvironment. *Current Drug Discovery Technologies, 8*(2), 102-106. doi:10.2174/157016311795563875

Sowter, H. M., Ratcliffe, P. J., Watson, P., Greenberg, A. H., & Harris, A. L. (2001). HIF-1-dependent regulation of hypoxic induction of the cell death factors BNIP3 and NIX in human tumors. *Cancer Research, 61*(18), 6669.

Spencer, C. E., Flint, L. E., Duckett, C. J., Cole, L. M., Cross, N., Smith, D. P., & Clench, M. R. (2020). Role of MALDI-MSI in combination with 3D tissue models for early stage efficacy and safety testing of drugs and toxicants. *Expert Review of Proteomics, 17*(11-12), 827-841. doi:10.1080/14789450.2021.1876568

Stauber, J., MacAleese, L., Franck, J., Claude, E., Snel, M., Kaletas, B. K., Wiel, I. M. V. D., Wisztorski, M., Fournier, I., & Heeren, R. M. A. (2010). On-tissue protein identification and imaging by MALDI-ion mobility mass spectrometry. *J Am Soc Mass Spectrom, 21*(3), 338-347. doi:10.1016/j.jasms.2009.09.016

Steiner, P., Joynes, C., Bassi, R., Wang, S., Tonra, J. R., Hadari, Y. R., & Hicklin, D. J. (2007). Tumor growth inhibition with cetuximab and chemotherapy in Non–Small cell lung cancer xenografts expressing wild-type and mutated epidermal growth factor receptor. *Clinical Cancer Research, 13*(5), 1540-1551. doi:10.1158/1078-0432.CCR-06-1887

Stiller, C. A., Botta, L., Brewster, D. H., Ho, V. K. Y., Frezza, A. M., Whelan, J., Casali, P. G., Trama, A., & Gatta, G. (2018). Survival of adults with cancers of bone or soft tissue in Europe—Report from the EUROCARE-5 study. *Cancer Epidemiology, 56*, 146-153. doi:10.1016/j.canep.2018.08.010

Stock, K., Estrada, M. F., Vidic, S., Gjerde, K., Rudisch, A., Santo, V. E., Barbier, M., Blom, S., Arundkar, S. C., Selvam, I., Osswald, A., Stein, Y., Gruenewald, S., Brito, C., van Weerden, W., Rotter, V., Boghaert, E., Oren, M., Sommergruber, W., Chong, Y., de Hoogt, R., & Graeser, R. (2016). Capturing tumor complexity in vitro: Comparative analysis of 2D and 3D tumor models for drug discovery. *Scientific Reports, 6*(1), 28951. doi:10.1038/srep28951

Stoeckli, M., Chaurand, P., Hallahan, D. E., & Caprioli, R. M. (2001). Imaging mass spectrometry: A new technology for the analysis of protein expression in mammalian tissues. *Nature Medicine, 7*(4), 493-496. doi:10.1038/86573

Stoeckli, M., Staab, D., Schweitzer, A., Gardiner, J., & Seebach, D. (2007). Imaging of a β-peptide distribution in whole-body mice sections by MALDI mass spectrometry. *Journal of the American Society of Mass Spectrometry, 18*(11), 1921-1924. doi:10.1016/j.jasms.2007.08.005

Strohalm, M., Kavan, D., Novák, P., Volný, M., & Havlíček, V. (2010). mMass 3: A cross-platform software environment for precise analysis of mass spectrometric data. *Analytical Chemistry, 82*(11), 4648-4651. doi:10.1021/ac100818g

Strohalm, M., Strohalm, J., Kaftan, F., Krásný, L., Volný, M., Novák, P., Ulbrich, K., & Havlíček, V. (2011). Poly[N-(2-hydroxypropyl)methacrylamide]-based

tissue-embedding medium compatible with MALDI mass spectrometry imaging experiments. *Analytical Chemistry, 83*(13), 5458-5462. doi:10.1021/ac2011679

Sukhanova, A., Gorin, A., Serebriiskii, I. G., Gabitova, L., Zheng, H., Restifo, D., Egleston, B. L., Cunningham, D., Bagnyukova, T., Liu, H., Nikonova, A., Adams, G. P., Zhou, Y., Yang, D-H., Mehra, R., Butness, B., Cai, K. Q., Klein-Szanto, A., Kraztz, L. E., Kelley, R. I., Weiner, L. M., Herman, G. E., Golemis, E. A., & Astsaturov, I. (2013). Targeting C4-demethylating genes in the cholesterol pathway sensitizes cancer cells to EGF receptor inhibitors via increased EGF receptor degradation. *Cancer Discovery, 3*(1), 96-111. doi:10.1158/2159-8290.CD-12-0031

Sun, J., Zhang, D., Bae, D., Sahni, S., Jansson, P., Zheng, Y., Zhao, Q., Yue, F., Zheng, M., Kovacevic, Z., & Richardson, D. R. (2013). Metastasis suppressor, NDRG1, mediates its activity through signaling pathways and molecular motors. *Carcinogenesis, 34*(9), 1943-1954. doi:10.1093/carcin/bgt163

Sutherland, R. M., McCredie, J. A., Inch, W. R., (1971). Growth of multicell spheroids in tissue culture as a model of nodular carcinomas. *JNCI: Journal of the National Cancer Institute, 47*(1), 113-120. doi: 10.1093/jnci/46.1.113

Suzuki, H., Hotta, T., Koyama, T., Komagata, M., Imakiire, A., Yanase, N., Yoshimoto, T., & Mizugughi, J. (2003). Retrovirus-mediated transduction of TRAIL and chemotherapeutic agents co-operatively induce apoptotic cell death in both sarcoma and myeloma cells. *Anticancer Research, 23*(4), 3247-3253.

Swales, J. G., Dexter, A., Hamm, G., Nilsson, A., Strittmatter, N., Michopoulos, F., Hardy, C., Morentin-Gutierrez, P., Mellor, M., Andren, P. E., Clench, M. R., Bunch, J., Critchlow, S. E., & Goodwin, R. J. A. (2018). Quantitation of endogenous metabolites in mouse tumors using mass-spectrometry imaging. *Analytical Chemistry, 90*(10), 6051-6058. doi:10.1021/acs.analchem.7b05239

Swales, J. G., Hamm, G., Clench, M. R., & Goodwin, R. J. A. (2019). Mass spectrometry imaging and its application in pharmaceutical research and development: A concise review. *International Journal of Mass Spectrometry, 437*, 99-112. doi:10.1016/j.ijms.2018.02.007

Swales, J. G., Strittmatter, N., Tucker, J. W., Clench, M. R., Webborn, P. J. H., & Goodwin, R. J. A. (2016). Spatial quantitation of drugs in tissues using liquid

extraction surface analysis mass spectrometry imaging. *Scientific Reports, 6*(1), 37648. doi:10.1038/srep37648

Swales, J. G., Tucker, J. W., Strittmatter, N., Nilsson, A., Cobice, D., Clench, M. R., Mackay, C. L., Andren, P.E., Takátz, Z., Webborn, P. J. H., & Goodwin, R. J. A. (2014). Mass spectrometry imaging of cassette-dosed drugs for higher throughput pharmacokinetic and biodistribution analysis. *Analytical Chemistry, 86*(16), 8473-8480. doi:10.1021/ac502217r

Swinson, D. E. B., & O'Byrne, K. J. (2006). Interactions between hypoxia and epidermal growth factor receptor in Non–Small-cell lung cancer. *Clinical Lung Cancer, 7*(4), 250-256. doi:10.3816/CLC.2006.n.002

Taban, I. M., Altelaar, A. F. M., van der Burgt, Yuri E.M, McDonnell, L. A., Heeren, R. M. A., Fuchser, J., & Baykut, G. (2007). Imaging of peptides in the rat brain using MALDI-FTICR mass spectrometry. *Journal of the American Society of Mass Spectrometry, 18*(1), 145-151. doi:10.1016/j.jasms.2006.09.017

Takahashi, M., Okazaki, H., Ogata, Y., Takeuchi, K., Ikeda, U., & Shimada, K. (2002). Lysophosphatidylcholine induces apoptosis in human endothelial cells through a p38-mitogen-activated protein kinase-dependent mechanism. *Atherosclerosis, 161*(2), 387-394. doi:10.1016/S0021-9150(01)00674-8

Takahashi, N., Cho, P., Selfors, L. M., Kuiken, H. J., Kaul, R., Fujiwara, T., Harris, I. S., Zhang, T., Gygi, S. P., & Brugge, J. S. (2020). 3D culture models with CRISPR screens reveal hyperactive NRF2 as a prerequisite for spheroid formation via regulation of proliferation and ferroptosis. *Molecular Cell, 80*(5), 828-844.e6. doi:10.1016/j.molcel.2020.10.010

Takahashi, Y., Sawada, G., Kurashige, J., Matsumura, T., Uchi, R., Ueo, H., Ishibashi, M., Takano, Y., Akiyoshi, S., Iwaya, T., Eguchi, H., Sudo, T., Sugimachi, K., Yamamoto, H., Doki, Y., Mori, M., & Mimori, K. (2013). Tumor-derived tenascin-C promotes the epithelial-mesenchymal transition in colorectal cancer cells. *Anticancer Research, 33*(5), 1927.

Takai, N., Tanaka, Y., & Saji, H. (2014). Quantification of small molecule drugs in biological tissue sections by imaging mass spectrometry using surrogate tissue-based calibration standards. *Mass Spectrometry, 3*(1), A0025. doi:10.5702/massspectrometry.A0025

Takáts, Z., Wiseman, J. M., & Cooks, R. G. (2005). Ambient mass spectrometry using desorption electrospray ionization (DESI): Instrumentation, mechanisms and applications in forensics, chemistry, and biology. *Journal of Mass Spectrometry, 40*(10), 1261-1275. doi:10.1002/jms.922

Takats, Z., Wiseman, J. M., Gologan, B., & Cooks, R. G. (2004). Mass spectrometry sampling under ambient conditions with desorption electrospray ionization. *Science, 306*(5695), 471-473. doi:10.1126/science.1104404

Taketomi, Y., Sugiki, T., Saito, T., Ishii, S., Hisada, M., Suzuki-Nishimura, T., Uchida, M K., moon, T-C., Chang, H-W., Natori, Y., Miyazawa, S., Kikuchi-Yanoshita, R., Murakami, M., & Kudo, I. (2003). Identification of NDRG1 as an early inducible gene during in vitro maturation of cultured mast cells. *Biochemical and Biophysical Research Communications, 306*(2), 339-346. doi:10.1016/S0006-291X(03)00942-2

Tanaka, T., Halicka, H. D., Huang, X., Traganos, F., & Darzynkiewicz, Z. (2006). Constitutive histone H2AX phosphorylation and ATM activation, the reporters of DNA damage by endogenous oxidants. *Cell Cycle, 5*(17), 1940-1945. doi:10.4161/cc.5.17.3191

Taylor, A. J., Dexter, A., & Bunch, J. (2018). Exploring ion suppression in mass spectrometry imaging of a heterogeneous tissue. *Analytical Chemistry, 90*(9), 5637-5645. doi:10.1021/acs.analchem.7b05005

Theiner, S., Schreiber-Brynzak, E., Jakupec, M. A., Galanski, M., Koellensperger, G., & Keppler, B. K. (2016). LA-ICP-MS imaging in multicellular tumor spheroids - a novel tool in the preclinical development of metal-based anticancer drugs. *Metallomics : Integrated Biometal Science, 8*(4), 398-42. doi:10.1039/c5mt00276a

Theiner, S., Van Malderen, Stijn J M, Van Acker, T., Legin, A., Keppler, B. K., Vanhaecke, F., & Koellensperger, G. (2017). Fast high-resolution laser ablation-inductively coupled plasma mass spectrometry imaging of the distribution of platinum-based anticancer compounds in multicellular tumor spheroids. *Analytical Chemistry, 89*(23), 12641-12645. doi:10.1021/acs.analchem.7b02681

Tian, X., Zhang, G., Zou, Z., & Yang, Z. (2019). Anticancer drug affects metabolomic profiles in multicellular spheroids: Studies using mass spectrometry

imaging combined with machine learning. *Analytical Chemistry, 91*(9), 5802-5809. doi:10.1021/acs.analchem.9b00026

Timmins, N. E., & Nielsen, L. K. (2007). Generation of multicellular tumor spheroids by the hanging-drop method. *Methods in Molecular Medicine, 140*, 141-151.

Toné, S., Sugimoto, K., Tanda, K., Suda, T., Uehira, K., Kanouchi, H., Samejima, K., Minatogawa, Y., & Earnshaw, W. C. (2007). Three distinct stages of apoptotic nuclear condensation revealed by time-lapse imaging, biochemical and electron microscopy analysis of cell-free apoptosis. *Experimental Cell Research, 313*(16), 3635-3644. doi:10.1016/j.yexcr.2007.06.018

Trim, P. J., Henson, C. M., Avery, J. L., McEwen, A., Snel, M. F., Claude, E., Marshall, P. S., west, A., Princivalle, A. P., & Clench, M. R. (2008). Matrix-assisted laser desorption/ionization-ion mobility separation-mass spectrometry imaging of vinblastine in whole body tissue sections. *Analytical Chemistry, 80*(22), 8628-8634. doi:10.1021/ac8015467

Tucker, L. H., Hamm, G. R., Sargeant, R. J. E., Goodwin, R. J. A., Mackay, C. L., Campbell, C. J., & Clarke, D. J. (2019). Untargeted metabolite mapping in 3D cell culture models using high spectral resolution FT-ICR mass spectrometry imaging. *Analytical Chemistry, 91*(15), 9522-9529. doi:10.1021/acs.analchem.9b00661

Ugarte, A., Corbacho, D., Aymerich, M., García-Osta, A., Cuadrado-Tejedor, M., & Oyarzabal, J. (2018). Impact of neurodegenerative diseases on drug binding to brain tissues: From animal models to human samples. *Neurotherapeutics, 15*(3), 742-750. doi:10.1007/s13311-018-0624-5

Van Acker, T., Buckle, T., Van Malderen, S. J. M., van Willigen, D. M., van Unen, V., van Leeuwen, F. W. B., & Vanhaecke, F. (2019). High-resolution imaging and single-cell analysis via laser ablation-inductively coupled plasma-mass spectrometry for the determination of membranous receptor expression levels in breast cancer cell lines using receptor-specific hybrid tracers. *Analytica Chimica Acta, 1074*, 43-53. doi:10.1016/j.aca.2019.04.064

Van Berkel, G. J., Kertesz, V., Koeplinger, K. A., Vavrek, M., & Kong, A. T. (2008). Liquid microjunction surface sampling probe electrospray mass spectrometry for

detection of drugs and metabolites in thin tissue sections. *Journal of Mass Spectrometry, 43*(4), 500-508. doi:10.1002/jms.1340

Van der Heide, P. (2014). *Secondary ion mass spectrometry* (1st ed.). Hoboken, NJ: Wiley.

Vanbellingen, Q., Castellanos, A., Rodriguez-Silva, M., Paudel, I., Chambers, J., & Fernandez-Lima, F. (2016). Analysis of chemotherapeutic drug delivery at the single cell level using 3D-MSI-TOF-SIMS. *Journal of the American Society of Mass Spectrometry, 27*(12), 2033-2040. doi:10.1007/s13361-016-1485-y

Veličković, D., Chu, R. K., Carrell, A. A., Thomas, M., Paša-Tolić, L., Weston, D. J., & Anderton, C. R. (2018). Multimodal MSI in conjunction with broad coverage spatially resolved MS2 increases confidence in both molecular identification and localization. *Analytical Chemistry, 90*(1), 702-707. doi:10.1021/acs.analchem.7b04319

Vernon, W. B. (1988). The role of magnesium in nucleic-acid and protein metabolism. *Magnesium, 7*(5-6), 234.

Vismeh, R., Waldon, D. J., Teffera, Y., & Zhao, Z. (2012). Localization and quantification of drugs in animal tissues by use of desorption electrospray ionization mass spectrometry imaging. *Analytical Chemistry, 84*(12), 5439-5445. doi:10.1021/ac3011654

Vos, D. R. N., Bowman, A. P., Heeren, R. M. A., Balluff, B., & Ellis, S. R. (2019). Class-specific depletion of lipid ion signals in tissues upon formalin fixation. *International Journal of Mass Spectrometry, 446*, 116212. doi:10.1016/j.ijms.2019.116212

Walker, G. M. (1986). Magnesium and cell cycle control: An update. *Magnesium, 5*(1), 9.

Wang, F., Zhang, Z., Li, Q., Yu, T., & Ma, C. (2020). Untargeted LC–MS/MS analysis reveals metabolomics feature of osteosarcoma stem cell response to methotrexate. *Cancer Cell International, 20*(1), 1-269. doi:10.1186/s12935-020-01356-y

Wang, L., Park, P., & Lin, C. (2009). Characterization of stem cell attributes in human osteosarcoma cell lines. *Cancer Biology & Therapy, 8*(6), 543-552. doi:10.4161/cbt.8.6.7695

Wang, Q., Li, L., Gao, G., Wang, G., Qu, L., Li, J., & Wang, C. (2013). HIF-1α up-regulates NDRG1 expression through binding to NDRG1 promoter, leading to proliferation of lung cancer A549 cells. *Mol Biol Rep, 40*(5), 3723-3729. doi:10.1007/s11033-012-2448-4

Wang, Z., Wei, Q., Han, L., Cao, K., Lan, T., Xu, Z., Wang, Y., Gao, Y., Xue, J., Shan, F., Feng, J., & Xie, X. (2018). Tenascin-c renders a proangiogenic phenotype in macrophage via annexin II. *Journal of Cellular and Molecular Medicine, 22*(1), 429-438. doi:10.1111/jcmm.13332

Warburg, O. (1956). On the origin of cancer cells. *Science, 123*(3191), 309-314. doi: 10.1126/science.123.3191.309

Weaver, E. M., & Hummon, A. B. (2013). Imaging mass spectrometry: From tissue sections to cell cultures. *Advanced Drug Delivery Reviews, 65*(8), 1039-1055. doi:10.1016/j.addr.2013.03.006

Weiskirchen, R., Weiskirchen, S., Kim, P., & Winkler, R. (2019). Software solutions for evaluation and visualization of laser ablation inductively coupled plasma mass spectrometry imaging (LA-ICP-MSI) data: A short overview. *Journal of Cheminformatics, 11*(1), 1-21. doi:10.1186/s13321-019-0338-7

Wenke Feng, Fei Ye, Wanli Xue, Zhanxiang Zhou, & Y. James Kang. (2009). Copper regulation of hypoxia-inducible factor-1 activity. *Molecular Pharmacology, 75*(1), 174-182. doi:10.1124/mol.108.051516

Weston, L. A., & Hummon, A. B. (2013). Comparative LC-MS/MS analysis of optimal cutting temperature (OCT) compound removal for the study of mammalian proteomes. *Analyst, 138*(21), 6380-6384. doi:10.1039/c3an01121f

Wilde, L., Roche, M., Domingo-Vidal, M., Tanson, K., Philp, N., Curry, J., & Martinez-Outschoorn, U. (2017). Metabolic coupling and the Reverse Warburg Effect in cancer: Implications for novel biomarker and anticancer agent development. *Semin. Oncol. 44*(3), 193-203. doi: 10.1053/j.seminoncol.2017.10.004.

Wolf, F. I., & Trapani, V. (2008). Cell (patho)physiology of magnesium. *Clinical Science, 114*(1-2), 27-35. doi:10.1042/CS20070129

Wright Muelas, M., Roberts, I., Mughal, F., O'Hagan, S., Day, P. J., & Kell, D. B. (2020). An untargeted metabolomics strategy to measure differences in metabolite uptake and excretion by mammalian cell lines. *Metabolomics, 16*(10), 107. doi:10.1007/s11306-020-01725-8

Wu, C., Dill, A. L., Eberlin, L. S., Cooks, R. G., & Ifa, D. R. (2013). Mass spectrometry imaging under ambient conditions. *Mass Spectrometry Reviews, 32*(3), 218-243. doi:10.1002/mas.21360

Wu, T. T., & Kabat, E. A. (1970). An analysis of the sequences of the variable regions of bence jones proteins and myeloma light chains and their implications for antibody complementarity. *The Journal of Experimental Medicine, 132*(2), 211-250. doi:10.1084/jem.132.2.211

Wu, Z., Zhang, W., & Kang, Y. J. (2019). Copper affects the binding of HIF-1α to the critical motifs of its target genes. *Metallomics : Integrated Biometal Science, 11*(2), 429-438. doi:10.1039/C8MT00280K

Xia, J., Psychogios, N., Young, N., & Wishart, D. S. (2009). MetaboAnalyst: A web server for metabolomic data analysis and interpretation. *Nucleic Acids Research, 37*(suppl_2), W652-W660. doi:10.1093/nar/gkp356

Xiao, Y., Deng, J., Yao, Y., Fang, L., Yang, Y., & Luan, T. (2020). Recent advances of ambient mass spectrometry imaging for biological tissues: A review. *Analytica Chimica Acta, 1117*, 74-88. doi:10.1016/j.aca.2020.01.052

Xie, P., Liang, X., Song, Y., & Cai, Z. (2020). Mass spectrometry imaging combined with metabolomics revealing the proliferative effect of environmental pollutants on multicellular tumor spheroids. *Analytical Chemistry, 92*(16), 11341-11348. doi:10.1021/acs.analchem.0c02025

Xu, J., Zhou, J., Wei, W., & Wu, G. S. (2010). Activation of the akt survival pathway contributes to TRAIL resistance in cancer cells. *PloS One, 5*(4), e10226. doi:10.1371/journal.pone.0010226

Xu, R. N., Fan, L., Rieser, M. J., & El-Shourbagy, T. A. (2007). Recent advances in high-throughput quantitative bioanalysis by LC–MS/MS. *Journal of*

Pharmaceutical and Biomedical Analysis, 44(2), 342-355. doi:10.1016/j.jpba.2007.02.006

Yang, J., & Caprioli, R. M. (2011). Matrix sublimation/recrystallization for imaging proteins by mass spectrometry at high spatial resolution. *Analytical Chemistry, 83*(14), 5728-5734. doi:10.1021/ac200998a

Yang, Q., Zeng, B., Dong, Y., Shi, Z., Jiang, Z., & Huang, J. (2007). Overexpression of hypoxia-inducible factor-1α in human osteosarcoma: Correlation with clinicopathological parameters and survival outcome. *Japanese Journal of Clinical Oncology, 37*(2), 127-134. doi:10.1093/jjco/hyl137

Yin, R., Burnum-Johnson, K. E., Sun, X., Dey, S. K., & Laskin, J. (2019). High spatial resolution imaging of biological tissues using nanospray desorption electrospray ionization mass spectrometry. *Nature Protocols, 14*(12), 3445-3470. doi:10.1038/s41596-019-0237-4

Yu, F., & Choudhury, D. (2019). Microfluidic bioprinting for organ-on-a-chip models. *Drug Discovery Today, 24*(6), 1248-1257. doi:10.1016/j.drudis.2019.03.025

Zang, Q., Sun, C., Chu, X., Li, L., Gan, W., Zhao, Z., Song, Y., He, J., Zhang, R., & Abliz, Z. (2021). Spatially resolved metabolomics combined with multicellular tumor spheroids to discover cancer tissue relevant metabolic signatures. *Analytica Chimica Acta, 1155*, 338342. doi:10.1016/j.aca.2021.338342

Zavalin, A., Todd, E. M., Rawhouser, P. D., Yang, J., Norris, J. L., & Caprioli, R. M. (2012). Direct imaging of single cells and tissue at sub-cellular spatial resolution using transmission geometry MALDI MS. *Journal of Mass Spectrometry, 47*(11), 1473-1481. doi:10.1002/jms.3108

Zhang, J. Z., Bryce, N. S., Siegele, R., Carter, E. A., Paterson, D., de Jonge, M. D., Howard, D. L., Ryan, C. G., & Hambley, T. W. (2012). The use of spectroscopic imaging and mapping techniques in the characterisation and study of DLD-1 cell spheroid tumour models. *Integrative Biology: Quantitative Biosciences from Nano to Macro, 4*(9), 1072-1080. doi:10.1039/c2ib20121f

Zhang, L., Hatzakis, E., & Patterson, A. (2016). NMR-based metabolomics and its application in drug metabolism and cancer research. *Current Pharmacology Reports, 2*(5), 231-240. doi:10.1007/s40495-016-0067-9

Zhang, X., Qu, P., Zhao, H., Zhao, T., & Cao, N. (2019). COX-2 promotes epithelial-mesenchymal transition and migration in osteosarcoma MG-63 cells via PI3K/AKT/NF-κB signaling. *Molecular Medicine Reports, 20*(4), 3811-3819. doi:10.3892/mmr.2019.10598

Zhang, Z., Wang, H., Ding, Q., Xing, Y., Xu, Z., Lu, C., Luo, D., Xu., L., Xia, W., Zhou, C., & Shi, M. (2018). Establishment of patient-derived tumor spheroids for non-small cell lung cancer. *PloS One, 13*(3), e0194016. doi:10.1371/journal.pone.0194016

Zhao, K., Zhou, H., Zhao, X., Wolff, D. W., Tu, Y., Liu, H., Wei, T., & Yang, F. (2012). Phosphatidic acid mediates the targeting of tBid to induce lysosomal membrane permeabilization and apoptosis. *Journal of Lipid Research, 53*(10), 2102-2114. doi:10.1194/jlr.M027557

Zhong, M., Lee, C. Y., Croushore, C. A., & Sweedler, J. V. (2012). Label-free quantitation of peptide release from neurons in a microfluidic device with mass spectrometry imaging. *Lab on a Chip, 12*(11), 2037. doi:10.1039/c2lc21085a

Zhu, T., Tsuji, T., & Chen, C. (2010). Roles of PKC isoforms in the induction of apoptosis elicited by aberrant ras. *Oncogene, 29*(7), 1050-1061. doi:10.1038/onc.2009.344

Zimnicka, A. M., Tang, H., Guo, Q., Kuhr, F. K., Oh, M., Wan, J., Chen, J., Smith, K. A., Fraidenburg, D. R., Choudhury, M. S. R., Levitan, I., Machado, R. F., Kaplan, J. H., & Yuan, J. X. (2014). Upregulated copper transporters in hypoxia-induced pulmonary hypertension. *PloS One, 9*(3), e90544. doi:10.1371/journal.pone.0090544